

**HEAT REMOVAL CAPABILITY OF CALANDRIA VAULT
WATER FROM MOLTEN CORIUM INSIDE THE
CALANDRIA VESSEL DURING SEVERE ACCIDENT
CONDITIONS**

By

SUMIT VISHNU PRASAD

ENGG01201504001

Bhabha Atomic Research Centre, Mumbai

*A thesis submitted to the
Board of Studies in Engineering Sciences*

*In partial fulfilment of requirements
for the Degree of*
DOCTOR OF PHILOSOPHY
of
HOMI BHABHA NATIONAL INSTITUTE



July, 2021

Homi Bhabha National Institute¹

Recommendations of the Viva Voce Committee

As members of the Viva Voce Committee, we certify that we have read the dissertation prepared by *Sumit Vishnu Prasad* entitled "*Heat Removal Capability of Calandria Vault Water from Molten corium Inside the Calandria Vessel during Severe Accident Conditions*" and recommend that it may be accepted as fulfilling the thesis requirement for the award of Degree of Doctor of Philosophy.

Chairman - Prof. B. K. Dutta

BK Dutta

Date 10/07/2021

Guide / Convener – Prof. A. K. Nayak

A. K. Nayak

Date 10-07-2021

Co-guide - Prof. M. K. Samal

M. K. Samal

Date 10.07.2021

Examiner - Prof. P. K. Das

P. K. Das

Date 10.07.2021

Member 1- Prof. J. Chattopadhyay

J. Chattopadhyay

Date 10-7-2021

Member 2- Prof. T. A. Dwarakanath

T. A. Dwarakanath

Date 10/07/2021

Member 3- Prof. R. Balasubramaniam

R. Balasubramaniam

Date 10/07/2021

Member 3- Prof. Imran Ali Khan

Imran Ali Khan

Date 10/07/2021

Final approval and acceptance of this thesis is contingent upon the candidate's submission of the final copies of the thesis to HBNI.

I/We hereby certify that I/we have read this thesis prepared under my/our direction and recommend that it may be accepted as fulfilling the thesis requirement.

Date: 10/07/2021

Place: Mumbai

M. K. Samal
Signature 10.07.2021

Co-guide (if any)

CDs. M. K. SAMAL

A. K. Nayak
Signature 10-07-2021

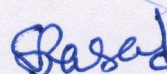
Guide

¹ This page is to be included only for final submission after successful completion of viva voce.

STATEMENT BY AUTHOR

This dissertation has been submitted in partial fulfilment of requirements for an advanced degree at Homi Bhabha National Institute (HBNI) and is deposited in the library to be made available to borrowers under rules of the HBNI.

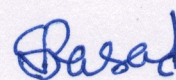
Brief quotations from this dissertation are allowable without special permission, provided that accurate acknowledgement of source is made. Requests for permission for extended quotation from or reproduction of this manuscript in whole or in part may be granted by the Competent Authority of HBNI when in his or her judgment the proposed use of the material is in the interests of scholarship. In all other instances, however, permission must be obtained from the author.



(Sumit Vishnu Prasad)

DECLARATION

I, hereby declare that the investigation presented in the thesis has been carried out by me. The work is original and has not been submitted earlier as a whole or in part for a degree /diploma at this or any other Institution / University.



(Sumit Vishnu Prasad)

List of Publications arising from the thesis

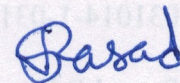
Journal

1. Prasad S.V. and Nayak A.K., 2020, Experimental evaluation of CHF in downward-facing boiling on SS304L flat plate relevant to in-calandria retention in PHWRs, ASME Journal of Nuclear Engineering and Radiation Science, Vol. 6, PP.031301-5
2. Sumit V. Prasad, A. K. Nayak and M. K. Samal, 2020, Development of correlation for natural convection heat transfer for large horizontal calandria vessel for in-calandria retention of corium in PHWRs, Nuclear Engineering and Design, Vol. 336, PP.1-8.
3. Prasad S.V., Kulkarni P.P., Yadav D.K., Verma P.K. and Nayak A.K., 2020, In-vessel retention of PHWRs: Experiments at prototypic temperatures, ASME Journal of Nuclear Engineering and Radiation Science, Vol. 06, PP. 011601-1- 011601-11.
4. Prasad S.V. and Nayak A.K., 2018, Experimental Study on melt coolability capability of calandria vault water during severe accident in Indian PHWRs for prolonged duration, ASME Journal of Nuclear Engineering and Radiation Science, Vol. 4, PP. 031014-1-031014-11.
5. Prasad S.V. and Nayak A.K., 2017, Investigation of thermo mechanical behaviour in the scaled PHWR stepped calandria vessel during severe accident, Nuclear Engineering and Design, Vol. 322, PP. 591–602.
6. Prasad S.V. and Nayak A.K., 2017, In-Calandria Retention of Corium in PHWR: Experimental Investigation and Remaining Issues, ASME Journal of Nuclear Engineering and Radiation Science, Vol.3, PP. 020909-1–020909-8.
7. Prasad S.V. and Nayak A.K., 2016, Experimental investigation of heat transfer during severe accident of a Pressurized Heavy Water Reactor with simulated decay heat generation in molten pool inside calandria vessel, Nuclear Engineering and Design, Vol. 303, PP.75–87.

8. Prasad S.V., Nayak A.K., Kulkarni P.P., Vijayan P.K., Vaze K.K., 2015, Study on heat removal capability of calandria vault water from molten corium in calandria vessel during severe accident of a PHWR, Nuclear Engineering and Design, Vol. 284, PP.130–142.

Conferences

1. Experimental Evaluation of Critical Heat Flux in Downward-Facing Boiling on Flat Plate Relevant to In-Vessel Retention in Indian PHWRs, Prasad S.V. and Nayak A.K., Indo US Science and technology Forum, 2018, 15th-19th December 2018, IITB.
2. “Experimental determination of CHF on downward facing flat plate simulating bottom of calandria vessel of PHWR, Prasad S.V., Kulkarni P. P., Verma P. K., Nayak A.K. and Sinha S. K., National Conference on Critical Heat Flux and Multiphase Flow, 2018, December 22-23.



(Sumit Vishnu Prasad)

DEDICATIONS

To my family

[For their unconditional support and incessant motivation]

ACKNOWLEDGEMENTS

Foremost, I would like to express my heartfelt gratitude to my Guide Dr A. K. NAYAK, O.S., (THS, RED, BARC) for the continuous support and enthusiastic encouragement throughout the research work. He spent innumerable hours proofreading my research papers, evaluating contemporary topics for me to investigate, and suggesting me with numerous ways to improve upon my dissertation.

I am highly obliged to my co-guide Dr M. K. SAMAL for giving me his reviews on my research work and specially on my seminar topic.

I would like to thank the doctoral committee members: Chairman of the committee, Dr. B. K. DUTTA and other members: Dr. J. CHATTOPADHYAY, Dr. T.A. DWARAKANATH, Dr. R. BALASUBRAMANIAM and Dr. IMRAN ALI KHAN for their insightful comments and encouragement but also the hard question which facilitated me to widen my research from various perspectives.

I am extremely thankful to Dr. G. SUGILAL, (PSDD, BARC), for letting me use his furnace for large amount of melt for the experiments. I am grateful to Dr. A. AWASTHI (MP&CED, BARC), who have provided special guidance towards high temperature melts; thermite and scientific aspects of materials helped me a lot during my research.

I would also like mention and thank Shri D. G. BELOKAR(Retired) and Shri S. NAWATHE (RED, BARC), who are the in-charge of all workshop activities. They not only helped me in fabrication of all experimental setup with high quality, but also suggested me lot of practical improvement in my design. I am highly indebted to their team of supervisors and workshop assistants for their efforts in machining and fabrication of my experimental facilities.

I am immensely thankful to Smt. R. DATAR and Shri S.P. LIMAYE (RED, BARC), for helping me in instrumentation of all my experimental facilities. I am also thankful to their entire team for their timely efforts.

I am also very thankful to Dr. R. D. KULKARNI and Shri G. D. SRIVASTAVA (RED, BARC), for all the electrical work of my experimental facilities. I am sincerely grateful to their efficient team for the same.

I am also thankful to Dr. NAVEEN KUMAR, Dr. ANUJ KUMAR KANSAL, Dr. P. P. KULKARNI, Dr. MUKESH KUMAR, Shri KAPIL BODKHA, Shri P. K. VERMA, Sri D.C. YADAV, Shri P. PANDEY and all Thermal Hydraulics Sections' members for their friendly support and wonderful encouragement. I also thank Dr. NITENDRA SINGH, Shri SAIRAJGOPAL, Shri RAKESH KUMAR and Shri SAMYAK MUNOT for their support.

I would also like to thank all Dean, Homi Bhabha National University, Dean, Academic, administration and staff members for their constant cooperation in all administrative activities.

Last but not the least; I would like to thank my family: my parents, my wife RAKHI, sons SHASHWAT and SHSHANK for supporting me throughout this journey and my life in general.

Thanks for all your encouragement!

Table of Contents

| | |
|--|-------------|
| Table of Contents | x |
| Synopsis | xiv |
| List of figures..... | xxix |
| List of tables | xli |
| List of abbreviations..... | xlii |
| Nomenclature..... | xliv |
| Chapter 1..... | 1 |
| Introduction..... | 1 |
| 1.1 Background..... | 1 |
| 1.2 Severe accidents | 3 |
| 1.3 Severe Accident progression in PHWR | 6 |
| 1.4 Motivation and Need of the study | 10 |
| 1.5 Outline of the thesis | 11 |
| 1.6 Closure | 12 |
| Chapter 2..... | 13 |
| Literature Survey | 13 |
| 2.0 Introduction..... | 13 |
| 2.1 Literature on In-Vessel Retention experiments | 13 |
| 2.1.1 RASPLAV | 13 |
| 2.1.2 FOREVER (Failure of Reactor Vessel Retention) experiments | 14 |
| 2.1.3 SIMECO..... | 15 |
| 2.1.4 LAVA (Lower-plenum Arrested Vessel Attack) | 16 |
| 2.1.5 CHF for downward-facing boiling on a coated hemispherical vessel RASPLAV..... | 17 |
| 2.1.6 LIVE (Late In-Vessel phase Experiments)..... | 17 |
| 2.1.7 COPRA (Corium Pool Research Apparatus) | 18 |
| 2.2 Literature on In-Vessel Retention analysis..... | 19 |
| 2.3 Summary and applicability of past literature to present study | 22 |
| 2.4 Challenges of In-Vessel Retention Studies for PHWRs | 24 |
| 2.4.1 Difficulty in mechanistic modelling of corium coolability in calandria vessel..... | 24 |

| | |
|---|-----------|
| 2.4.2 Difficulty in conducting experiment of corium coolability in calandria vessel | 24 |
| 2.5 Gap Areas | 25 |
| 2.5 Main Objective/ Scope of research work | 26 |
| 2.6 Strategy for solving the scientific issues | 27 |
| 2.7 Closure | 28 |
| Chapter 3..... | 29 |
| Heat transfer behaviour from molten corium inside CV to the vault water - | |
| Decay heat dominated regime | 29 |
| 3.1 Introduction..... | 29 |
| 3.2 Heat transfer from corium inside CV to the vault water in decay heat dominated regime | |
| 32 | |
| 3.2.1 Scaling philosophy for decay heat dominated regime | 32 |
| 3.2.2 Experimental setup | 34 |
| 3.2.3 Instrumentation of the experimental setup..... | 40 |
| 3.2.4 Experimental procedure..... | 42 |
| 3.2.5 Results without Decay heat | 43 |
| 3.2.6 Results with decay heat..... | 50 |
| 3.2.7 Estimation of local heat flux and CV outer surface heat transfer coefficient | 59 |
| 3.2.8 Estimation of overall heat transfer coefficient | 66 |
| 3.3 Study of integrity of CV with stepped weld joints against high thermal load..... | 69 |
| 3.3.1 Experimental setup | 70 |
| 3.3.2 Instrumentation of experimental setup..... | 72 |
| 3.3.3 Experimental procedure..... | 76 |
| 3.3.4 Results | 76 |
| 3.4 Closure | 83 |
| Chapter 4..... | 85 |
| <i>Heat transfer behaviour from molten corium inside CV to the vault water -</i> | |
| <i>Stored heat dominated regime.....</i> | 85 |
| 4.1 Introduction..... | 85 |
| 4.2 Scaling for Stored Heat Dominated Regime | 85 |
| 4.3 Experimental setup..... | 87 |
| 4.4 Instrumentation of experimental set up..... | 89 |
| 4.5 Experimental Procedure: | 90 |
| 4.6 Experimental Results | 90 |
| 4.7 Estimation of CV outer heat flux and heat transfer coefficient | 95 |

| | |
|---|------------|
| 4.8 Closure | 97 |
| Chapter 5..... | 98 |
| Limiting heat flux on the outer CV- CHF in downward facing boiling | |
| surface..... | 98 |
| 5.1 Introduction..... | 98 |
| 5.2 Preceding studies on downward-facing CHF..... | 98 |
| 5.3 Experimental needs for CHF studies for PHWR CV..... | 99 |
| 5.4 Details of experimental setup | 100 |
| 5.5Details of instrumentation..... | 102 |
| 5.6 Experimental procedure | 104 |
| 5.7 Results discussion | 104 |
| 5.8 CHF mechanism..... | 111 |
| 5.9 Comparison with other experiments for downward-facing boiling..... | 112 |
| 5.10 Closure | 114 |
| Chapter 6..... | 115 |
| Correlation development of heat transfer coefficient for curved CV outer | |
| surface..... | 115 |
| 6.1 Introduction..... | 115 |
| 6.2 Natural convection heat transfer correlation development..... | 117 |
| 6.2.1 Dimensionless number and scaling in natural convection | 117 |
| 6.2.2 Correlation development for natural convection heat transfer | 121 |
| 6.3 Development of boiling natural convection heat transfer coefficient correlation.... | 126 |
| 6.3.1 Dimensionless number and Scaling..... | 127 |
| 6.3.2 Correlation for boiling natural convection heat transfer | 128 |
| 6.4 Validation of Correlation..... | 130 |
| 6.5 Closure | 133 |
| Chapter 7..... | 134 |
| Scaling effects of melt volume, decay heat, melt material on heat transfer | |
| behaviour | 134 |
| 7.1 Introduction..... | 134 |
| 7.2 Scaling effects of melt volume on heat transfer behaviour | 134 |
| 7.2.1 Details of test setup..... | 135 |

| | |
|---|------------|
| 7.2.2 Results of melt volume on heat transfer..... | 137 |
| 7.3 Scaling effects of decay heat on heat transfer behaviour..... | 140 |
| 7.3.1 Details of test setup..... | 140 |
| 7.3.2 Results of decay heat on heat transfer behaviour | 140 |
| 7.4 Scaling effects of different melt material on heat transfer behaviour..... | 142 |
| 7.4.1 Details of test setup..... | 142 |
| 7.4.2 Results of different melt simulant on heat transfer behaviour | 144 |
| 7.5 Closure | 145 |
| Chapter 8..... | 146 |
| CFD Simulation of Corium coolability in In-vessel retention | 146 |
| 8.1 Introduction..... | 146 |
| 8.2 CFD model –equations of corium coolability..... | 147 |
| 8.3 Boundary conditions | 149 |
| 8.4 Simulation of experiment | 149 |
| 8.5 Comparison of simulation results with experiment..... | 153 |
| 8.5.1 Without decay heat..... | 153 |
| 8.5.2 With decay heat..... | 156 |
| 8.6 CFD model extended to prototypic condition..... | 159 |
| 8.7 Prediction of CFD model for prototypic condition..... | 160 |
| 8.8 Applicability of experiment result to prototype | 165 |
| 8.9 Closure | 167 |
| Chapter 9..... | 168 |
| Conclusions and recommendation for future works | 168 |
| 9.1 Conclusions | 168 |
| 9.2 Future recommendation | 171 |
| 9.2.1 Conducting experiment with prototypic material and temperature | 171 |
| 9.2.2 Chemical interaction of corium with CV at different higher temperature..... | 171 |
| 9.2.3 Heat transfer study of in vessel heating of debris inside the CV..... | 171 |
| Reference | 172 |
| Appendix -1: Uncertainties in measurements | 181 |

Synopsis

1. Introduction

The Pressurised Heavy Water Reactors (PHWRs) have number of Engineered Safety Systems (ESSs) to restore the reactor to safe shutdown condition in the event of accidents. Most of the ESSs have redundant and diverse features. The purpose is to enhance the availability of these ESSs so that malfunction of one of them does not lead to the progression of accidents. In spite of all these, a low probability accident can be cast beyond the acceptable design basis envelope, which can lead to severe accident by failure of multiple ESSs. In such a scenario, the accident may cause failure of core cooling eventually leading to core collapse. The relocated fuel assembly forms a terminal debris bed which continues to generate decay heat. With time, the calandria vessel (CV) water is evaporated and terminal debris bed ultimately melts down forming a molten pool of corium. If the corium breaches the CV and enters the calandria vault, large amount of hydrogen and other gases will be generated due to molten core concrete interaction (MCCI), which pressurise the containment and may lead to early containment failure. Hence, In-vessel retention (IVR) of corium is the only option in PHWRs for mitigation of core melt down accident. In this approach, the molten corium is retained inside the CV by continually removing the stored heat and decay heat through the outer surface of the vessel by cooling using vault water and without hampering the integrity of the vessel. Therefore, for successful IVR, the integrity of CV is of upmost important. The motivation of this thesis is to demonstrate the robustness of the IVR strategy in PHWRs which mainly depend upon heat removal capability of calandria vault water from molten corium inside the CV.

2. Gap areas and scope of work

Based on the literature survey, it is now identified that no prior study has been done for IVR of molten corium in such large PHWR CV. The heat transfer phenomena inside the CV

which contains molten corium is very complex as it involves multiple modes of heat transfer (conduction through crust and CV, natural convection inside the melt and radiation heat transfer from top of crust to the vessel) associated with phase change (melting and solidification). The crust formation and its growth, during the cooling of molten corium, needs to be understood. The influence of decay heat inside the corium on heat transfer and crust formation rate is never established which needs to be understood. The natural convection heat transfer behaviors from single-phase to bulk boiling on the curved outer CV are not known. The phenomenology of Critical Heat Flux (CHF) on outer surface of CV under severe accident condition is very complex due to downward facing heating, boiling natural convection and geometry of very large diameter and length. The CHF for PHWR CV geometry is not established.

Mechanistic modeling of corium coolability is very difficult as corium is mixture of UO_2 , ZrO_2 , Zr, steel, etc. with occurrence of phase changes in melt during cooling i.e. melt to crust formation, transient heat transfer condition on outer curved vessel from single-phase to partial boiling and then fully boiling natural convection, multi-mode heat transfer inside the melt i.e. conduction, convection and radiation, non-uniform angular heating of CV due to partial filled corium in CV and lack of melt properties at wide temperatures ranging from 2500 °C to room temperatures. Current computational models are not robust enough to handle such multi component, multi-phase, multi-mode heat transfer and in fact, applicability of existing CFD codes for these simulations are not known. In view of this, experiments are mandatory for not only understanding the coolability behavior of molten corium located in the CV to the vault water but also data generation and empirical model developments.

Conducting experiments with prototype material and with large quantities are prohibitory. So, over the years, many investigators have used simulant materials with different volume to clarify the coolability behavior of molten corium. These tests involve complex high

temperature experiments (more than 2500 °C) which are highly challenging for melt creation with different simulant materials in large quantity. The conventional technologies for melt creation can produce up to a few liters using electrical heating furnace or by induction furnace. However, the temperature limits in electrical heating furnace are around 1500 °C and that of induction furnace limited to 2000 °C. To create simulant melt at temperatures close to 2500 °C is beyond the above capabilities. In addition, measurements at such high temperatures inside the melt are beyond the capability of existing technologies. Creating decay heat inside the corium melt is also equally challenging as heater material should withstand against high temperature melt for prolonged period. The scaling effect of melt volume and melt material on heat transfer behavior are never known, which needs to be understood.

In view of the above, there is a strong need for in-depth scientific understanding and detailed investigations of heat removal capability of calandria vault water from molten corium inside the CV during severe accident.

The above issues have been addressed in the following chapters of the thesis. Chapter 1 introduces the problem and detailed literature review is done in Chapter 2. Chapter 3 discusses the experiments carried out and insights obtained on heat transfer behavior from molten corium to the vault water in the decay heat dominated regime (i.e., when corium melt temp. < 1423 °C). Chapter 4 presents the experiments carried out and insights obtained on the heat transfer behavior from molten corium to the vault water in the stored heat dominated regime (i.e., when corium melt temp. > 1423 °C). Chapter 5 discusses the measured limiting heat flux, i.e., Critical Heat Flux on the outer CV for downward facing boiling surface. In chapter 6, new correlations on heat transfer coefficient for curved CV outer surface under single phase natural convection and full boiling conditions are presented. Chapter 7 discusses the adequacy of scaling effects of melt volume, decay heat, and melt material on heat transfer

behavior. In chapter 8, applicability of CFD code for simulation of corium coolability in the present severe accident scenario was discussed. Chapter 9 presents the conclusions of the entire study.

3. Heat transfer behavior from molten corium to vault water - Decay heat dominated regime

Scaling philosophy for decay heat dominated regime experiment has been worked out which includes material properties and heat transfer parameters. A scaled experimental facility, has been designed and fabricated to investigate the heat transfer of simulated molten corium from inside the CV to vault water for an Indian 700 MWe PHWR. Scaled experimental facility consists of high temperature molten melt generating induction furnace, cylindrical test section (300 NB) simulating CV, simulated calandria vault and high-density cartridge type heaters for simulating decay heat inside the melt. The test setup was fully instrumented and total 68 thermocouples were installed inside melt, inner and outer surface of CV and vault water. Experiments were conducted with and without decay simulation inside the melt. The glass was used as simulant melt as the thermal diffusivity and volumetric expansion coefficient of the simulant and corium are nearly same. These two parameters are very important in case of transient natural convection heat transfer from melt to water. 60 kg of molten glass at 1200 °C was poured into the setup. Figure 1 shows the experimentally observed temperature distribution of melt, CV inner and outer surface temperature, and crust thickness growth without decay heat under single phase natural convection on CV outer surface. High temperature gradient was observed within molten pool along the radial direction. Within two minutes from the start of the experiment, crust of about 20 mm thickness was formed. It took almost 2.5 hours to completely solidify the melt. Maximum average inner surface temperature of vessel is 265 °C and maximum average outer surface

temperature of vessel is 94 °C. No steam generation took place and when the vessel was opened, no gap between the crust and vessel was observed.

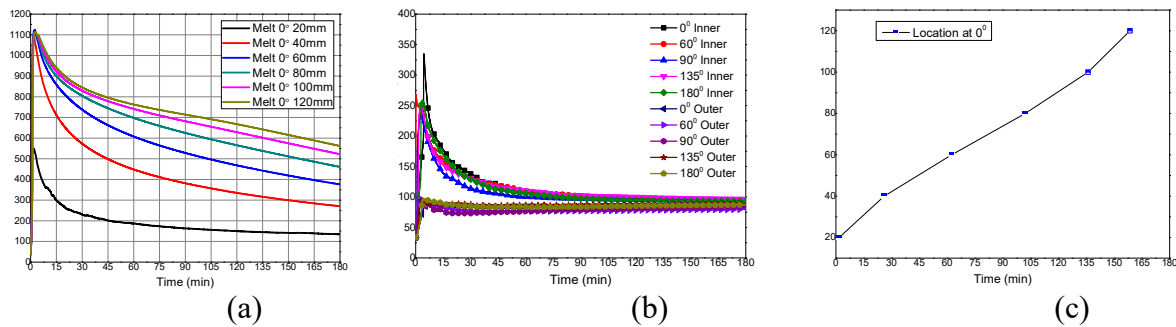


Figure 1: Without decay heat under single phase natural convection (a) Temperature distribution of melt from bottom of CV (b) Temperature distribution of CV inner and outer surface (c) crust thickness growth

The experiments were repeated with decay heat. Figure 2 shows the temperature distribution of melt, CV inner and outer surface and crust thickness growth with decay heat under single phase natural convection on CV outer surface. Maximum melt temperature reduced from 1100 °C to 830 °C and became steady. Crust thickness continuously grew up to 12 mm and CV inner and outer surface temperature reached steady state and maximum temperature is found 255°C and 102°C respectively. No steam formation was observed.

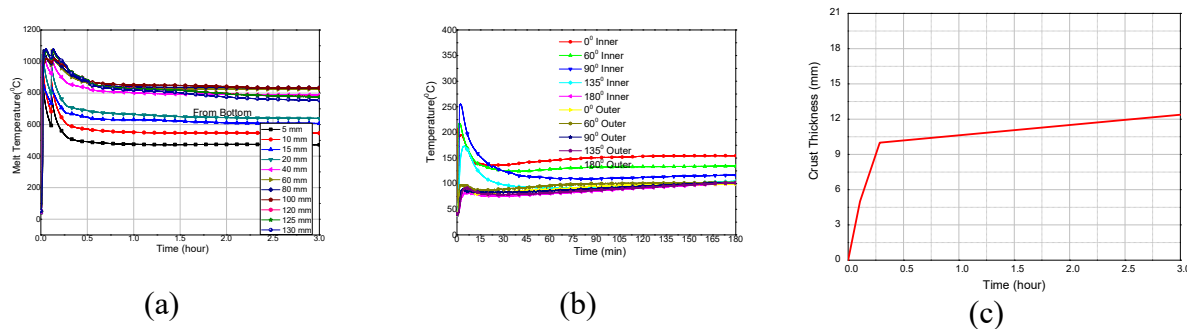


Figure 2: Decay heat under single phase natural convection (a) Temperature distribution of melt from bottom of CV (b) Temperature distribution of CV inner and outer surface (c) crust thickness growth

Figure 3 shows the temperature distribution of melt, CV inner and outer surface and crust thickness growth with decay heat underboiling natural convection on CV outer surface. No change in melt temperature condition was observed; crust thickness reached steady state and was found around 15 mm. Similarly, no change in CV inner and outer surface temperature

condition was observed. Boiling started in the vault water which leads to steam formation and drop in vault water level.

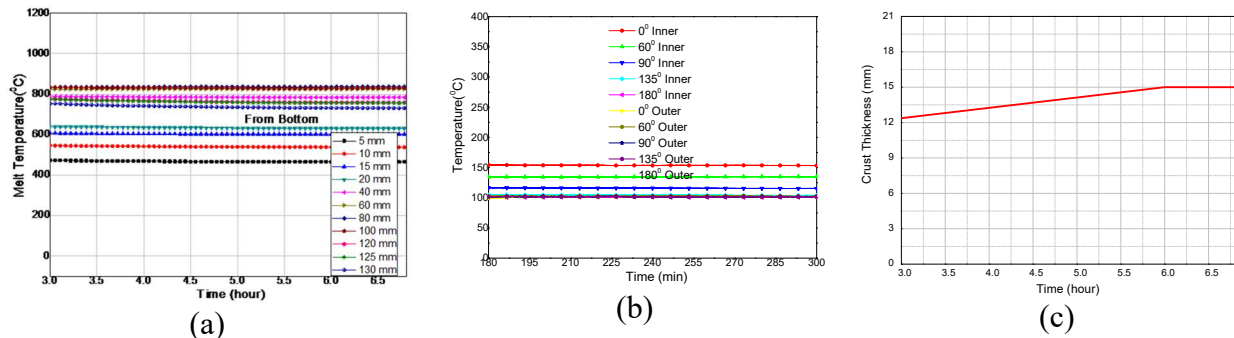


Figure 3: Decay heat under boiling natural convection (a) Temperature distribution of melt from bottom of CV (b) Temperature distribution of CV inner and outer surface (c) crust thickness growth

Based on the experimental results, heat flux and outer heat transfer coefficient were estimated and compared with all three cases (figure 4 (a) and 4 (b)). The maximum heat flux incident on the curved surface of CV is found to be $\sim 110 \text{ kW/m}^2$. The maximum local heat transfer coefficient is found to vary from $10000 \text{ W/m}^2\text{K}$ to $15000 \text{ W/m}^2\text{K}$ for single phase and boiling natural convection conditions respectively for decay heat cases. Also, overall heat transfer coefficients were estimated and found that it does not change with the convection regimes in outer surface of CV (i.e., single phase, partial boiling and full boiling) due to dominance of heat transfer resistance of crust which is very poor because of ceramic nature of the material. In decay heat case, main mode of heat transfer in melt is found to be conduction plus convection whereas in case of without decay heat, main mode is conduction only. The thermal strains on the outer wall of stepped CV during the experiments were measured and found to be maximum of 0.18%; thus, there were no deformations on the CV wall.

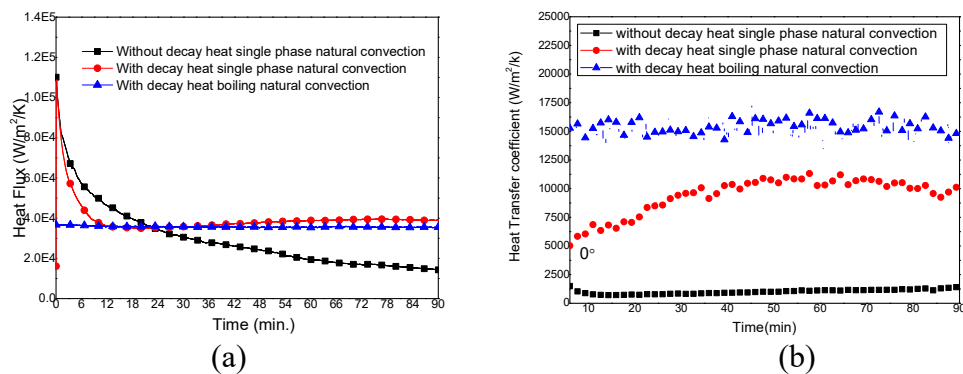


Figure 4: Comparison of all three cases for (a) heat flux (b) outer surface heat transfer coefficient at 0° location

4. Heat transfer behavior from molten corium to vault water – Stored heat dominated regime

The decay heat dominated regime experiments of in vessel corium coolability demonstrated the capability of long-term removal of the decay heat from corium melt by vault water. The integrity of CV in stored-heat dominated regime at high temperatures (~ 2500 °C) needs to be demonstrated experimentally. Scaling philosophy for this regime has been worked out which includes material properties and heat transfer parameters. Scaled experimental facility has been designed and fabricated which consists of integral thermite reactor used to generate high temperature melt above 2500 °C, cylindrical test section (450 NB) simulated CV and simulated calandria vault. The test setup was fully instrumented and total 30 thermocouples were installed inside melt, outer surface of CV and vault water. Near prototype simulant melt (CeO_2 (PuO_2 surrogate) + ZrO_2 + Al_2O_3 + Fe) was used.

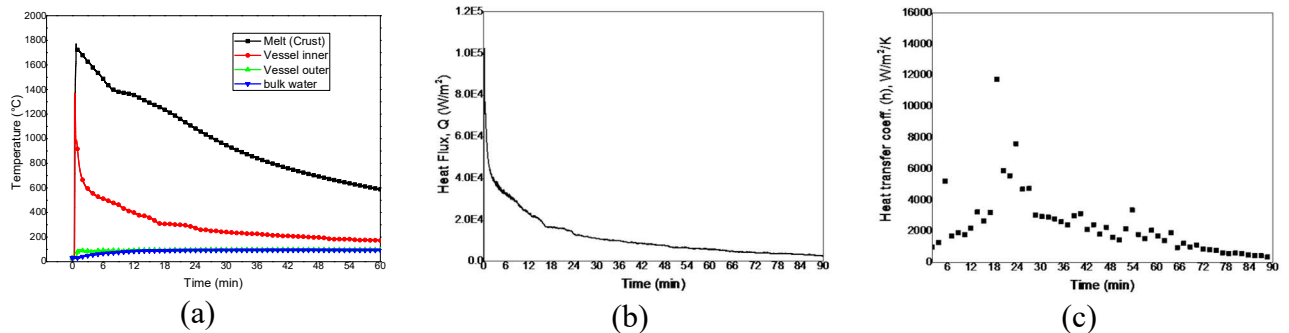


Figure 5: (a) Temperature distribution of melt, CV surface and vault water (b) heat transfer coefficient

Figure 5(a) shows the melt, CV surface and water temperature distribution. Melt at very high temperature ~ 2500 °C was poured inside of scaled CV but maximum melt temperature recorded inside vessel was ~ 2300 °C due to limitations of C-type thermocouples. Vessel temperatures initially shot up for a short period of time \sim a few minutes. Subsequently, due to crust formation, there is a rapid decrease in temperatures. CV outer surface remained near 100 °C, the vessel integrity was maintained and no deformation was observed. Based on the experimental results, heat flux and CV outer surface heat transfer coefficient (figure 5 (b) and

(c)) were estimated. The maximum heat flux incident on the CV wall is found to be ~ 110 kW/m².

The spatial average heat transfer coefficient in decay heat dominated regimes under single phase natural convection, conducted on 300 NB pipe is estimated to be in the range of 550 W/m²/k -5300 W/m²/k varying with time, whereas, the spatial average heat transfer coefficient in stored heat dominated regimes under single phase natural convection, conducted on 450 NB pipe, is estimated to be in the range of 400 W/m²/k -6200 W/m²/k varying with time. Subsequently, experiments were conducted on prototype sector of CV with same radius of curvature to determine the natural convection heat transfer behavior. It was found that under single phase natural convection, the spatial average heat transfer coefficient is in the range of 600 W/m²/k -5945 W/m²/k varying with time. Hence, the natural convection heat transfer behavior in the scaled facilities captures the prototype heat transfer behavior quite accurately.

5. Limiting heat flux on the outer CV- CHF in downward facing boiling surface

The above studies showed that the vault water can remove the maximum heat flux of ~ 100 - 110 kW/m² successfully by cooling the melt using the vault water. The question arises, what is the limiting heat flux the vault water can remove. This depends on the critical heat flux (CHF).

The phenomenology of CHF in CV under severe accident condition is very complex. This is due to downward facing natural convection boiling on the large CV outer surface. Due to large geometry, the bottom most part of CV almost behaves like a flat surface with downward natural convection boiling. The bubbles created under these conditions do not find a path to escape unlike the upward boiling conditions, thus resulting pre-matured CHF. These effects are difficult to simulate numerically. Hence, experimental study was conducted to estimate the CHF on outer surface of CV. The experimental setup (figure 6 (a)) consists of flat plate made of same SS304 L material (same as prototype CV material),

simulating the bottom portion of CV, water tank simulating vault water, bus bar and flexible for electrical connection and power supply. The experimental setup was extensively instrumented with thermocouples. The temperatures of flat test section and water pool were measured by Inconel sheathed 1 mm ungrounded K-type thermocouples. Six thermocouples were installed on upper as well as bottom surface of test section and three thermocouples were installed in water pool at different locations (total-15 thermocouples).

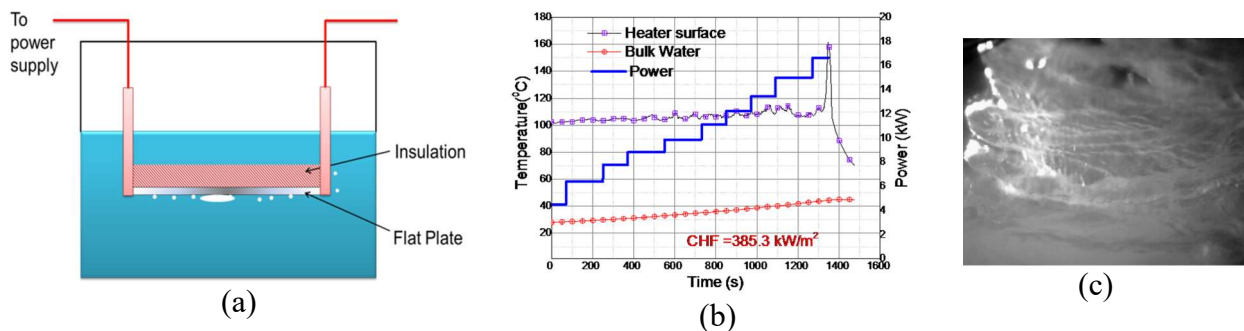


Figure 6: (a) schematic of CHF test setup assembly (b) Time history of temperature at 385 kW/m² (c) Bubble cover heated plate bottom at CHF

Figure 6 (b) show the experimentally observed heater surface temperature and power at CHF.

Measured values of CHF are 385 kW/m² and 251 kW/m² at water temperature 44 °C and 50 °C respectively. The experimental observation shows that CHF is strongly dependent on bulk liquid temperature up to 56 °C and beyond that with rise in temperature of the bulk liquid, CHF does not vary significantly. Instantaneous picture of bubble at bottom of the heated surface at CHF is shown in figure 6 (c).

The maximum imposed heat flux due to corium during the stored heat dominated experiments was found in the range of ~100-110 kW/m² whereas the minimum limiting heat flux on downward heated surface was measured ~210 kW/m². Hence, the maximum heat flux during core melt down is well below the limiting heat flux at CV outer surface.

6. Correlation development of heat transfer coefficient for curved CV outer surface

No empirical correlation is available in literature for large curved surface like CV with different outer heat transfer regimes (single phase and boiling natural convection) with non-uniform heating in confined geometry. The decay heat dominated regime experiments data are

used for development of the correlations. A natural convection heat transfer correlation (eq. (1) and (2)) have been developed for confined geometry of CV at different angles for single phase heat transfer regime, in which the non-dimensional Nusselt number (Nu) is defined as h^*D/k and modified Rayleigh number (Ra^{**}) is defined as $Pr^*Ra^*(Geom)^{-4.48}$ whereas Pr is Prandtl number and Ra is Rayleigh number. Based on the equation (1), angular variation of local heat transfer coefficient around cylinder can be calculated once modified Rayleigh number is determined, and, similarly by the equation (2), angular variation of local heat transfer coefficient can be estimated once averaged heat transfer coefficient is known.

$$\frac{Nu_{\theta}}{(Ra^{**})^{1/5}} = 0.934 - 0.0208\theta + 4.44 * 10^{-4}\theta^2 - 3.67 * 10^{-6}\theta^3 + 9.82 * 10^{-9}\theta^4 \quad (1)$$

$$\frac{Nu_{\theta}}{Nu_{avg}} = 1.596 - 0.039\theta + 8.27 * 10^{-4}\theta^2 - 6.86 * 10^{-6}\theta^3 + 1.85 * 10^{-8}\theta^4 \quad (2)$$

$$Nu = 0.106 \frac{Gr * pr^{1.81}}{Ja * Bo^{2.52}} Geom^{3.083} \quad (3)$$

Boiling natural heat transfer coefficient can be calculated by using equation (3) after estimating the non-dimensional Grashof number (Gr), Jakob Number (Ja), Prandtl number (Pr) and Bond number (Bo). The equation is valid in the nucleate boiling regime only. The above equations predict the heat transfer coefficient within 4.0% error.

7. Adequacy of scaling - effects of melt volume, decay heat, melt material on heat transfer behavior

There are concerns on scalability of the simulated experiments to the prototypic conditions, especially with regard to melt volume (experiments we use a few liters of melt vis-à-vis several tons of corium in the reactor), melt material (simulants vis-à-vis prototype corium), and presence of decay heat. To address these concerns, experiments were conducted with different volumes of melt, different decay heat and different melt compositions. Our results showed that the experiments conducted with different melt volumes produce similar results on

the CV outer surface temperature. Similar results were observed with different melt materials. The decay heat was found to have strong effect on crust formation and growth which has strong influence on heat transfer from melt to vault water.

8. CFD Simulation of corium coolability in PHWR

For the first time, an attempt has been made to apply the CFD code for simulation of corium coolability in the present severe accident scenario. The CFD model was first benchmarked with experiments and then extended to prototypic condition.

2-D analysis was carried out for experimental geometry. The molten pool, air -vapor domain above molten pool and vessel wall were taken as interior condition. The inner and outer surfaces of cylindrical vessel were stationary wall hence no slip shear and coupled thermal condition were applied. At the outer surface of vessel, heat transfers were due to natural convection for single phase and nucleate boiling regimes. The heat transfer coefficient on CV outer surface was simulated by applying our developed correlation.

An illustration of the domain mesh is shown in figure 7(a), figure 7(b) shows the temperature profile for scaled model at 2-minute time and figure 7(c, d) show the comparison of CFD predictions and experiments of melt on CV inner surface temperature distribution. It is observed that the predicted and experimental results are in very good agreement.

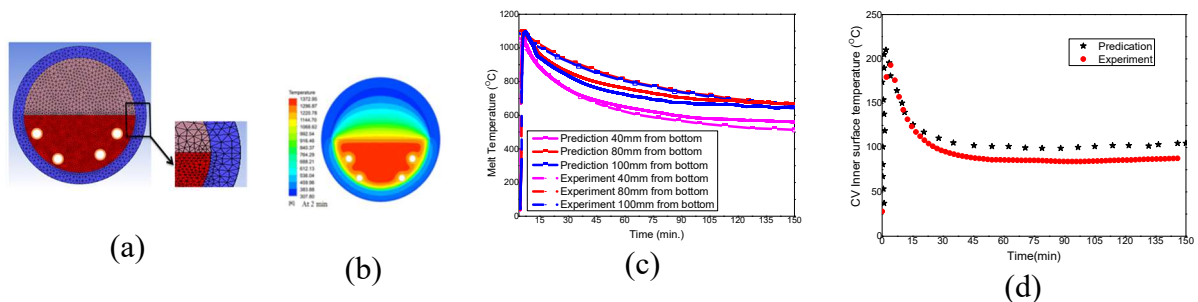


Figure 7: (a) Geometry meshing (b) Temperature contour profile at 2-minute (c) Comparison of melt temperature at different radial locations (d) Comparison of CV Inner surface temperature

CFD model is extended to prototypic condition and actual CV was modeled in 2-D. Similar boundary conditions were considered and same grid pattern (figure 8 (a)) was used with higher grid size. The phenomena considered are natural convection in melt pool, solidification

and melting in molten debris, conduction in vessel, convection on outer side of vessel. The simulation starts when the moderator has already boiled off and the debris bed is at liquidus temperature ($\approx 2677\text{ }^{\circ}\text{C}$) with decay heat generation of 1 MW/m^3 and being indirectly cooled by calandria vault water, which is at $60\text{ }^{\circ}\text{C}$.

Figure 8 (b) shows the contours of corium temperature inside CV at 2 hours. As CFD analysis progresses, the temperature of corium increases due to decay heat, melt pool is formed at the center and convection was observed inside it. It was observed that, melt was completely surrounded by the solid crust which was at low temperature (average crust temperature was $\sim 1873\text{ K}$ ($1600\text{ }^{\circ}\text{C}$)). Because of crust formation, CV inner surface was insulated from high temperature corium.

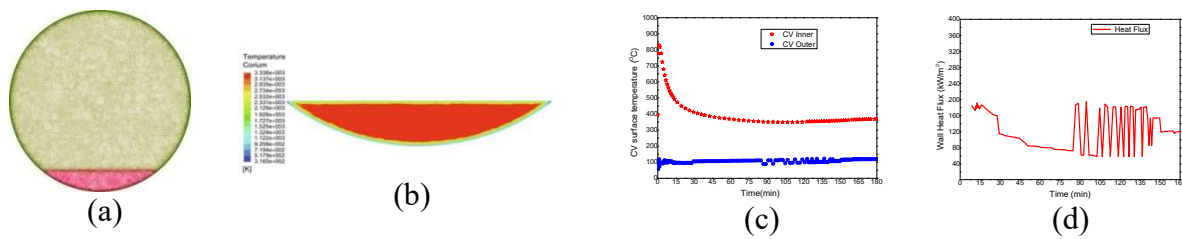


Figure 8: (a) Geometry meshing (b) Temperature contour profile at 2 hours (c) CV Inner and outer surface temperature (d) heat flux

Figure 8 (c) shows the CV inner and outer surface temperature variation with time. After 1.5-hours, partial nucleate boiling was observed on the outer surface of CV and this was evident as CV outer surface temperature starts fluctuating with time. After 3 hours, the vessel outer temperature remains close to $120\text{ }^{\circ}\text{C}$ (393 K) and inner temperature remains around $400\text{ }^{\circ}\text{C}$ (673 K). Figure 8 (d) shows the CV outer wall surface heat flux variation with time. The predicted peak wall heat flux is $\sim 190\text{ kW/m}^2$ which is lower than the experimentally CHF value and hence demonstrating the IVR in the calandria of PHWRs.

9. Conclusions

The present research brought out the physics of corium coolability inside the large curved CV by vault water during the severe accident conditions of PHWRs. It also gave new insights regarding several unexplained phenomena of heat transfer in IVR of corium. The heat

removal capability of vault water from molten corium inside the CV was determined at both decay heat dominated regimes and stored heat dominated regimes, effects of different parameters on the coolability were determined, CHF on outer surface of CV was measured, heat transfer correlations were developed and finally, coolability in reactor severe accident conditions was predicted. On the basis of this study, the following conclusions can be drawn.

1. As soon as the melt comes in contact with the cold CV surface, crust formation occurs. Due to the crust formation around the melt, the vessel temperatures remained very low although the melt temperature was very high; decay heat was safely removed as long as water is present in the vault. The low CV temperatures ensure no stresses in the vessel which help in maintaining its structural integrity.
2. Even though the melt is at very high temperature inside the vessel (more than 2500 °C), the CV wall temperatures were very low, CV integrity was maintained and no deformation was observed.
3. CHF was found to be strongly dependent on water temperature up to 56 °C only and beyond that temperature, it does not vary significantly. From CHF value ($\sim 210 \text{ kW/m}^2$) and the imposed heat flux ($\sim 110 \text{ kW/m}^2$) on the CV due to corium, it is evident that sufficient thermal margin is available in current PHWRs for IVR.
4. Comprehensive insights of main mode of heat transfer from melt to vault water in stored heat dominated regime as well as decay heat dominated regime were obtained. The outer CV heat transfer coefficient was found to be of the order $\sim 3000 \text{ W/m}^2 \text{ K}$ and $\sim 11000 \text{ W/m}^2 \text{ K}$ in single phase and boiling regimes respectively. An empirical model has been developed for the local heat transfer coefficient on CV wall outer surface for both single phase and boiling two phase conditions.
5. The decay heat was found to have strong effect on crust formation and growth which has strong influence on heat transfer from melt to vault water. Effect of decay heat on crust

growth is also understood. Results showed that the experiments conducted with different melt volumes and different melt material produce similar results on the CV outer surface temperature.

6. CFD model was benchmarked with experimental data which has given lot of confidence and insights regarding analysis of in-vessel retention. The analysis was extended to prototypic condition and it now evident that CV wall temperature remains very low during severe accident conditions and heat flux was well below $\sim 210 \text{ kW/m}^2$.

Bibliography

1. IAEA-TECDOC-1594, 2008, Analysis of Severe Accidents in Pressurized Heavy Water Reactors, International Atomic Energy Agency, Vienna, PP. 1-139.
2. Bajaj, S.S., Gore, A.R., 2006, The Indian PHWR. Nuclear Engineering Design, Vol. 236 (7–8), PP. 701–722.
3. S. Y. Park and K.I. Ahn, 2012, Comparative analysis of station blackout accident progression in typical PWR, BWR, and PHWR, Nuclear Engineering and Technology, Vol.44 (3), PP. 311-322
4. Mathew, P. M., Nitheanandan, T., and Bushby, S. J., 2008, “Severe Core Damage Accident Progression Within a CANDU 6 Calandria Vessel,” ERMSAR Seminar, 3rd European Review Meeting on Severe Accident Research, Nessebar, Bulgaria, Sept. 23–25.
5. Sehgal B.R.et. al., 2003, Assessment of reactor vessel integrity (ARVI), Nuclear Engineering and Design, Vol. 221, PP. 23-53.
6. Sugilal, G., Sengar, P.B.S, 2008, Cold Crucible induction melting technology for vitrification of high-level waste: development and status in India. In: WM 2008 Conference, Phoenix, AZ, February 24–28, PP. 1-12.

7. Holman, J.P., 2008. Heat Transfer, 9th edition, Tata McGraw Hill.
8. Jeong Y.H., Chang S.H., Baek W.P., 2005, Critical heat flux experiments on the reactor vessel wall using 2-D slice test section, Nuclear technology, Vol. 152 (2), PP.162–169.
9. Cheung F.B., Haddad K.H., Liu Y.C., 1997, Critical Heat Flux (CHF) Phenomenon on the downward facing curved surface, NUREG/CR-6507 PSU/ME-7321, PP. 1-172.
10. Theofanous, T.G., Maguire, M., Angelini, S., Salmassi, T., 1997. The first results from the ACOPO experiment, Nuclear Engineering Design, Vol. 169, PP. 49-57.

List of figures

| | | |
|--|---|----|
| <i>Figure 1.1: (a) In Vessel corium Retention</i> | : | 5 |
| <i>Figure 1.1: (b) Core catcher</i> | : | 5 |
| <i>Figure 1.2: (a) PHWR core assembly (without vault water)</i> | : | 7 |
| <i>Figure 1.2: (b) Coolant Channel Assembly</i> | : | 7 |
| <i>Figure 1.3: Severe accident progression inside the calandria vessel</i> | : | 10 |
| <i>Figure 3.1: Heat input and heat loss variation with temperature</i> | : | 31 |
| <i>Figure 3.2: Melt configuration</i> | : | 33 |
| <i>Figure 3.3: Experiment set up: (a) without decay heat</i> | : | 34 |
| <i>Figure 3.3: Experiment set up: (b) with decay heat</i> | : | 35 |
| <i>Figure 3.3: Experiment set up (c) 3D model</i> | : | 35 |
| <i>Figure 3.3: Experiment set up (d) actual photograph of set up</i> | : | 36 |
| <i>Figure 3.3: Experiment set up (e) Top view of set up</i> | : | 36 |
| <i>Figure 3.4: (a) Schematic details of cartridge Heater</i> | : | 38 |
| <i>Figure 3.4: (b) Actual cartridge heater</i> | : | 38 |
| <i>Figure 3.4: (c) heater location inside melt</i> | : | 38 |

| | | |
|--|---|----|
| <i>Figure 3.5: Locations of thermocouples: (a) molten pool</i> | : | 41 |
| <i>Figure 3.5: Locations of thermocouples: (b) circumferential on test section</i> | : | 41 |
| <i>Figure 3.5: Locations of thermocouples: (c) longitudinal on test section</i> | : | 41 |
| <i>Figure 3.5: Locations of thermocouples: (d) water tank</i> | : | 42 |
| <i>Figure 3.6:(a) Temperature distribution inside molten pool at different radial height at 0°(bottom)</i> | : | 44 |
| <i>Figure 3.6:(b) Temperature distribution inside molten pool at different radial height at 45°</i> | : | 44 |
| <i>Figure 3.6: (c) Crust thickness variation with time</i> | : | 45 |
| <i>Figure 3.7: Temperature distribution of inner surface of test section (a) at axial location at 60°</i> | : | 46 |
| <i>Figure 3.7: Temperature distribution of inner surface of test section (b) at different circumferential location</i> | : | 46 |
| <i>Figure 3.8: Temperature distribution of outer surface of test section (a) at axial location at 90°</i> | : | 47 |
| <i>Figure 3.8: Temperature distribution of outer surface of test section (b) at</i> | : | 47 |

different circumferential location

Figure 3.9: (a) water level in water tank : 49

Figure 3.9: (b) water temperature in water tank at different elevation : 49

Figure 3.9: (c) Picture from top of the solidified melt after the test, no gap is : 50

observed between melt and vessel

Figure 3.10: With decay heat and single-phase natural convection on outer : 52

wall (a) Melt temperature

Figure 3.10: With decay heat and single-phase natural convection on outer : 52

wall (b) Crust thickness

Figure 3.10: With decay heat and single-phase natural convection on outer : 53

wall (c) Inner CV temperature

Figure 3.10: With decay heat and single-phase natural convection on outer : 53

wall (d) Outer CV temperature

Figure 3.10: With decay heat and single-phase natural convection on outer : 54

wall (e) Water temperature

Figure 3.10: With decay heat and single-phase natural convection on outer : 54

wall (f) Water level

Figure 3.11: With decay heat and boiling heat transfer on vessel outer : 56

surface (a) Melt temperature

Figure 3.11: With decay heat and boiling heat transfer on vessel outer : 56

surface (b) Crust thickness

Figure 3.11: With decay heat and boiling heat transfer on vessel outer : 57

surface (c) Inner CV temperature

Figure 3.11: With decay heat and boiling heat transfer on vessel outer : 57

surface (d) Outer CV temperature

Figure 3.11: With decay heat and boiling heat transfer on vessel outer : 58

surface (e) Water temperature

Figure 3.11: With decay heat and boiling heat transfer on vessel outer : 58

surface (f) Water level

Figure 3.12: Outer wall heat flux (a) without decay heat : 61

Figure 3.12: Outer wall heat flux (b) with decay heat : 61

Figure 3.13: Comparison of outer heat transfer at different circumferential : 63

location (a) 0°

Figure 3.13: Comparison of outer heat transfer at different circumferential : 63

location (b) 45

Figure 3.13: Comparison of outer heat transfer at different circumferential : 64

location (c) 90°

Figure 3.13: Comparison of outer heat transfer at different circumferential : 64

location (d) 135°

Figure 3.13: Comparison of outer heat transfer at different circumferential : 65

location (e) 180°

Figure 3.13: Comparison of outer heat transfer at different circumferential : 65

location (f) averaged

Figure 3.14: (a) Variation of inner and overall heat transfer coefficient for : 68

decay heat with single phase natural convection

Figure 3.14: (b) Variation of inner and overall heat transfer coefficient for : 68

decay heat with two phase boiling natural convection

Figure 3.14: (c) comparison of overall heat transfer coefficient at different : 69

circumferential locations for both cases

Figure 3.15: (a) schematic of Stepped calandria : 71

Figure 3.15: (b) Stepped calandria : 71

Figure 3.15: (c) Stepped calandria vessel set up : 72

Figure 3.16: (a) longitudinal location of thermocouples on inner surface : 73

Figure 3.16: (b) circumferential location of thermocouples on inner surface : 74

Figure 3.16: (c) longitudinal location of thermocouples on outer surface : 74

Figure 3.16: (d) circumferential location of thermocouples on outer surface : 75

Figure 3.16: (e) location of thermocouples in melt pool : 75

Figure 3.16: (f) location of strain gauges on outer surface : 76

Figure 3.17: (a) Temperature distribution of molten pool at different radial : 77

heights

Figure 3.17: (b) Crust thickness variation with time : 77

Figure 3.18: Temperature distribution in stepped test section (a) Main shell : 79

Figure 3.18: Temperature distribution in stepped test section (b) Annular : 79

plate

| | | |
|--|---|----|
| <i>Figure 3.18: Temperature distribution in stepped test section (c) Small shell</i> | : | 80 |
| <i>Figure 3.18: Temperature distribution in stepped test section (d) Weld</i> | : | 80 |
| <i>Figure 3.19: Measured experimental strain variation in stepped test section</i> | : | 81 |
| <i>of (a) Main shell</i> | | |
| <i>Figure 3.19: Measured experimental strain variation in stepped test section</i> | : | 82 |
| <i>of (b) Annular plate</i> | | |
| <i>Figure 3.19: Measured experimental strain variation in stepped test section</i> | : | 82 |
| <i>of (c) Small shell</i> | | |
| <i>Figure 3.19: Measured experimental strain variation in stepped test section</i> | : | 83 |
| <i>of (d) Weld</i> | | |
| <i>Figure 4.1: Experimental setup (a) Schematic</i> | : | 88 |
| <i>Figure 4.1: Experimental setup (b) Actual</i> | : | 88 |
| <i>Figure 4.2: Instrumentation scheme (a) Inside Melt</i> | : | 89 |
| <i>Figure 4.2: Instrumentation scheme (b) Cylindrical test vessel</i> | : | 90 |
| <i>Figure 4.3: Melt temperature variation at different radial height</i> | : | 91 |
| <i>Figure 4.4: Melted Molybdenum sheath of thermocouple</i> | : | 91 |

| | | |
|--|---|-----|
| <i>Figure 4.5: Vessel inner wall temperature</i> | : | 92 |
| <i>Figure 4.6: Vessel outer wall temperature</i> | : | 93 |
| <i>Figure 4.7: Vault water temperature</i> | : | 93 |
| <i>Figure 4.8: Comparison of temperatures of melt, vessel inner, vessel outer and bulk water</i> | : | 94 |
| <i>Figure 4.9: (a) CV outer Heat flux</i> | : | 96 |
| <i>Figure 4.9: (b) Outer heat transfer coefficient</i> | : | 96 |
| <i>Figure 5.1: (a) PHWR vault with CV consist of molten pool</i> | : | 100 |
| <i>Figure 5.1: (b) test section from CV</i> | : | 101 |
| <i>Figure 5.1: (c) schematic of test setup assembly</i> | : | 101 |
| <i>Figure 5.2: Downward facing test section</i> | : | 102 |
| <i>Figure 5.3: (a) thermocouples on test section</i> | : | 103 |
| <i>Figure 5.3: (b) thermocouples in test setup</i> | : | 103 |
| <i>Figure 5.4: Typical CHF experiment results</i> | : | 105 |
| <i>Figure 5.5: (a) Time history of temperature at 385kW/m²</i> | : | 106 |
| <i>Figure 5.5:(b) Time history of temperature at 252kW/m²</i> | : | 106 |

Figure 5.5: (c)CHF variation with bulk fluid temperature : 107

Figure 5.6: Instantaneous pictures observed for Case1: When the heat flux 109
at 50% of CHF

Figure 5.7: Instantaneous pictures observed for Case2: When the heat flux : 111
at CHF

*Figure 6.1: (a) Variation of $Nu_{\theta}/Ra^{**0.2}$ with angular angle at different* : 123
bulk temperature

*Figure 6.1: (b) Variation of average $Nu_{\theta}/Ra^{**0.2}$ with angular angle* : 123

Figure 6.2: (a) Variation of Nu_{θ}/Nu_{avg} with angular angle at different bulk : 124
temperature

Figure 6.2: (b) Variation of average Nu_{θ}/Nu_{avg} with angular angle : 124

Figure 6.3: comparison of predicted and experimental measured value of (a) : 125
 *$Nu_{\theta}/Ra^{**0.2}$*

Figure 6.3: comparison of predicted and experimental measured value of (b) : 126
 Nu_{θ}/Nu_{avg}

Figure 6.4: Comparison of predicted and experimental measured value : 130

boiling natural convection heat transfer

Figure 7.1: 100 kg Test setup : 136

Figure 7.2: Instrumentation scheme for 100 kg test setup : 137

Figure 7.3: Comparison of Temperature with different melt volume (a) Melt : 138

Figure 7.3: Comparison of Temperature with different melt volume (b) CV : 139

inner surface

Figure 7.3: Comparison of Temperature with different melt volume (c) CV : 139

outer surface

Figure 7.4: Effect decay heat on crust thickness : 141

Figure 7.5: Comparison of CV outer surface temperature at different decay : 142

heat

Figure 7.6: CV outer temperature with different melt simulant : 144

Figure 8.1: Heat transfer modes in CV : 147

Figure 8.2: Schematic of 2D model domain for (a) Without decay heat case : 150

Figure 8.2: Schematic of 2D model domain for (b) Decay heat case : 150

Figure 8.3: Geometry meshing(a) without decay heat : 151

| | | |
|--|---|-----|
| <i>Figure 8.3: Geometry meshing (b)Decay heat</i> | : | 152 |
| <i>Figure 8.4: Temperature contour profile at (a) 2 minutes</i> | : | 153 |
| <i>Figure 8.4: Temperature contour profile at (b) 30 minutes</i> | : | 154 |
| <i>Figure 8.5: Comparison of melt temperature at 40 mm radial location</i> | : | 154 |
| <i>Figure 8.6: Comparison of CV Inner surface temperature</i> | : | 155 |
| <i>Figure 8.7: Comparison of CV Outer surface temperature</i> | : | 155 |
| <i>Figure 8.8: Melt Temperature contour profile with decay heat at (a) 2 minutes</i> | : | 156 |
| <i>Figure 8.8: Melt Temperature contour profile with decay heat at (b) 30 minutes</i> | : | 157 |
| <i>Figure 8.9: Comparison of melt temperature with decay heat at 40 mm radial location</i> | : | 157 |
| <i>Figure 8.10: Comparison of CV Inner surface temperature with decay heat</i> | : | 158 |
| <i>Figure 8.11: Comparison of CV Outer surface temperature with decay heat</i> | : | 159 |
| <i>Figure 8.12: Mesh pattern of the prototypic CV geometry</i> | : | 160 |
| <i>Figure 8.13: Temperature contours in the corium (a) 1800 s</i> | : | 161 |

| | | |
|---|---|-----|
| <i>Figure 8.13: Temperature contours in the corium (b) 3600 s</i> | : | 161 |
| <i>Figure 8.13: Temperature contours in the corium (c) 7200 s</i> | : | 162 |
| <i>Figure 8.13: Temperature contours in the corium (d) 10800</i> | : | 162 |
| <i>Figure 8.14: Temperature variation of CV inner and CV outer wall at the bottom</i> | : | 163 |
| <i>Figure 8.15: Temperature of corium in vertical direction from bottom of calandria wall</i> | : | 164 |
| <i>Figure 8.16: Heat flux on the CV outer surface</i> | : | 165 |

List of tables

| | | |
|--|---|-----|
| <i>Table 2.1: Design difference between Lower head of PWR/BWR and PHWR</i> | : | 23 |
| <i>Table 3.1: Heat Transfer parameter</i> | : | 39 |
| <i>Table 3.2: Material properties comparison of glass and PHWR corium</i> | : | 39 |
| <i>Table 3.3: Experimental setup details</i> | : | 40 |
| <i>Table 3.4: Experimental stepped setup details</i> | : | 72 |
| <i>Table 3.5: Experimental average values of heat transfer coefficient for various cases</i> | : | 84 |
| <i>Table 4.1: Heat transfer scaling</i> | : | 86 |
| <i>Table 4.2: Properties of the simulant and corium</i> | : | 87 |
| <i>Table 5.1: Comparison of experimental value of downward heating CHF</i> | : | 113 |
| <i>Table 6.1: Constants of boiling correlations</i> | : | 129 |
| <i>Table 6.2: Comparison of dimensionless Rayleigh number in Experiment and prototype</i> | : | 131 |
| <i>Table 6.3: Comparison of Experiment and predicted value</i> | : | 132 |
| <i>Table 6.4: Comparison of Experiment and PHWR Vessel</i> | : | 133 |
| <i>Table 7.1: Comparison of simulant material property</i> | : | 143 |
| <i>Table 8.1: Comparison in stored heat dominated regime</i> | : | 166 |
| <i>Table 8.2: Comparison in decay heat dominated regime</i> | : | 166 |

List of abbreviations

| | | |
|---------|---|--|
| AP-600 | : | Advanced Passive pressurized water reactor 600MWe |
| AP-1000 | : | Advanced Passive pressurized water reactor 1000MWe |
| APR1400 | : | Advanced Power Reactor 1400 MWe |
| BWR | : | Boiling Water Reactor |
| CANDU | : | Canada Deuterium Uranium |
| CAP1400 | : | Chinese enlarged version of the AP1000 |
| CC | : | Core Catcher |
| CCLM | : | Cold Crucible Induction Melting |
| CFD | : | Computational Fluid Dynamics |
| CHF | : | Critical Heat Flux |
| COPRA | : | Corium Pool Research Apparatus |
| CT | : | Calandria Tube |
| DAS | : | Data Acquisition System |
| DNB | : | Departure from Nucleate Boiling |
| EPR | : | European Pressurized Reactor |
| ERVC | : | External Reactor Vessel Cooling |
| ESS | : | Engineered Safety Systems |
| FOREVER | : | Failure of Reactor Vessel Retention |
| GOI | : | Government of India |
| GW | : | Giga-Watt (unit of power) |
| HPR1000 | : | Hua-long Pressurized Reactor |
| IAEA | : | International Atomic Energy Agency |
| IVR | : | In-Vessel corium Retention |
| KAIST | : | Korea Advanced Institute of Science and Technology |

| | | |
|---------|---|--|
| LAVA | : | Lower-plenum Arrested Vessel Attack |
| LCDAs | : | Limited Core Damage Accidents |
| LIVE | : | Late In-Vessel phase Experiments |
| LOCA | : | Loss of Coolant Accident |
| LOECC | : | Loss of Emergency Core Cooling |
| MAAP -4 | : | Modular Accident Analysis Program Version 4 |
| MELCOR | : | Methods For Estimation Of Leakages And Consequences Of Releases |
| MCCI | : | Molten Corium Concrete Interaction |
| MOP | : | Ministry of Power |
| MW | : | Mega-Watt (unit of power) |
| NPP | : | Nuclear Power Plants |
| OPRD | | Over Pressurization Rapture Disc |
| PHWR | : | Pressurized Heavy Water Reactor |
| PT | | Pressure Tube |
| PWR | | Pressurized Water Reactor |
| RASPLAV | | RASPLAV Project (RASPLAV means “melt” in Russian language) |
| RELAP | : | Reactor Excursion and Leak Analysis Program |
| RPV | : | Reactor Pressure Vessel |
| SAM | : | Severe Accident Management |
| SAMG | | Severe Accident Management Guideline |
| SBLB | : | Subscale Boundary Layer Boiling |
| SCDAs | : | Severe Core Damage Accidents |
| SIMECO | : | SIMECO Facility at the Royal Institute of Technology |

| | | |
|--------|---|---|
| SULTAN | : | SULTAN facility (France/CEA/CENG) |
| TMI | : | Three Mile Island |
| TWh | : | Terawatt-hour (measure of electrical energy) |
| ULPU | : | A IVR-related full-scale boiling heat transfer facility at University of California at Santa Barbara |
| UN | : | United Nation |
| USA | : | United states of America |
| USD | : | US Dollar |
| VVER | : | Voda Voda Energo Reactor (Russian PWR) |
| WNA | : | World Nuclear Association |

Nomenclature

| | | |
|------------|---|---|
| A | : | Area (m^2) |
| Bo | : | Bond number ($(\rho_l - \rho_v) g D^2 / \sigma$) |
| Δc | : | Crust thickness, m |
| Cp | : | Specific heat (J/kg.K) |
| D | : | Diameter (m) |
| g | : | Acceleration due to gravity (m/s^2) |
| Gr | : | Grashof number ($g \beta \Delta T D^3 / \nu^2$) |
| h | : | local heat transfer coefficient ($\text{W/m}^2 \text{K}$) |
| h_{lv} | : | Latent heat of vaporization (J/kg) |
| ht | : | Height (m) |
| H | : | Enthalpy (J) |
| I | : | Current (A) |
| Ja | : | Jakob Number ($C_p \Delta T / h_{lv}$) |
| k | : | Thermal Conductivity (W/m K) |
| L | : | Characteristic length (m) |
| mC_p | : | Thermal Inertia (J/K) |
| M | : | Mass (kg) |
| MH | : | Melt height (m) |
| Nu | : | Nusselt number (hL/k) |
| Pr | : | Prandtl number (ν/α) |
| q'' | : | Heat flux (W/m^2) |
| Q | : | Heat (W) |
| Q''' | : | Heat per volume (W/m^3) |
| r | : | radius of cylinder, m |

| | | |
|------------|---|---|
| Ra | : | Rayleigh number |
| Ra** | : | Modified Rayleigh number |
| T | : | Temperature (°C) |
| ΔT | : | Temperature difference (°C) |
| t | : | Time (s) |
| u,v | : | Velocity components (m/s) |
| U | : | Characteristic velocity for x=L (m/s) |
| Uo | : | Overall heat transfer coefficient, W/m ² K |
| V | : | Volume (m ³) |
| Volt | : | Voltage |
| x | : | Thickness (m) |
| W | : | Width (m) |

Sub-script

| | | |
|------------------|---|----------------------|
| <i>avg</i> | : | Average |
| <i>c</i> | : | crust |
| <i>decay</i> | : | Decay Heat |
| <i>dn</i> | : | downward |
| <i>exp</i> | : | Experiment |
| <i>inner</i> | : | Vessel inner surface |
| <i>l</i> | : | Liquid |
| <i>melt</i> | : | Melt |
| <i>outer</i> | : | Vessel outer surface |
| <i>prototype</i> | : | Prototype |

| | | |
|----------------|---|-------------------|
| <i>s</i> | : | Surface/Wall |
| <i>surf</i> | : | Surface |
| <i>surr</i> | : | Surrounding |
| <i>th</i> | : | Total heat |
| <i>the</i> | : | Thermal |
| <i>totmelt</i> | : | Total melt |
| <i>tsh</i> | : | Total Stored Heat |
| <i>up</i> | : | upward |
| <i>v</i> | : | Vapour |
| <i>vault</i> | : | Calandria Vault |
| <i>vess</i> | : | Vessel |
| <i>water</i> | : | Water |
| θ | : | Angular variation |
| ω | : | Bulk |

Greek letters

| | | |
|----------|---|--|
| θ | : | Angular |
| ρ | : | Density (kg/m ³) |
| μ | : | Dynamic viscosity (Pa s) |
| ν | : | Kinematic viscosity (m ² /s) |
| σ | : | Surface Tension (N/m) |
| α | : | Thermal diffusivity (m ² /s) |
| β | : | Volumetric thermal expansion coefficient (1/K) |

Chapter 1

Introduction

1.1 Background

India is one of the largest developing economies and 2nd most populated country [1]. In year 2019, the government of India has also set the aim of USD 5 trillion economy by 2024 [2]. To achieve this challenging target, the development in the field of infrastructure is very crucial driver for economic growth. In infrastructure sector, power sector is considered as key component for sustained growth of the Indian economy. Country needs electricity to fuel its expanding industrial growth. A growing population also requires uninterrupted and adequate supply of energy for improvement of living standard. Based upon several estimates, massive addition of installed electric power generation is required by 2032.

Source of India's power sector is diversified [3] ranging from thermal, hydro, nuclear, wind, solar, agricultural and domestic waste. Sustainability and climate change are big concerns in power sector. Thermal power plants comprise ~65% of total capacity in the country which is also responsible for half of country's CO₂ emissions. As per action plan put forwarded by India in 2015 under the Paris Agreement sets target [4], to increase the share of non-fossil fuels to 40% of the total electricity generation capacity. It can be achieved by tapping vast potential solar, wind and nuclear power. Hence, the nuclear power installed capacity should increase by many folds from the present. The advantage of nuclear power with other non-fossil fuels is steady and un-interrupted power supply with no storage technology required compensating for the lean period when wind does not blow or sun does not shine.

At present, 31 countries are operating nuclear power plants. Most of these nuclear plants are located in North America, Europe, South Asia and East Asia. The USA is the biggest

producer of nuclear electricity whereas France has the largest share of electricity from nuclear. At the end of 2018, global nuclear generation is 2563 TWh [5] and the installed capacity of the world's 449 operable reactors is 397GWe. The number of total reactors under construction at the end of 2018 was 55. Out of this a considerable number of new reactors are under construction in China (11 in numbers) and India (7 in numbers). In India, Pressurized Heavy Water Reactors (PHWRs) are the main driver of nuclear power. At present 18 PHWRs are in operation which contributes the two - third of India installed nuclear power. Several PHWRs are under construction and many are in the planning stage.

However, the nuclear power growth worldwide has seen strong deceleration due to the following three major core melt accidents. In 1979, after the 25 years of start of first commercial nuclear power in the world, first major accident occurred in Three Mile Island unit 2 [6] which resulted in partial core melt down and radiation leakage threats in public domain. In 1986, one of the worst nuclear disasters in the history occurred at unit 4 of Chernobyl Nuclear Power Plant [7]. Another major disaster occurred [8] at Fukushima Daiichi nuclear power plant in year 2011. The root cause of Three Mile Island accident was component failure and operator errors, Chernobyl accident was due to design flaws and system failure whereas Fukushima accidents were due to natural disaster with prolonged power unavailability.

All these three major accidents create concerns in the society about the safety of nuclear power. Due to this, nuclear energy has taken a back seat around the world because of some concerns about safety of reactors. Hence, for growth of nuclear power and to fizzle out apprehension about nuclear safety, severe accident should be considered in design of advanced reactors and severe accident management guideline (SAMG) is being persuaded in operating nuclear reactors.

1.2 Severe accidents

As per IAEA [9], severe accident is considered to be more severe than a design basis accident, occurs with multiple failures of safety systems/components and involves significant core degradation. In case of PHWR, severe accident is further categorized as follow:

- a) Limited Core Damage Accidents (LCDAs): Accident in which the core geometry is preserved.
- b) Severe core damage accidents (SCDAs): Accident in which the core geometry is lost.

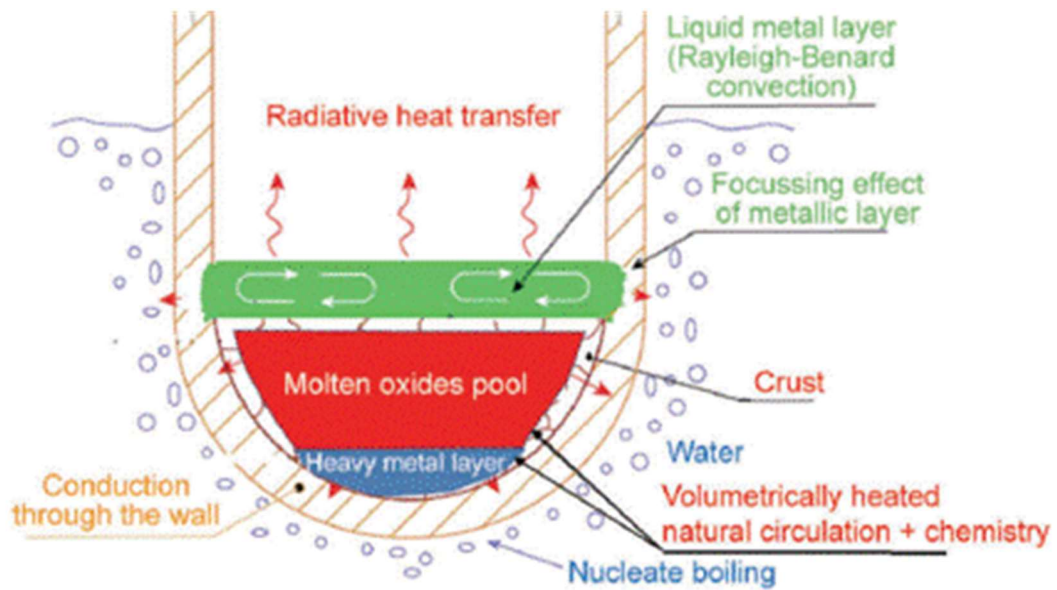
The core geometry lost means substantial melting of core. The core melt consists of molten fuel, clad and metallic structural material which is called '*Corium*'. Corium is extremely radioactive with high melting temperature ($\sim 2850^{\circ}\text{C}$). In PHWRs, after core collapse, the debris is relocated at the bottom of the reactor vessel. If the debris is not quenched, it can melt down and can cause calandria vessel (CV) failure, corium can relocate in the containment. Corium concrete interaction takes place in the raft which releases non-condensable gases such as CO, CO₂, hydrogen, etc. having potential threat of inducing containment failure and release of radioactivity in public domain. Hence, managing corium is extremely important inside the CV while dealing with severe accident scenario.

To mitigate the consequences of a severe accident, main strategy of severe accident management (SAM) for NPP is first to contain the corium and then ensure long term safe cooling for indefinite period. The first idea to contain the molten corium within the reactor vessel during severe accident was proposed by Theofanous [10] in early nineties. But due to the complexities in the cooling of the molten corium inside the reactor vessel, the distribution of the heat flux over the boundaries of the melt or vessel, it was impossible to establish the

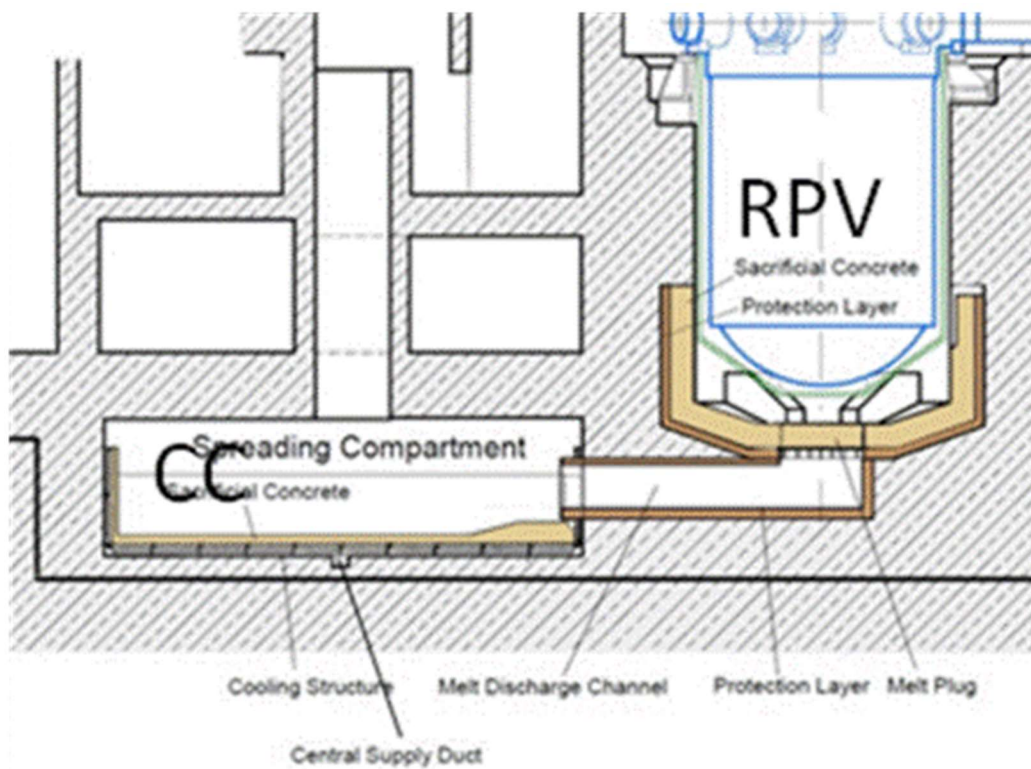
retention of corium in the reactor vessel of the high-capacity reactors. This gave rise to the ex-vessel core catcher concept.

In case of In-Vessel corium Retention (IVR) [11, 12] (inside the vessel) concept, when the core melt relocates to the bottom of the vessel and a molten pool is formed inside the lower vessel, at this time, the reactor cavity is flooded with cooling water from outside. Hence, if the decay heat is efficiently removed from the molten corium to surrounding water, then long-term integrity can be maintained. IVR design is adopted in AP-600 [13], AP-1000 [14], Advanced Chinese PWRs, APR1400 etc. Figure 1.1 (a) shows the concept of IVR. In case of Core Catcher (CC) [15], a device is provided at the bottom of vessel to catch and spread the molten core material during core meltdown and cooling the corium by addition of water to prevent it from escaping the containment building. Figure 1.1 (b) shows the concept of core catcher. Core catcher designs are deployed in the European Pressurized Reactor (EPR) [16], Russian VVER [17] etc.

The PHWR has horizontal thin pressure tubes which house fuel assemblies and cooled by heavy water. The pressure tubes are located in a horizontal position, inside a thin horizontal calandria tubes which is surrounded by a low-pressure heavy water moderator. These calandria tubes are housed inside the CV. The CV is surrounded by a light water-filled steel-lined concrete vault, called a calandria vault. A significant quantity of heavy water surrounding the fuel acts as a heat sink to remove the decay heat after a reactor shutdown. As design features of PHWR are different from Pressurized Water Reactor (PWR) or Boiling Water Reactor (BWR), the severe accident progression [18] and impact in PWR or BWR will be completely different from severe accident progression/conditions in PHWR.



(a)



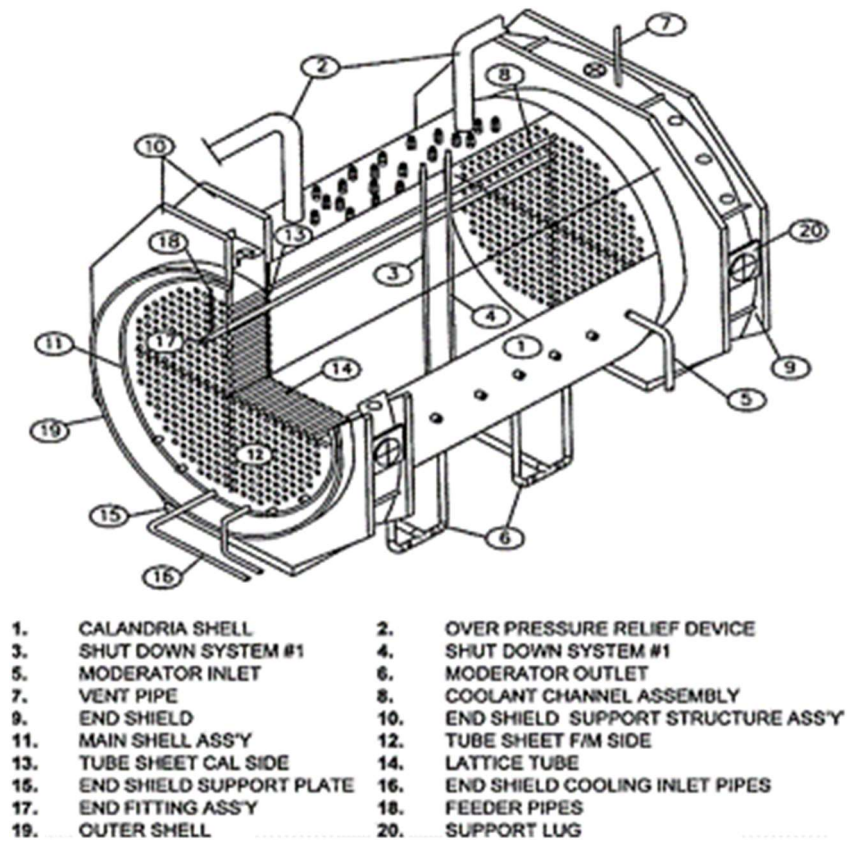
(b)

Figure 1.1: (a) In Vessel corium Retention [11] (b) core catcher [15]

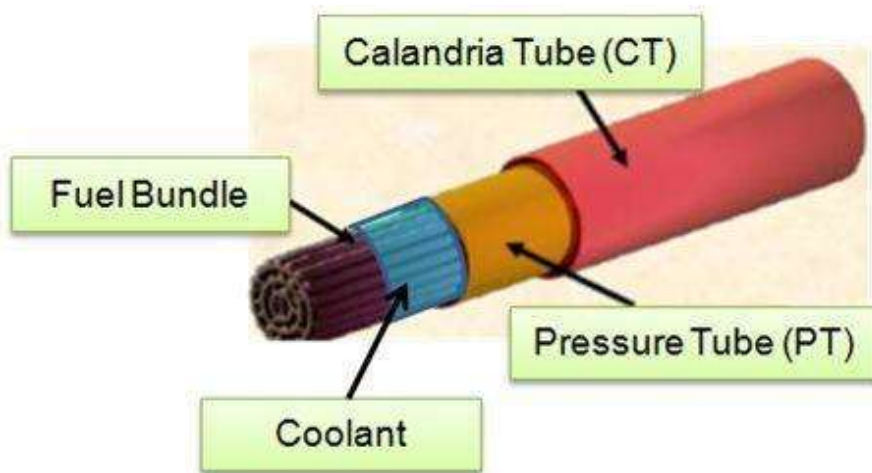
1.3 Severe Accident progression in PHWR

Indian 220 MWe PHWR core consists of 306 horizontal coolant channels whereas 540/700 MWe PHWR core consists of 392 horizontal coolant channels in a large cylindrical CV. Each pressure tube (PT) consists of 12 uranium dioxide (UO_2) fuel bundles of 19 elements configuration in 220 MWe, and 13 uranium dioxide (UO_2) fuel bundles of 37 elements configuration in 540 MWe. Hot pressurized heavy water as primary coolant flows inside the PT. The fuel is natural uranium dioxide and each fuel bundles has length of about 0.5 m. A calandria tube (CT) envelopes the PT and an insulating gas is filled between the CT-PT annulus. To maintain CT-PT annular gap throughout the length, garter springs are provided. Hence, the coolant channel assemblies house the fuel bundles, PT and CT and are mounted horizontally inside the CV. Figure 1.2 (a) shows a schematic of PHWR core assembly [19] and Figure 1.2 (b) shows the coolant channel assembly.

The low temperature heavy-water moderator is 100% filled in the CV and each coolant channel assembly is fully submerged in it. The calandria vessel has number of rupture discs, which open and release the moderator pressure in case of pressure rise in the CV due to unanticipated events. CV is surrounded by rectangular calandria vault, which is made of reinforced heavy concrete, approximately 11.0 m long, 5.7 m wide and 17 m high. This vault contains a large volume of low temperature light water to provide thermal shielding. To avoid water seepage to vault wall, SS liner is provided. The PHWRs have many engineered safety systems (ESSs) [20] to restore the reactor to safe shutdown condition in the event of accidents. Most of the ESSs have redundant and diverse features. The purpose is to enhance the availability of these ESSs so that malfunction of one of them does not initiate the progression of accidents.



(a)



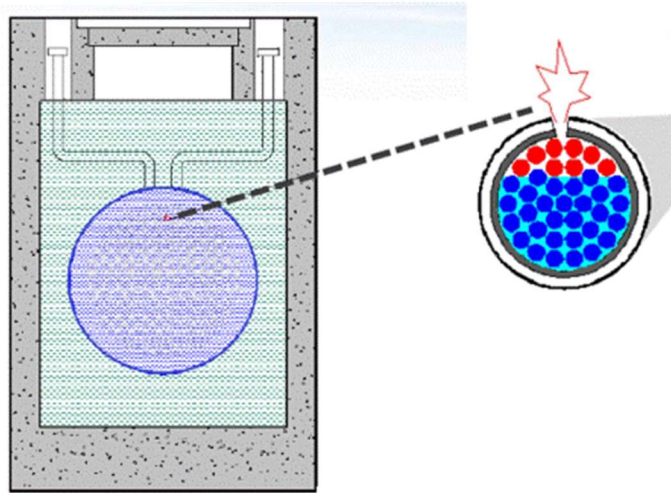
(b)

Figure 1.2: (a) PHWR core assembly (without vault water) [19] (b) Coolant Channel Assembly

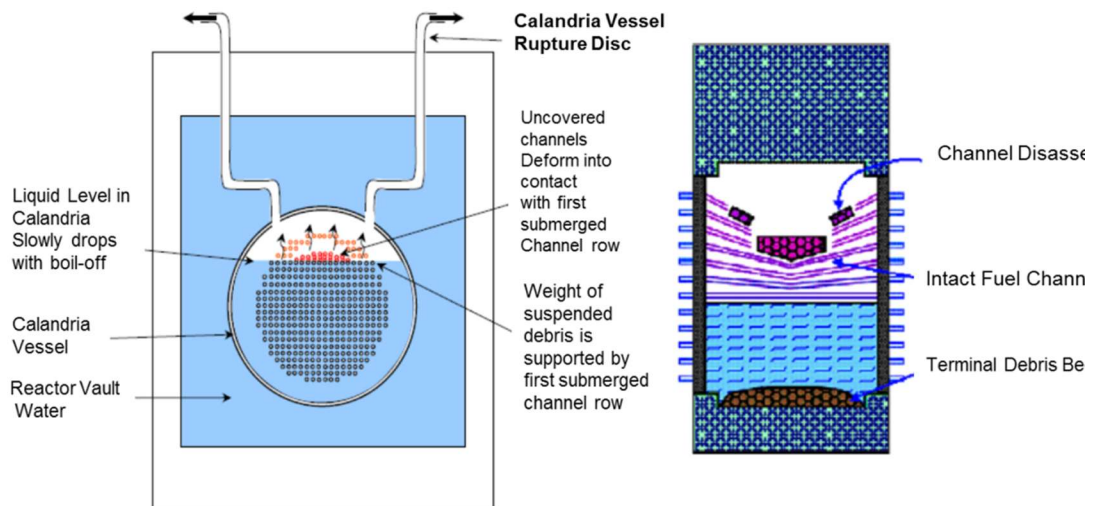
In spite of all these, a low probability accident can lead to beyond the acceptable design basis envelope which may lead to severe accident by failure of multiple ESSs. The initiating event which can lead to severe accident in PHWR are as follows:

- a) Prolonged Station Blackout with unavailability of cooling systems
- b) Loss of Coolant Accident (LOCA) with Loss of Emergency Core Cooling (LOECC) accompanied by loss of moderator cooling

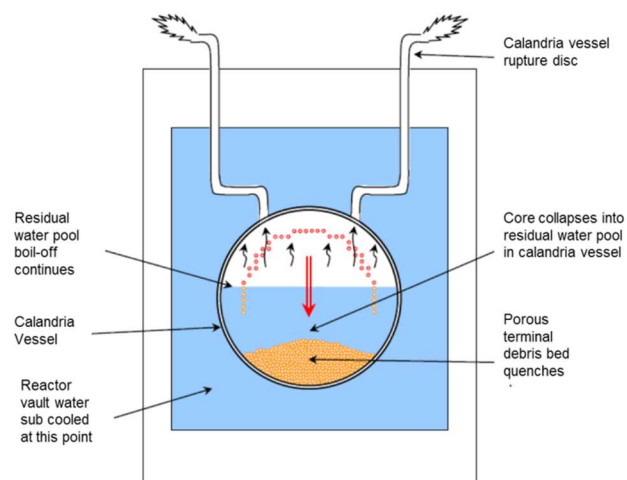
In such types of scenarios, loss of heat sink leads to fuel bundles heat-up, fuel bundles failure, PT-CT ballooning/sagging, PT-CT contact and subsequent heat transfer to moderator. If moderator cooling system is not available, moderator will start boiling which will pressurize the CV leading to opening of the Over Pressurization Rapture Discs (OPRDs). This will lead to moderator loss due to continuous boiling off and coolant channel uncover. These uncovered coolant channels will start sagging and after some time ultimately disassemble and the core will collapse. This abrupt collapsed core will form a debris bed at the bottom of the CV which still generates decay heat [21]. With time, the moderator is completely evaporated and the terminal debris bed ultimately melts down and forms a molten pool of corium. This heat is transferred to surrounding calandria vault water through CV wall. So, in this scenario, one side of CV has high temperature molten corium and other side of CV has low temperature vault water. Due to this, CV faces the high thermal load and its integrity is in question. Figure 1.3 shows different stages of severe accident progression inside the CV of an PHWR [22]. Figure 1.3 (a) shows the loss of heat sink which leads to fuel heat-up and fuel failure. Figure 1.3 (b) shows the moderator boiling and channel uncover whereas figure 1.3 (c) illustrates the core collapse and its relocation at the bottom of vessel. Finally, debris bed is converted into molten pool as shown in figure 1.3 (d).



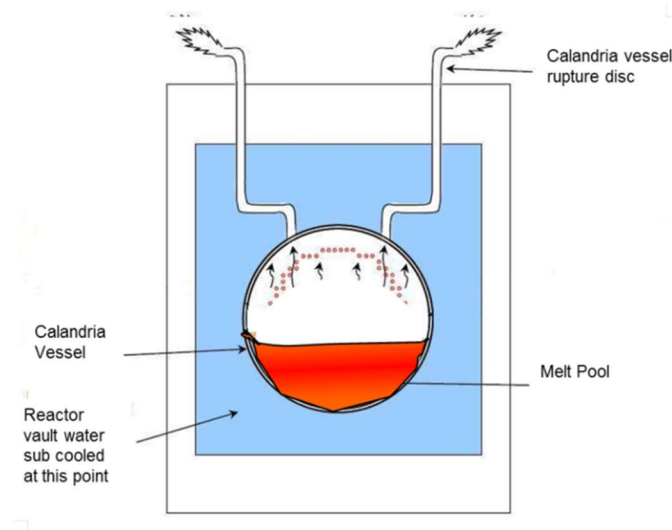
(a) Failure of fuel bundle



(b) Channel uncover



(c) Collapse and relocation of core at bottom of CV



(d) Molten pool inside CV

Figure 1.3: Severe accident progression inside the calandria vessel [22]

1.4 Motivation and Need of the study

IVR is only option in PHWRs for mitigation of core melt down. Literature shows that if molten corium penetrates the CV wall and enters the calandria vault, large amount of hydrogen, steam and other non-condensable gases will be generated due to metal steam reaction and molten corium concrete interaction (MCCI). This may lead to over pressurization of containment and may cause its early failure [23].

Therefore, IVR by CV external cooling using vault water is an important accident management programme in PHWR. In this approach, the molten corium is arrested or immobilized inside the CV by continually disposing the stored heat and decay heat through outer surface of the vessel by cooling water and without hampering the integrity of the vessel. Hence, for successful IVR, the integrity of CV is up most important. Integrity of vessel depend upon

- a) Coolability of high temperature molten corium by vault water through thin CV
- b) Withstand thermal load of corium

In summary, the robustness of IVR strategy in PHWR mainly depends on heat removal capability of calandria vault water from molten corium inside the CV.

1.5 Outline of the thesis

The research study is divided into nine chapters. Each chapter ends with a closure. The essence of each chapter is given as follows:

Chapter 1 discusses the introduction of the thesis presenting the background of the nuclear power scenario, severe accident and various designs for NPP to manage the core melt down accidents. This chapter also highlights the design features and various stage of severe accident progression in PHWR, the motivation and need of the study of in-vessel retention of PHWR.

Chapter 2 presents the detail insights from literature survey on in-vessel retention studies, identifies the unresolved scientific issues /gap area and scope of research work with strategy for solving it.

Chapter 3 focuses on the proposed scaling philosophy, details of experiments carried out with and without decay heat in the decay heat dominated regime (i.e., when corium melt temperature $< 1423\text{ }^{\circ}\text{C}$). Insights obtained from experiments with regards to melt temperature contours, crust growth and the influence of decay heat on melt coolability are presented. Estimated heat flux and heat transfer coefficient with angular variation for various cases are also discussed. Also, the details of experimental study for investigation of thermo mechanical behaviour in simulated stepped calandria vessel with weld joints are presented.

Chapter 4 discusses the proposed scaling philosophy, details of experiments carried out in the stored heat dominated regime (i.e., when corium melt temperature $> 1423\text{ }^{\circ}\text{C}$). Estimated heat flux and heat transfer coefficient are also discussed.

Chapter 5 discusses the details of experiments conducted to measure the limiting heat flux, i.e., Critical Heat Flux on the outer CV for downward facing boiling surface and its influence by vault water temperature.

Chapter 6 provides the details on development of new correlations on heat transfer coefficient for curved CV outer surface under single phase natural convection and full boiling conditions.

Chapter 7 highlights the adequacy of scaling effects of melt volume, effect of decay heat and type of simulant melt material on heat transfer behaviour.

Chapter 8 presents the development of a CFD model and its benchmarking with experimental results. The model is extended to prototypic condition for predicting the vessel behaviour during severe accident.

Chapter 9 concludes the thesis with the key findings of the research and future recommendations of the work.

1.6 Closure

This chapter introduces the potential of nuclear power as alternative energy source in Indian scenario. Though this is a sustainable and greenhouse free energy source, but it is associated with a history of severe accidents. Various design like in-vessel retention and core catcher are discussed for NPP to mitigate the consequences of a severe accident. Design features and various stage of severe accident progression in PHWR are highlighted. It also draws attention, the motivation and need of the study in vessel retention of PHWR. The outline of thesis chapters is also discussed.

Chapter 2

Literature Survey

2.0 Introduction

The literature review shows that no prior study has been done for IVR of molten corium in PHWR CV. IVR of the corium by external cooling of the reactor pressure vessel was extensively studied and implemented in some existing NPPs and in new reactor designs (Generation III reactors), including VVER-440[12], AP600 [13], AP1000 [14, 24], APR1400 [25], HPR1000 and CAP1400 [26, 27, 28]. Worldwide lot of efforts had been put to understand the complex melt pool heat transfer through vessel wall which induced extreme thermal load on the wall and estimating the Critical heat Flux (CHF) on the outer surface of the Reactor Pressure Vessel (RPV). These are the two key parameters in assessment of IVR design. IVR concept is now well recognized as an effective severe accident mitigation measure for elimination of large radioactive release in public domain. With the purpose of insights of melt coolability phenomenon in vessel retention during severe accident condition, a detailed literature survey has been carried out. The findings of major studies from the literature are summarized below

2.1 Literature on In-Vessel Retention experiments

After TMI-2 and Chernobyl severe accident, lot of reactors scaled in-vessel retention studies were performed for PWR or BWR reactor vessel. Some of the important experiments conducted in this regard are discussed here.

2.1.1 RASPLAV

The aims of the RASPLAV experiments [29] were to generate data on molten core materials behaviour on the RPV lower head under severe accident conditions and possible assessment of physio-chemical interactions between molten corium and the vessel wall. Numbers of

physical properties of corium of different composition were measured up to the temperatures of 2850 °C. Investigation of melts of different salts as corium simulators were obtained which allowed to understand the impact on natural convection, presence of transient zone, melting, formation and re-solidification of the crust. Analytical and software tools were developed based upon the experimental investigations.

Also, a set of experiments with binary molten salt mixtures has been performed to investigate the effects of non-prototypic conditions such as side-wall heating instead of volumetric heating and non-isothermal conditions at the upper pool boundary. The experiments conducted with the molten salts at the temperatures 750 °C and in prototypical Rayleigh numbers from 9.8×10^{11} to 3.5×10^{13} . The results showed the similarity of the processes of heat transfer (conduction) in inner vessel wall to outer cooled wall in directly heating as well as heat-generating liquid experiments. Also, it was first to obtain data on the effects of large difference between solidus and liquidus temperatures on heat transfer and had provided valuable data for modelling heat transfer and crust formation from complex mixture.

2.1.2 FOREVER (Failure of Reactor Vessel Retention) experiments

The FOREVER experiments [30] conducted in 1:10 scaled (i.e., Its outer diameter was ~ 400 mm and wall thickness was ~15 mm) pressurized vessels with different carbon steel lower heads to study the melt pool natural convection and lower head creep failure and rupture. The experiment was conducted by pouring simulant melt at 1200 °C. The simulant material used in experiment was binary oxide melt of 30 wt. % CaO and 70 wt. % B₂O₃. Heaters were used to heat the melt and maintain it at 1100–1200 °C. Argon gas was used to pressurise the vessel up to 25 bars. It also simulated the high temperature natural circulation inside the melt which was confined in the spherical pressure vessel head and provided thermo mechanical load on vessel head for creep rupture. In the experiments, there was no internal or external cooling of

the lower vessel head. The lower vessel head lost heat mainly by radiation and to some degree by convection.

These tests showed that the time and location of vessel failure occurred at maximum temperature location on vessel wall which depends upon the imposed thermal load. It was observed that the imposed thermal load distribution on vessel due to fully filled melt pool convection, failure occurred at $\sim 70^\circ$ from the bottom of the vessel. Different location was observed when head was partially filled (different melt volume) or lower head had penetration (weld joints). It was also observed that failure always occurs in the hot zone which was directly associated to heat transfer from melt pool to vessel wall. In one of experiments, water was poured on top of molten pool the wall temperature at angle 90° drop almost immediately whereas below 90° , cooling rate was slow. This means that there was no gap created between the wall and the crust.

2.1.3 SIMECO

RASPLAV experiments [31] established the melt stratification in molten pool and confirmed the natural convection heat transfer behaviour comparable in both prototypic molten corium and simulant materials. In order to examine the significance of stratification on the heat transfer of the lower head of reactor vessel and to the top of the molten pool, the SIMECO experiments were conducted in two and three layers simulated stratified pools. The effect of various parameters like different layer thickness, miscible and immiscible simulant melt layer, with or without decay heat generation and different densities were performed during the experimental studies of heat transfer in stratified pool. It consists of a slice type vessel, which includes a semi-circular section and a vertical section, representing the lower head of the reactor vessel. The size of the facility is scaled to 1/8 of prototype PWR type reactors. The height, diameter and width of the test section were 530 mm, 620 mm and 90 mm respectively. The thickness of the vessel wall was 230 mm.

The temperature variation inside the pool was measured at different powers. Under steady state, it was observed that the temperature rose gradually along the height of the pool, until it reached the interface between two upper layers. At that point, due to the interface resistance to the upward heat flow, the temperature of pool suddenly fell down. Then there was a small increase in temperature in the upper layer due to convection. Similar temperature variation was measured in the three-layer experiments. The heat flux was calculated for different Rayleigh numbers for both two- and three-layer experiments. The heat flux increases along with the radius, reaching its maximum, and then decreases again in the upper part of the sidewall. Similar results had been seen in case of three-layer experiments. The maximum heat flux observed for two- and three-layers tests were 57° and 64° respectively.

2.1.4 LAVA (Lower-plenum Arrested Vessel Attack)

The LAVA experiments [32] were performed to validate the concept of in-vessel gap cooling. These tests were performed inside the pressure vessel of inner diameter of 2.4m and a height of 4.8 m with simulant thermite melt ($\text{Al}_2\text{O}_3/\text{Fe}$ or Al_2O_3) in the range of 30-70 kg. Hence, the aims of these experiments were to achieve the gap formation between melt and the vessel lower head and its effect on the in-vessel coolability. The experimental results confirmed the formation of a gap between the debris and the vessel lower head only in oxide layer (Al_2O_3). The main reason for the gap formation was the difference of materials between the debris and the vessel, the existence of water inside the lower plenum and the internal pressure load. The heat removal capacity in the gap was dependent upon the gap size, melt volume and water ingress into the gap. In the case of a small gap size, effective heat removal to the extent of the vessel bottom could not be achieved. The cooling rates of melt and vessel lower head at different locations were measured for various melt composition and mass of melt.

2.1.5 CHF for downward-facing boiling on a coated hemispherical vessel RASPLAV

The Korean Advanced Power Reactor APR1400 uses IVR method with external reactor vessel cooling (ERVC). With water on the lower external surfaces of the reactor pressurized vessel, nucleate convection heat transfer would be the dominant regime if the wall heat flux from the corium is well below the CHF limit for downward-facing boiling on the vessel outer surface. Experimental study [33] was carried out to evaluate the critical heat flux on the outer surface of a hemispherical vessel with and without coatings with downward facing boiling process. Steady-state boiling tests were performed by using an enhanced vessel/insulation design for the cases. From boiling data, CHF correlations were obtained for both cases and compared. With thermal insulation design, the local CHF limit tend to increase from the bottom centre at first, then decrease and finally increase toward the equator. This behaviour was due to the local variation of the two-phase motions in the annular channel between the test vessel and the insulation structure. For a coated surface using an enhanced insulation, local CHF enhanced 200% to 330% over a plain vessel without insulation.

2.1.6 LIVE (Late In-Vessel phase Experiments)

In-Vessel Retention experiments in LIVE [34] were conducted in a scaled 1:5 semi-spherical lower head for typical PWR. The main objectives were to investigate the melt pool coolability behaviour with different cooling conditions (air or water) on external surface of vessel. It also studied the effect of different initial melt temperature (300 °C to maximum 350 °C), different melt pouring location like central or near wall, non-eutectic and eutectic simulant melts, different melts volume (120 L and 210 L) and internal heat generation on melt pool heat transfer during in-vessel retention. The well recognized simulant material $\text{KNO}_3\text{-NaNO}_3$ in non-eutectic composition (80 mole % KNO_3 -20 mole % NaNO_3) and in eutectic composition (50 mole % KNO_3 – 50 mole % NaNO_3) was used in these experiments. The heat flux distribution was estimated through vessel wall, melt pool temperature and crust

thicknesses which were measured. Steady state and transient results had been obtained concerning the melt pool thermal hydraulic behaviour.

The experimental investigations found that increasing heat generation (decay heat) in melt led to an increase of overall melt temperature in the melt pool and intensified the heat flux focusing at the upper portion of vessel (near melt surface) compared to lower portion of vessel. It was observed that cooling boundary conditions (air/water) on external surface of vessel had significant effect on melt phase change (crust formation). The melt solidified significantly faster under the water-cooling condition than the air cooling and the crust growth period was shorter under water cooling condition. The air cooling could not cool the melt pool sufficiently so the melt temperature increased continuously in comparison to the water cooling where the melt pool temperature reduced immediately. The material composition of the simulant melt (non-eutectic and eutectic) had influence on heat transfer inside melt pool which resulted in differences in solidification process (with and without mushy zone) and crust formation, but the observed heat flux distributions were comparable through the vessel sidewall.

2.1.7 COPRA (Corium Pool Research Apparatus)

As the natural convection heat transfer phenomenon in corium pools is a very complicated subject, earlier experiments were conducted to specific design or conditions of PWRs. Based on earlier research, COPRA experimental facility [35] was designed to study the in-vessel molten corium pool heat transfer behaviour during severe accidents in Chinese specific PWRs. The test vessel of the COPRA was 2D $\frac{1}{4}$ circular slice test section simulating reactor vessel at 1:1 scale with inner radius of the vessel of 2200 mm and width of 200 mm. All the vertical walls of the vessel had the thickness of 25 mm and were kept thermally insulated. The curved vessel wall had a thickness of 30 mm and was enclosed from outside to keep the boundary temperature nearly isothermal. COPRA experiments had been performed in

different melt volumes, heat generation rates and multiple injection of the melt. The simulant material $\text{NaNO}_3\text{--KNO}_3$ in non-eutectic composition (20 mole % NaNO_3 –80 mole % KNO_3) was used. The behaviour of a large-scale homogenous melt pool regarding the melt pool temperature, heat flux distribution through the vessel wall and crust thickness in transient and steady state conditions were estimated. Thermal stratification was observed with higher temperature gradient in the lower part of the melt pool. Heat transfer along the curved vessel wall below 40° angle appeared to be constant and from 40° up to the top, increase of heat flux was observed. The maximum heat transfer occurred in the upper portion just below the pool surface. The radiation heat transfer from the top melt surface to the upper atmosphere led to the decrease in heat transfer to the side wall. With increase of angle, crust thickness was found to decrease due to the larger heat flux in the upper part (large angle). Heat transfer obtained in vessel wall during test was compared with previous experiments and experimental correlations. It was found that the downward heat transfer was lower than other experiments with same range of Rayleigh numbers.

2.2 Literature on In-Vessel Retention analysis

Unlike the experimental studies which are limited due to difficulty in performing such high temperature experiments, there are several numerical studies performed to investigate the melt coolability inside the vessel during the severe accident. Some of the latest analytical studies in this regard are discussed here.

To obtain more realistic assessment of reactor vessel structural integrity, a precise temperature distribution at the reactor vessel outside wall is required. For APR1400 reactor vessel, IVR-ERVC was investigated where insulator was also considered in the analysis for more realistic model by Ihn-Namgung [36]. The general-purpose Computation Fluid Dynamic (CFD) code, ANSYS Fluent was used to model the natural convection in the cavity

and to obtain temperature profile of reactor vessel outside surface, coolant flow pattern and evaporation amount. The heat flux on reactor vessel from corium inside the reactor lower head was obtained from MELCOR analysis and used as input boundary condition of CFD analysis. The main focus of this study was to develop a method of fluid flow pattern and the temperature change in the reactor outer surface wall.

From the analysis, it was observed that cooling effect on the wall was very sensitive to initial temperature of water. CFD analysis showed that side injection of coolant created less stratification within cavity compared to bottom injection of coolant; hence it was appropriate to design ERVC coolant injection to side elevation. Study was done with two basic turbulence models to save time, but the author suggested use of more advanced multiphase turbulence model as ERVC involved more complex heat and phase change phenomena.

Rae-Joon Park [37] had performed the analysis of two-phase natural circulation in the reactor cavity of the APR1400 and the advanced OPR1000 under IVR-ERVC to estimate the natural circulation mass flow rate for different thermal powers by using the RELAP5/MOD3 computer code. The effects of coolant injection temperature and water level on the coolant circulation flow rate were investigated. Heat fluxes considered on the wall of reactor vessel during the analysis were obtained from MAAP4 software results. The results had shown that an increase in the coolant injection temperature leads to an increase in the CHF on the outer vessel wall. By reducing water level in the reactor cavity, decrease in the coolant circulation mass flow rate was observed due to a decrease of local pressure and an increase of local average void fraction.

Fei-Jan Tsai [38] used the RELAP5-3D code to simulate the natural convection flow within the water channel of the AP-1000IVR device. Two layers and three layers configuration were considered for input heat load on IVR. Result showed that the impact of configuration was

significant on the performance of IVR design. The results of simulations were also substituted into ULPU, SULTAN, SBLB, and KAIST critical heat flux correlations to determine the safety margin of the AP-1000 IVR design.

Mindaugas [39] had investigated the application of in-vessel retention (IVR) severe accident management strategy in a BWR reactor. A full plant model of a ~2000 MW thermal power BWR reactor was used. Full accident sequence from normal operation conditions to core heat-up, melting, and relocation into lower head was modeled by using RELAP/SCDAPSIM code for predicting the heat fluxes and reactor pressure vessel wall temperatures. The ex-vessel heat transfer correlation used in analysis was obtained from US Nuclear regulatory commission [40] report. Further to investigate the influence of oxidic and metallic layers in the molten pool on the heat transfer through the wall of the lower head, the analytical study was also conducted.

It was observed that in RELAP5 based heat transfer analysis, the RPV wall temperature was overestimated compared to the COUPLE based heat transfer analysis. Reason behind this was COUPLE computer code was using experimental based correlations for ex-vessel heat transfer. The results of layers formation (oxide + metallic) study in melt pool showed that the focusing effect was significant and local heat flux from reactor vessel could exceed the critical heat flux under some extreme conditions. It was also recommended that the existing RELAP/SCDAPSIM models of the processes in the debris should be updated in order to simulate more complex phenomena.

David [41] had carried out finite element analysis to study heat transfer from a corium pool at the bottom of the calandria to its surroundings during severe accident in CANDU-6 reactor [42]. The breakup of heat transfer from top, bottom and end shield side surfaces of the pool and the angular distribution of heat flux in main shell were calculated. The model comprised of one-quarter of the corium crust together with all contacting surfaces of the calandria (but

not the corium pool). All surfaces of the corium pool (including the top) were modelled as isothermal walls. Melting and freezing of the crust and heat generation in the crust were not modelled. Several additional cases were solved to examine the sensitivity of results. From analysis it was found that only half of the heat transfer occurred through the top surface of the corium pool, which is less than previously calculated. Heat flux generally increased with elevation along the curved surface of the calandria main shell and little over end shield surfaces. Author highlighted the limitations in the computational method used for such scenario and need of more sophisticated CFD models. More experimental studies were also suggested.

2.3 Summary and applicability of past literature to present study

From literature survey on IVR, it can be inferred that for assessment of IVR in any reactor, the following factors need to be understood fully:

- I. The coupling of different heat transfer mode in molten pool like the melt pool convection, vessel side wall conduction, lower curved wall conduction, pool upper surface radiation or convection and gap cooling
- II. Phase change inside molten pool i.e., solidification (crust), its growth rate and thickness variation along vessel
- III. Thermal load on vessel wall due to heat generation inside molten pool
- IV. External vessel surface heat transfer (single phase or boiling)
- V. Heat flux and CHF on external vessel surface
- VI. Effect of simulant material and volume of melt

Most of the experimental studies for melt coolability under the severe accident conditions are related to lower head of PWR or BWR vessel. No such experimental studies are found for PHWR CV. In case of numerical analysis, heat transfer and critical heat flux correlations

developed for PWR/BWR vessel type geometry, are used in commercial CFD codes to enable them to predict for some of severe accident phenomena. In case of PHWR, due to non-availability of heat transfer correlations, analyses were done with assumed value.

In PHWRs, the coolant channels are submerged in the cold moderator which is contained inside the thin CV and CV itself surrounded by huge vault water. Therefore, PHWRs hold large quantity of cold water compared to PWRs or BWRs. That is why severe accident progression differs in PHWRs as compared to PWRs or BWRs. Table 2.1 shows the geometry differences between Lower head of PWR or BWR and CV of PHWR.

Table 2.1: Design difference between Lower head of PWR/BWR and PHWR

| S.No. | PWR /BWR Lower head | PHWR calandria Vessel |
|-------|------------------------------------|-----------------------|
| 1 | Spherical Head | Cylindrical vessel |
| 2 | Thick head (170-250 mm) | Thin vessel (~32 mm) |
| 3 | High to moderate internal pressure | Low internal pressure |
| 4 | Surrounded by air | Surrounded by water |

The core internal and fuel are different in case of PHWRs; hence, their compositions of corium differ from that of PWRs/BWRs which results different thermal loads on CV wall. The corium composition of typical PWRs/BWRs is: UO_2 (~60%), Zr - ZrO_2 (~25%), and stainless steel (~14%) [43] by weight where as in case of PHWRs, the typical corium composition is: UO_2 (~70%) and Zr - ZrO_2 (~29%) [44]. In PWRs/BWRs, at initial stage of severe accident progression, the corium behaves as a homogeneous mixture of molten materials. But due to addition of lower density metal (like stainless steel etc.), some metals and oxide materials do not mix and form different layers in the corium pool [45]. First, two layers are formed and if the rates of oxidation of metals are less, then three layers could be formed [46, 47, 48]. On the other hand, PHWR corium is not found to stratify due to its

composition and here it could be safely treated as a homogenous mixture. In view of this the heat transfer behaviour from corium pool to surrounding [would be different](#).

Therefore, severe accident studies related to IVR of PWRs or BWRs cannot be directly applied to PHWRs.

2.4 Challenges of In-Vessel Retention Studies for PHWRs

To investigate the IVR in PHWRs, two approaches may be taken up, viz. mechanistic modelling and experimental studies.

2.4.1 Difficulty in mechanistic modelling of corium coolability in calandria vessel

Mechanistic modelling of corium coolability is very difficult as corium is a multi-component mixture of UO_2 , ZrO_2 , Zr, control rods, traces of steel, etc. with occurrence of phase changes in melt during cooling i.e. melt to crust formation; transient heat transfer on outer curved vessel of CV from single-phase to partial boiling and then fully boiling natural convection; multi-mode heat transfer inside the melt, i.e. conduction, convection and radiation; non-uniform angular heating of CV due to partial filled corium inside CV and lack of melt properties at wide temperatures ranging from 2500 °C to room temperatures. Current computational models are not robust enough to handle such multi-component, multi-phase, multi-mode heat transfer and in fact, applicability of existing CFD codes for these simulations are not known.

In view of this, experiments are mandatory for not only understanding the coolability behaviour of molten corium inside the CV to the vault water but also data generation and empirical model developments.

2.4.2 Difficulty in conducting experiment of corium coolability in calandria vessel

Conducting experiments with prototype material and with large quantities are prohibited. So, over the years, many investigators have used simulant materials with different volume to

clarify the coolability behaviour of molten corium. These tests involve complex high temperature experiments (more than 2500 °C) which are highly challenging for melt creation with different simulant materials in large quantity. The conventional technologies for melt creation can produce up to a few litres using electrical heating furnace or by induction furnace. However, the temperature limits in electrical heating furnace are around 1500 °C and that of induction furnace is limited to 2000 °C. To create simulant melt at temperatures close to 2500 °C is beyond the above capabilities.

In addition, measurements at such high temperatures inside the melt are beyond the capability of existing technologies. Creating decay heat inside the corium melt is also equally challenging as heater material should withstand against high temperature melt for prolonged period.

2.5 Gap Areas

Based on the literature survey, the following gap areas on the heat removal capability of calandria vault water from molten corium inside the CV in PHWR during severe accident are identified as

- a) The heat transfer phenomena inside the CV which contains molten corium is very complex as it involves multiple modes of heat transfer (conduction through crust and CV, natural convection inside the melt and radiation heat transfer from top of crust to the vessel) associated with phase change (melting and solidification). Formation of crust and its growth needs to be understood. Effect of decay heat inside the corium on heat transfer and crust formation rate is never established.
- b) The heat transfer phenomena outside the curved CV which is surrounded by cold vault water is also complex as heat transfer behaviours for different regimes, i.e., single phase natural convection, nucleate boiling and film boiling are not known.

- c) The phenomenology of CHF on outer surface of CV under severe accident condition is very complex due to downward facing heating, boiling natural convection and geometry of very large diameter and length. The CHF for PHWR CV geometry is not established.
- d) CV is stepped vessel and due to this large number of weld joints are present. Apprehensions are raised regarding the CV integrity against sudden high temperature corium thermal load on welded stepped joint. Hence, CV integrity needs to be established against above load for successful IVR.
- e) The scaling effect of melt volume and melt material on heat transfer behaviour are never known, which needs to be understood.

2.5 Main Objective/ Scope of research work

The main objectives are to understand and evaluate

- a) Heat transfer behaviour from molten corium to the vault water in following regime
 - i. Decay heat dominated regime ($<1423\text{ }^{\circ}\text{C}$)
 - ii. Stored heat dominated regime ($>1423\text{ }^{\circ}\text{C}$)
 - iii. CHF in downward facing surface
- b) Evaluation of heat transfer coefficient in curved CV under single phase natural convection, partial boiling and full boiling conditions with molten corium inside the calandria vessel
 - a. Development of outer vessel wall heat transfer correlation
- c) Scaling effects of melt volume, decay heat and simulant melt material on heat transfer behaviour.

- d) Assessment of the capability of CFD for corium coolability for the PHWR CV geometry

2.6 Strategy for solving the scientific issues

The following approach are adopted to solve the scientific issues of research work.

A. For evaluation of natural convection heat transfer from corium to vault water

- a) Experiments have been conducted with
 - i. Various simulant melt
 - ii. With and without decay heat in melt
 - iii. Stored heat regime (high temperature) and decay heat regime
- b) Based on experiments results, heat transfer correlation for outer surface CV has been developed

B. For estimation of CHF of CV geometry

Experiment on heating surface facing downward flat plate simulating the bottom portion of PHWR CV has been conducted

C. For assessment of the capability of CFD for evaluations of corium coolability

- a) Validation of models against experiment results by simulation of experiment has been conducted
- b) Extension of CFD model to prototypic condition for predicting the vessel behaviour during severe accident has been carried out.

2.7 Closure

Detailed literature review was carried out on the melt coolability phenomenon in In-Vessel Retention during severe accident condition. These experimental and numerical studies gave the insights on melt coolability phenomenon and assisted in identifying the scientific gap areas. Subsequently, challenges in In-Vessel Retention Studies, the objective of the thesis and the strategy to address them have been discussed.

Chapter 3

Heat transfer behaviour from molten corium inside CV to the vault water - Decay heat dominated regime

3.1 Introduction

During severe accidents in PHWRs, high temperature melt is accumulated at the bottom of the CV. This melt still generates the decay heat. Outside the CV, vault water is present which acts as a heat sink. The heat transfer from the debris/melt to the vault water is combination of both stored heat as well as decay heat and it depends upon the temperature of the debris/melt. When the temperature of melt is high, the stored heat is dominant as compared to decay heat whereas when the temperature of melt is low, decay heat is more dominant as compared to stored heat. The total heat transfer from debris/melt to vault water is

$$Q_{th} = Q_{decay} + Q_{tsh} \quad (3.1)$$

Where

Q_{th} = Total Heat (J/s)

Q_{decay} = Decay Heat (It may be noted that the accident progression time period in PHWRs from core disassembly, relocation, debris formation to melting of debris is more than 40 hours. After this period, the decay heat is almost 1% of reactor thermal power and remains practically constant. In view of the above, a constant decay heat of 21 MW which is 1 % of 700 MWe (2166 MW_{the}) PHWR has been considered in this analysis).

The total stored heat is a sum of stored heat in melt/debris and vessel, i.e.

$$Q_{\text{tsh}} = \text{Total Stored heat} = Q_{\text{melt}} + Q_{\text{vess}}$$

where,

$$Q_{\text{melt}} = \text{Stored heat in debris/melt} = (MCp)_{\text{melt}} \Delta T_{\text{melt}} / \Delta t$$

$$Q_{\text{vess}} = \text{Stored heat in vessel} = (MCp)_{\text{vess}} \Delta T_{\text{vess}} / \Delta t$$

Where

M= mass

Cp=specific heat

ΔT_{melt} =temperature difference between melt/debris and the vessel

ΔT_{vess} =temperature difference between the vessel and vault water

t= time

Figure 3.1 shows the variation of total heat transfer rate due to stored heat and decay heat of corium for a 700 MWe PHWR to the vault water as a function of melt/debris temperature.

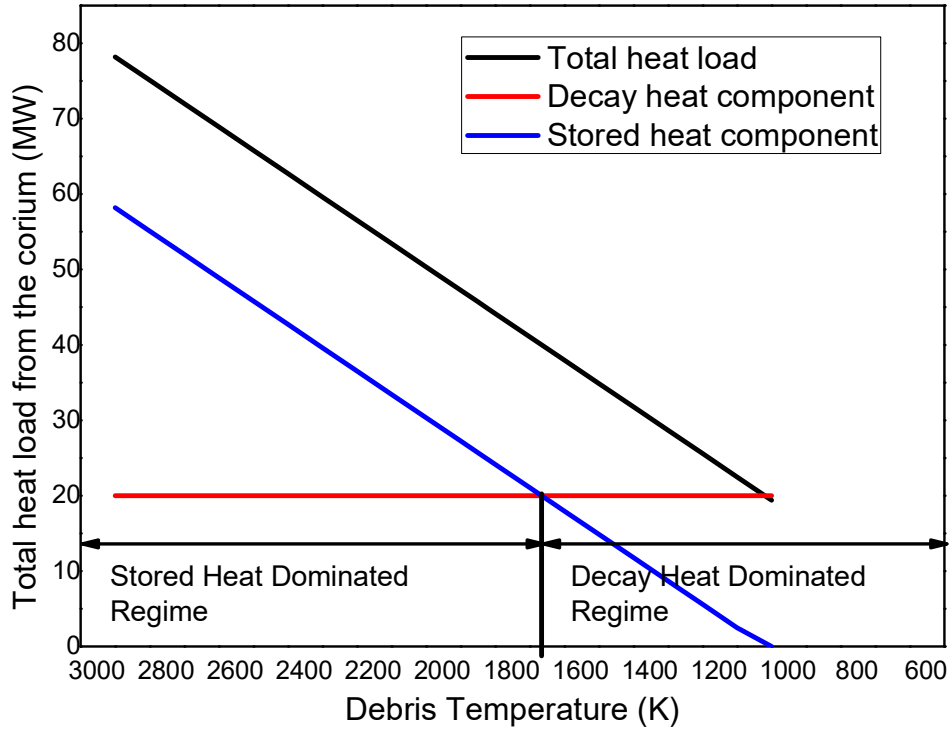


Figure 3.1: Heat input and heat loss variation with temperature

From figure 3.1, it may be noted that when melt temperature is below 1700 K, the incident heat flux due to temperature difference between melt and vessel is small and the decay heat becomes more dominant compared to stored heat. If decay heat is not removed from debris/melt, the debris/melt temperature keeps on rising causing high temperature melt pool formation. At high melt temperature (i.e., >1700 K), the decay heat is negligible compared to the stored heat.

Hence, when the melt temperature is below 1700 K ($\sim 1423^\circ\text{C}$), it can be termed as ***decay heat dominated regime*** whereas when the melt temperature is above 1700 K, it can be termed as ***stored heat dominated regime***.

3.2 Heat transfer from corium inside CV to the vault water in decay heat dominated regime

3.2.1 Scaling philosophy for decay heat dominated regime

In order for experiment to simulate the actual reactor condition, proper scaling philosophy has to be followed. For in vessel retention, there is no established scaling philosophy in the literature. In view of this, a new scaling philosophy has been used in the experiment. In decay heat dominated regime, power to volume scaling has been considered. The heat transfer behaviour constitutes convection within the heat generated melt pool, conduction in crust and vessel, and convection in vault water (Figure 3.2). At the top of the melt pool, crust may form; the heat is transferred by radiation from crust to vessel top inner surface (Figure 3.2). For heat transfer scaling, following three parameters have been preserved, i.e.

- a) Volumetric heat generation in melt
- b) Ratio of volume of melt to coolant
- c) Ratio of heat transfer rate per unit volume of the melt

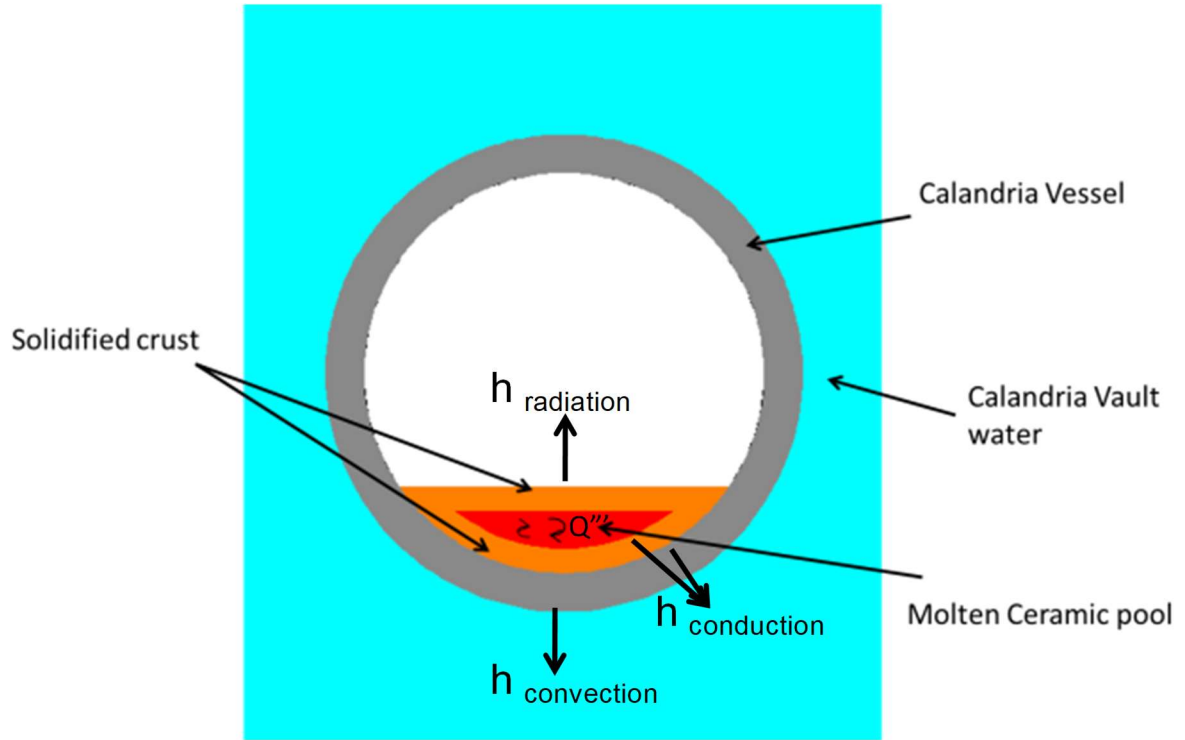


Figure 3.2: Heat transfer behaviour from debris melt to water

In other words,

- 1) Decay heat per unit volume in prototype = Decay heat per unit volume in experiment

$$(Q''')_{prototype} = (Q''')_{exp} \quad (3.2)$$

- 2) $(V_{melt}/V_{vaultwater})$ in CV for prototype = $(V_{melt}/V_{vaultwater})$ in CV for experiment

$$i.e. \left(\frac{V_{melt}}{V_{vaultwater}} \right)_{prototype} = \left(\frac{V_{melt}}{V_{vaultwater}} \right)_{exp} \quad (3.3)$$

- 3) Heat load in prototype condition /Heat Load in experiments= $V_{prototype} /V_{exp}$

$$\frac{(q'' \times A)_{prototype}}{(q'' \times A)_{exp}} = \frac{V_{prototype melt}}{V_{exp melt}} \quad (3.4)$$

Where

q'' = Heat flux

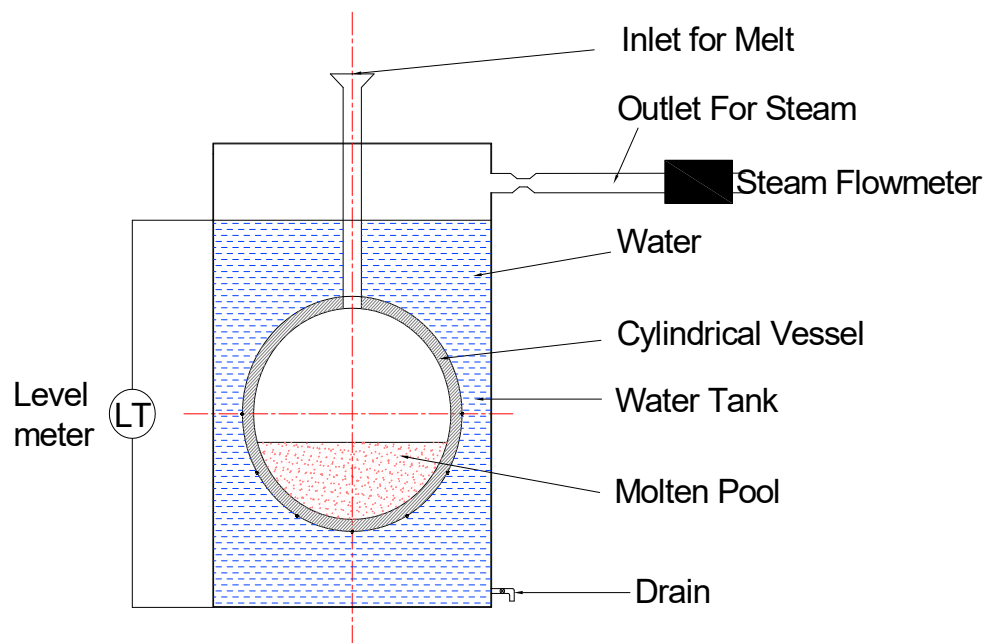
Q''' = decay heat per unit volume

V = volume

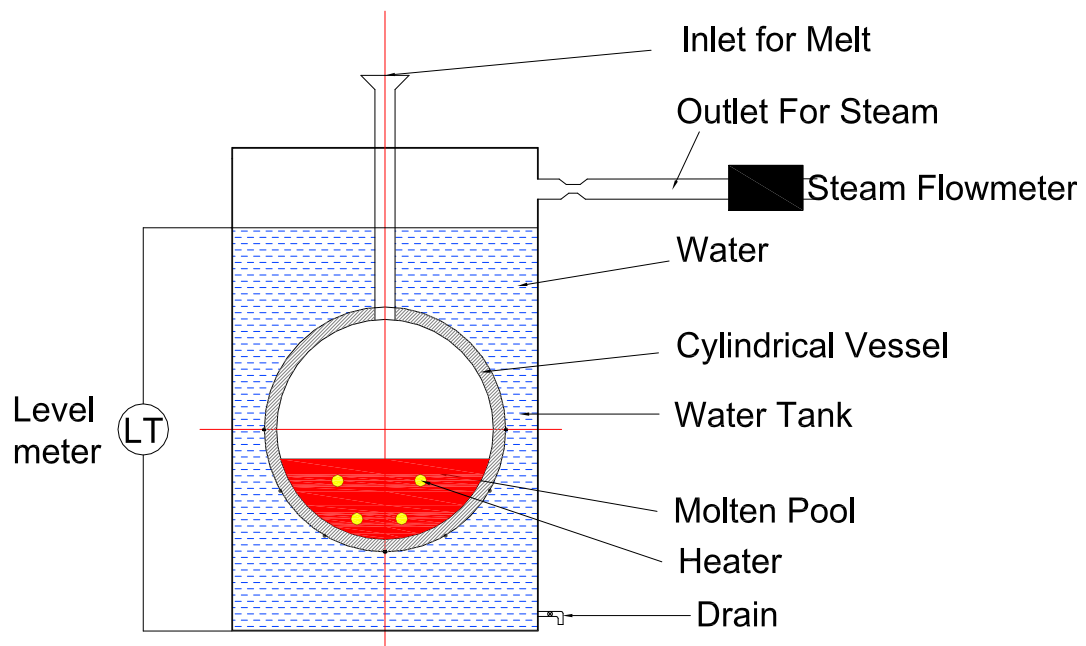
A = Area

3.2.2 Experimental setup

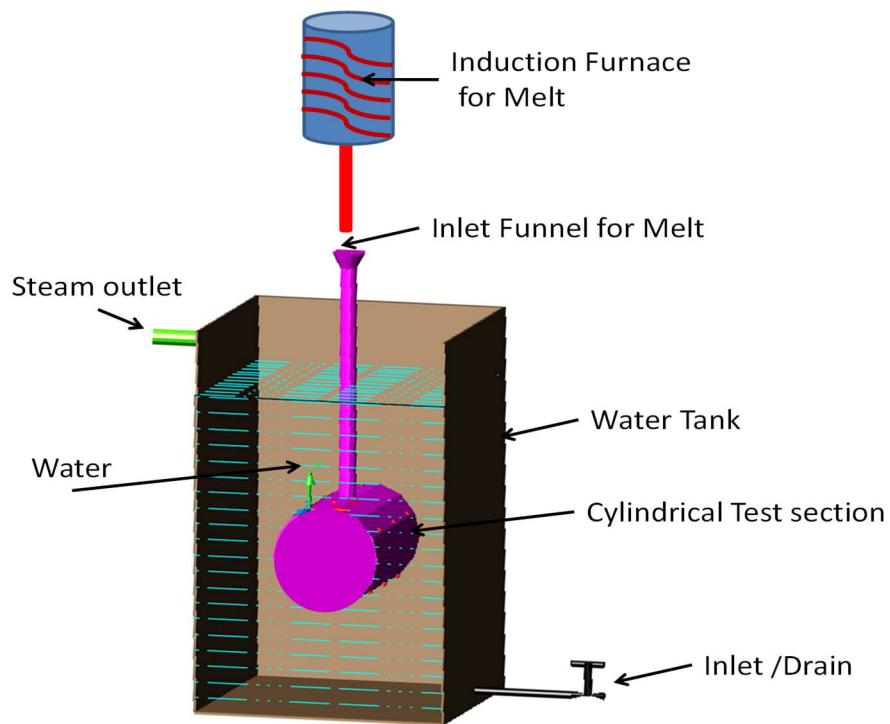
A scaled experimental facility based on above scaling philosophy has been designed and fabricated to investigate the heat transfer from simulated melt pool inside the CV to vault water. The scaled experimental facility consists of a high temperature melt generating induction furnace, cylindrical test section simulating CV, a rectangular tank simulating the calandria vault and high-density cartridge type heaters for simulating decay heat inside the melt pool. The diameter of cylindrical test section is 270 mm ($1/26^{\text{th}}$ scaling ratio as compared to 700 MWe PHWR) and length is 456 mm ($1/13^{\text{th}}$ scaling ratio as compared to 700 MWe PHWR). The details of scaled experimental facility are shown in figure 3.3.



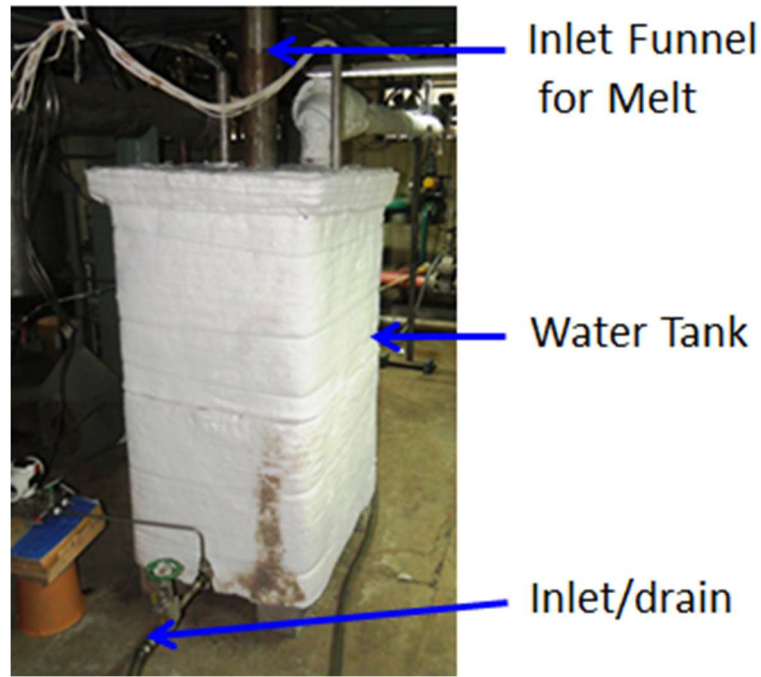
(a)



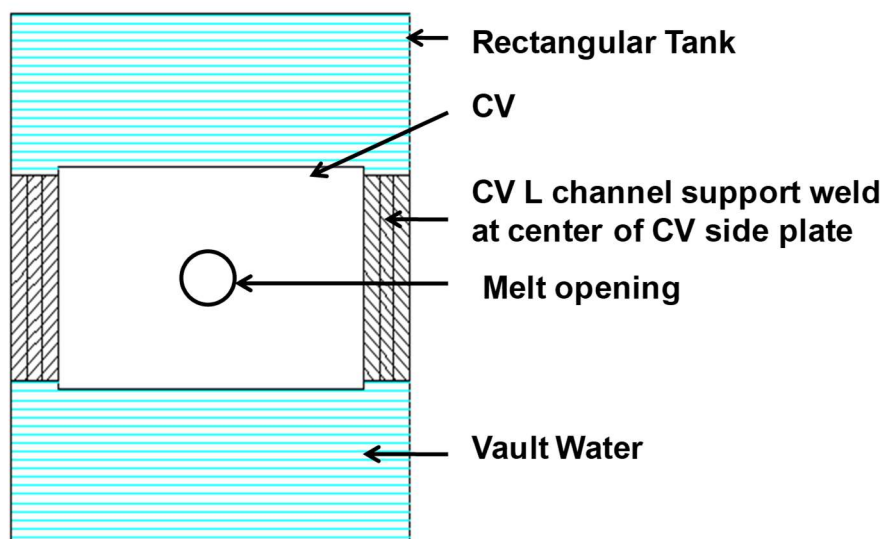
(b)



(c)



(d)



(e)

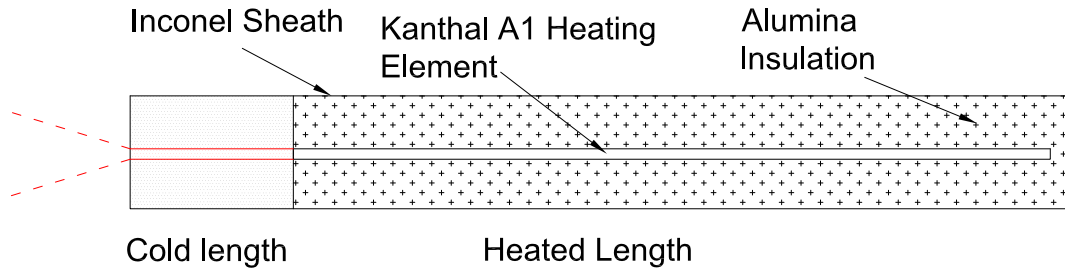
Figure 3.3. Experiment set up: (a) without decay heat (b) with decay heat (c) 3D model (d) actual photograph of set up (e) Planview of set up

For pouring of melt inside the test section from furnace, an inlet funnel with long pipe was provided at top of test section (as shown in figure 3.3). On both side of the cylindrical test vessel, a circular plate was welded which were submerged in water simulating the end shield inner plate. The test section was made of stainless steel 304L of same material as prototype

CV in PHWR so that thermal conductivity of material remains same. The thickness of test section was kept same as CV of reactor to achieve the same resistance to heat transfer ($\Delta x/k$). Also, heat transfer rate ($=k \Delta T/\Delta x$) depends upon conductivity (k) and thickness (Δx). Therefore, for 1:1 scaling of heat transfer rate, actual material and actual thickness of the CV of 700 MWe PHWR was kept. This will ensure similar temperature gradients during the transient.

The water tank contained 0.5 m³ volume of water having scaling ratio of 1:13 as compared to the calandria vault water of 700 MWe PHWR. The dimension of tank is 0.66 m (Width) \times 0.77 m (Length) \times 1.2 m (Height). The melt pool height was kept 135 mm in the experiment. Sodium borosilicate glass was used as the simulant melt.

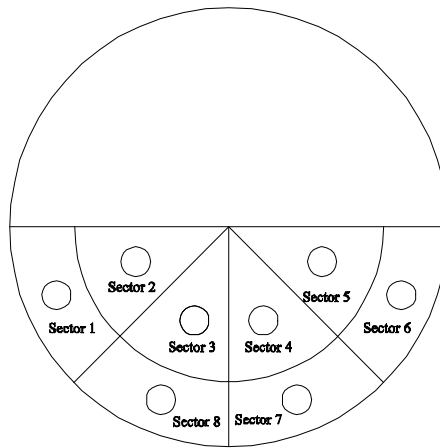
For simulating the volumetric decay heat in melt, high density watt cartridge type heater (as shown in figure 3.4) was developed which can withstand high temperature melt. These high watt density cartridge heaters were installed at lower bottom portion of the cylindrical vessel in longitudinal direction and cold length of heaters were welded to side end plate. Each cartridge heater is Inconel sheathed and can produces about 2.3 -2.5 kW power. The maximum power that can be generated in the melt is ~20 kW which is equivalent to decay heat of ~1.0 MW/m³ in the melt pool. There is limitation in mimicking exact decay heat generation in severe accident experiment and some amount of deviation is always be there. However, precaution has been taken such that each heater almost produces equal amount of heat/volume inside the melt so, that uniform heat generation could be achieved inside of the melt (as shown in figure 3.4 (c)). Moreover, the presence of several heaters inside the melt pool assured the near volumetric heat generation.



(a)



(b)



(c)

Figure 3.4: (a) Schematic details of cartridge Heater (b) Actual cartridge heater (c) Heater location inside melt

Scaling of Heat Transfer parameters

Table 3.1 shows the scaling of heat transfer parameter comparison between the simulant material and corium. The total heat transfer rate per unit volume, which is the main scaling parameter, is in good agreement with that of prototype. From the table, it is observed that, the

Rayleigh number is in turbulent region both in tests and in prototype. Hence, the heat transfer behaviour is expected to be same in both the cases.

Table 3.1: Heat Transfer parameter

| Parameter | Scaled facility | Prototypic |
|--|-----------------|------------|
| Heat generation per unit volume (Q''') | 1e6 | 1e6 |
| $Vol_{melt}/Vol_{vaultwater}$ | 0.032 | 0.03 |
| Heat transfer rate/volume, $q'' \times A/V$, (kW/m ³) | 717 | 758 |
| Rayleigh Number (Ra) | 1.55e11 | 8.75e14 |

Material properties scaling

Table 3.2 shows the material properties comparison between the simulant material and corium

Table 3.2: Material properties comparison between glass and PHWR corium

| Property | Glass simulant | PHWR Corium |
|--|----------------|-------------|
| Density (ρ)(kg/m ³) | 2400 | 8800 |
| Viscosity (μ)(Pa.s) | 0.0025 | 0.00336 |
| Conductivity (k) (W/m/k) | 1 | 2.88 |
| Specific heat (Cp) (J/kg/K) | 730 | 565 |
| Volumetric expansion coefficient (β) (1/K) | 1.03e-04 | 1.05e-4 |
| Thermal diffusivity (α) (J/(m ³ /K)) | 5.71e-07 | 5.79e-07 |
| Gap between solidus and liquids (°C) | ~250 | ~200 |

From the table, it can be observed that, the thermal diffusivity and volumetric thermal expansion coefficient of the simulant and corium are nearly same. These two parameters are very important in case of transient natural convection heat transfer from melt to water. The viscosity is also closer.

Table 3.3 shows the details of the experimental setup.

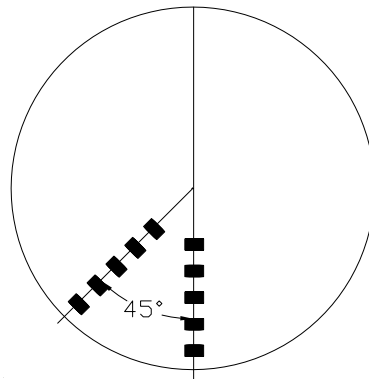
Table 3.3: Experimental setup details

| | |
|---------------------------|--------------------|
| Calandria vessel diameter | 300 mm |
| Calandria vessel Length | 456 mm |
| Thickness | 25-32 mm |
| Material | SS 304L |
| Volume of water | 0.5 m ³ |
| Melt quantity | 60 kg |
| Melt material | Glass |

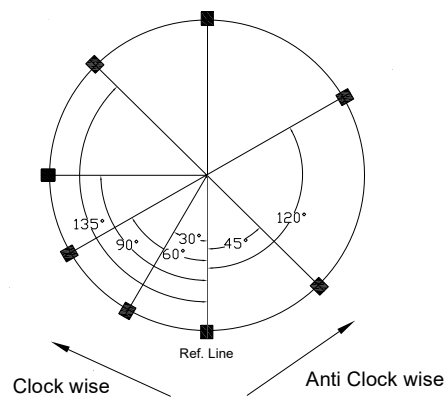
3.2.3 Instrumentation of the experimental setup

In order to estimate the heat transfer from the melt pool to the outside vault water through vessel, the temperature distribution inside the melt pool, the cylindrical vessel inner and outer wall and water pool needs to be measured. A total of 68 thermocouples were installed on the inner and outer surface of cylindrical vessel, in the molten pool and water tank at different heights. Locations of these thermocouples are shown in figure 3.5. Figure 3.5 (a) shows the thermocouples locations inside the melt pool at an angle 0° and 45°. Figure 3.5 (b) and (c) show the circumferential and longitudinal locations of thermocouples on cylindrical test vessel, whereas figure 3.5 (d) shows the thermocouples location of the water tank. Temperatures were measured by using Inconel sheathed 1 mm ungrounded K-type

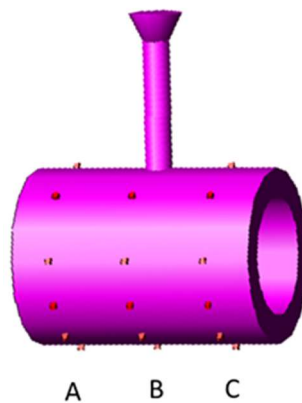
thermocouples. In addition, water level was measured by a level transmitter and steam flow was measured by the steam flow meter. All these measurements were recorded by two 48 channel DAS with a time span of 1 s.



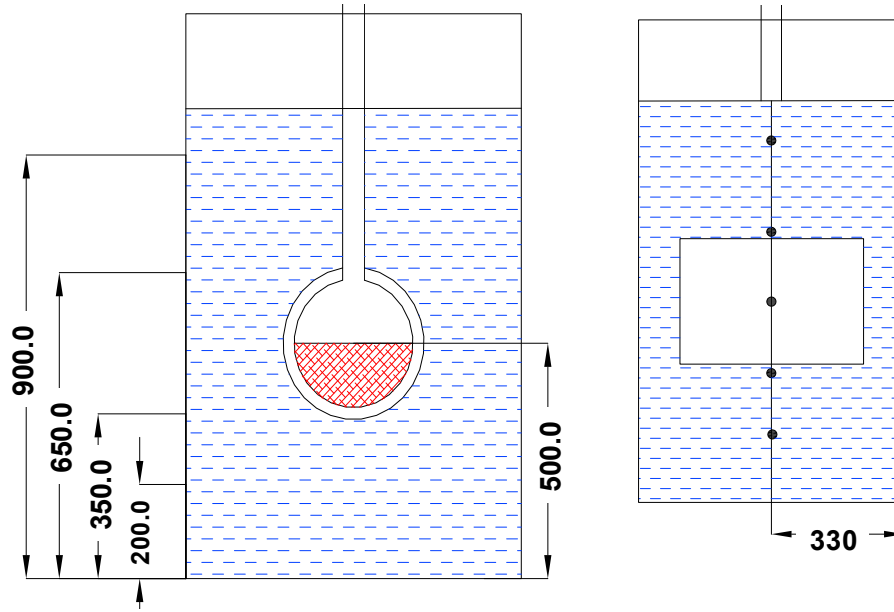
(a)



(b)



(c)



(d)

Figure 3.5. Locations of thermocouples: (a) molten pool, (b) circumferential on test section, (c) longitudinal on test section and (d) water tank thermocouples.

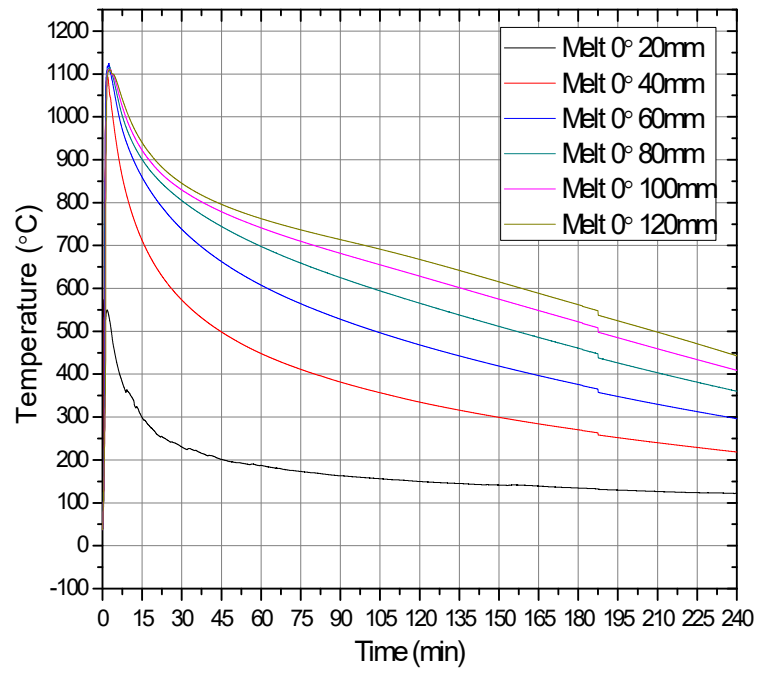
3.2.4 Experimental procedure

Small glass pebbles were charged in the cold crucible induction melting (CCLM) furnace. In CCLM, glass is directly heated by electromagnetic induction. The direct heating is accomplished in segmented crucible and it facilitates electromagnetic field into interior of the crucible resulting in eddy current and associated heating in glass [49]. Since glass has poor electrical conductivity, induction melting of glass requires high frequency for efficient heating. Therefore, induction furnace of 200 kHz and 350 kW was utilized. 60 kg glass was melted at temperature ~ 1200 °C before pouring into the experimental setup. Before the start of experiment, cold water was filled in the water tank through inlet line provided at the bottom of the water tank and the valve was closed throughout the experiment. Molten glass was poured into the cylindrical test section, which lies beneath the furnace, through a funnel

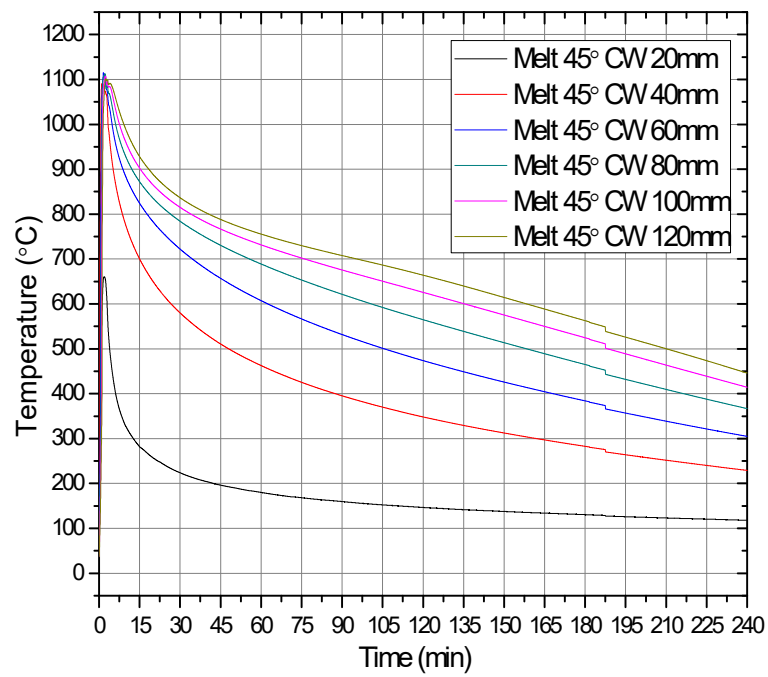
located at the top of the test section. At the start of experiment, the initial temperature of water was ambient and initial water level was nearly ~1100 mm. In case of decay heat experiment, when the temperature of melt was higher than 1200°C, the glass might react with Inconel. As cartridge heater sheath material was Inconel, so to avoid the failure of heater during experiment the heaters power was 'ON' only when pouring of melt was completed.

3.2.5 Results without Decay heat

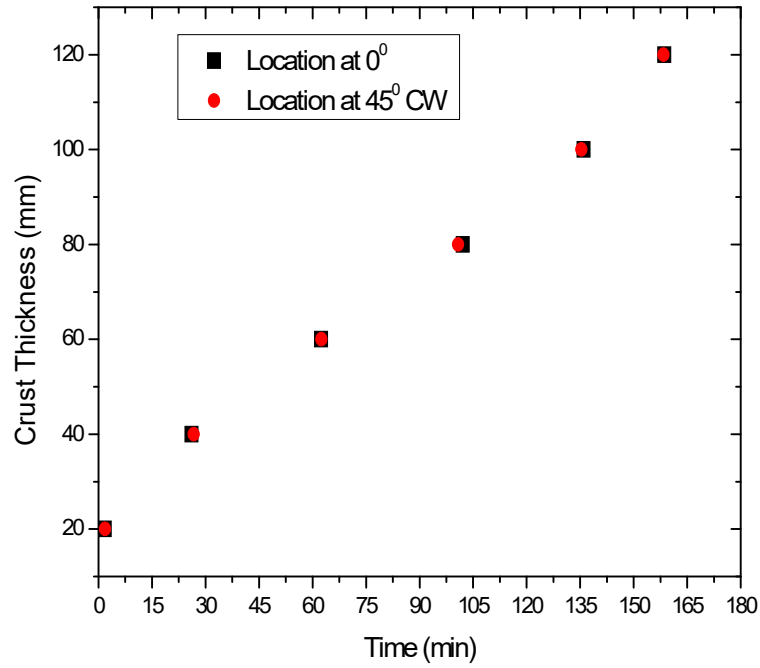
Figures 3.6 (a) and (b) show the temperatures in the melt pool at 0° and 45° locations (reference line as shown in figure 3.5 (a)) at different radial locations. From the figure 3.6 (a), it can be observed that there is a large temperature gradient inside the melt pool along the radial height. At 20 mm from bottom of cylindrical vessel, the maximum temperature observed was below 600 °C, whereas at 120 mm from bottom of vessel, the maximum temperature of melt observed was 1125 °C. Similar trend of temperature profile was observed at location 45° with respect to bottom of the vessel as shown in figure 3.6 (b). The solidus temperature of glass melt is around 600 °C and the temperature below this indicates the formation of solid crust at that position. Figure 3.6 (c) shows the crust formation with time from the bottom of cylindrical vessel. The crust thickness was varying almost linearly with time as there was no heat generation in the melt and heat transfer from the melt was mostly by conduction mode. The crust thickness variation at both 0° and 45° locations were identical since the temperature distributions were almost the same at both locations, and that is why the crust formation rate were almost the same. From figure 3.6 (c), it was observed that within 2 min from the pour of melt, crust of nearly 20 mm thickness was formed and it took almost 2.75 hours to completely solidify the melt (figure 3.6 (a)). After four hours of cooling, the maximum temperature of melt was 430 °C and minimum temperature was 120 °C. This maximum temperature is well below the $0.5 T_{mp}$ where T_{mp} is the melting temperature, i.e., 1400 °C for stainless steel test section.



(a)



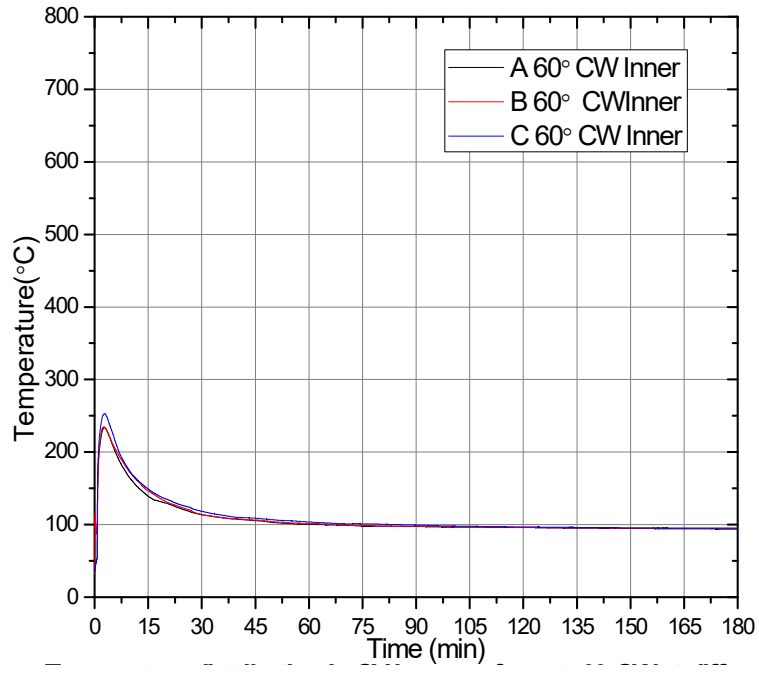
(b)



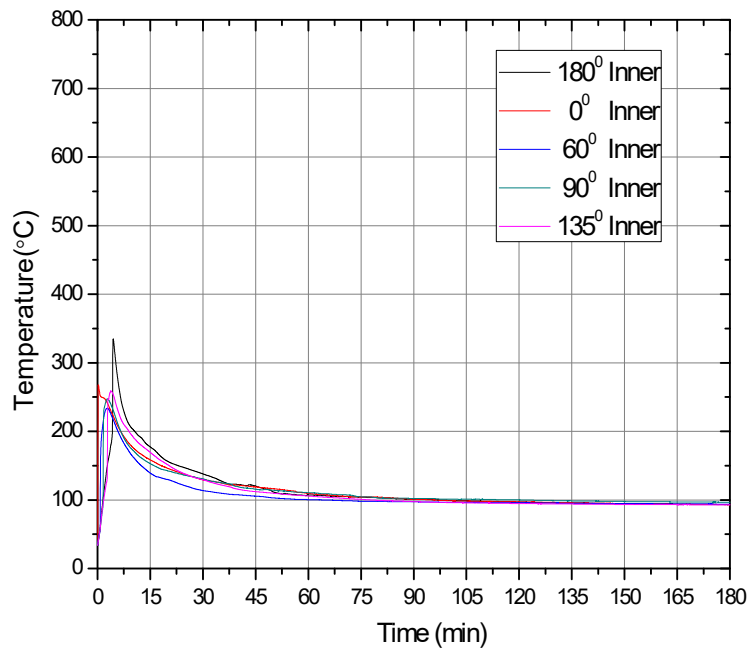
(c)

Figure 3.6: (a) Temperature distribution inside molten pool at different radial height at 0° (bottom) (b) Temperature distribution inside molten pool at different radial height at 45° (c) Crust thickness variation with time

Figure 3.7 (a) and (b) shows the axial (at 60°) and circumferential temperature variation of inner surface of cylindrical test section. In the experiment, at any particular circumferential location, no temperature difference was observed along the axial locations A, B and C as shown in figure 3.7 (a) for circumferential location 60°. However, it was observed that temperature was increasing from circumferential location 0° (225 °C) to 180° (325 °C) as shown in figure 3.7 (b). The heat dissipated in the form of radiation from the upper surface of molten pool whereas the heat transfer in the lower surface of pool took place in the form of conduction due to formation of crust. It is observed that after two hours of cooling, the temperature of inner surface of test section at different circumferential location was approximately the same. Maximum average inner surface temperature of vessel observed was 265 °C.

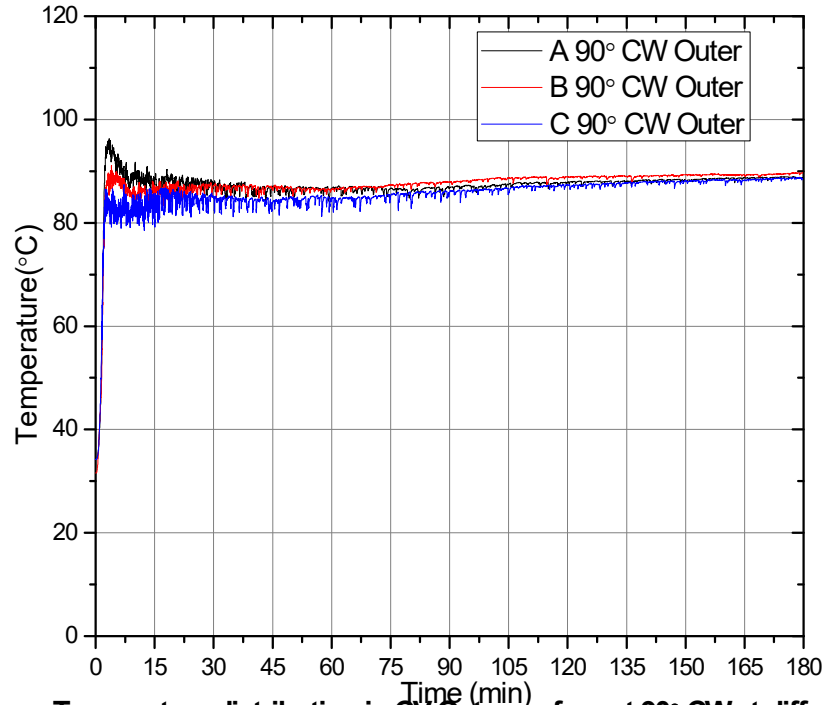


(a)

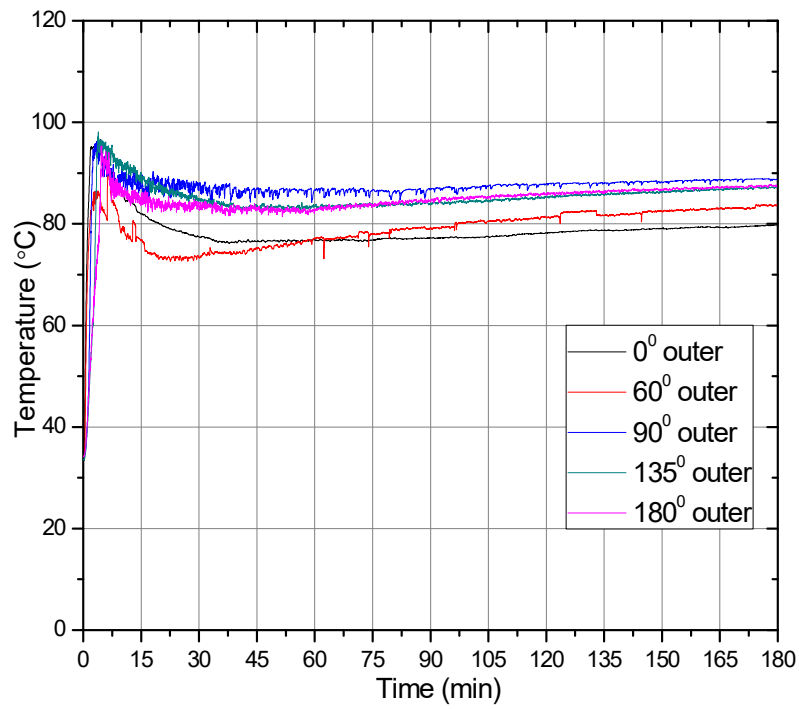


(b)

Figure 3.7: Temperature distribution of inner surface of test section (a) at axial location at 60°
(b) at different circumferential location



(a)

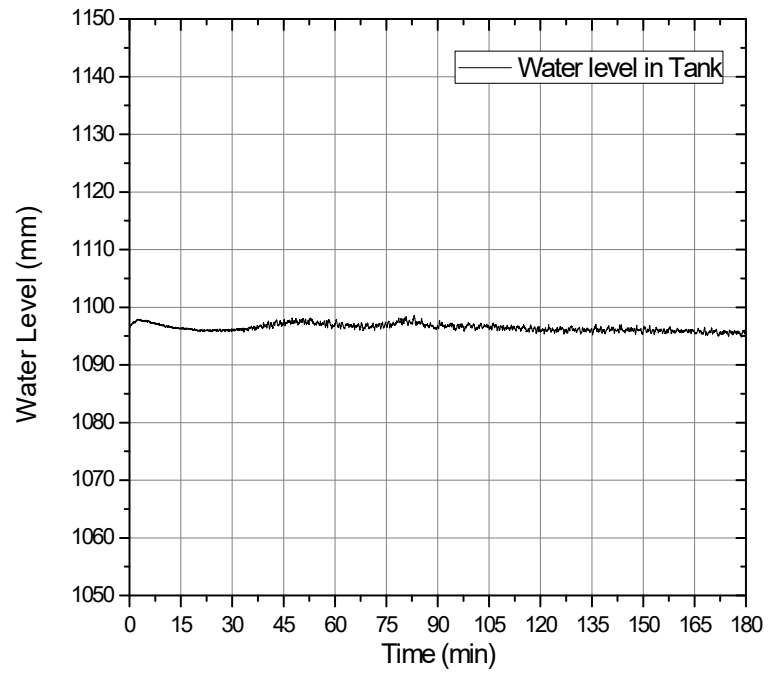


(b)

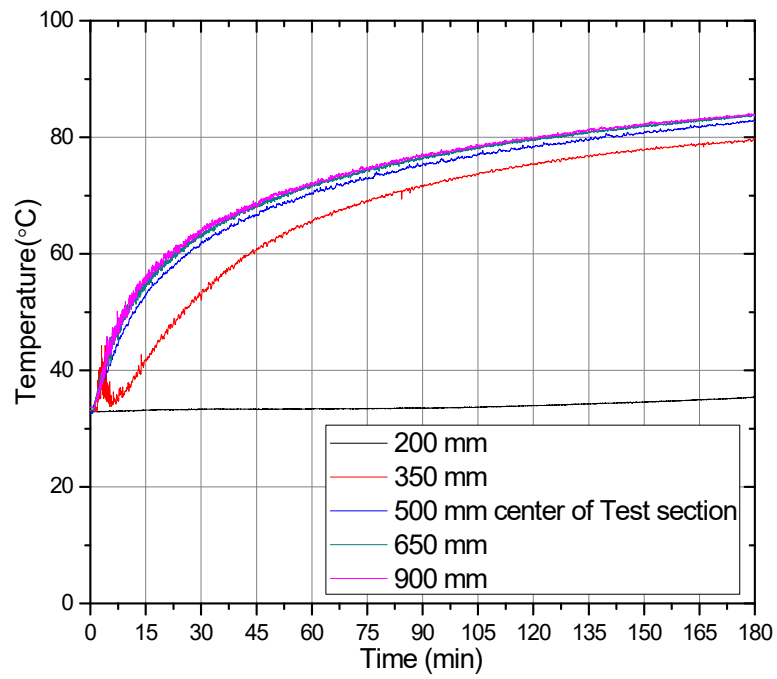
Figure 3.8: Temperature distribution of outer surface of test section (a) at axial location at 90°
(b) at different circumferential location

Figure 3.8 (a) and (b) shows the axial (at 90°) and circumferential temperature variation of outer surface of cylindrical test section. In the experiment, similar trend was observed in this case too, i.e. at any particular circumferential location, no temperature difference was observed along the axial locations A, B and C as shown in figure 3.8 (a) for circumferential location 90°. Initially, the temperature of water suddenly rose very sharply followed by reduction before it reached steady state. Maximum reduction was observed at location 0° and 60° and minimum reduction was observed at 90° locations as shown in figure 3.8 (b). Maximum average outer surface temperature of vessel observed was 94 °C.

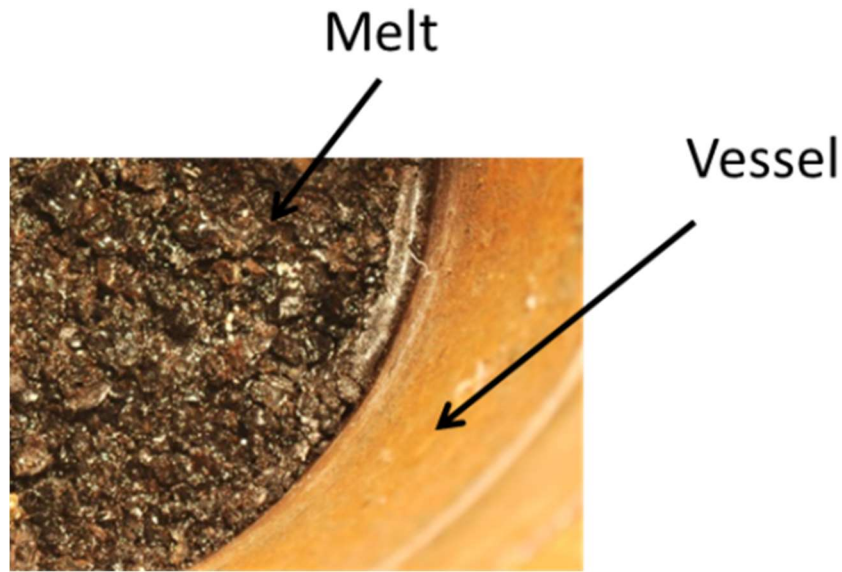
The bulk averaged temperature of water in the tank was found well below 100 °C. Also, there was no steam generation which was confirmed by steam flow meter. This was further confirmed from the level of the water tank which practically remained constant as shown in figure 3.9 (a). Figure 3.9 (b) shows the temperature profiles of water inside the water tank at different elevations, showing thermal stratification in water tank. It was also observed that water below 200 mm of tank level, remains at ambient temperature and did not take part in heat transfer during the initial phase of cooling. Once the melt was completely cooled down to room temperature, the vessel was opened up and no gap was observed between the vessel and crust by visual inspection (figure 3.9 (c)). This was further confirmed by pouring the water on the top surface of the crust for 10 min.



(a)



(b)



(c)

Figure 3.9: (a) water level in water tank (b) water temperature in water tank at different elevation (c) Picture from top of the solidified melt after the test, no gap is observed between melt and vessel

3.2.6 Results with decay heat

In the above experiment, the decay heat was not simulated in molten corium pool. Hence, the decay heat effect on the heat transfer behaviour and its thermal load on the vessel wall could not be evaluated. Apart from this, vault water was also well below the boiling temperature and heat transfer from vessel outer surface was in single phase natural convection regime. Hence, a lot of doubts remain unexplained, i.e., what happens to temperature inside molten pool, temperature across thickness of CV, crust thickness, heat transfer rate and effect of reducing water level of calandria vault due to boiling of vault water. It was decided to conduct the experiment with decay heat for extended period to understand the above unanswered issues. Experiments were conducted for prolonged period which can be subdivided in the following phases

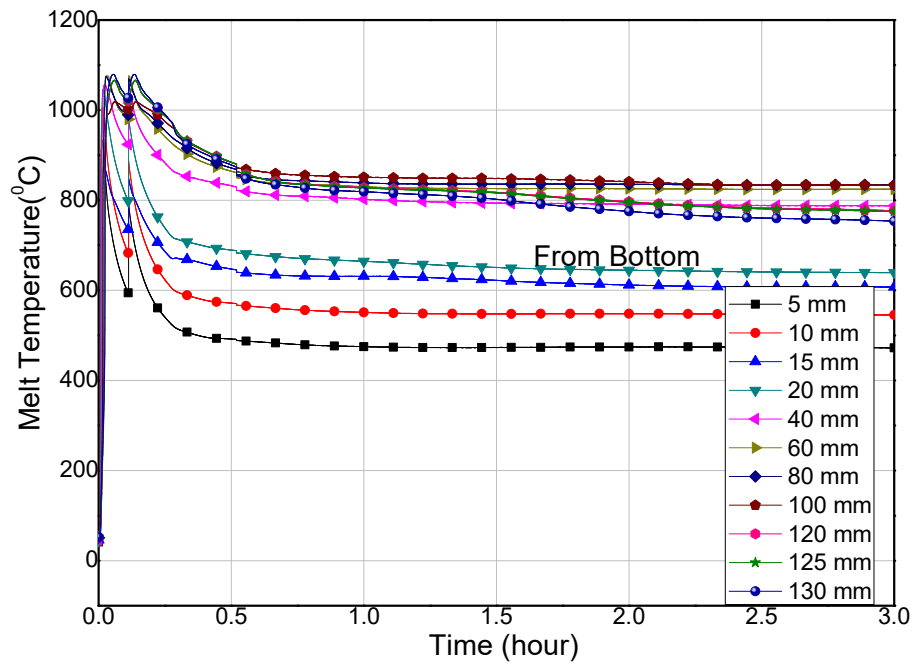
3.2.6.1 Single phase natural convection on CV outer wall

In this phase, water temperature in water tank was below the boiling point of water and CV outer surface heat transfer was in sub cooled regime. Figure 3.10 (a) showed the melt pool temperature variation with time at different radial location from bottom. From the figure, it could be observed that the temperature of melt almost reached steady state in 30 minutes after melt pouring. Considerable stratification was observed in the melt pool, which could be divided broadly into two zones. The lower zone-I has temperature below ~ 700 °C and upper zone-II has temperature above ~ 800 °C. The temperature of topmost thermocouple from bottom of vessel (i.e., at 130 mm) had lower temperature than thermocouples at 120 mm, 100 mm, 80 mm, etc. This confirmed the heat loss by radiation from upper surface of melt.

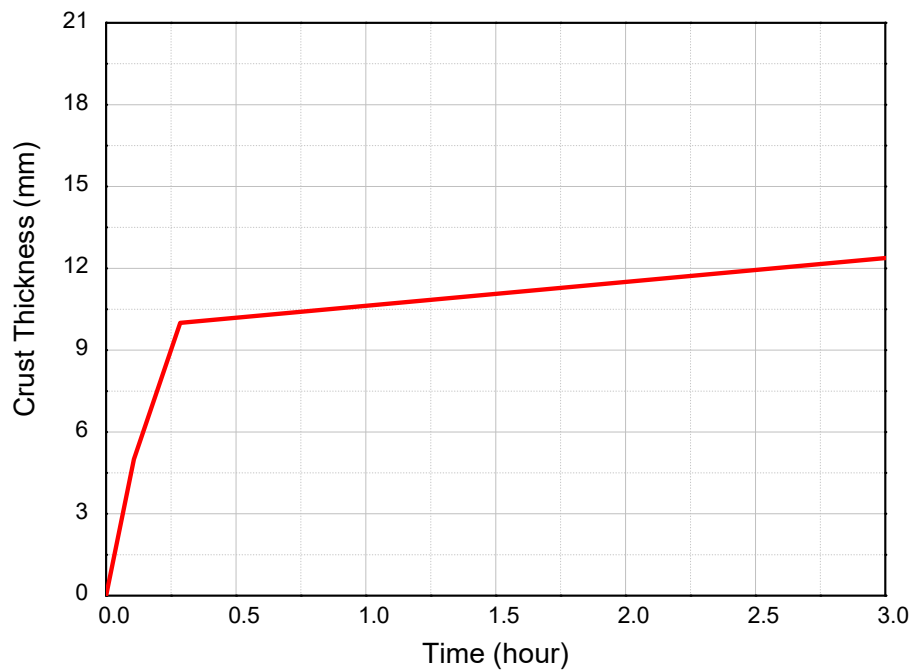
Crust formation started around the melt pool as soon as the melt was poured inside the cylindrical vessel. This was due to heat transfer from bottom melt surface to the vault water by conduction and from the top melt surface by radiation. The solidus temperature of melt is around 600 °C and temperature below this indicates formation of crust at that position. Figure 3.10 (b) shows the crust formation with time from the bottom of the cylindrical vessel. At first, the crust thickness grew very fast and afterwards, rate of crust formation was reduced. Crust thickness was measured to grow continuously up to 12 mm in 3 hrs.

Figure 3.10 (c) shows the circumferential temperature variation of inner surface of cylindrical vessel. The maximum inner surface temperature of CV was observed 255 °C. After initial transient, the temperature of inner surface vessel had almost reached steady state and maximum inner surface temperature was found at circumferential location 0°. Figure 3.10 (d) shows the circumferential temperature variation of outer surface of cylindrical vessel. Similar trend was observed as in case of without decay heat experiment. Initially, the temperature of water suddenly rose very sharply followed by reduction and then it was continuously

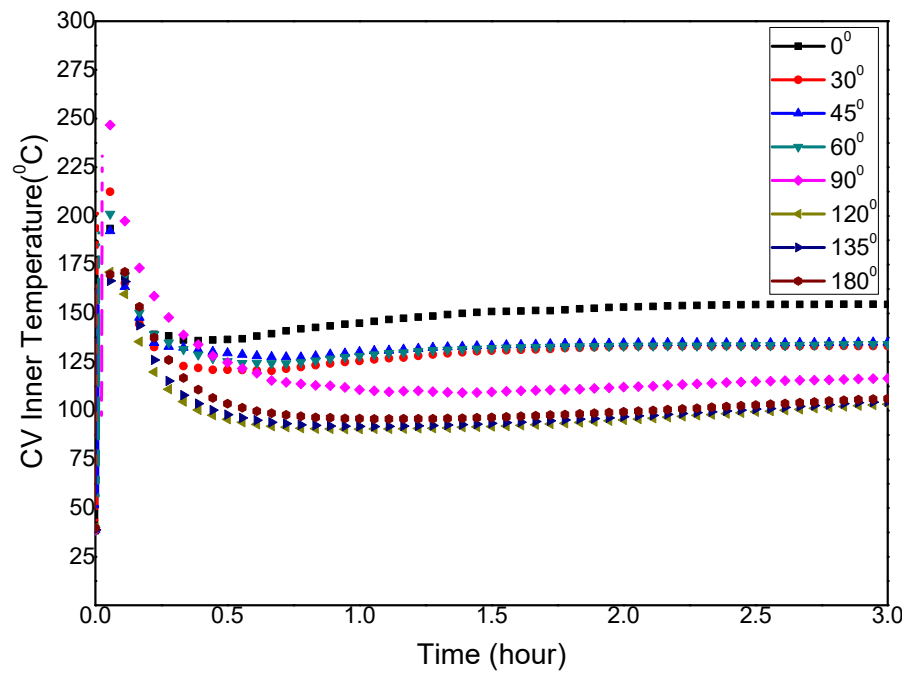
increasing. The maximum outer surface temperature of CV was found to be 102 °C after 3 hours of pouring.



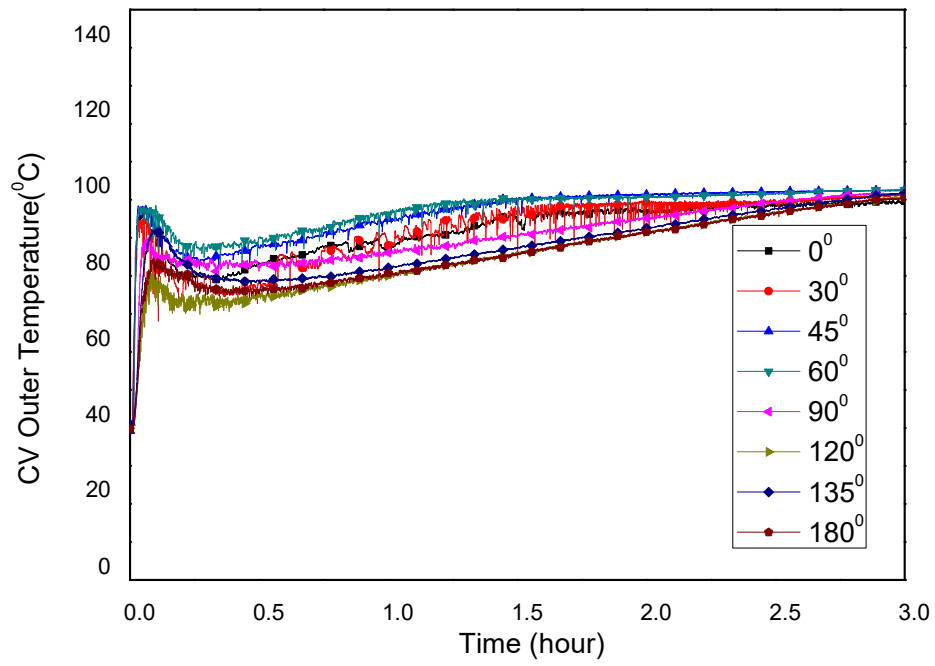
(a)



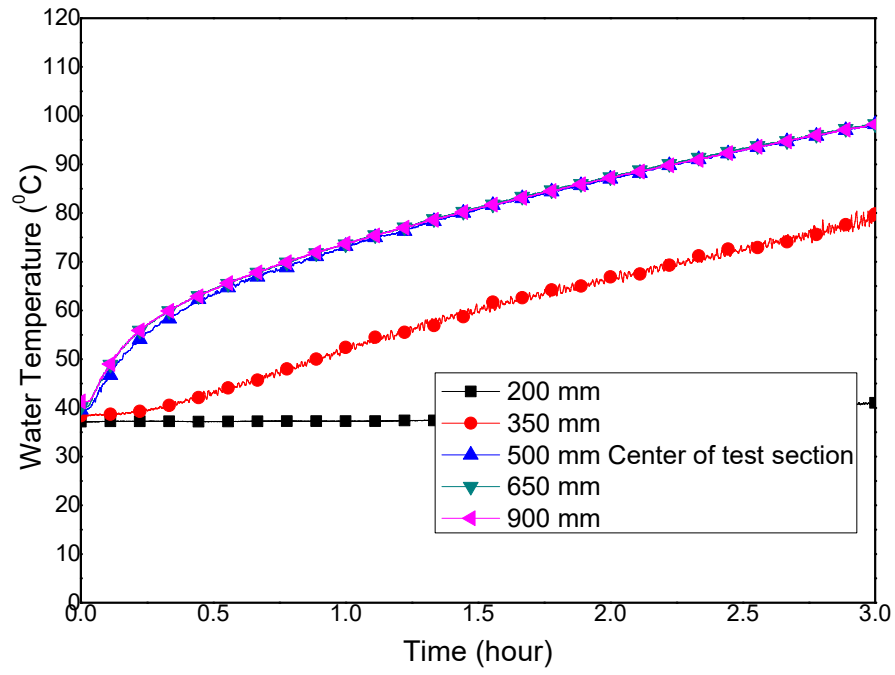
(b)



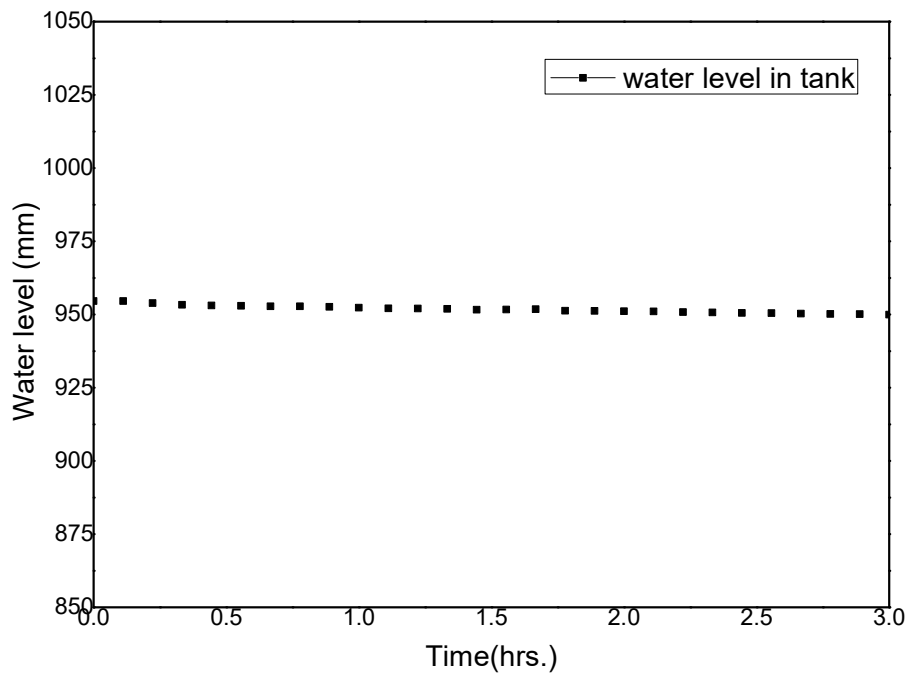
(c)



(d)



(c)



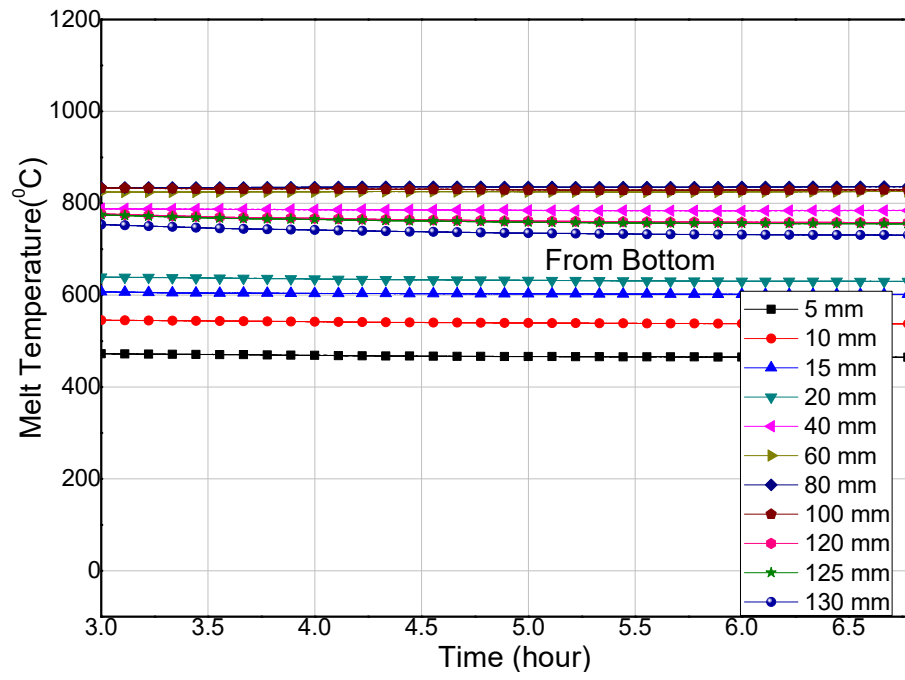
(f)

Figure 3.10: With decay heat and single-phase natural convection on outer wall (a) Melt temperature (b) Crust thickness (c) Inner CV temperature (d) Outer CV temperature (e) Water temperature (f) Water level

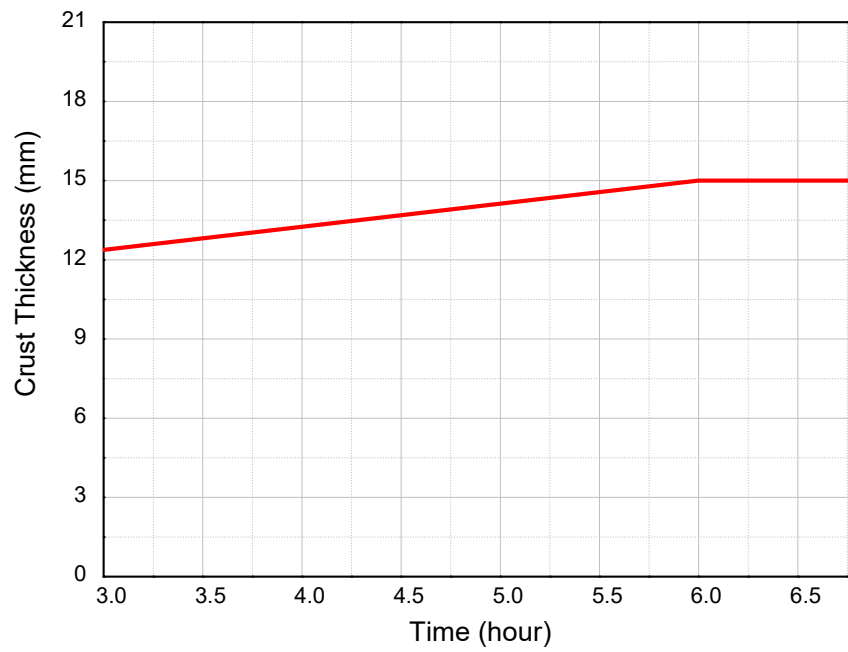
Large thermal stratification in water tank was observed (figure 3.10 (e)) and water below 200 mm of tank level, the temperature almost remained at ambient temperature and practically did not take part in heat removal process. Again, no steam generation was observed in this phase. This finding was further confirmed from the level of the water tank that remained practically constant (figure 3.10 (f)).

3.2.6.2 Boiling heat transfer on CV outer wall

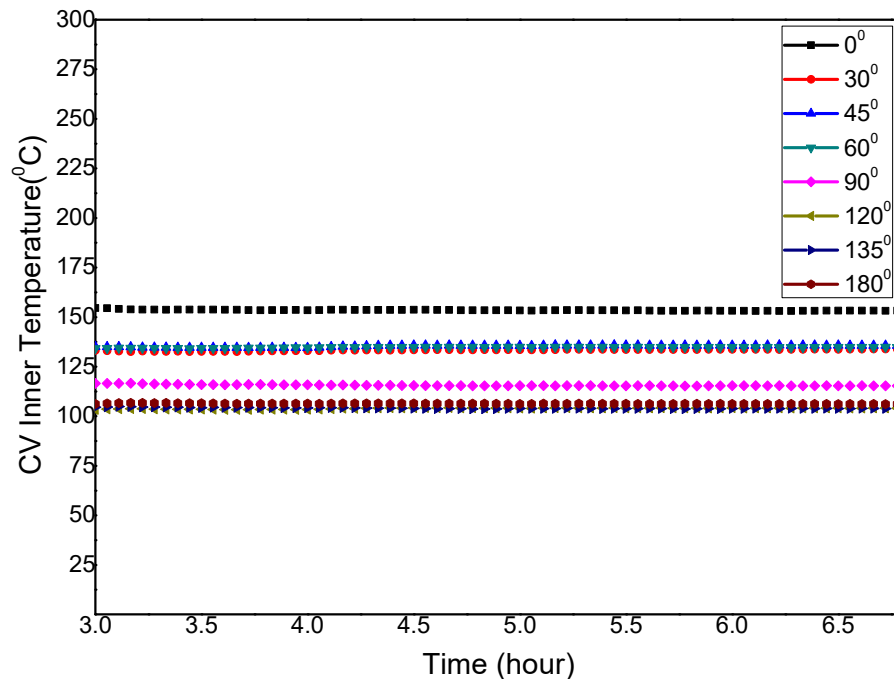
In this phase, water was boiling and heat transfer on vessel outer surface was in boiling two phase regimes. Figure 3.11 (a) shows the melt temperature variation with time at different radial location from bottom during the boiling regime. It was observed that the temperature of melt remains constant and remains unaffected with the nucleate boiling heat transfer on vessel outer wall. Figure 3.11 (b) shows the crust thickness variation. Due to the change in heat transfer regime from single phase natural convection to nucleate boiling, initially the crust thickness slightly grew from 12 mm to 15 mm. The rise in crust thickness also increases the crust thermal resistance to heat transfer which led to reduction of heat transfer to water. With these two opposite phenomena, a steady state reaches between heat transfer and heat removal which results in constant crust thickness. Inner and outer surface temperature of vessel also became steady. Figure 3.11 (c) and figure 3.11 (d) shows the circumferential temperature variation of inner and outer surface of cylindrical vessel. The inner surface temperature of CV was almost constant.



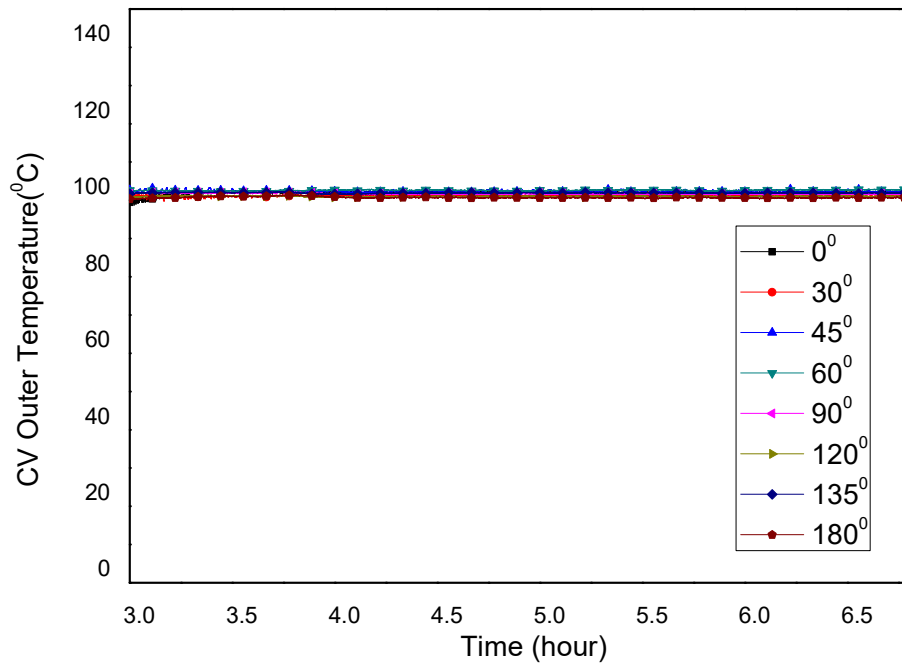
(a)



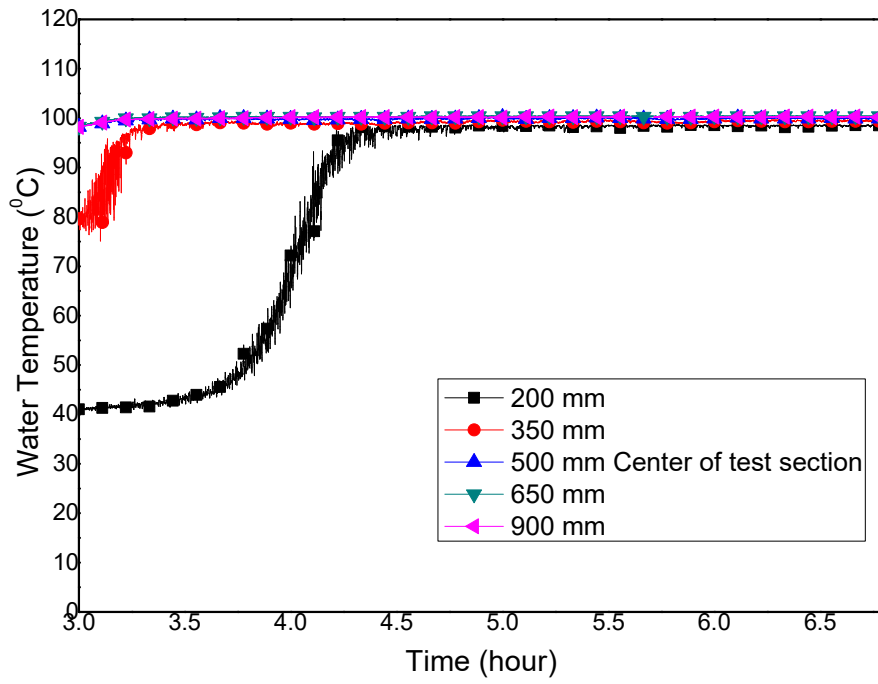
(b)



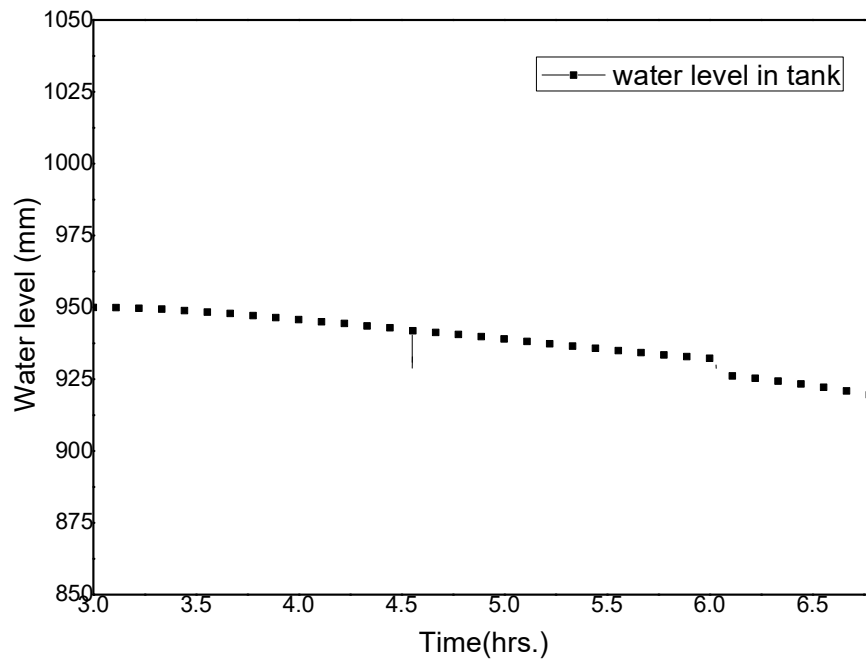
(c)



(d)



(e)



(f)

Figure 3.11: With decay heat and boiling heat transfer on vessel outer surface (a) Melt temperature (b) Crust thickness (c) Inner CV temperature (d) Outer CV temperature (e) Water temperature (f) Water level

The outer surface temperature of CV was found to be uniform in the range of 102-103 °C and became independent of circumferential location. Due to nucleate boiling, thermal stratification in water tank was disturbed (figure 3.11 (e)) and uniform mixing of water in water tank was observed. The temperature of water was steady at 100 °C. Steam generation was observed. This finding was further confirmed from the reducing level of the water tank (figure 3.11 (f)).

3.2.7 Estimation of local heat flux and CV outer surface heat transfer coefficient

The experiments showed that the heat transfer in radial and circumferential direction are more dominant compared to that in the axial direction. Hence, the outer surface heat transfer coefficient has been evaluated at different angles i.e., $r=R_{outer}$. The CV radial outer heat flux and heat transfer coefficient at different locations were calculated by using Equations (3.5) and (3.6) [50] respectively.

$$\frac{Q}{A} = k_{vess} \frac{\Delta T_{vess}}{\Delta x_{vess}} \quad (3.5)$$

where

- Q : Heat Transfer rate, W/m²
- k_{vess} : thermal conductivity of vessel, W/mK
- A : heat transfer area, m²
- ΔT_{vess} : temperature difference across vessel, K
- Δx_{vess} : thickness of cylinder, m

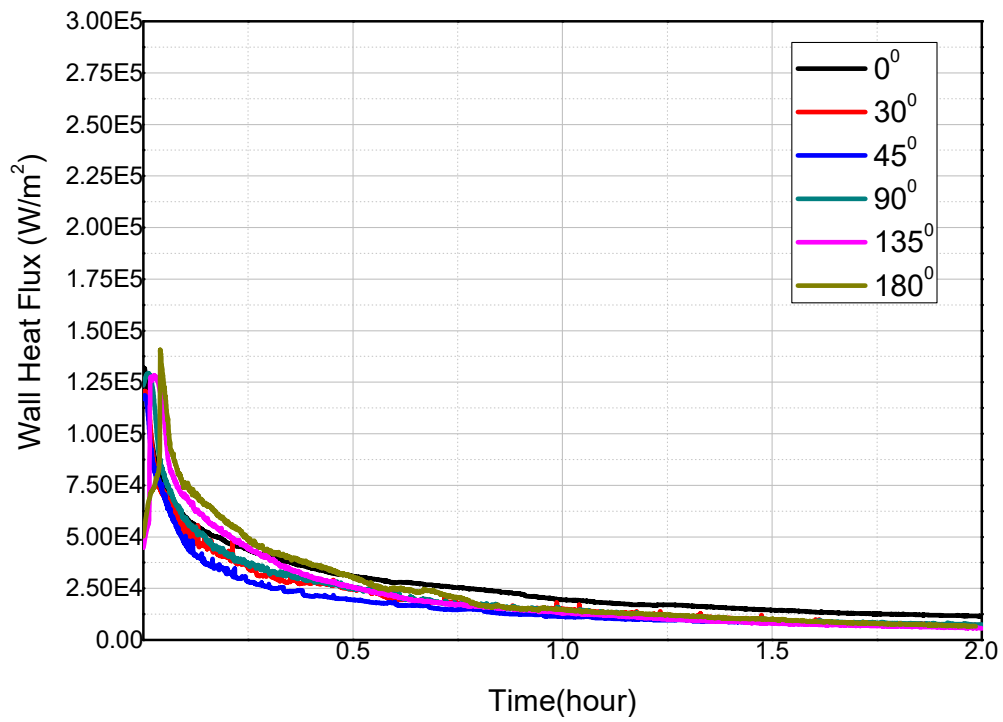
$$k_{vess} A \frac{\Delta T_{vess}}{\Delta x_{vess}} = h_{outer} A \Delta T \quad (3.6)$$

where

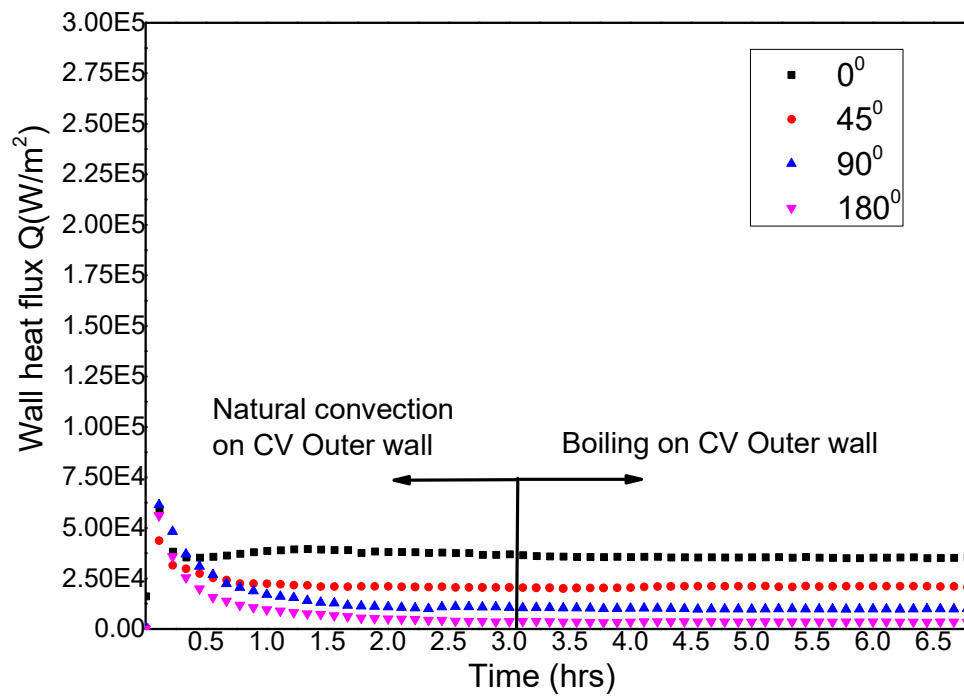
- h_{outer} : local outer heat transfer coefficient, W/m² K
- k_{vess} : thermal conductivity of vessel, W/mK
- A : heat transfer area, m²
- ΔT_{vess} : temperature difference across vessel, K
- ΔT : temperature difference between vessel outer surface and vault water,
K
- Δx_{vess} : thickness of cylinder, m

3.2.7.1 Heat Flux on CV outer wall

Figure 3.12 (a) shows the variation of CV outer wall heat flux without decay heat estimated by using the equation (3.5) whereas figure 3.12 (b) show the variation of wall heat flux with decay heat for both. single phase natural convection and nucleate boiling regimes. After initial transient, the heat flux become steady and maximum heat flux was observed at 0° circumferential location in both cases.



(a)



(b)

Figure 3.12: Outer wall heat flux (a) without decay heat (b) with decay heat

3.2.7.2 CV outer surface heat transfer coefficient

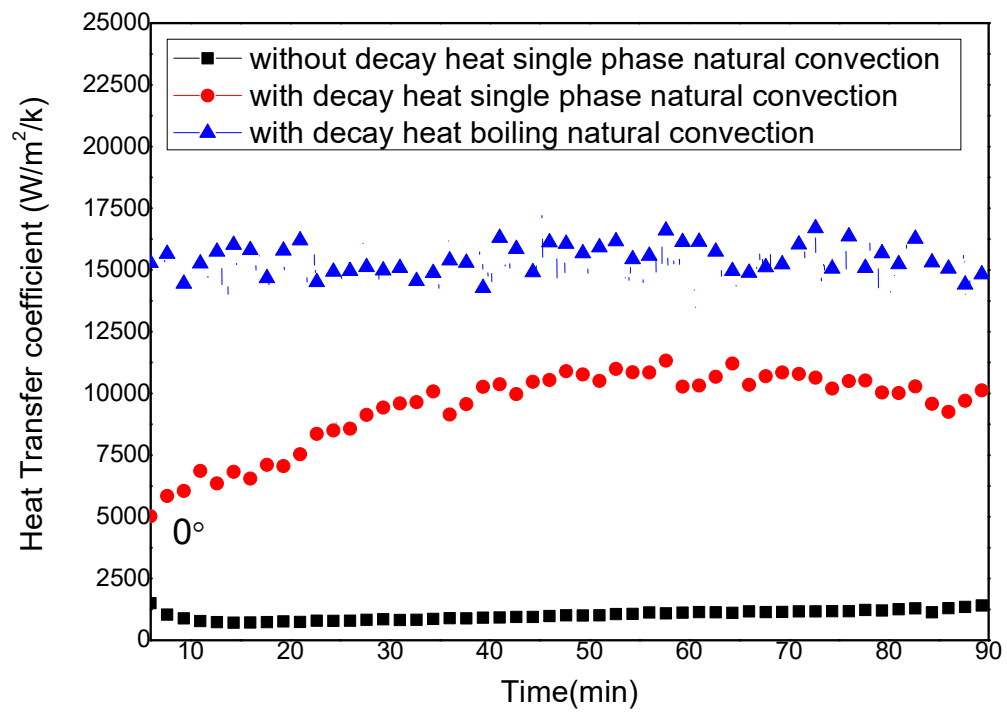
The CV outer surface heat transfer coefficient was calculated by using equation (3.6). Figure 3.13 shows the comparison of estimated CV outer surface heat transfer coefficient at various circumferential locations for the following boundary cases

- I. Without decay heat and single-phase natural convection on outer CV wall
- II. With decay heat and single-phase natural convection on outer CV wall
- III. With decay heat and boiling on outer CV wall

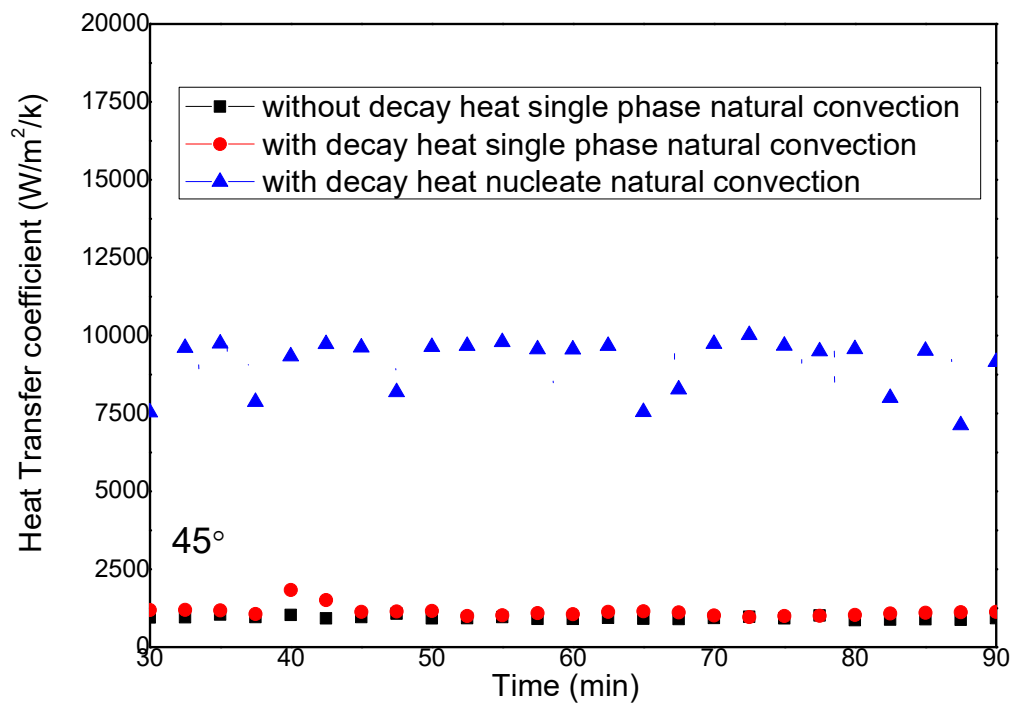
From the figure 3.13 (a), it was observed that the maximum CV outer surface heat transfer coefficient was found for case (III), i.e., decay heat with nucleate boiling heat transfer on outer CV wall and minimum outer surface heat transfer coefficient was for case (I), i.e., without decay heat with single phase natural convection heat transfer on outer CV wall at 0° location. From the figure 3.13 (b), (c), (d) and (e), that is at locations namely 45° , 90° , 135° & 180° respectively, the maximum CV outer surface heat transfer coefficient were found for case (III) whereas CV outer surface heat transfer coefficient were found comparable for case (I) and case (II) in these locations.

Figure 3.13 (f) shows the average value of CV outer surface heat transfer coefficient calculated by taking average of temperatures. The waviness or scatter data points in the figure 3.13 are due to the boiling in vault water. With nucleate boiling, the thermocouple tip frequently saw the bubble and liquid which resulted in a fluctuation of temperature.

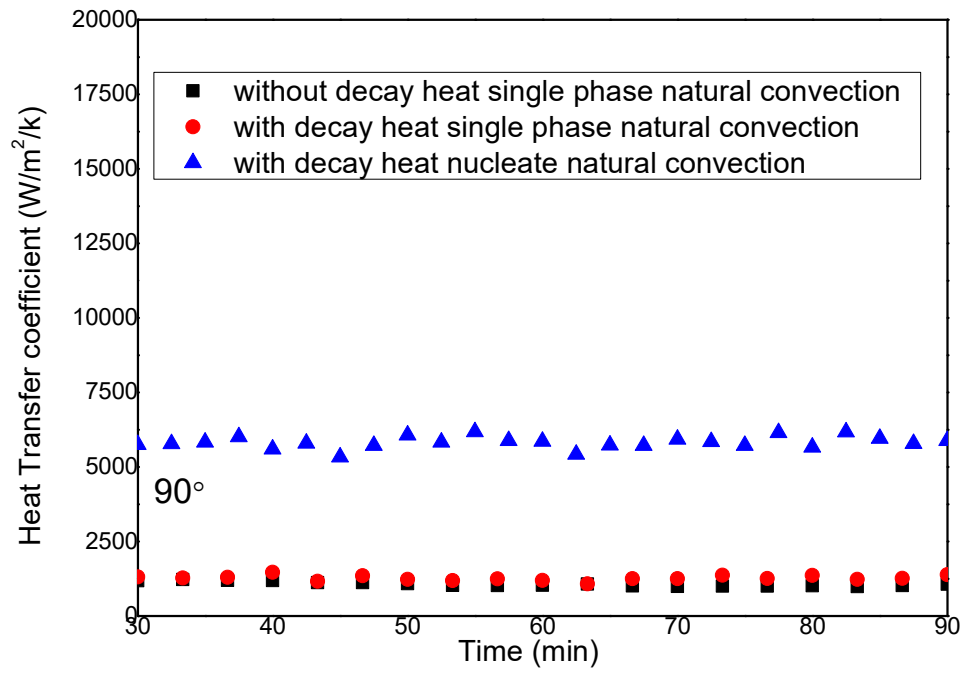
The average value of CV outer surface heat transfer coefficient for cases without decay heat and single-phase natural convection, with decay heat and single-phase natural convection and with decay heat and nucleate boiling were found $1.26 \text{ kW/m}^2 \text{ K}$, $3.08 \text{ kW/m}^2 \text{ K}$ and $10.9 \text{ kW/m}^2 \text{ K}$ respectively.



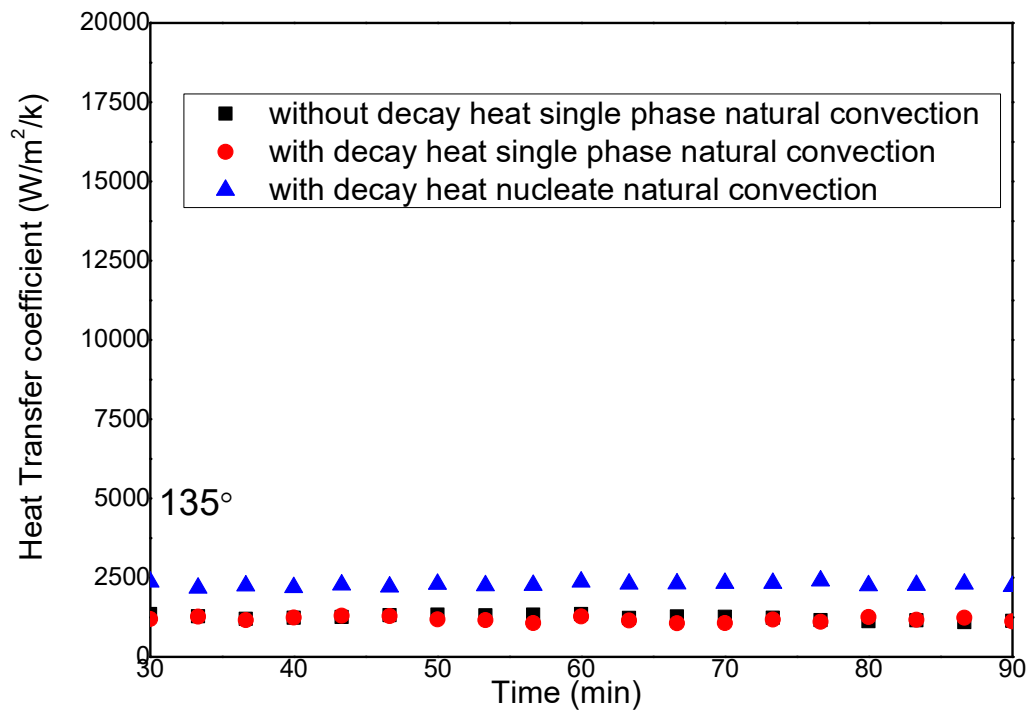
(a)



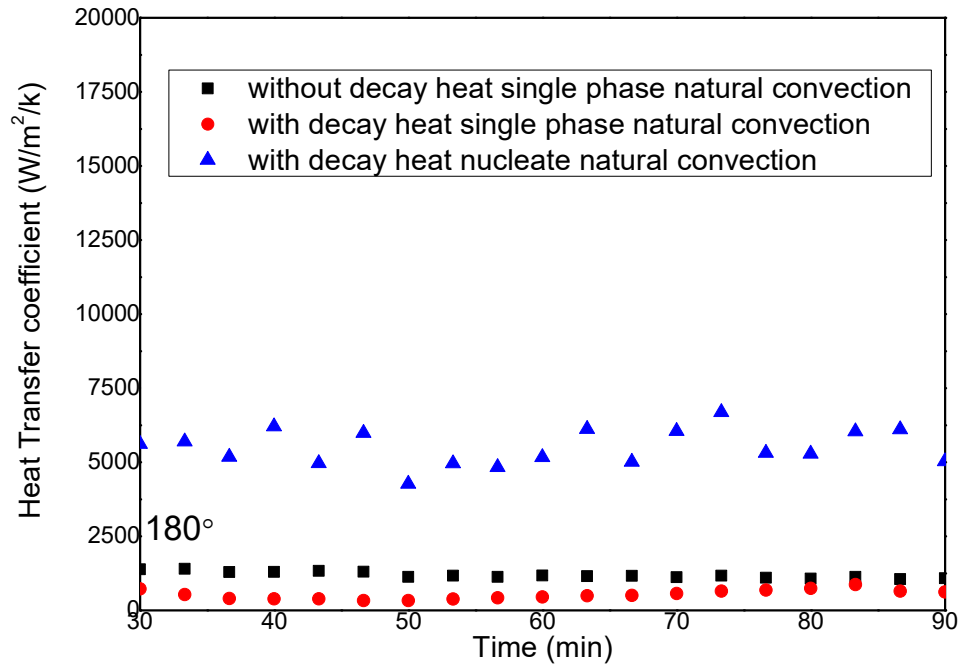
(b)



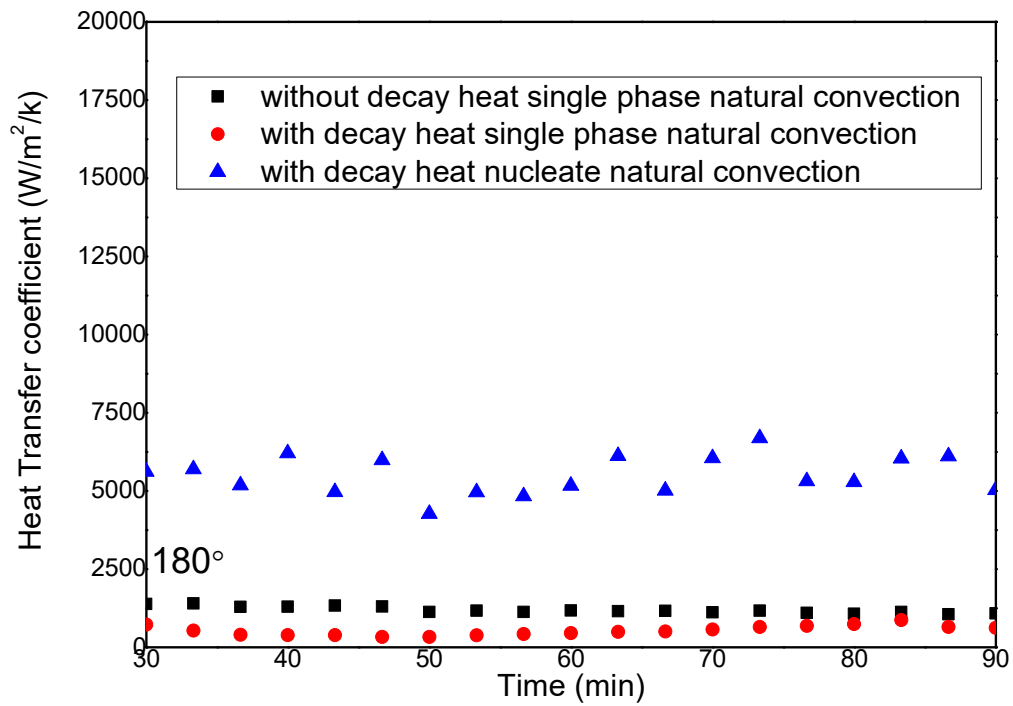
(c)



(d)



(e)



(f)

Figure 3.13: Comparison of outer heat transfer at different circumferential location (a) 0° (b) 45° (c) 90° (d) 135° (e) 180° (f) averaged

3.2.8 Estimation of overall heat transfer coefficient

As said before, the heat transfer in radial and circumferential direction are more dominant as compared to axial direction. Hence, the inner surface heat transfer coefficient has been evaluated at different angle on the calandria vessel inner surface (i.e. $r=R_{inner}$). The CV inner heat transfer coefficient was calculated by using Equations (3.7) [50]

$$k_c A \frac{\Delta T_c}{\Delta c} = h_{inner} A \Delta T \quad (3.7)$$

where

- h_{inner} : local inner heat transfer coefficient, $W/m^2 K$
- k_c : thermal conductivity of crust, W/mK
- A : heat transfer area, m^2
- ΔT_c : temperature difference across crust thickness, K
- ΔT : temperature difference between melt and crust, K
- Δc : crust thickness, m

The overall heat transfer coefficient (U_o) was calculated by using equation (3.8) as given below

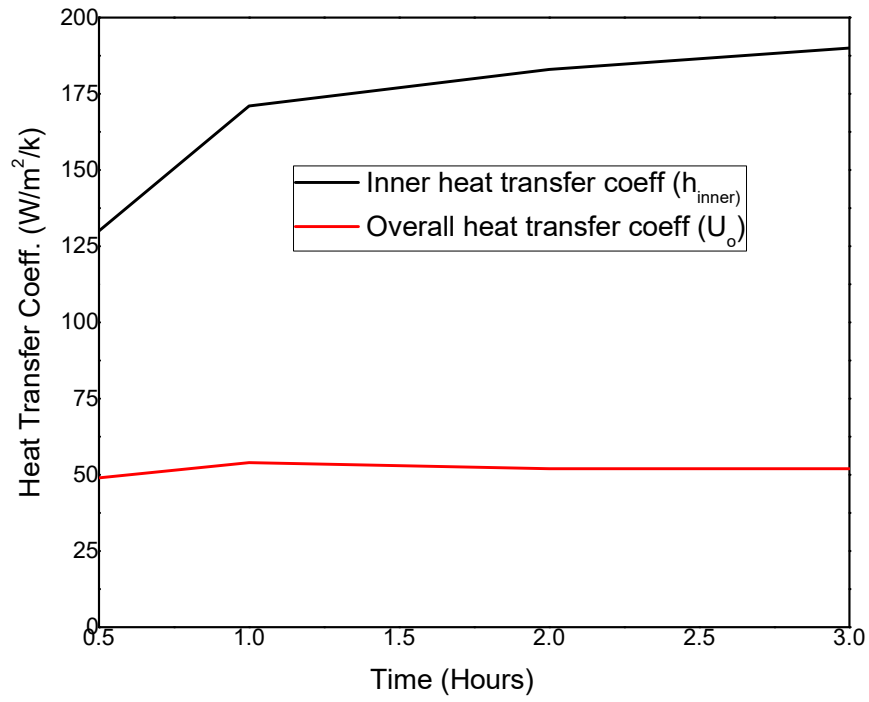
$$U_o = \frac{1}{\left(\frac{1}{h_{inner}} + \frac{\Delta c}{k_c} + \frac{\Delta x_{vess}}{k_{vess}} + \frac{1}{h_{outer}} \right)} \quad (3.8)$$

where

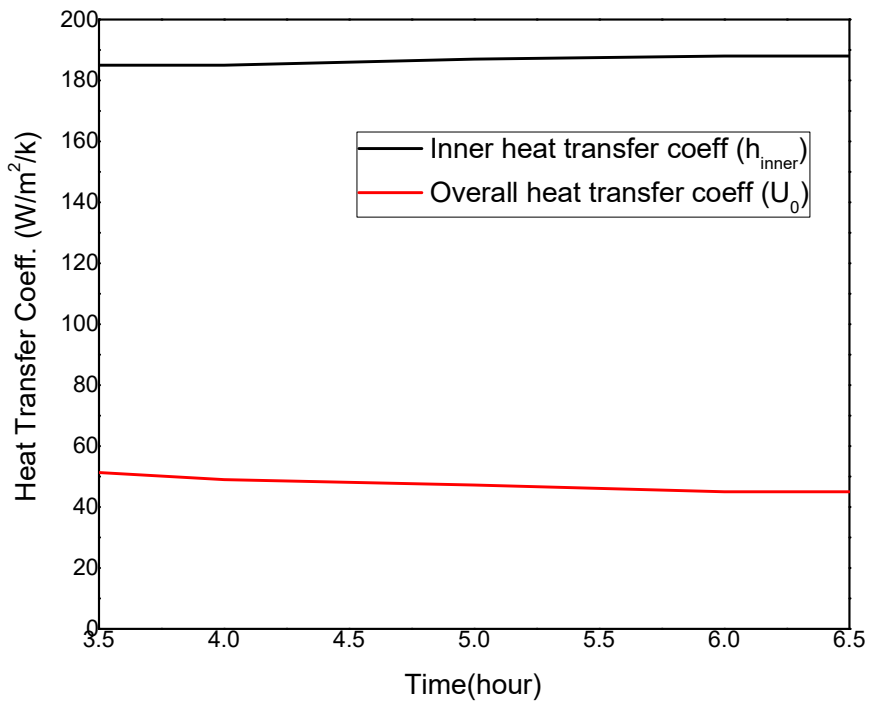
- U_o : overall heat transfer, $W/m^2 k$
- h : heat transfer coefficient, $W/m^2 k$

| | |
|-------------------|------------------------------|
| Δc | : crust thickness, m |
| Δx_{vess} | : vessel thickness, m |
| k | : thermal conductivity, W/mk |
| c | : Crust |
| $vess$ | : Vessel |
| $inner$ | : inner vessel surface |
| $outer$ | : outer vessel surface |

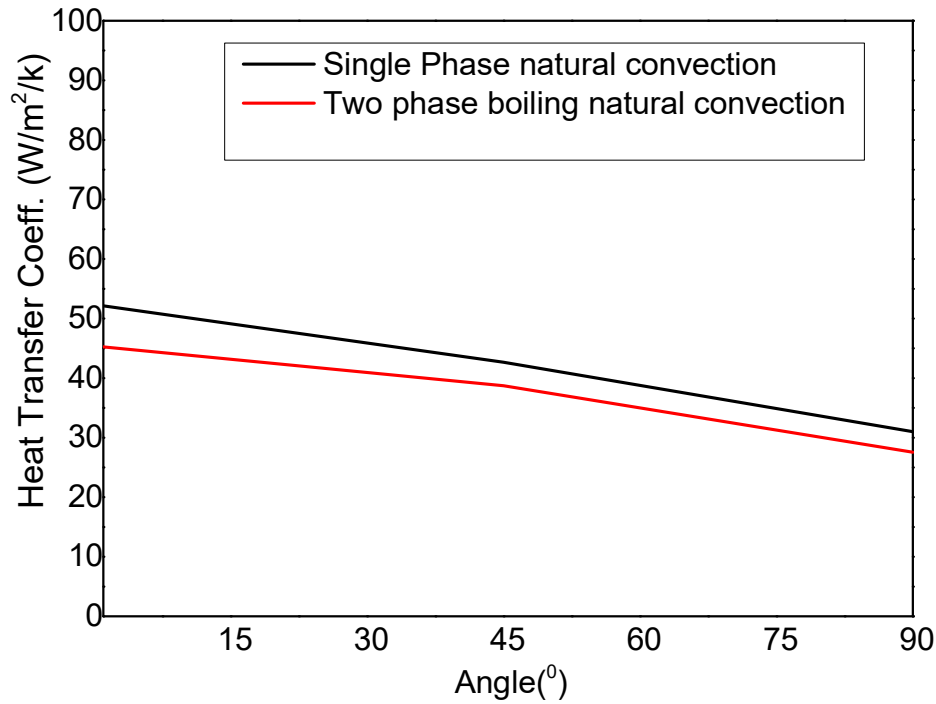
Figure 3.14 (a) show the variation of CV inner and overall heat transfer coefficient for decay heat with single phase natural convection on outer wall of vessel. Initially the heat transfer from molten pool is very high. With time as crust thickness grows, it offers thermal resistance to heat transfer. Due to this, both crust thickness growth and heat transfer decreases. Figure 3.14 (b) show the variation of CV inner and overall heat transfer coefficient for decay heat with boiling natural convection on CV outer wall of vessel.



(a)



(b)



(c)

Figure 3.14: (a) CV inner and overall heat transfer coefficient with single phase natural convection (b) CV inner and overall heat transfer coefficient with two phase boiling natural convection (c) overall heat transfer coefficient for both cases

Figure 3.14 (c) shows the comparison overall heat transfer coefficient at different circumferential locations. It was observed that even though the CV outer heat transfer coefficient (h_{outer}) has decade difference between the single-phase natural convection and two phase boiling natural convection, but overall heat transfer coefficient is of comparable order.

This is because of dominance of crust resistance ($\Delta c/k_c$) in heat transfer.

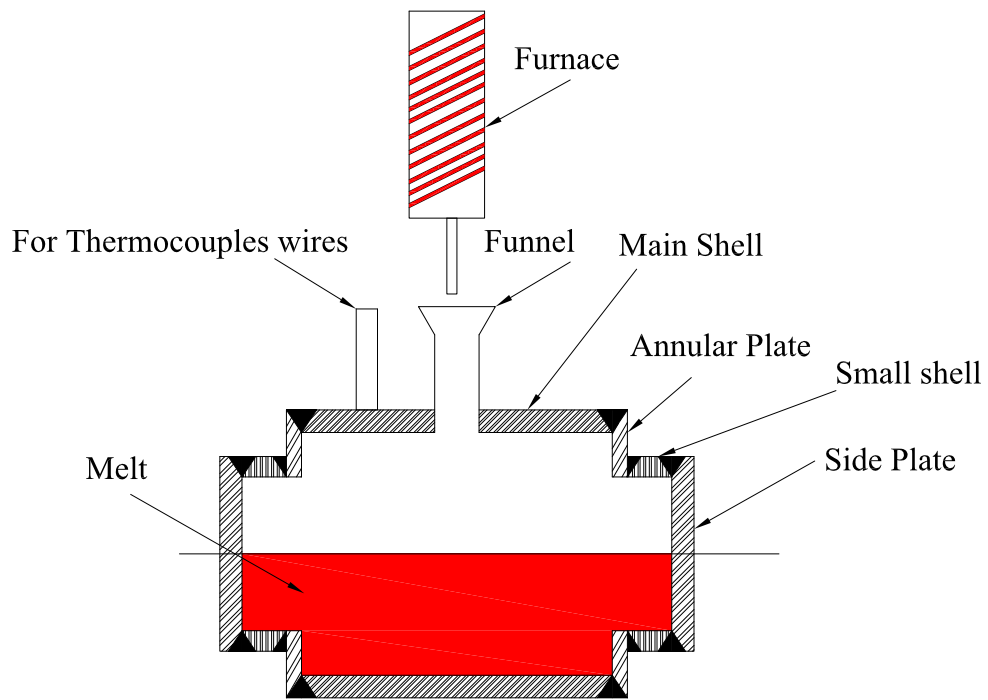
3.3 Study of integrity of CV with stepped weld joints against high thermal load

In PHWRs, the thin CV thicknesses varies from 22 mm to 32 mm and have number of weld joints resulting from the steps involved unlike the reactor pressure vessel lower head of a PWR which is made from forging with limited number of weld joints. Hence, there is a

concern about the integrity of the thin vessel with stepped weld joints due to the sudden thermal loading of high temperature corium melt. Also, due to sudden thermal load, there may be chance of excessive thermal strain of vessel and weld joints and it may result in failure before the corium stabilization inside the vessel is achieved. There are almost no experimental studies on the structural behaviour of stepped calandria vessel during the high temperature corium relocation in PHWRs. Hence, the objective of this experimental study is to investigate the thermal strain and integrity of simulated stepped calandria vessel with weld joints against thermal load of corium.

3.3.1 Experimental setup

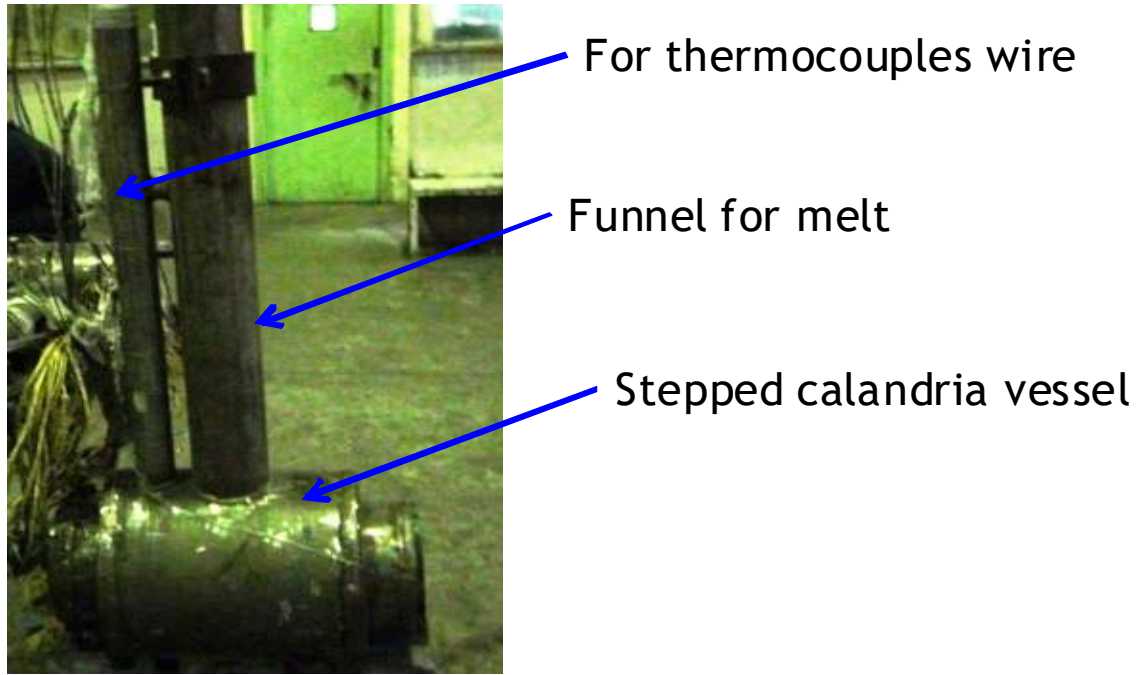
The scaled test facility as shown in figure 3.15 has been designed to study the thermal strain and integrity behaviour of stepped calandria vessel of an Indian 700 MWe PHWR. The experimental facility consists of an induction furnace for producing high temperature melt pool and stepped cylindrical test vessel simulating CV. The stepped test vessel is made up of main shell, small shell, annular plate and side plates as shown in figure 3.15 (a). The diameter of the test vessel varies from 300 mm to 200 mm and vessel thickness varies from 26 mm to 22 mm. The stepped calandria vessel was simulated in the experiment by diameter scaling ratio of 1:26 and length scaling ratio of 1:13. The thickness of cylindrical test section was kept nearly same as calandria vessel of the reactor. The scaling ratio of various components of stepped test section is shown in table 3.4. The cylindrical test section is made of same material (SS304L) as of prototype calandria vessel in PHWR. The heat transfer parameter and material properties are same as given in table 3.1 and 3.2. During the experiment, the whole experimental setup was kept in ambient air to get more severe thermal condition compared to that of keeping the simulated calandria submerged in water in calandria vault as in actual case in PHWR. Hence, strain recorded in experiment was much more than in actual case.



(a)



(b)



(c)

Figure 3.15: (a) schematic of Stepped calandria (b) Stepped calandria (c) Stepped calandria vessel set up

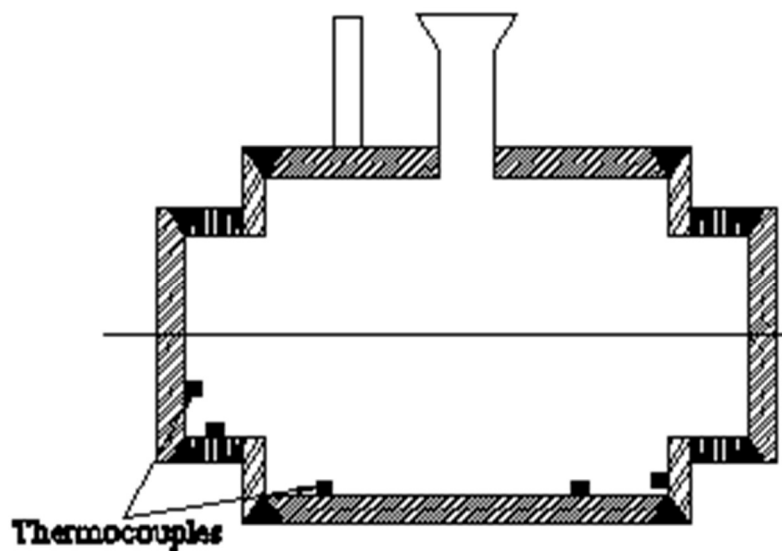
Table 3.4: Experimental stepped setup details

| Components | Dimension | Scaling ratio |
|----------------|-----------|---------------|
| Main shell | 300 mm | 1:26 |
| Small Shell | 200 mm | 1:26 |
| Overall length | 456 mm | 1:13 |
| Thickness | 22/26 mm | 1:12 |

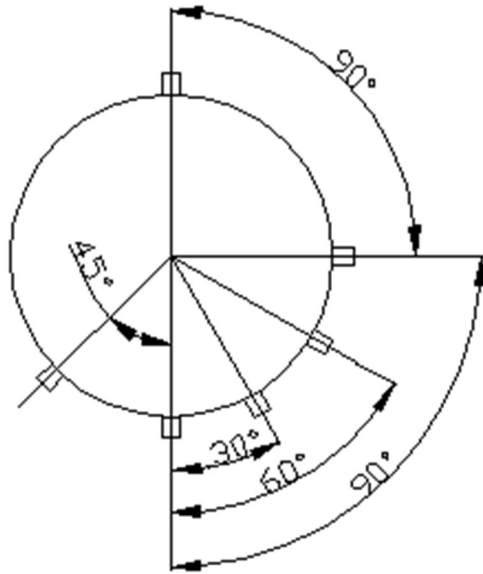
3.3.2 Instrumentation of experimental setup

The experimental setup was comprehensively instrumented with thermocouples and strain gauges. There were six thermocouples installed inside the molten pool in radial direction for melt temperature measurement. Approximately sixty thermocouples were mounted on the stepped cylindrical test vessel of inner and outer wall at different longitudinal and

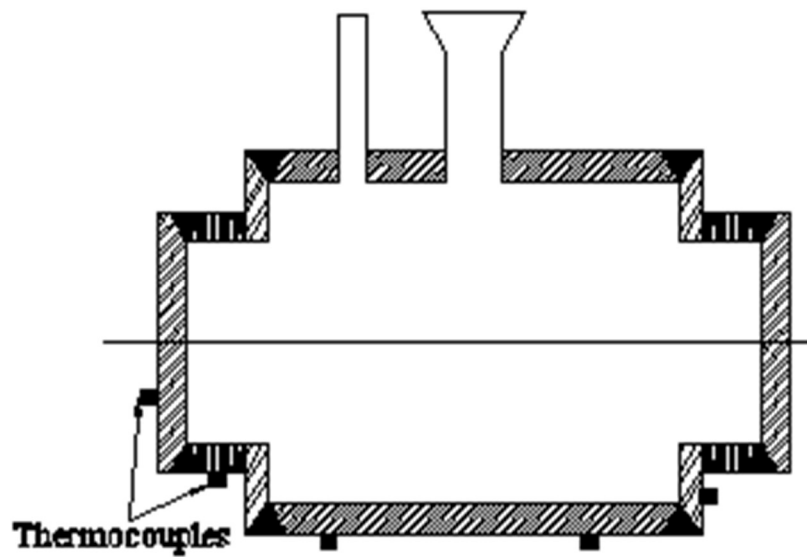
circumferential locations. Four thermocouples were installed at various weld locations. Temperatures were measured by using Inconel sheathed 1 mm ungrounded K-type thermocouples. For strain contour measurement, strain gauges were installed at outer surface of cylindrical test vessel at various locations like main shell, small shell, annular plate and side plates. Also strain gauges were installed on some of the weld locations to see the weld strain contours. The detailed locations of these thermocouples and strain gauges are shown in figure 3.16. Figure 3.16 (a) and (b) show the longitudinal and circumferential location of thermocouples on inner surface cylindrical test vessel, whereas figure 3.16 (c) and (d) shows the longitudinal and circumferential location of thermocouples provided on outer surface of test section. Figure 3.16 (e) shows the locations of thermocouples inside the melt. Strain contour on outer surface of cylindrical test vessel was measured by strain gauges and their locations are shown in figure 3.16 (f).



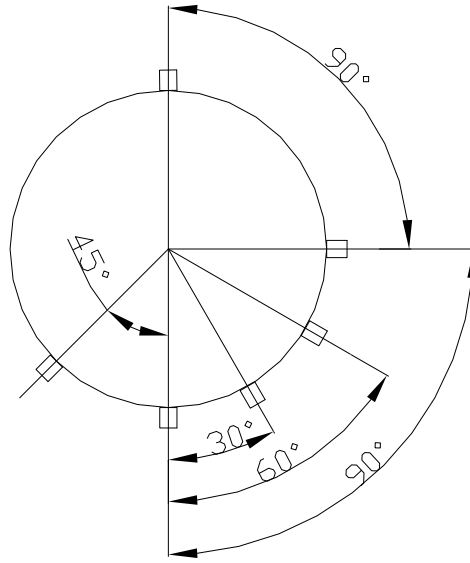
(a)



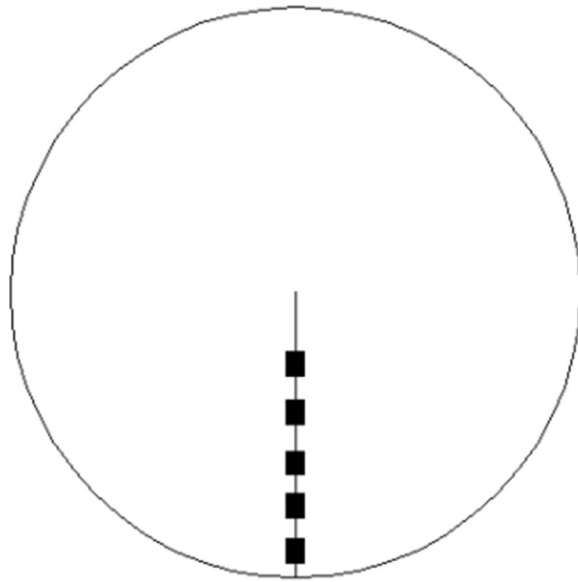
(b)



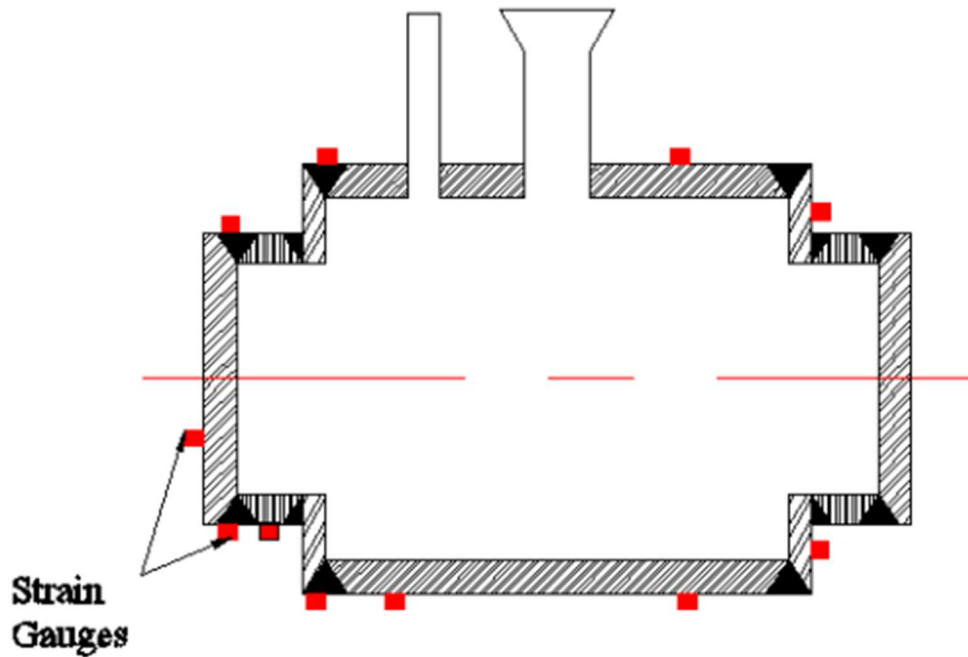
(c)



(d)



(e)



(f)

Figure 3.16 (a) longitudinal location of thermocouples on inner surface (b) circumferential location of thermocouples on inner surface (c) longitudinal location of thermocouples on outer surface (d) circumferential location of thermocouples on outer surface (e) location of thermocouples in melt pool (f) location of strain gauges on outer surface

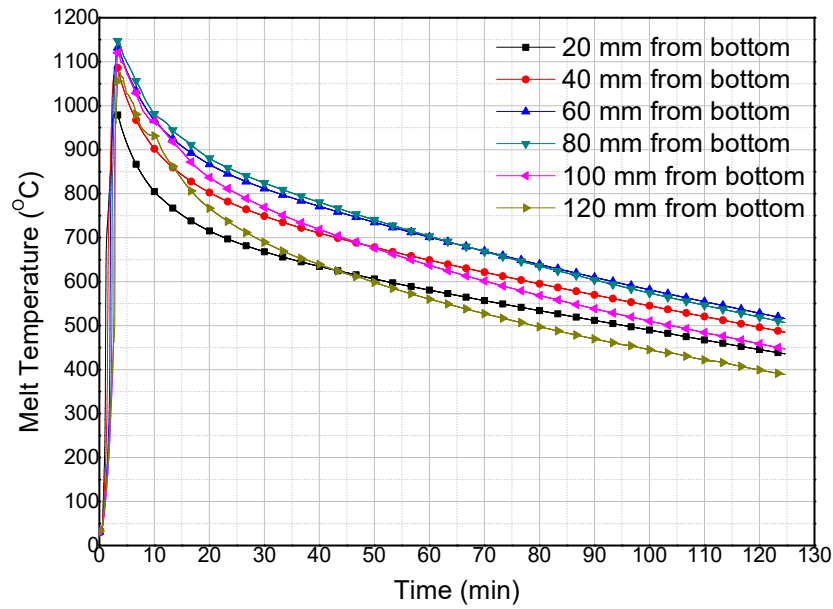
3.3.3 Experimental procedure

Glass was used as a simulant melt. The glass was heated up to 1200 °C before pouring and then poured into the cylindrical test vessel lying beneath the furnace through a funnel located at the top of the test section. The setup was cooled by ambient air whose temperature was 30 °C.

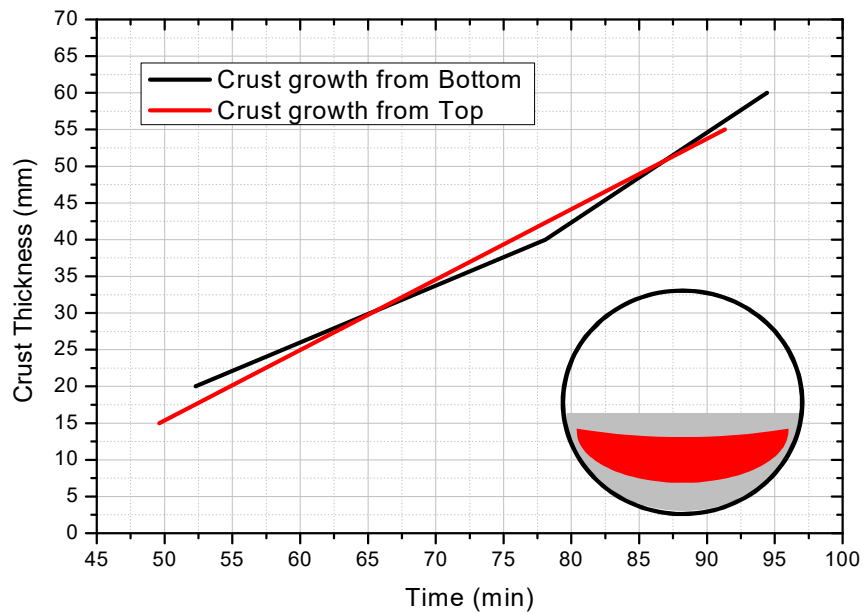
3.3.4 Results

Figure 3.17 (a) shows the temperature variation of melt pool at different radial locations. From the figure, it was observed that peak temperature of melt at different radial location was above the 980 °C. But with time, the temperature gradient inside the melt pool along the radial height was observed and it varied from 700 °C to 550 °C after one hour of pouring.

The formation of crust at inner bottom of the vessel and at the top surface of melt resulted in reduction of heat transfer from melt pool to ambient as crust acts as insulation due to its poor thermal conductivity.



(a)



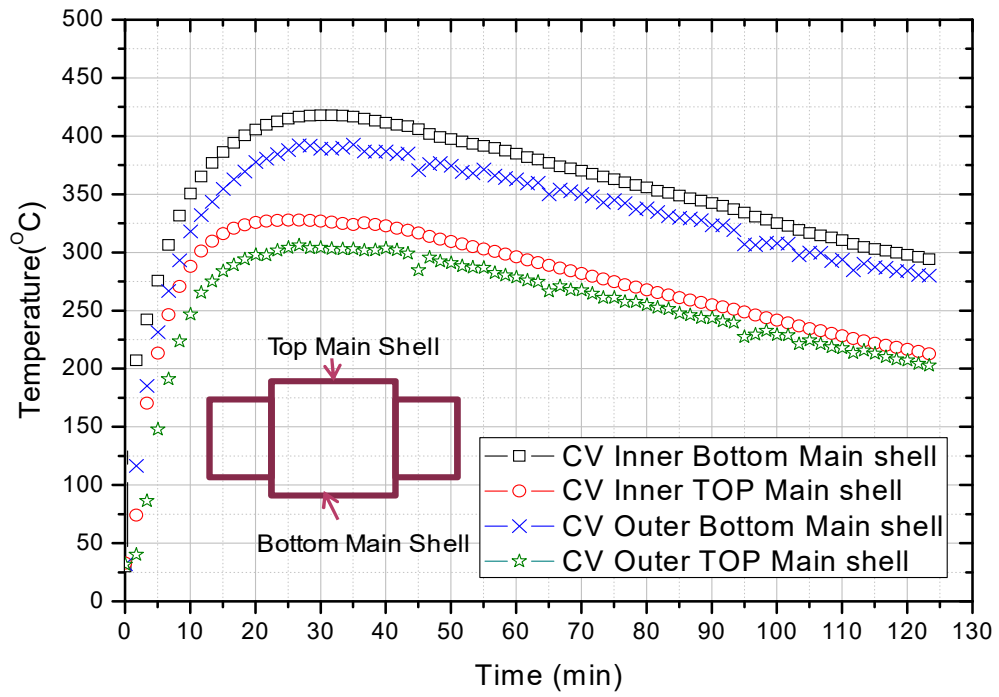
(b)

Figure 3.17: (a) Temperature distribution of molten pool at different radial heights (b)

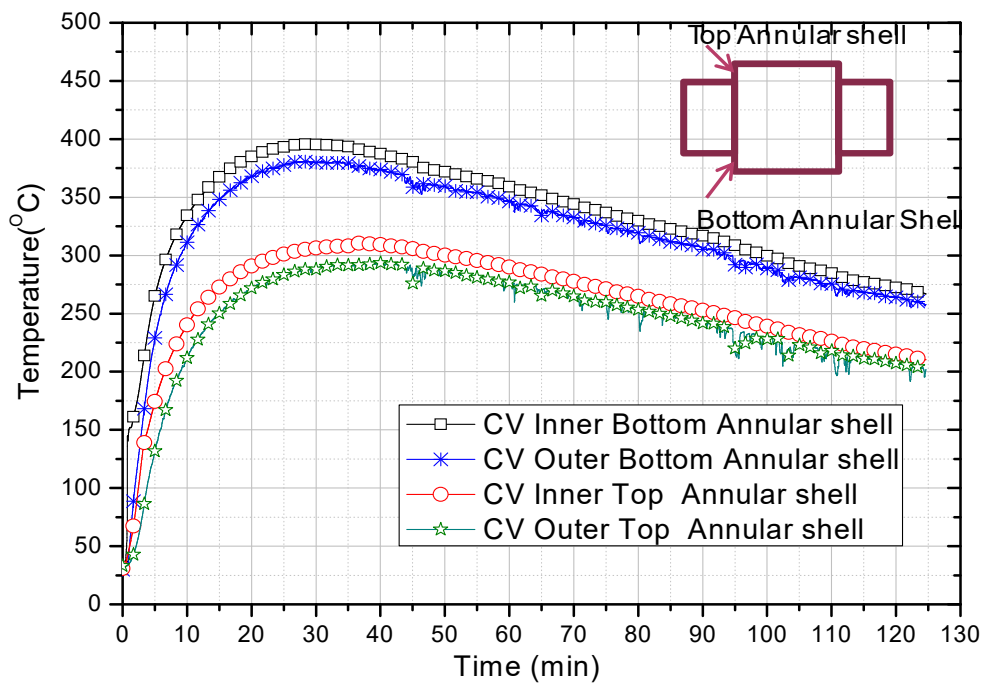
Crust thickness variation with time:

The temperature below the solidus temperature ($\sim 600\text{ }^{\circ}\text{C}$) of melt indicates the formation of solid crust at that position. Figure 3.17 (b) shows the crust growth variation from bottom and top surface of melt of the stepped test section. As bottom thermocouple is located 20 mm from melt bottom and top thermocouple is located 15 mm from melt top, that is why delay of time are observed in figure 3.17 (b). From the figure 3.17 (b), it is observed that the crust growth from bottom is similar to the crust growth from top despite different heat transfer mechanisms. For bottom surface, heat removal from crust bottom surface to vessel is by conduction whereas for top surface, it is by convection and radiation. Once the crust formed, it introduces high thermal resistance which governs the heat transfer from the crust to its surroundings from top and bottom surfaces. This leads to approximately similar temperature condition at both surfaces of crust. Thus, heat transfer mechanism from the crust surfaces doesn't affect the formation of crust thickness.

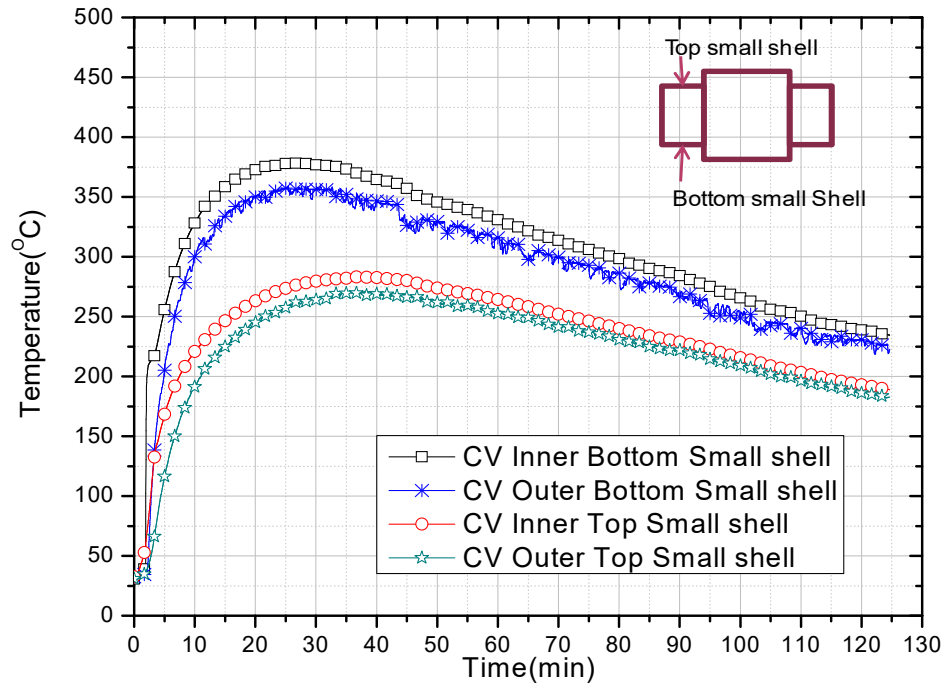
Figure 3.18 shows the temperature variation of inner and outer surface of main shell, annular plate, small shell and weld of cylindrical test vessel. From the figure, it is clear that even though the pour temperature of melt was above $1100\text{ }^{\circ}\text{C}$, still the maximum temperature of stepped test vessel was observed approximately $420\text{ }^{\circ}\text{C}$ in inner bottom surface of main shell and $392\text{ }^{\circ}\text{C}$ in bottom outer surface of main shell. The maximum temperatures observed at bottom of main shell, annular plate, small shell, weld of cylindrical test section was $420\text{ }^{\circ}\text{C}$, $400\text{ }^{\circ}\text{C}$, $378\text{ }^{\circ}\text{C}$ and $370\text{ }^{\circ}\text{C}$ respectively whereas the maximum temperature observed at top of main shell, annular plate, small shell, weld of cylindrical test vessel was $327\text{ }^{\circ}\text{C}$, $310\text{ }^{\circ}\text{C}$, $282\text{ }^{\circ}\text{C}$ and $242\text{ }^{\circ}\text{C}$ respectively. Hence, the maximum temperature difference between bottom and top (i.e., along the diametrical opposite location) of cylindrical test vessel was recorded in the range of $93\text{ }^{\circ}\text{C}$ whereas the maximum temperature difference across the test section thickness along main shell, annular plate and small shell were recorded in the range of $27\text{ }^{\circ}\text{C}$, $20\text{ }^{\circ}\text{C}$ and $25\text{ }^{\circ}\text{C}$ respectively.



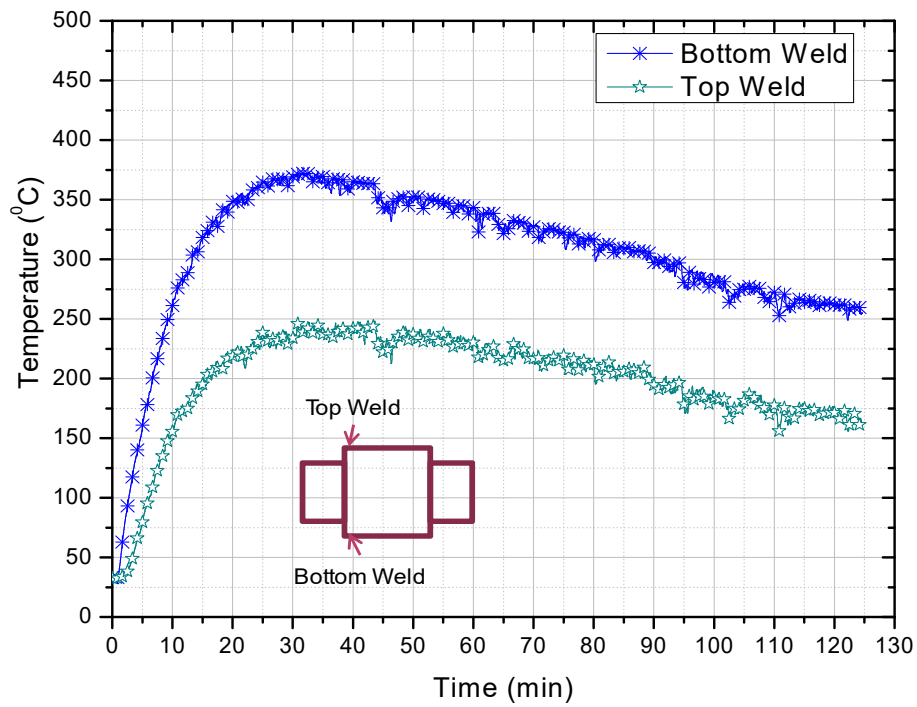
(a)



(b)



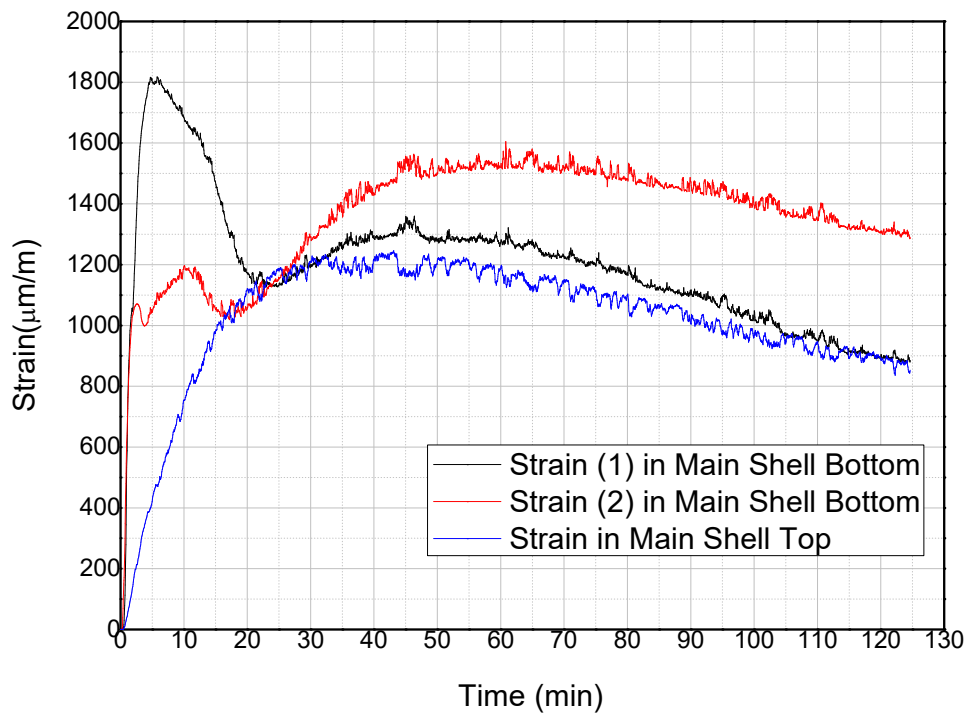
(c)



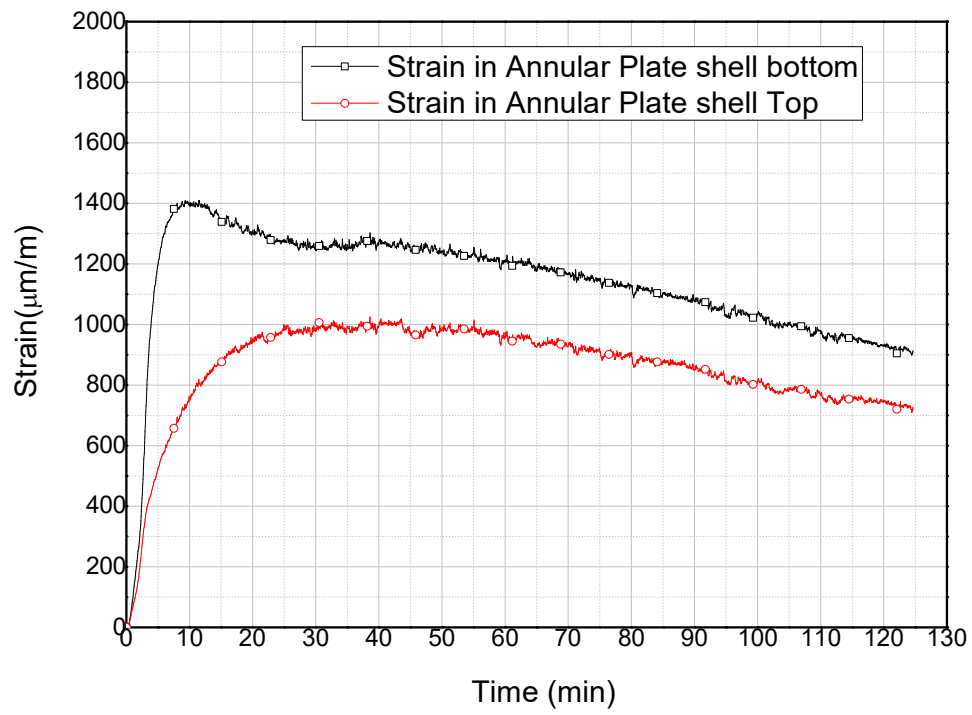
(d)

Figure 3.18: Temperature distribution in stepped test section (a) Main shell (b) Annular plate (c) Small shell (d) Weld

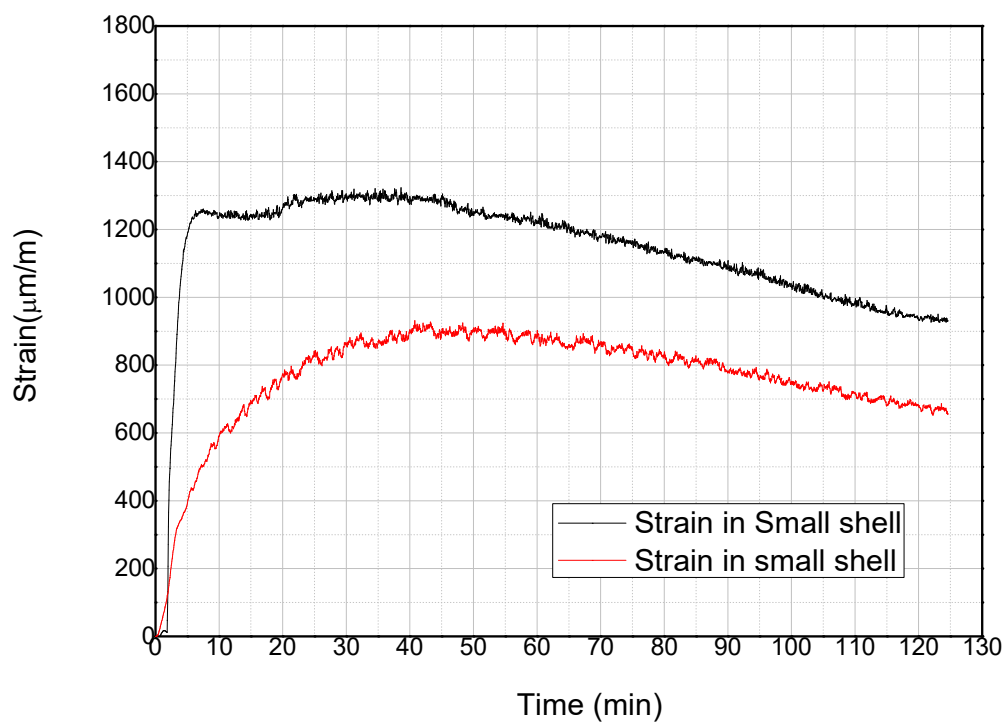
Figure 3.19 (a), (b), (c) and (d) show the strain variation on outer surface of main shell, annular plate, small shell and weld locations in cylindrical test section respectively. From the figure, the maximum strains measured in any part of stepped test vessel were $1800\mu\text{m/m}$ ($\sim 0.18\%$) which is well below the ultimate strain ($\sim 35\%$) [51] at this temperature for failure to occur. As expected, the lower portion of test section had higher strain compared to upper portion of test section as lower portion was occupied by the high temperature melt. The initial fluctuation of strain observed in main shell was due to the sudden pouring of high temperature melt from furnace into stepped cylindrical vessel. In main shell bottom (figure 3.19 (a)), strain was decreased between 5 minutes and 20 minutes as the location of strain gauge in main shell bottom was just below the pouring funnel. Thus, high temperature melts first directly fell at that location and then spread slowly. This was the reason behind the sudden jump and then dropping of the strain at this location.



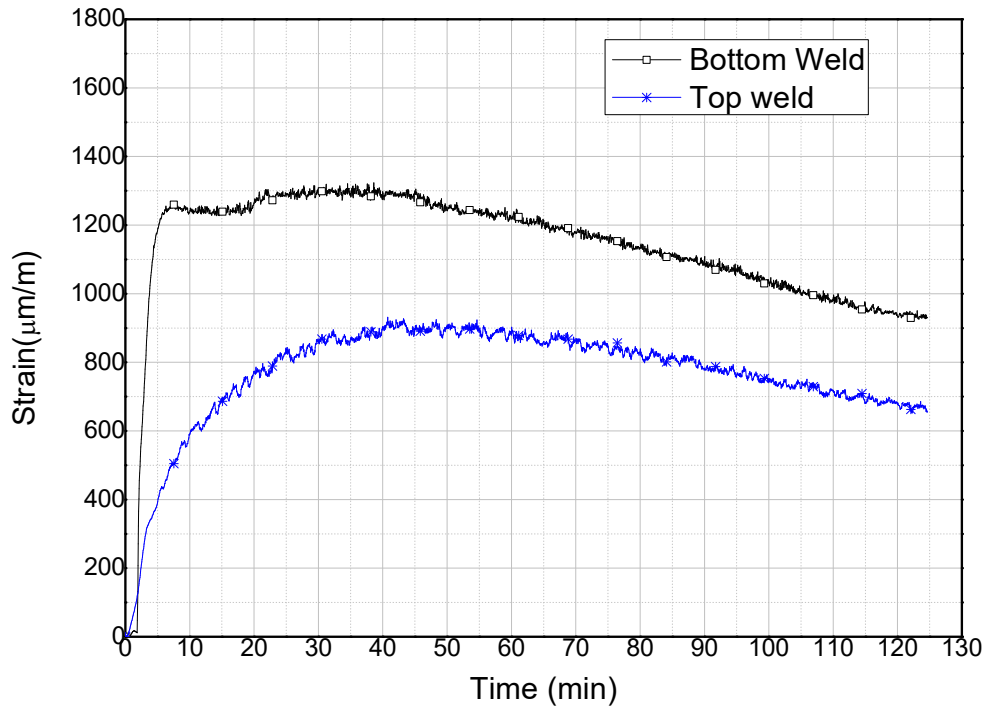
(a)



(b)



(c)



(d)

Figure 3.19: Measured experimental strain variation in stepped test section of (a) Main shell (b) Annular plate (c) Small shell (d) Weld

3.4 Closure

Two different regimes, i.e., stored heat dominated and decay heat dominated regimes were identified for basis of IVR experiments. Scaling philosophy for decay heat dominated regime which included material properties and heat transfer parameters were worked out. Heat transfer and strain behaviour experiments were conducted for decay heat dominated regime.

It was observed that as soon as the melt was poured (at 1200 °C) inside vessel, high temperature gradient from 1100 °C to 830 °C was formed within molten pool. With decay heat generation in melt, crust thickness grew up slowly up to 15 mm and then it stabilized at that thickness. Crust rate formation was found slow compared to no decay heat. Thus, the maximum crust thickness is limited by the decay heat. No gap was observed between the

crust and the vessel. CV inner and outer surface temperature reached steady state and maximum temperature is found to be 255 °C and 102 °C respectively. Due to crust formation, the CV outer surface temperature remained near saturation temperature of the water. The maximum heat transfer coefficient was found for cases with decay heat and no boiling and with decay heat and boiling at 0° location.

The average values of heat transfer coefficient for various cases are given in the table below

Table 3.5: Experimental average values of heat transfer coefficient for various cases

| Cases | Heat transfer coefficient (kW/m² K) |
|--|---|
| Without decay heat and single-phase natural convection on CV outer surface | 1.26 |
| With decay heat and single-phase natural convection on CV outer surface | 3.08 |
| With decay heat and two-phase natural convection boiling on CV outer surface | 10.9 |

The crust resistance is found to be dominating resulting in very poor overall heat transfer coefficient. Hence, the overall heat transfer coefficient is not influenced by either single phase natural convection or boiling two phase natural convection on outer wall of vessel. In decay heat case, main mode of heat transfer in melt is by conduction plus convection; whereas, in without decay heat case, main mode is conduction only. The maximum strains in any part of stepped test section including weld joints were found to be 0.18% which is well below the ultimate strain (35%) at corresponding temperature.

Chapter 4

Heat transfer behaviour from molten corium inside CV to the vault water - Stored heat dominated regime

4.1 Introduction

The decay heat dominated regime experiments of in vessel corium coolability were carried out earlier with molten glass at 1200 °C. Although these experiments demonstrated the capability of long-term removal of the decay heat from corium melt by vault water, the integrity of CV in stored-heat dominated regime at high temperatures (in the range ~ 2300 °C – 2500 °C) needs to be demonstrated experimentally. Also, crust formation surrounding the melt, which is crucial for in-vessel retention scheme, could vary with different simulant melt materials at high temperatures and with melt mass. In order to study these effects, high temperature experiments were carried out for IVR. Generation of high temperature melt is very difficult to produce in large quantities. No thermocouples are available above 2300 °C and pyrometer can't be used to measure inside melt temperature. Hence, for stored heat dominated experiments, thermite reactor was used for high temperature melt generation. It is based on thermite reaction which is exothermic in nature. And for temperature measurement inside melt, molybdenum sheath C-type thermocouples are used.

4.2 Scaling for Stored Heat Dominated Regime

In stored heat dominated regime, the heat loss from the melt is transferred to the vessel structure and then to the vault water pool. In this scenario, the ratio of internal energy content of melt to the thermal inertia of the vessel is an important parameter and to be conserved for prototype and experiment.

$$\frac{\text{Enthalpy of melt}}{\text{therm inertia of vessel}} = \left(\frac{H_{to}}{(mCp)_{vess}} \right)_{\text{prototype}} = \left(\frac{H_{totmelt}}{(mCp)_{vess}} \right)_{\text{expt}} \quad (4.1)$$

Scaling of Heat Transfer parameters

Table 4.1 shows the scaling of heat transfer parameter and comparison of the prototype and experiment. The ratio of internal energy content of melt to the thermal inertia of the vessel, which is the main scaling parameter, is scaled in very good agreement with that of prototype. This gives similar vessel temperature rise in experiment as in prototype calandria vessel.

Table 4.1: Heat transfer scaling

| Parameter | Experiment | Prototype |
|--|------------|-----------|
| Change in Enthalpy (MJ) of melt to form stable crust | 172 | 27214 |
| Thermal inertia of vessel, mC_p (kJ/K) | 113 | 18080 |
| Enthalpy of melt/thermal inertia | 1.52 | 1.5 |

Material properties scaling

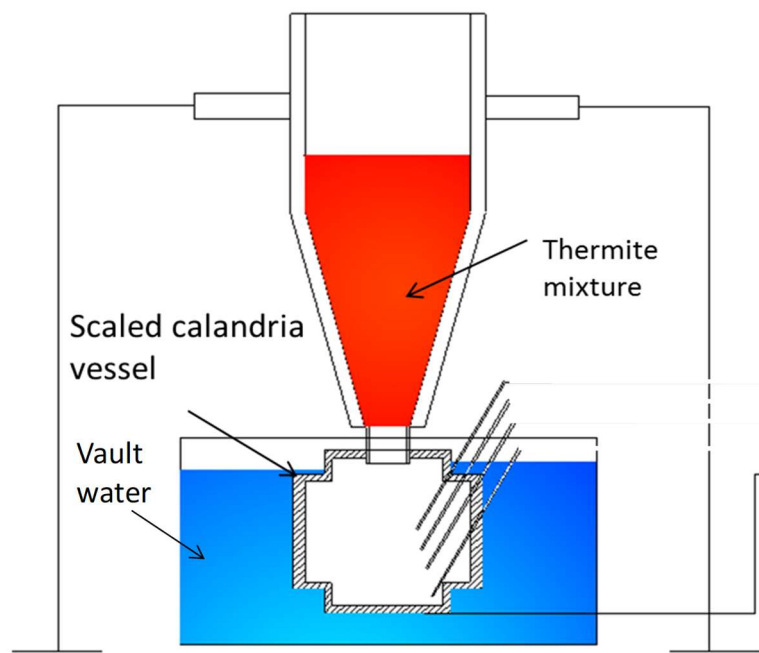
Table 4.2 shows the material properties and comparison of the simulant material and corium. From the table, it can be observed that the thermal diffusivity and volumetric thermal expansion coefficient of the simulant and corium are nearly same. These two parameters are very important in case of transient natural convection heat transfer from melt to water.

Table 4.2: Properties of the simulant and corium

| Property | Experiment | Prototype |
|---|--|-----------|
| Material | ZrO ₂ + CeO ₂ + Al ₂ O ₃ + Fe mixture | Corium |
| Density(ρ) (kg/m ³) | 5074 | 8800 |
| Conductivity (k) (W/mk) | 2.3 | 2.88 |
| Specific heat (Cp) (J/kg.K) | 700 | 565 |
| Thermal diffusivity (α) (J/(m ³ ·K)) | 6.4e-7 | 5.79e-7 |
| Volumetric thermal expansion coefficient (β) (/K) | 1.04e-4 | 1.05e-4 |
| Viscosity (Pa.s) | 0.0026 | 0.00336 |

4.3 Experimental setup

Experimental setup consists of thermite reactor for generating the near prototype corium melt, stepped test vessel and tank for simulating vault. The experimental setup details are shown in the figure 4.1. The stepped test vessel made of the main shell, small shell, annular plate and side plates are similar to prototype CV of PHWR. The diameter of the test section varied from 450 mm to 300 mm and vessel thickness varied from 32 mm to 22 mm. The total length of the calandria vessel was 2200 mm. The cylindrical test vessel was submerged inside a tank with dimensions 2900 mm x 800 mm x 800 mm. Water was partially filled till 600 mm height which was equivalent to 1000 litres of water.



(a)



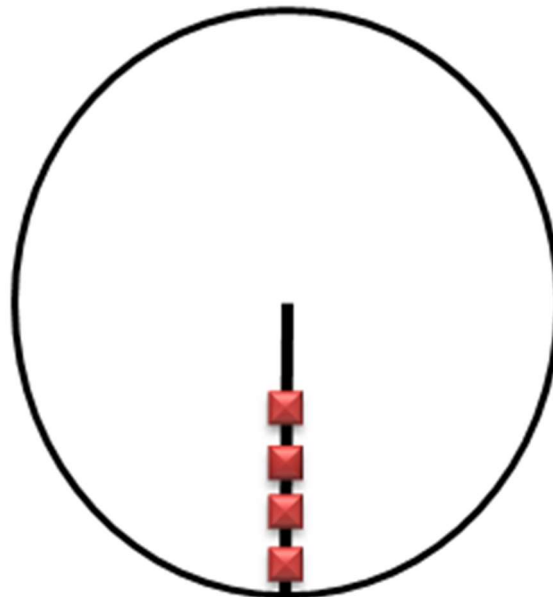
(b)

Figure 4.1: Experimental setup (a) Schematic (b) Actual

Three numbers of thermite reactors were placed on top of the test vessel in which high temperature melt was generated by thermite reaction. This was also simulated the possible difference in melt relocation time at the bottom of calandria vessel. The material of cylindrical test vessel was similar to prototype CV material.

4.4 Instrumentation of experimental set up

The experimental setup was extensively equipped with thermocouples. To measure the temperature inside the melt, four C-type thermocouples were installed inside the melt pool at 25 mm, 50 mm, 100 mm and 150 mm from the bottom of vessel. For the outer surface of the test section, the K-type thermocouples were installed at various locations on the main shell, small shell and annular plate. A total twenty-four thermocouples were installed. The locations of C and K-type thermocouples are shown in figure 4.2. All these measurements were recorded by a 48 channel DAS with a sample interval of 1 s.



(a)

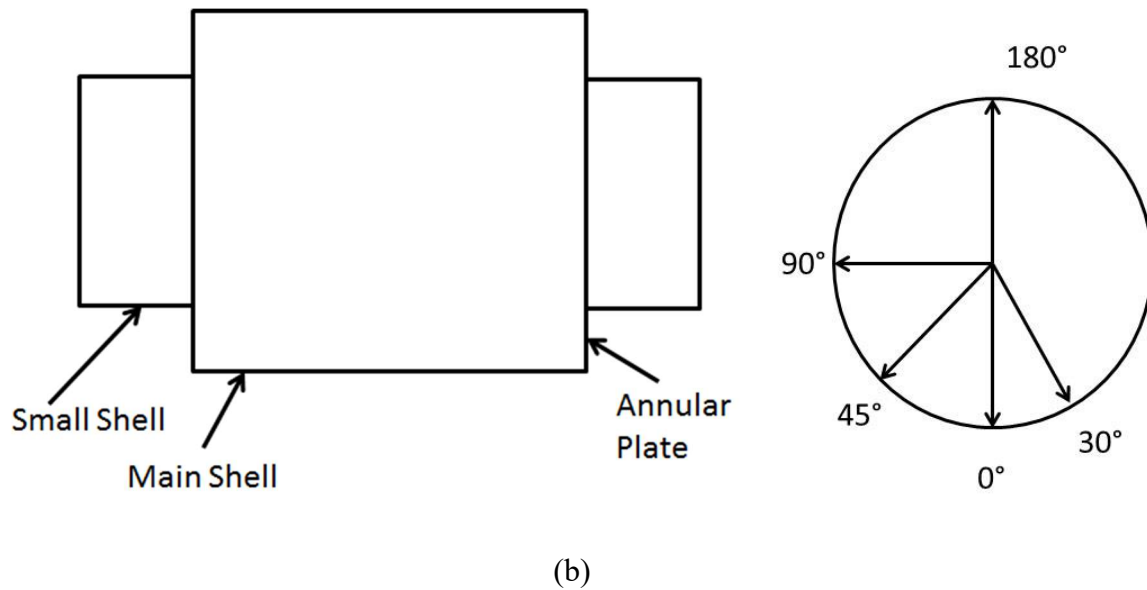


Figure 4.2: Instrumentation scheme (a) Inside Melt (b) Cylindrical test vessel

4.5 Experimental Procedure:

In this experiment, thermite reaction was used to generate high temperature melt inside the thermite reactor and from reactor it was engineered for in-situ pouring of melt inside the cylindrical test vessel. In this, mixture of aluminium metal and ferric oxide was ignited by electric trigger to generate a self-sustaining exothermic reaction which yields alumina and iron in molten state. To simulate corium properties, ZrO_2 and CeO_2 (surrogate for PuO_2) were added. The resultant product after the reaction contains molten oxide mixture of Al_2O_3 , CeO_2 , ZrO_2 and metallic iron which has properties closer to prototypic material. The melt was in-situ poured in cylindrical test vessel at temperature more than 2500°C . The thermocouples located inside the test section and tank recorded the data after the melt fell inside the vessel.

4.6 Experimental Results

The melt temperature variations inside the melt at different radial distance from bottom of vessel are shown in figure 4.3. The maximum temperature measured was 2300°C due to limitation of the thermocouple range. Due to high temperature of the melt, most of the thermocouples were damaged.

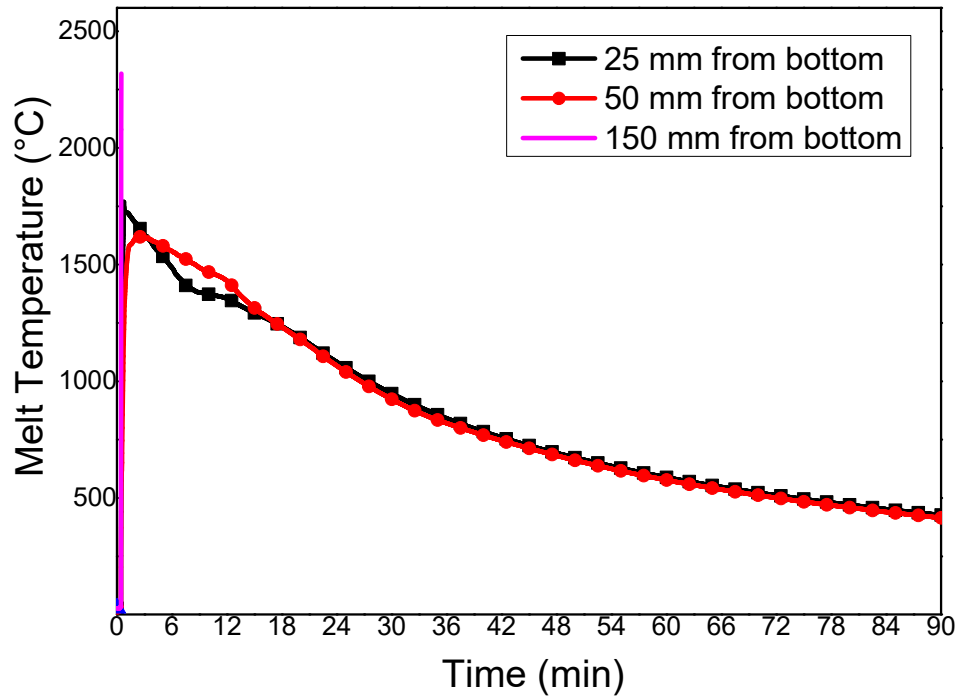


Figure 4.3: Melt temperature variation at different radial height

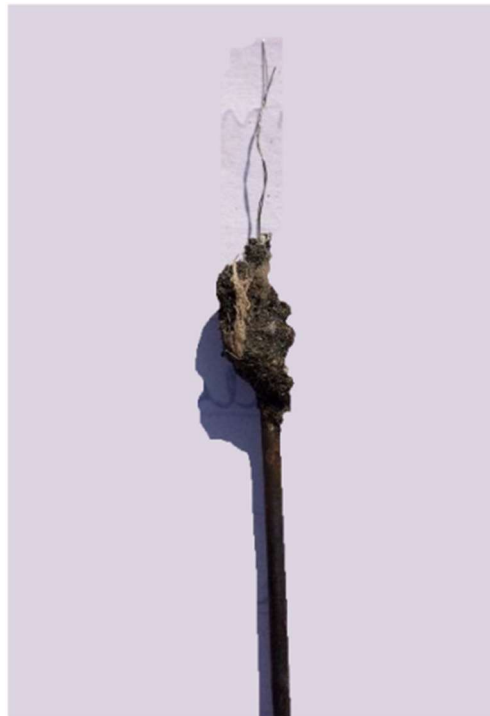


Figure 4.4: Melted Molybdenum sheath of thermocouple

Figure 4.4 show the melted thermocouple sheath made of molybdenum indicating a temperature of melt was exceeding 2500 °C. It is seen from the figure 4.3 that, initially the

rate of decrease of temperature was higher. Once the stable crust was formed, the rate of change of melt temperature reduced.

Figure 4.5 shows the vessel inner wall temperatures at two different locations. At 30° from the bottom of the vessel, the thermocouple was in touch with the melt. Hence, initially the temperature rose sharply and after the crust was formed, within short time (~3 min), inner vessel surface temperature came down below 600 °C. Thereafter, it decreased slowly. This shows that, when crust was formed, the vessel's inner temperature was also low irrespective of melt temperature. At 180° (top), there was no melt and also no water outside the vessel.

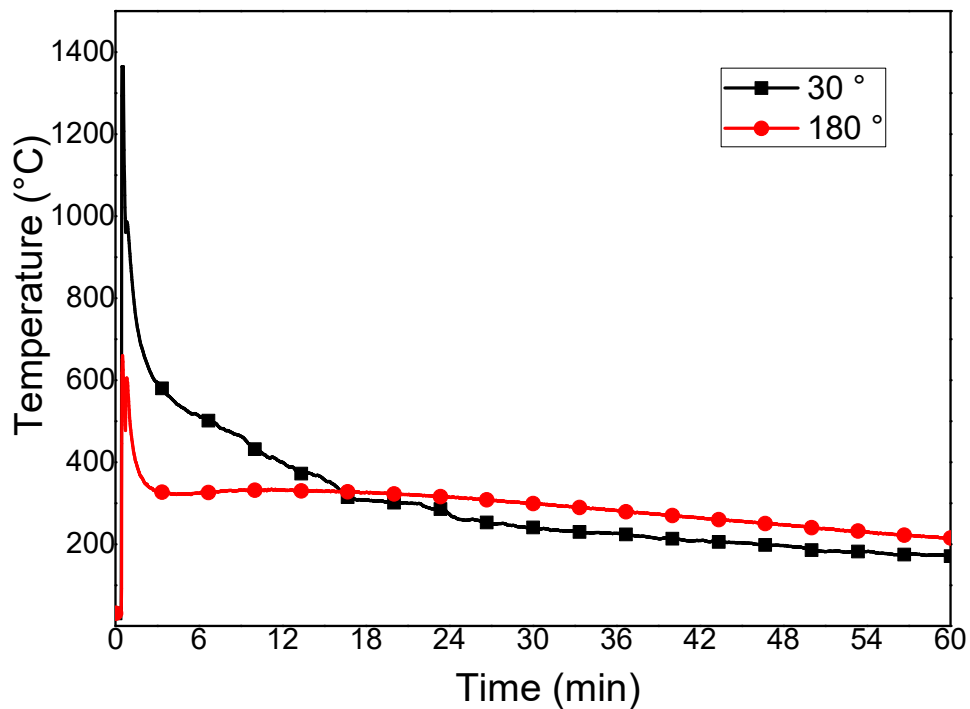


Figure 4.5: Vessel inner wall temperature

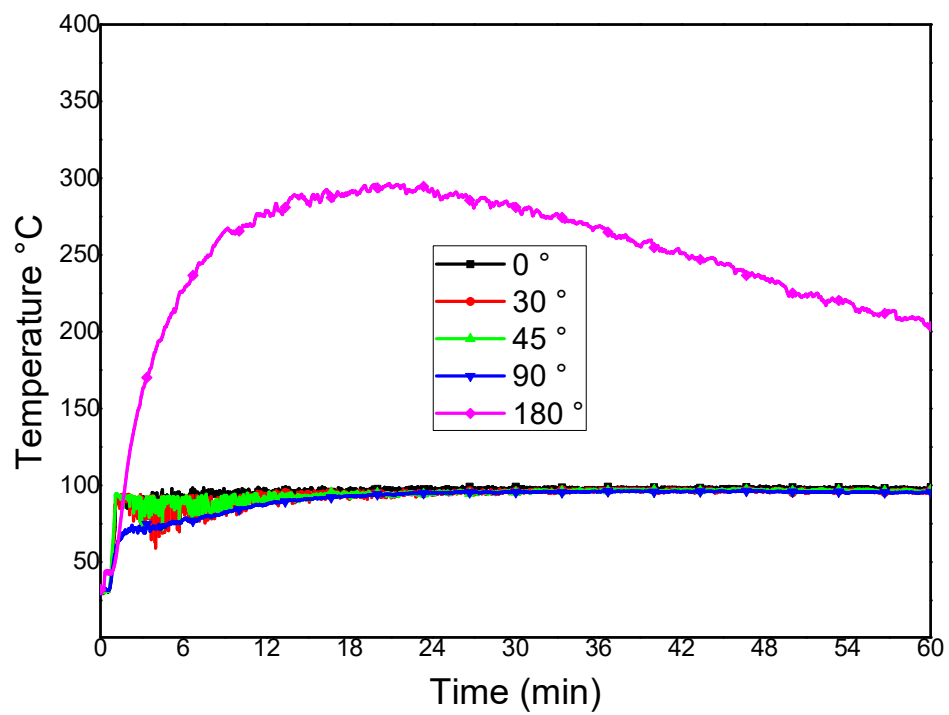


Figure 4.6: Vessel outer wall temperature

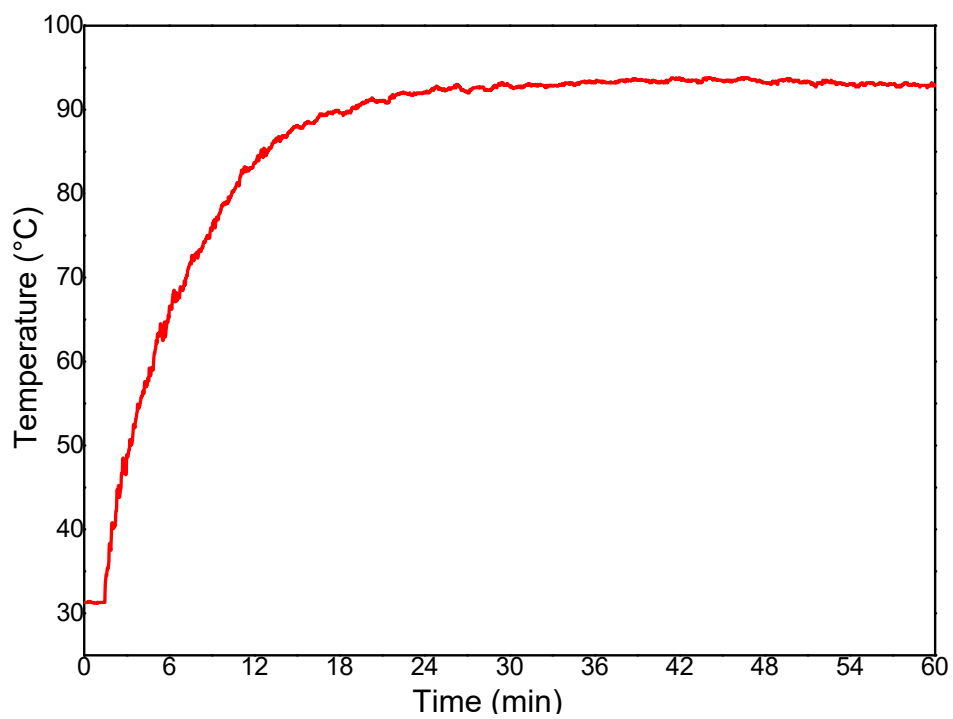


Figure 4.7: Vault water temperature

Figure 4.6 shows the outer surface temperature of the vessel at different circumferential locations. Except for the top (180°) location, which was exposed to air, all the outer vessel temperatures remained near the saturation temperature of the water. Initial rapid fluctuations observed in the temperatures show the presence of local boiling on the surface. Even with a melt temperature of 2500°C , the vessel outer surface remained quite cool. Figure 4.7 shows tank water temperature variation which remains well below the saturation temperature. Figure 4.8 shows a comparison of temperatures of crust, vessel inner surface, vessel outer surface and water. The melt at high temperature was well contained inside the calandria vessel without increasing the vessel wall temperatures and there was large temperature gradient in the melt from centre to the wall. The vessel integrity was maintained and no deformation was observed in cylindrical test vessel.

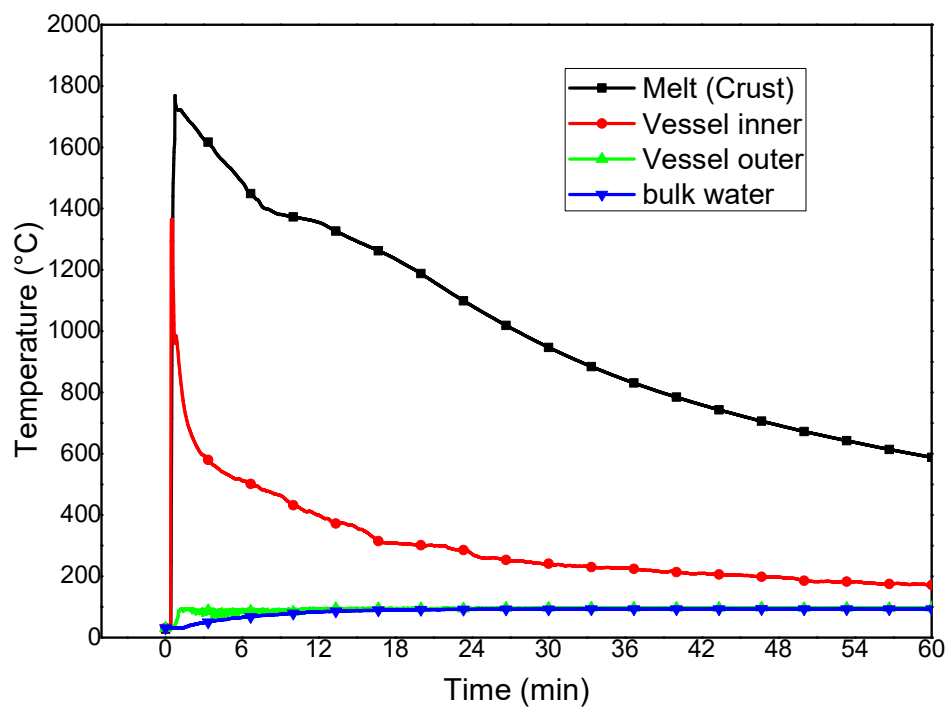


Figure 4.8: Comparison of temperatures of melt, vessel inner, vessel outer and bulk water

4.7 Estimation of CV outer heat flux and heat transfer coefficient

The experiments showed that the heat transfer in radial and circumferential direction are more dominant compared to that in the axial direction. Hence, the outer surface heat transfer coefficient has been evaluated at different angles i.e. $r=R_{outer}$. The CV outer radial heat flux and heat transfer coefficient at different locations were calculated by using Equations (4.1) and (4.2) (Holman, J.P., 2008.) respectively.

$$\frac{Q}{A} = k_{vess} \frac{\Delta T_{vess}}{\Delta x_{vess}} \quad (4.1)$$

Where

- Q : Heat Transfer rate ,W/m²
- k_{vess} : thermal conductivity of vessel, W/mK
- A : heat transfer area, m²
- ΔT_{vess} : temperature difference across vessel, K
- Δx_{vess} : thickness of cylinder, m

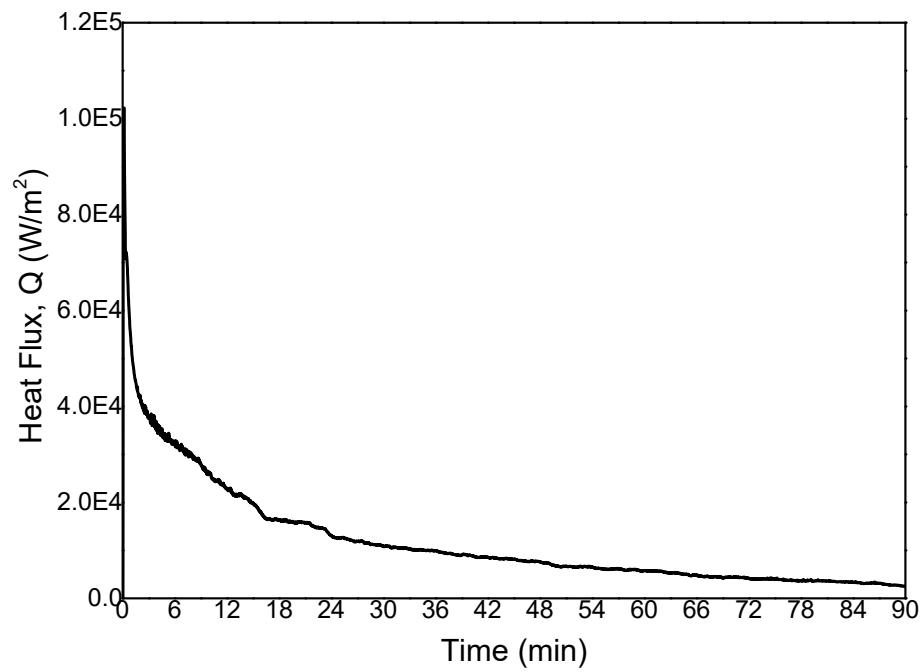
$$k_{vess} A \frac{\Delta T_{vess}}{\Delta x_{vess}} = h_{outer} A \Delta T \quad (4.2)$$

where

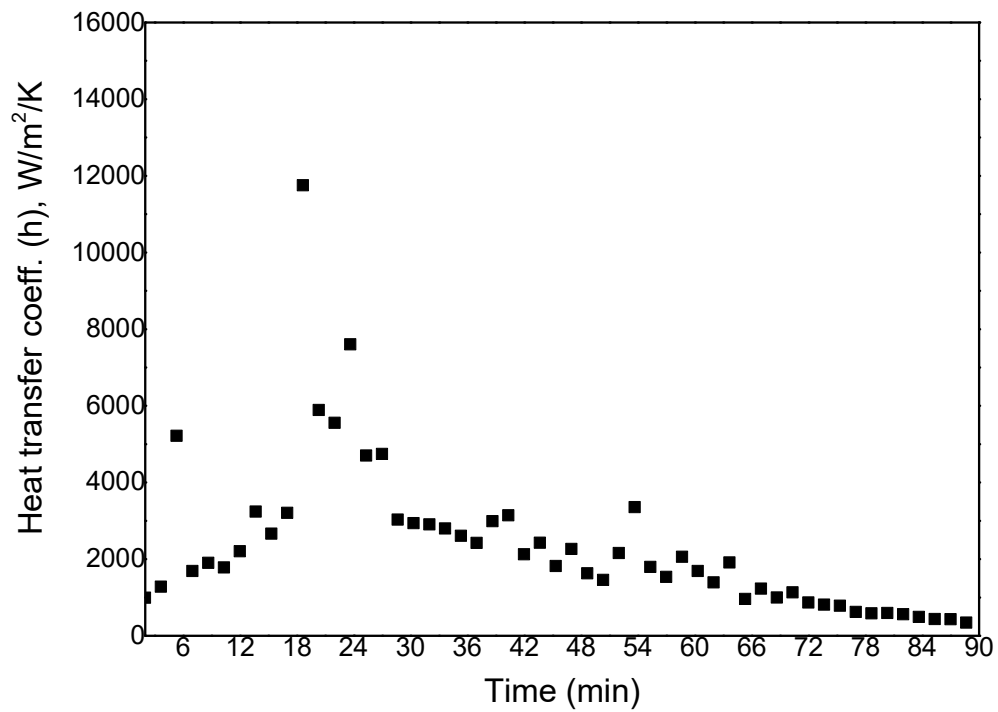
- h_{outer} : local outer heat transfer coefficient, W/m² K
- k_{vess} : thermal conductivity of vessel, W/mK
- A : heat transfer area, m²
- ΔT_{vess} : temperature difference across vessel, K
- ΔT : temperature difference between vessel outer surface and vault water,

K

Δx_{vess} : radius of cylinder, m



(a)



(b)

Figure 4.9: (a) CV outer Heat flux (b) Outer heat transfer coefficient

There is no simplification in heat transfer calculations and these are based on experimental observations. Figure 4.9 shows the CV outer heat flux and outer heat transfer coefficient variation. The cause of scatter in the figure 4 (b) is local boiling. The maximum observed heat transfer coefficient and heat flux were $8 \text{ kW/m}^2\text{K}$ and $\sim 110 \text{ kW/m}^2$ respectively.

On comparing maximum heat flux in stored heat dominated regime with decay heat dominate regime, the range is of $\sim 110 \text{ kW/m}^2$ and 125 kW/m^2 respectively. Whereas maximum heat transfer coefficient in stored heat dominated regime with decay heat dominate regime, are in the $8 \text{ kW/m}^2\text{K}$ and $9.5 \text{ kW/m}^2\text{K}$ respectively.

4.8 Closure

Scaling philosophy for conducting experiment in stored heat dominated regime which included material properties and heat transfer parameters were figured out. High temperature heat transfer experiments were conducted for IVR. During experiment, melt at very high temperature $\sim 2500^\circ\text{C}$ was poured into the scaled CV. Maximum melt temperature recorded inside vessel was $\sim 2300^\circ\text{C}$ due to limitations of C-type thermocouples. It was seen that as soon as corium melt comes into contact with calandria vessel, crust was formed ($\sim 50 \text{ mm}$) immediately. CV inner surface temperature reached steady state ($\sim 400^\circ\text{C}$) and maximum temperature was found 1400°C for a very short period. Due to crust formation, the CV outer surface temperature remained near saturation temperature of the water. Even though melt temperature was very high inside the vessel, no deformation in vessel was observed. Maximum CV outer surface heat transfer coefficient and heat flux were $8 \text{ kW/m}^2\text{K}$ and $\sim 110 \text{ kW/m}^2$ respectively. Main heat transfer mode in melt was “conduction”.

Chapter 5

Limiting heat flux on the outer CV- CHF in downward facing boiling surface

5.1 Introduction

As heat transfer drastically deteriorates at CHF, so the determination of limiting heat flux or CHF on outer surface of calandria vessel is very important. It will assist in assessment of the maximum heat removal capability of vault water from the melt inside the CV during severe accident scenario. The CHF phenomena is very complex in PHWR CV under severe accident condition. This is due to downward facing heating surface, boiling two phase natural convection on outer surface of CV, and influence of very large geometry of calandria vessel on limiting heat flux. It is very difficult to numerically simulate these effects simultaneously. To assess the limiting or maximum heat removal capability of vault water from the heat generating corium, it is important to experimentally determine the CHF value on outer surface of CV.

5.2 Preceding studies on downward-facing CHF

CHF is influenced by sub-cooling, quality, geometry, material and orientation of the vessel. Literature has very limited studies available on critical heat flux in downward-facing boiling (orientation). Very few experiments on CHF on downward facing curved surfaces have been conducted related to IVR in PWRs. Full scaled experiment on 3 different kinds of configuration for the AP600 and AP1000 were conducted by Theofanous [52]. They estimated the heat removal limit on internally heated hemispherical reactor vessel, which was submerged in water, for various configurations. Experiments were conducted in SULTAN facility [53] to investigate the coolability of vessel under two-phase natural convection. In the KAIST facility [54], CHF experiments on 2D slice test section simulating the APR1400

vessel configuration were also conducted. In the subscale boundary layer boiling (SBLB) facility [55, 56]; experiments on the outside surface of hemispherical lower head with both saturated and sub-cooled conditions were conducted to obtain CHF databases

It is observed that the CHF value reduced significantly for downward facing as compared to upward facing. The probable reason [57] explained about this behaviour was, in upward surface, the bubble could leave the surface freely, so the orientation would not affect the CHF; whereas in the downward surface, the heater plate constrains the bubbles movement (buoyancy) on heater surface. It increases its residence time and hence decreases the CHF. Vessel material also plays an important role on CHF. Many studies were performed with various material likes copper [58, 59], aluminium, carbon steel [59, 60], SS [58, 59], Titanium, etc and also with different vessel surface coating [61]. In downward-facing heaters, apart from the orientation and materials, the size of heater also have great influence on CHF. Yang [58] used flat type plates for various widths (20 mm, 25 mm, 30 mm and 40 mm) and studied the behaviour of CHF.

5.3 Experimental needs for CHF studies for PHWR CV

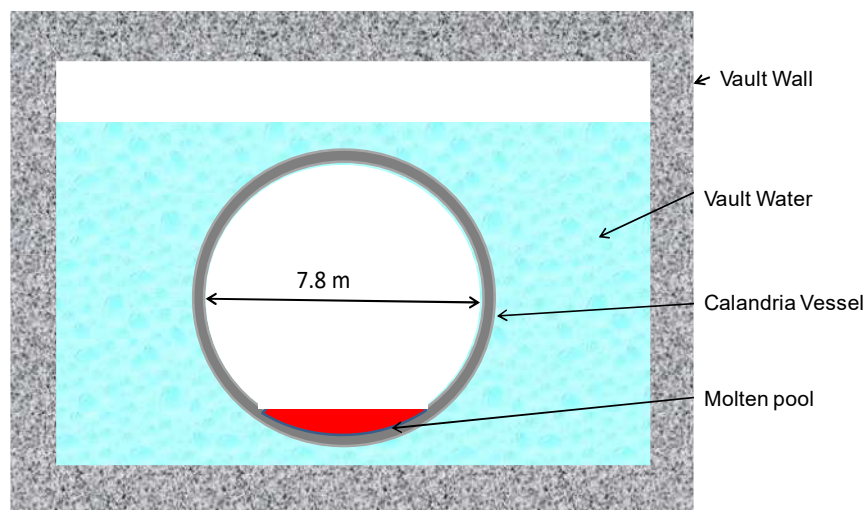
The PHWR CV has cylindrical geometry with very large diameter (7.8 m) and length (~ 6 m) and it is submerged in calandria vault water having temperature below 52 °C. The material of CV is SS 304L [62]. Due to large cylindrical geometry, the bottom most part of the CV almost behaves like a flat surface with downward facing with sub-cooled boiling in natural convection mode. At the bottom of CV, it is likely that the value of CHF will be the minimum compared to other curved locations of CV where upward natural convective heat transfer can take place.

As CHF strongly depends on orientations, geometry, material of construction and different operating conditions such as sub-cooling, pressure, etc; hence the investigations of earlier studies cannot be directly extrapolated to PHWR CV. In order to evaluate the CHF on PHWR

CV with local boiling on outer surface, experiments need to be carried out on actual material, i.e., SS 304L, with a simulated surface with downward facing boiling. Since bottom most surface of CV is like a flat plate, hence, the purpose of this experimental study is to evaluate the CHF of a downward facing flat plate simulating the bottom portion of PHWR CV with sub-cooled water similar to the conditions of prototype vault water.

5.4 Details of experimental setup

Figure 5.1 (a) shows the schematic of PHWR calandria vault which is filled with water. Inside the calandria vault, CV is submerged in vault water and it is partially filled with molten corium. As PHWR CV has very large diameter and length. Due to this, the bottom most part of the CV behaves as a flat plate as shown in figure 5.1 (b). This is the most limiting section for earliest CHF occurrence. Based on this, a scaled test facility (figure 5.1 (c)) has been designed and fabricated to determine the CHF of CV of the Indian 700 MWe PHWR. It consists of water tank simulating PHWR vault of size 700 mm by 600 mm and height 500 mm, and is made of carbon steel. Toughen glass windows are provided in the water tank for capturing the boiling process.



(a)

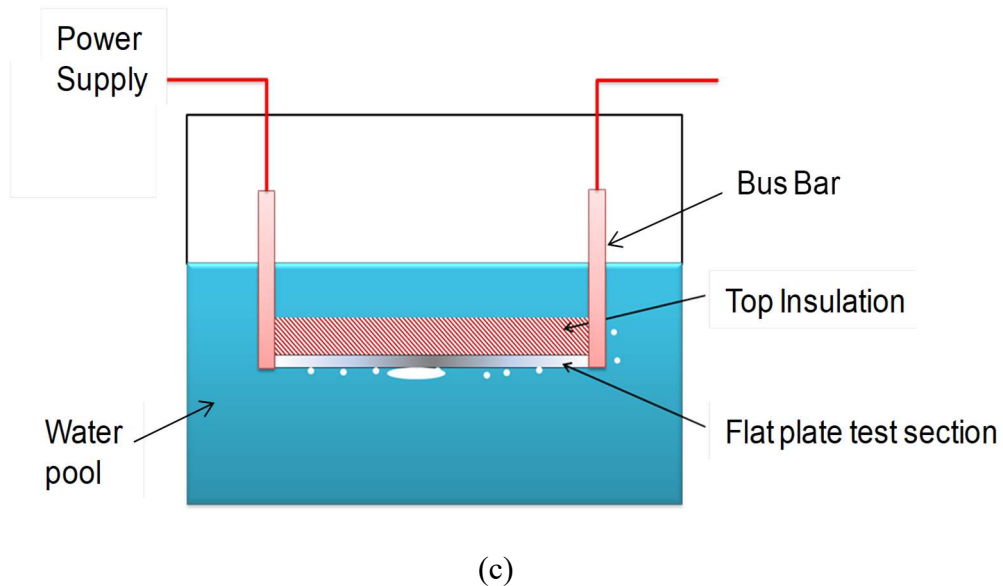
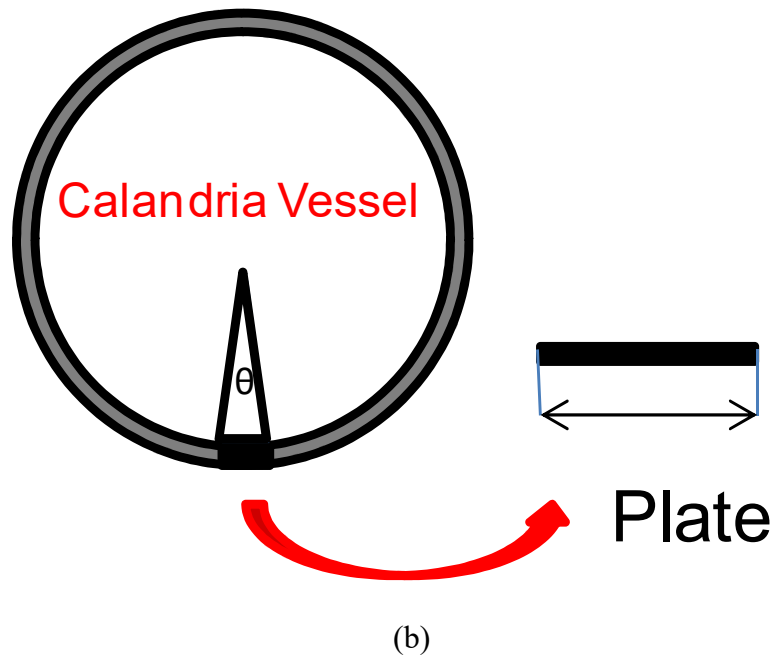


Figure 5.1: (a) CV consist of molten pool submerged in vault water (b) test section from CV (c) schematic of test setup assembly

The flat test section was fabricated from SS 304 L material which is same as prototype CV material and having dimension of 400 mm length, 100 mm width and 3 mm thickness. It was submerged horizontally lengthwise in the water tank. The ends of test section had provision of bus bar connections. It was directly heated by Joule heating with a DC power supply system with maximum capacity of 16 V and 7500 Amps. The schematic diagram of the test set up is shown in figure 5.1 (c). On top of the test section, insulation layers were provided to

make the test section with downward facing heating surface as shown in figure 5.2. Hence, all the heat was dissipated from bottom only. Insulation was also placed around the water tank to reduce the heat loss from tank water to environment. The power of test section was controlled by regulating the current. During the experiment, heat flux in test section could be varied in the range 0-1 MW/m².

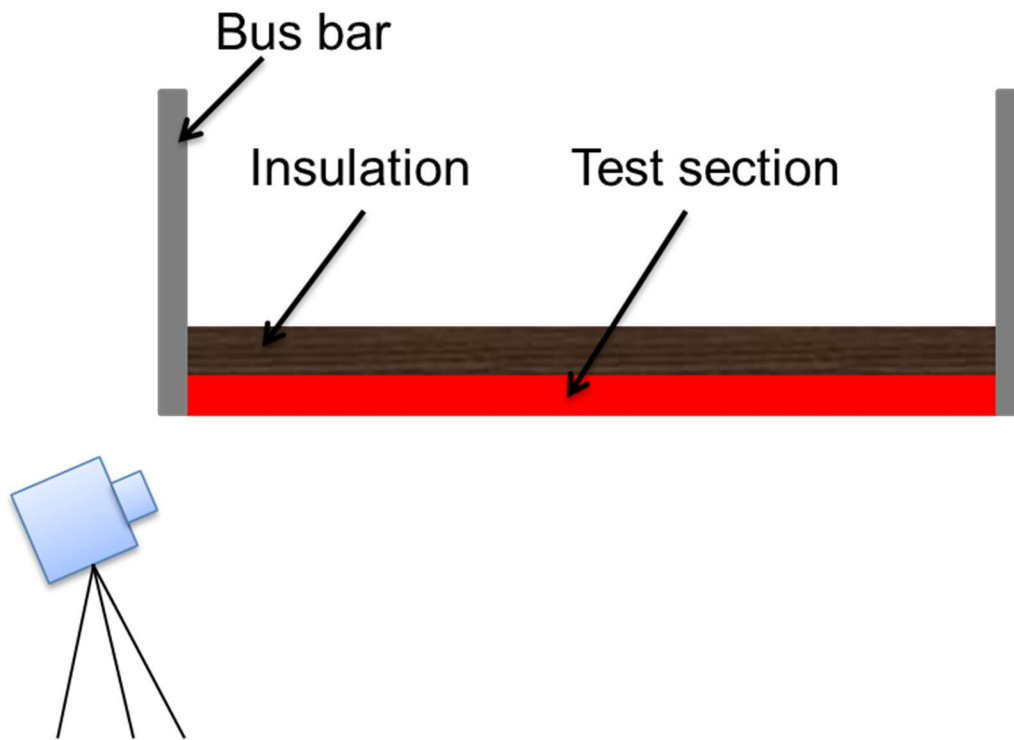


Figure 5.2: Downward facing test section

5.5 Details of instrumentation

The experimental setup was significantly instrumented. Temperature measurement sensors, i.e., thermocouples were installed on the upper as well as bottom surface of test section and in water pool. The temperatures of flat test section and water pool were measured by Inconel sheathed 1 mm ungrounded K-type thermocouples. 6 thermocouples were installed on upper

as well as bottom surface of test section and 3 thermocouples were installed in water pool at different locations (total-15 thermocouples). Power supply trips were provided for temperature exceeding $150\text{ }^{\circ}\text{C}$ on heater surface to protect the test section from melting or burning out. All these measurements were recorded by 48 channel data acquisition system (DAS) with a time span of 1s. Details of instrumentation are shown in figure 5.3.

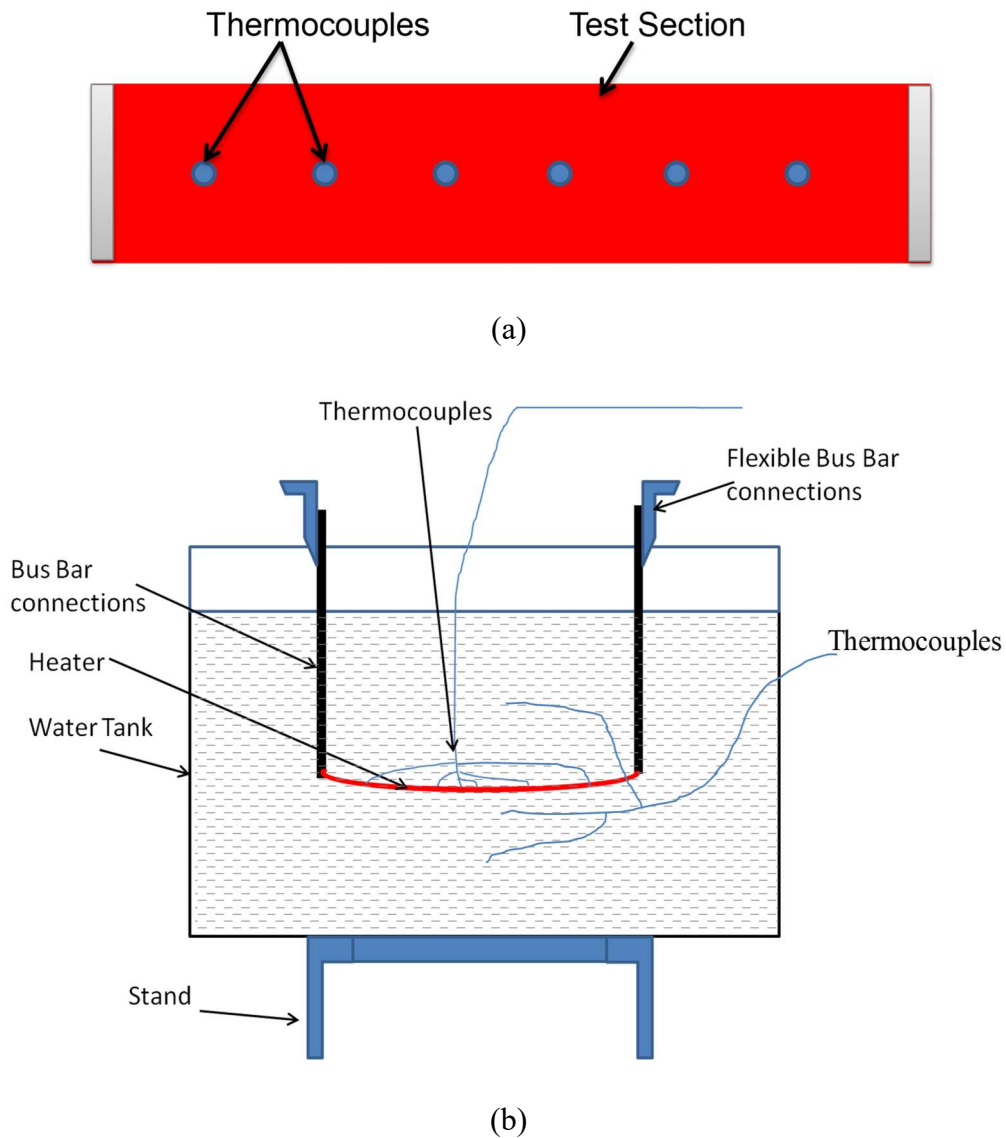


Figure5.3: (a) thermocouples on test section (b) thermocouples in test set up

5.6 Experimental procedure

Before the experiment, the test section surface was cleaned thoroughly. Then we filled the demineralised water in the water tank up to 450 mm from the bottom and heated for half an hour to degas the water to avoid early trap of bubble under test section during experiments. After that all trips were checked in sequence. Power was turned on and heating the test section was made directly by current which was passing through silver coated flexible bus bar connected to test section (as shown in figure 5.3 (b)). Initially, power was raised in steps of around 1000 Amps and when the surface temperature came close to 115 °C, the increase of current for each step was reduced to 200 Amps. When test section surface temperature suddenly jumped beyond 150 °C, the power supply was cut off automatically. All The temperatures measured by thermocouples were recorded by the DAS.

5.7 Results discussion

Experimental surface heat flux (q'') is calculated from equation (5.1) which is based on heat balance method. In the equation, “Volt” and “I” are voltage and current value measured across the test section directly and “A” is the heater surface area.

$$q'' = \frac{Volt * I}{A} \quad (5.1)$$

The uncertainty in the experiment was analysed by the error propagation method. The uncertainty in current, voltage and heater size are 0.5%, 1.0% and 0.5%, respectively and the uncertainty of the heat flux is less than 3%.

Figure 5.4 shows the result of a typical CHF experiment obtained. In general, the heater surface temperature varies between ~ 6-30 °C above the saturation temperature of water in the nucleate boiling regime. The heater surface temperature rose slowly from 100 °C till 120 °C. After that fluctuation of surface temperature observed between 120-130 °C for some time

and with further increase of power, all of a sudden, temperature rose above the 150 °C, where heater power tripped. This sudden rise of temperature signified the onset of departure from nucleate boiling (DNB). It is well acknowledged that DNB occurs in the low-quality or sub-cooled region and at high heat fluxes. Due to this, lot of bubbles formation took place which formed the vapour layer adjacent or below on the flat plate surface, causing a dramatic reduction in heat transfer capability.

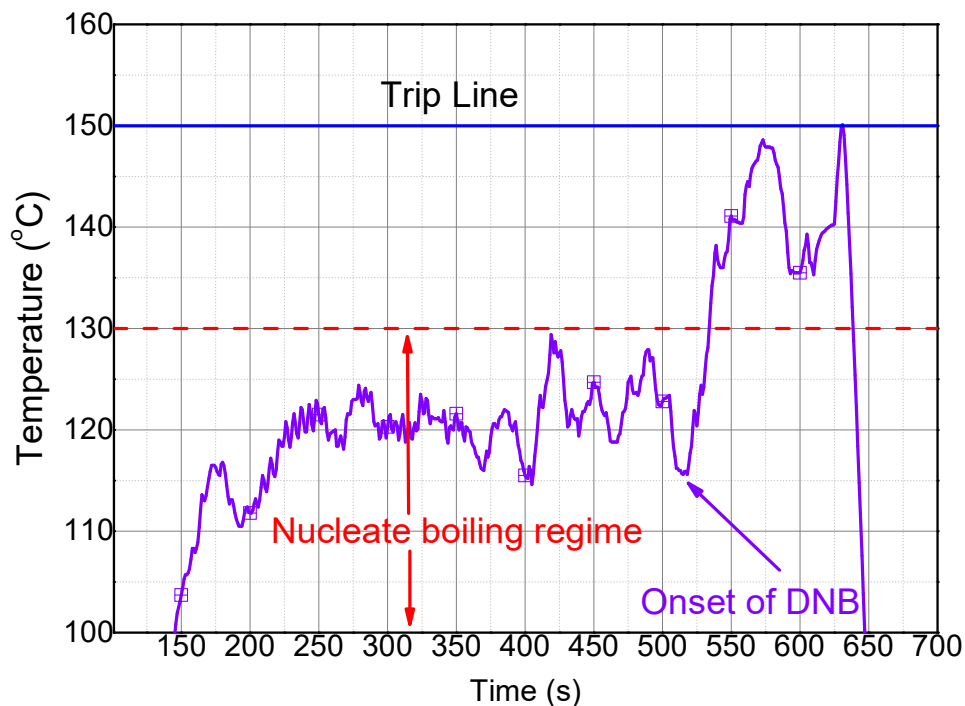
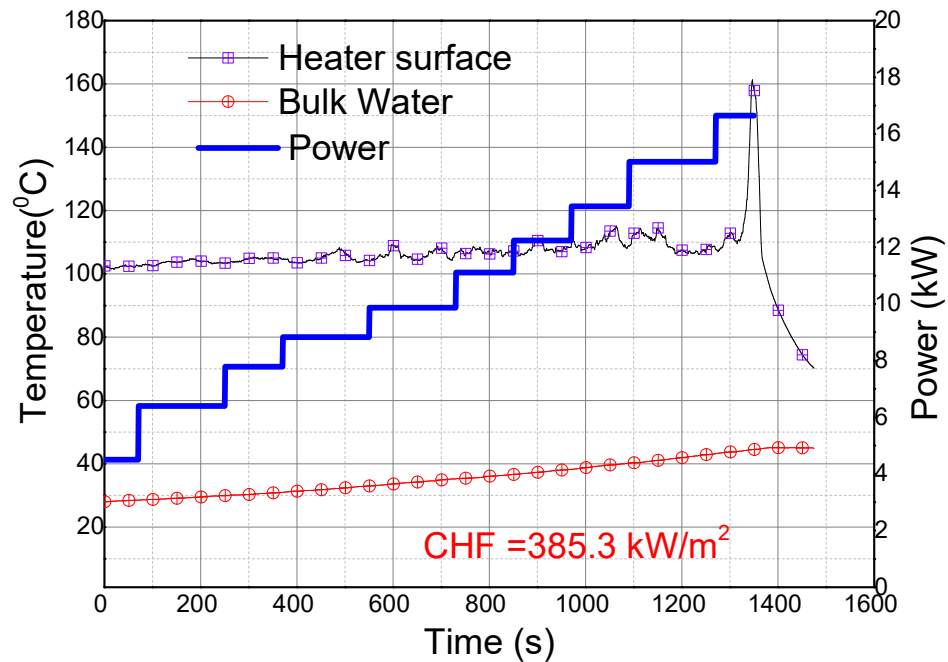


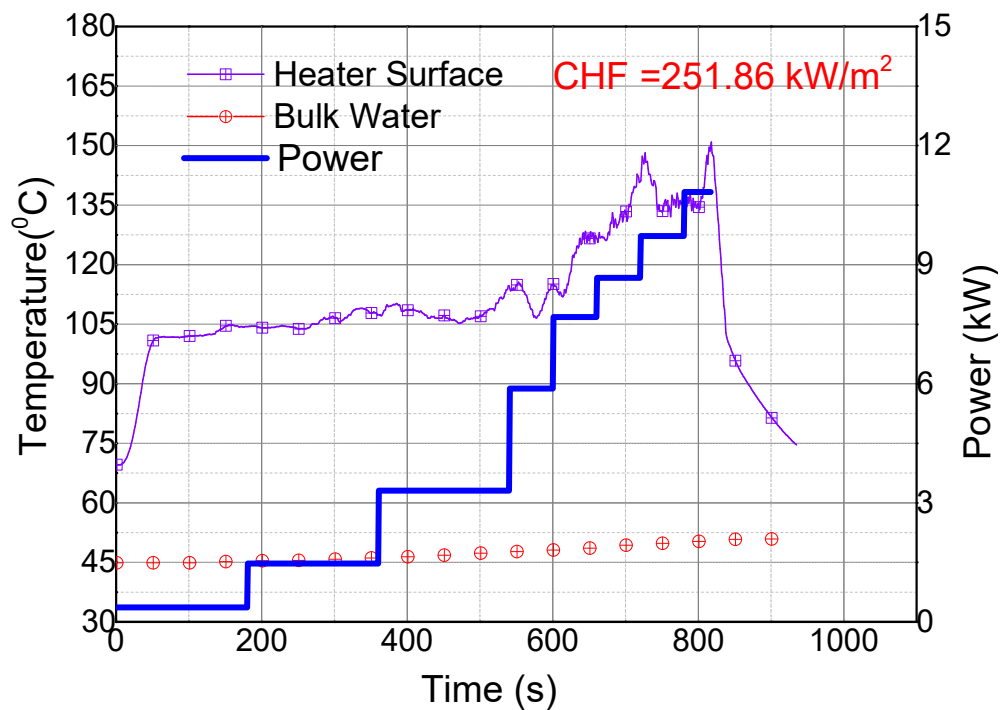
Figure 5.4 Typical CHF experiment results

CHF is found to reduce with increase in calandria vault water temperature. Figure 5.5 (a) and (b) show the experimentally observed heater surface temperature at two different CHF conditions, i.e. at CHF of 385 kW/m² and 251 kW/m² for bulk water temperature of 44 °C and 50 °C respectively. Number of experiments were carried out with different bulk water temperature. Figure 5.5 (c) shows variation of CHF with bulk water temperature. It is observed that, even though the temperature just below the test section plate always remains in the range of 95-97 °C (film), but the temperature 100 mm below the plate varied from 28 – 65 °C (i.e., calandria vault water temperature range). At 28 °C bulk temperature, CHF

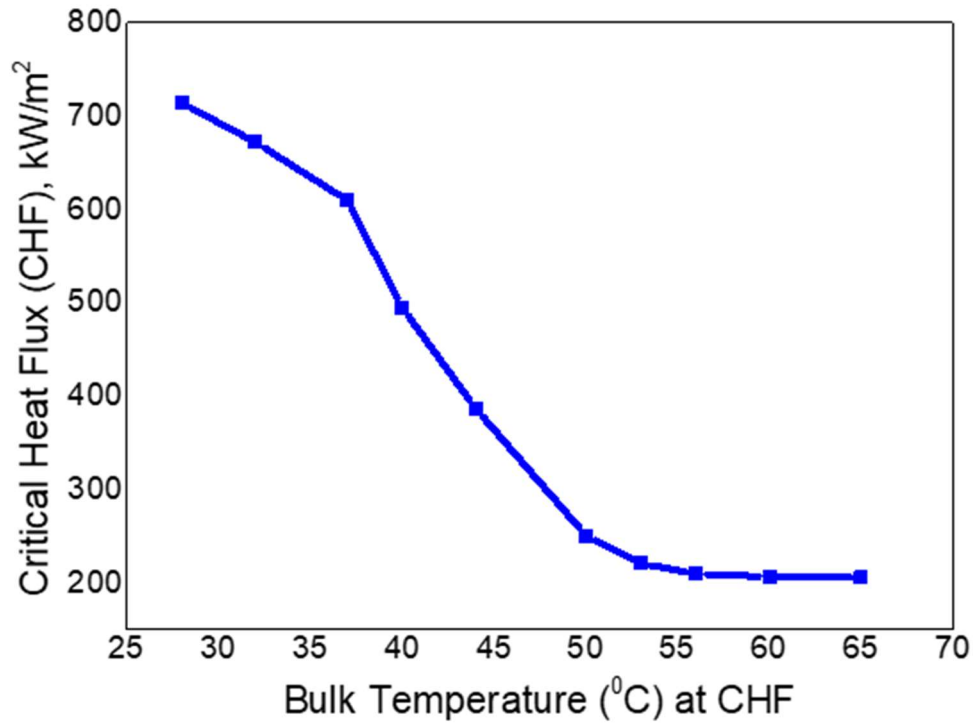
occurred at 714 kW/m^2 ; at 44°C bulk water temperature, CHF occurred at 385 kW/m^2 ; and at 56°C of bulk water temperature, CHF decreased to 210 kW/m^2 . CHF is found to gradually reduce and become almost constant at higher bulk temperature.



(a)



(b)



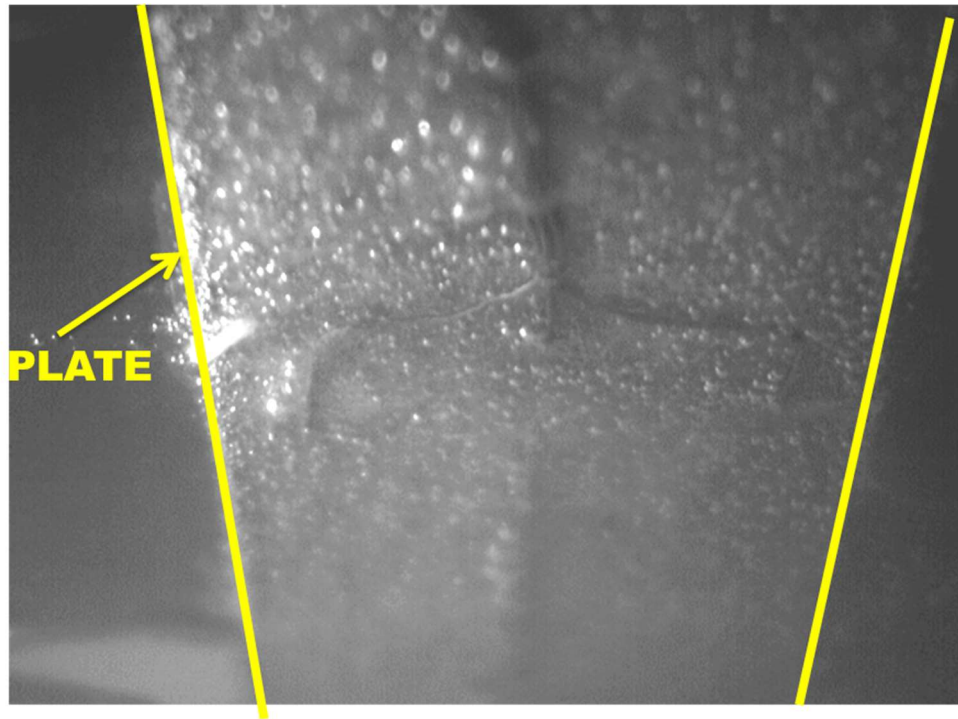
(c)

Figure 5.5 (a) Time history of temperature at 385 kW/m^2 (b) Time history of temperature at 252 kW/m^2 (c) CHF variation with bulk fluid temperature

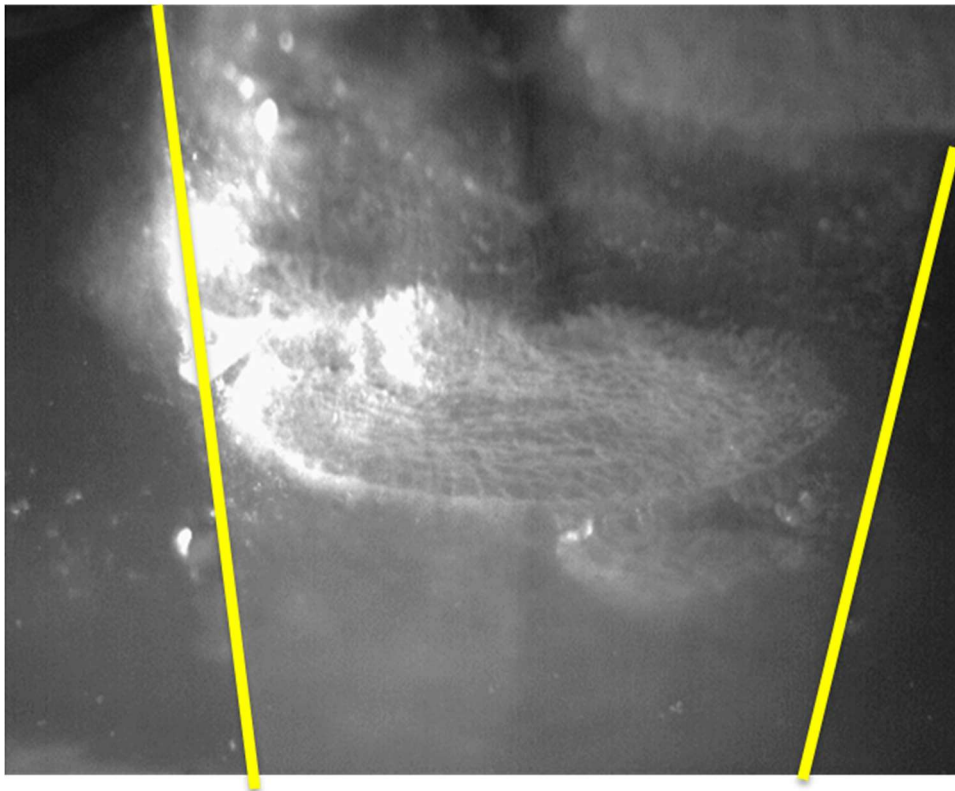
Figure 5.6 and 5.7 show various phase of boiling phenomena at low heat flux and at CHF condition captured by camera.

Case-1: When the heat flux was lower than CHF (at 50% of CHF).

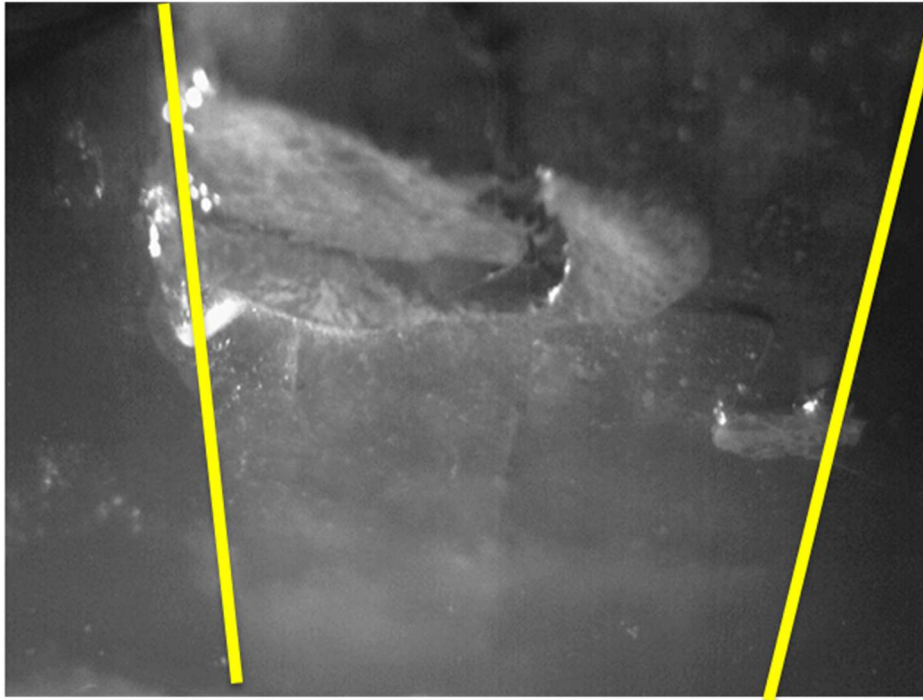
During this phase, liquid was able to wet the heated surface although some small size bubbles were present. Faster replenishment rate of liquid on the heated surface was observed due to departure of bubbles from the surface. Instantaneous pictures of the heated surface were captured at various times are shown in figure 5.6. It could be seen in the figure that, at nearly 6 ms, large number of small bubbles were present on the heated surface (figure 5.6 (a)). At around 42 ms (figure 5.6 (b)), the sizes of bubbles increased, but still, they stick to the surface. At about 60 ms (figure 5.6 (c)), the bubbles were found to slide and move on the surface, the liquid replenished the portion of bubbles.



a) 6 ms



b) 42 ms

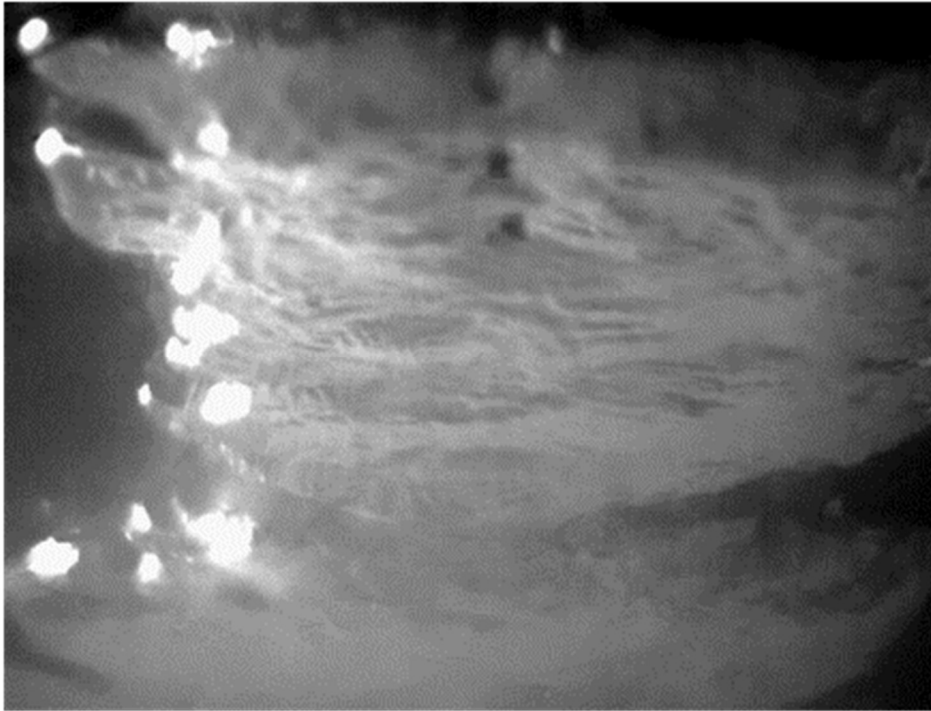


c) 60 ms

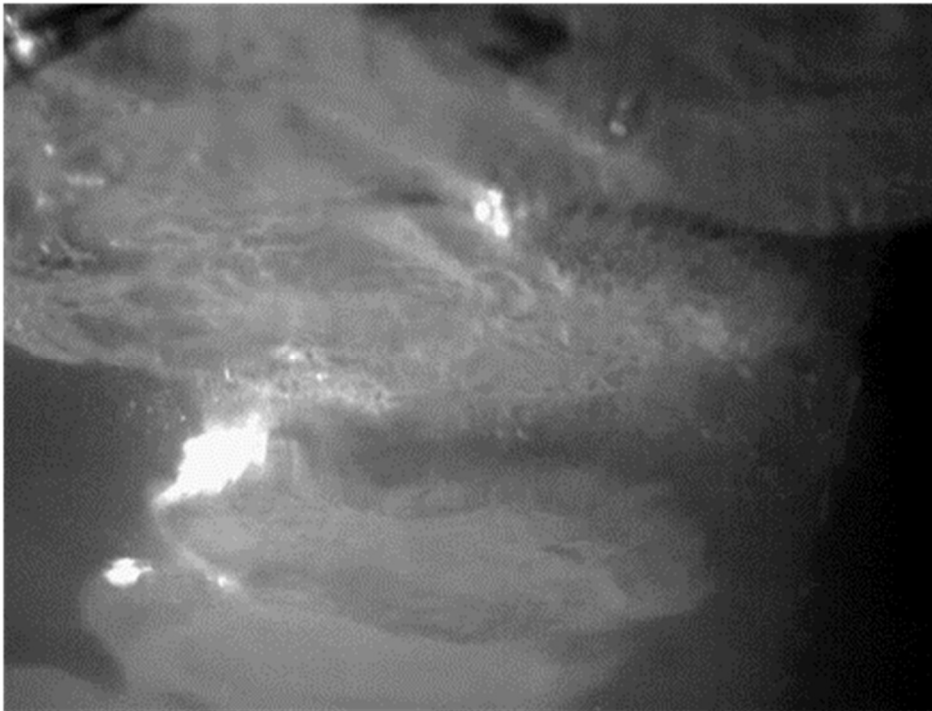
Figure 5.6: Instantaneous pictures observed for Case 1: When the heat flux is at 50% of CHF

Case-2: When the heat flux was at CHF.

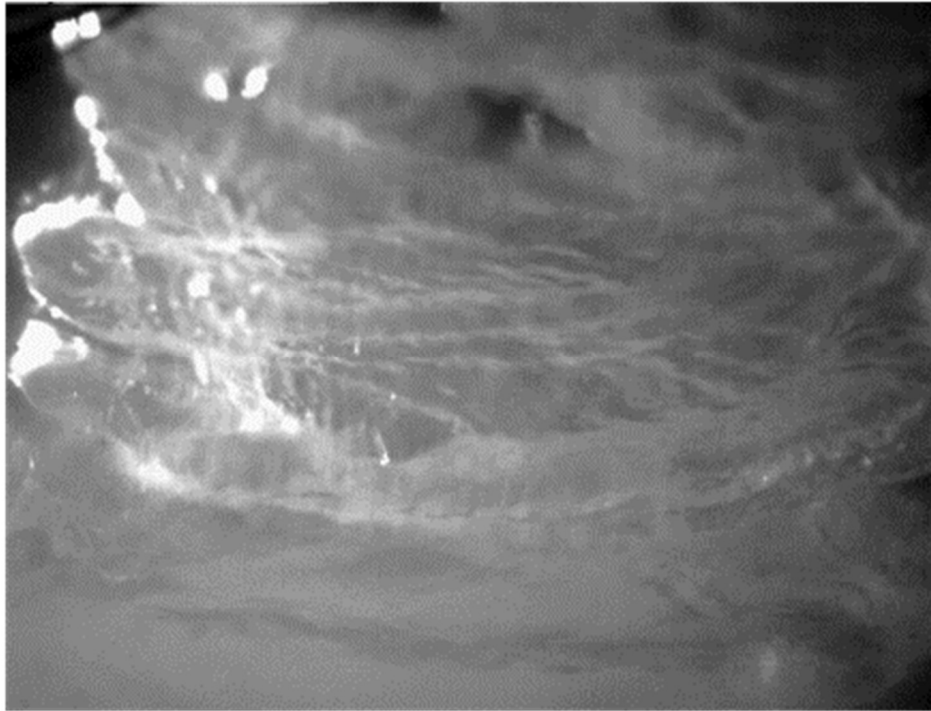
At high heat flux (CHF), intermittent film of vapour was seen on the heated surface. Most part of the surface was always remained covered with the vapour film and liquid was not able to displace this film completely. This condition prevails over the entire period ((figure 5.7 (a-c)) causing large degradation of heat transfer and hence resulted in CHF.



a) 5 ms



b) 44 ms



c) 60 ms

Figure 5.7: Instantaneous pictures observed for Case 2: When the heat flux at CHF

5.8 CHF mechanism

Addition of heat in water pool of water tank resulted in build-up of natural convection. In case of upward face heating plate, the bubbles departed easily from the heater surface due to buoyancy. Conversely, for the downward face heater plate, due to buoyancy the bubbles couldn't rise up easily from the surface as it couldn't lift the heater surface. Initially, natural convection current was responsible for the bubble sliding and movement. As the bubbles departed from the heater surface and condensed in the bulk sub cooled liquid, it resulted in increase of bulk temperature (near the bubble vicinity) leading to a temperature gradient which in turn resulted in increase in convection. With increase in heat flux, the bubble diameter and number of active nucleation sites increased. At higher heat flux, bubbles coalesced to form a large bubble or vapour film. As the size of the bubble increased, the residence time of bubbles also increased. Large bubbles hampered the heat transfer, leading

to an increase in the temperature of the heater surface; however, as the bubble departed from the heater surface, the heat transfer was reinstated.

At CHF, the bubbles production rate was significantly higher and the residence time at heater surface increased. The water didn't reach the heater surface due to the larger bubbles leading to a dramatic increase in the heater surface temperature. Bulk fluid temperature played a vital role, as the bulk temperature increased, the condensation of bubble decreased leading a decrease in convection which in turn resulted in decrease in CHF value. Beyond a certain bulk temperature of liquid, the effect of sub-cooling reduced as the process of bubble condensation might not create enough temperature gradient to induce convection.

5.9 Comparison with other experiments for downward-facing boiling

Present experimental investigation shows that at bulk temperature above 56 °C, CHF value become independent of temperature and doesn't vary much with temperature. This is because, the bubbles after leaving the heater surface move up and dispel the heat to the sub-cooled water present at the top of the heater. The fluid lying below 100 mm from the surface of the heater does not take part in heat transfer and remains more or less invariable throughout the experiment. Due to this, with the increase in heat flux, the bulk water temperature rise has insignificant effect on CHF especially above 56 °C. In fact, at nearly saturation temperature of water, Kam [63, 64] found CHF values in the range of 210 kW/m² which is closer to our tests. Table 5.1 shows the comparison of various downward heating CHF value with experiments performed on large scale curved surface. It is observed that curvature of test section increases the CHF value and hence the results of flat surface are the most limiting one.

Table 5.1: Comparison of experimental value of downward heating CHF

| S.No. | Experiment | CHF value at 0° | Test Material | Size | Remark |
|-------|------------------------------|------------------------------|------------------|---|-----------------|
| 1 | Present study | 210-385 kW/m ² | SS 304L | 400 mm x 100 mm X 3 mm | Pool boiling |
| 2 | Theofanous Configuration I | 300 kW/m ² | Carbon steel | 60° arc of length 1.66 m with 150 mm (height) x 760 mm (width) | Pool boiling |
| 3 | Theofanous Configuration II | 500 kW/m ² | Carbon steel | 90° arc of length 2.49 m with 150 mm (height) x 760 mm (width) | Flow boiling |
| 4 | Theofanous Configuration III | 490 kW/m ² | Carbon steel | 90° arc of length 2.49 m with 150 mm (height) x 760 mm (width) | Flow boiling |
| 5 | Cheung, SBLB | 434 kW/m ² | Carbon steel | hemispherical vessel of 0.3 m dia. | Pool boiling |

5.10 Closure

This chapter provides valuable insights of the phenomenology of CHF in PHWR CV under severe accident condition, previous work on downward heating surface CHF and need to conduct experiment for evaluating the CHF for PHWR. Several experiments were conducted on a SS 304L flat plate simulating the bottom most part of CV submerged in vault water with downward facing heating surface from single phase natural convection to boiling two phase natural convection. Measured values of CHF are 385 kW/m^2 and 251 kW/m^2 at calandria vault bulk temperature of 44°C and 50°C respectively. The experimental observation shows that CHF is strongly dependent on bulk liquid temperature upto 56°C . Beyond that temperature of the bulk liquid, CHF does not vary significantly. The measured value of CHF compares well with the measured value of CHF in curve surface of PWR lower head.

Chapter 6

Correlation development of heat transfer coefficient for curved CV outer surface

6.1 Introduction

The heat removal capability of vault water from the molten corium through CV is very complex phenomenon. As discussed earlier, it involves multi-mode (conduction, convection and radiation), multi phases (solid, liquid phases of corium and liquid and vapour phases of water) and multi component (corium, steel, water, steam, hydrogen, etc.) heat transfer. Hence for assessment of capability of retention of molten corium in CV through external vessel cooling, it is important to evaluate the natural convection heat transfer on outer surface of the vessel with unsteady bulk pool water temperature. Here apart from above, CV is partly filled with corium which results in non-uniform heating of CV. The CV is also completely submerged in a confined rectangular vault tank which affects the heat transfer behaviours.

In literature, a few experimental studies have been conducted in the past for the heat transfer in heat generating melt. Experiments conducted at UCLA [65] were targeted to investigate the natural convection heat transfer behaviour in internally heated hemispherical pools with external cooling. In the experiments, a Pyrex bell jar containing Freon-113 as test liquid was used, and the vessel was cooled externally by water. Both local and average heat transfer coefficients were obtained based on maximum bulk pool temperature. Investigations were conducted for the natural convection heat transfer [66] in a 300 mm diameter of hemisphere with bottom inner surface heated and bottom outer surface cooled. Four liquids, i.e., water, ethyl alcohol, 78% and 44% aqueous glycerine were used as working fluids. The range of Rayleigh number was $9 \times 10^6 < Ra < 7 \times 10^9$ which lies in laminar natural convection regime. In LAVA facility, number of experiments [67] were performed in a 1/8 linear scale of a lower

head of PWR with $\text{Al}_2\text{O}_3/\text{Fe}$ thermite melt (or Al_2O_3 only) as corium simulant. The main objectives of these experiments were to study the effects of the internal pressure inside the lower head vessel, cooling of the vessel wall and the gap formation between molten material and vessel. Park [68] conducted experiments for natural convection heat transfer of melted core at the bottom of the reactor vessel of PWR. CuSO_4 - H_2SO_4 electroplating system was used to simulate the buoyant situation of the melted core. Mean and local Nusselt numbers were measured and compared for two different configurations of the molten core: two layers and three layers oxide pools. The ACOPO [69] (hemispherical model for AP600 lower head with a diameter of 2 m) and mini ACOPO [70] (hemispherical model for AP600 with a diameter of 0.4 m) experimental program at UCSB aimed to simulate natural convection heat transfer from volumetrically heated hemispherical pools at high Rayleigh numbers. Based on the above experiments, number of correlations were developed and CFD analyses were performed using these correlations as boundary conditions.

Hence, in literature, significant studies are available for heat transfer for hemi-spherical geometry relevant to PWR/BWRs. Heat transfer coefficient correlations had been developed from these measurements. However, they can't be applied to PHWR CV. The major difference is the CV geometry which is a large diameter cylindrical vessel unlike that of lower head of a PWR. Due to this, at the bottom (0°) most part of the CV almost behaves like a flat surface whereas other location behaves like a curved surface. Also, the height of melt pool generating decay heat is hardly $\sim 15\%$ of diameter of CV in case of PHWR whereas the height of melt pool generating decay heat is more than $\sim 75\%$ of lower head vessel in PWR. The literature lacks suitable empirical correlations for heat transfer coefficient for PHWR CV geometry.

Hence, the objective of this chapter is to develop the heat transfer coefficient correlations for PHWR CV outer surface.

6.2 Natural convection heat transfer correlation development

In general, the relationship between Nusselt number (Nu) and Rayleigh number (Ra) is given as

$$Nu = C Ra^m Pr^n \quad (6.1)$$

Where Pr is Prandtl number and C, m and n are the empirical constants.

Many investigations [71, 72, 73] have reported the strong influence of confinement on convection heat transfer of horizontal cylinder. PHWR horizontal CV is also submerged in confined water. Hence, geometry plays a crucial role. For confined boundary, relationship between Nusselt number (Nu) and Rayleigh number (Ra) is modified as

$$Nu = Nu(Ra, Pr, Geom) \quad (6.2)$$

where Geom = geometry

6.2.1 Dimensionless number and scaling in natural convection

Equations (6.3), (6.4) and (6.5) are the governing equations for natural convection considering the Boussinesq approximation.

$$\frac{\partial u}{\partial x} + \frac{\partial v}{\partial y} = 0 \quad (6.3)$$

$$u \frac{\partial u}{\partial x} + v \frac{\partial v}{\partial x} = g\beta(T - T_\infty) + \nu \frac{\partial^2 u}{\partial y^2} \quad (6.4)$$

$$u \frac{\partial T}{\partial x} + v \frac{\partial T}{\partial y} = \alpha \frac{\partial^2 T}{\partial y^2} \quad (6.5)$$

In order to understand functional dependence of the solution of natural convection flow, the above equation needs to be non-dimensionalised by introducing the dimensionless quantities.

Dimensionless quantities are

$$\tilde{x} = \frac{x}{L}; \tilde{y} = \frac{y}{L}; \tilde{u} = \frac{u}{U}; \tilde{v} = \frac{v}{U}; \tilde{\theta} = \frac{T - T_{\infty}}{T_s - T_{\infty}}; U = \sqrt{g\beta(T_s - T_{\infty})L} \quad (6.6)$$

where

L= Characteristic length

U= Characteristic velocity for x=L

u, v = Velocity components

T_s= Wall temperature

T_∞= Outside boundary temperature

After introducing dimensionless quantities, equations (6.3), (6.4) and (6.5) become the non-dimensionalised equations as given below

$$\frac{\partial \tilde{u}}{\partial \tilde{x}} + \frac{\partial \tilde{v}}{\partial \tilde{y}} = 0 \quad (6.7)$$

$$\tilde{u} \frac{\partial \tilde{u}}{\partial \tilde{x}} + \tilde{v} \frac{\partial \tilde{u}}{\partial \tilde{y}} = \theta + \frac{1}{\sqrt{Gr}} \frac{\partial^2 \tilde{u}}{\partial \tilde{y}^2} \quad (6.8)$$

$$\tilde{u} \frac{\partial \theta}{\partial \tilde{x}} + \tilde{v} \frac{\partial \theta}{\partial \tilde{y}} = \frac{1}{Pr\sqrt{Gr}} \frac{\partial^2 \theta}{\partial \tilde{y}^2} \quad (6.9)$$

where

Gr = Grashof number

$$Gr = \frac{g\beta(T_s - T_\infty)L^3}{\nu^2} \quad (6.10)$$

Pr= Prandtl number

Ra = Rayleigh number = Gr*Pr

From the non-dimensionalised equations (6.9), the dimensionless number “Grashof number” and “Prandtl number” were reduced to,

$$Pr\sqrt{Gr} = \sqrt{Pr^2Gr} = \sqrt{PrRa} \quad (6.11)$$

From equation (6.11), it is evident that if the product of dimensionless numbers, i.e., Rayleigh and Prandtl are kept same or maintained in same ratio for both test facility as well as for prototype, then experimental results capture the prototypic phenomena or behaviour more accurately, i.e.

$$(Pr * Ra)_{prototype} = (Pr * Ra)_{model} \quad (6.12)$$

As Nusselt number (Nu) depends upon Gr/Ra and Pr number, by satisfying equation (6.12) in both experiment and prototype, the heat transfer correlations developed from experimental study can be safely applied to prototype condition.

Similarly for the confined geometry, natural convection heat transfer is dependent on geometry parameters apart from dimensionless number (Rayleigh and Prandtl) as shown in equation (6.13)

$$(Pr * Ra * Geom^a)_{prototype} = (Pr * Ra * Geom^a)_{model} \quad (6.13)$$

where Geom= geometry

In our case, the geometry parameters which influence the natural convection heat transfer in confined geometry is in the ratio of melt height (MH) to diameter (D), height of vault (ht) to width of vault (W), and length of vault (L) to width of vault (W). So, equation (6.13) becomes

$$\frac{(Pr * Ra * (\frac{D}{MH} * \frac{W}{ht} * \frac{W}{L})^a)_{prototype}}{(Pr * Ra * (\frac{D}{MH} * \frac{W}{ht} * \frac{W}{L})^a)_{model}} = \frac{(Pr * Ra * (Geom)^a)_{prototype}}{(Pr * Ra * (Geom)^a)_{model}} = 1 \quad (6.14)$$

$$Geom = ((D/MH) * (W/ht) * (W/L))$$

For finding out the constant ‘a’, the following steps are adopted.

$$\frac{Pr_{prototype}}{Pr_{model}} = 1 \text{ Since both are using same fluid.}$$

Ra for prototype and model have been calculated and their ratio is

$$\frac{Ra_{prototype}}{Ra_{model}} = 17576 \quad (6.15)$$

Substituting the dimensional values we get

$$\frac{(\frac{D}{MH} * \frac{W}{ht} * \frac{W}{L})^a_{prototype}}{(\frac{D}{MH} * \frac{W}{ht} * \frac{W}{L})^a_{model}} = \frac{(\frac{8}{1} * \frac{11}{17} * \frac{11}{6.5})^a}{(\frac{2}{1} * \frac{.65}{1.1} * \frac{.65}{.77})^a} = (8.87)^a$$

By putting the above ratio of prototype to model in equation (6.14), we get constant $a=-4.48$.

Hence, the equation become

$$Pr * Ra * (Geom)^{-4.48} \quad (6.16)$$

Now equation (6.2) for Nusselt number for confined geometry become

$$Nu = Nu(Pr * Ra * (Geom)^{-4.48}) \quad (6.17)$$

Equation (6.17) is applicable to both model and prototype for natural convection heat transfer.

6.2.2 Correlation development for natural convection heat transfer

Experimental results (from chapter 3) are used to develop correlation which gives the variation of the local Nusselt number in terms of the Rayleigh number and angle. As the heat transfer from CV to vault water is in transient state, the temperature of bulk fluid of vault water is also in transient state at different angular location of CV. To estimate the heat transfer at various angular location of CV, the heat transfer coefficient is calculated with respect to constant value of temperatures which is prevailing at various angular locations at different time.

Figure 6.1 (a) shows the plot for ratio of local heat transfer coefficient (Nu_θ) to modified Rayleigh number (Ra^{**}) with respect to the different angles from bottom of the CV at different bulk temperature of vault water.

Here local Nusselt number and modified Rayleigh number are defined as

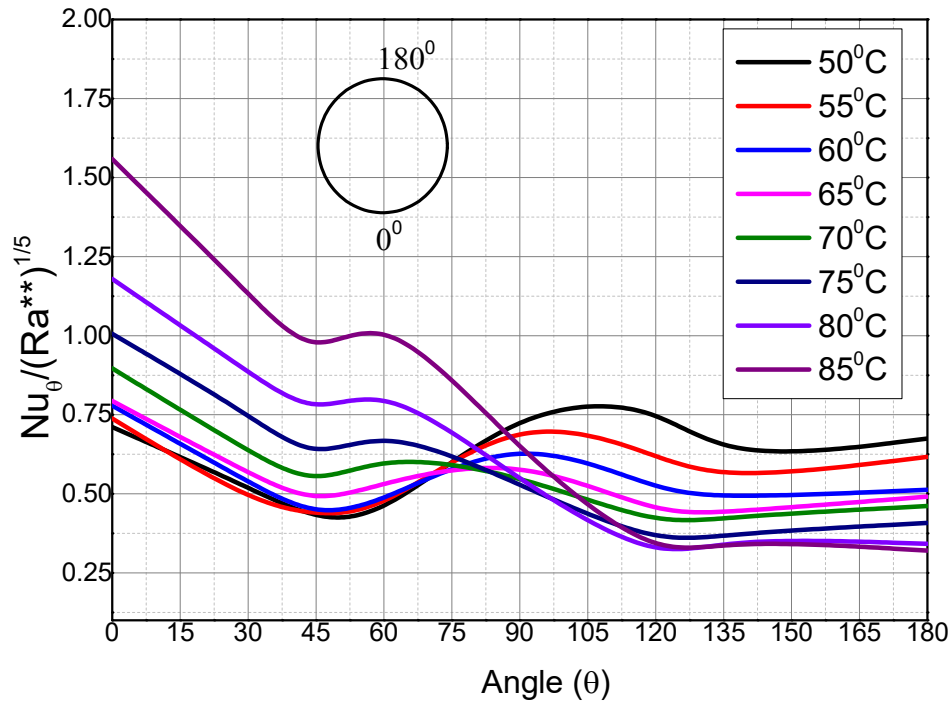
$$Nu_{\theta} = \frac{h_{\theta} D}{K}$$

$$Ra^{**} = Pr * Ra * (Geom)^{-4.48} \quad (6.18)$$

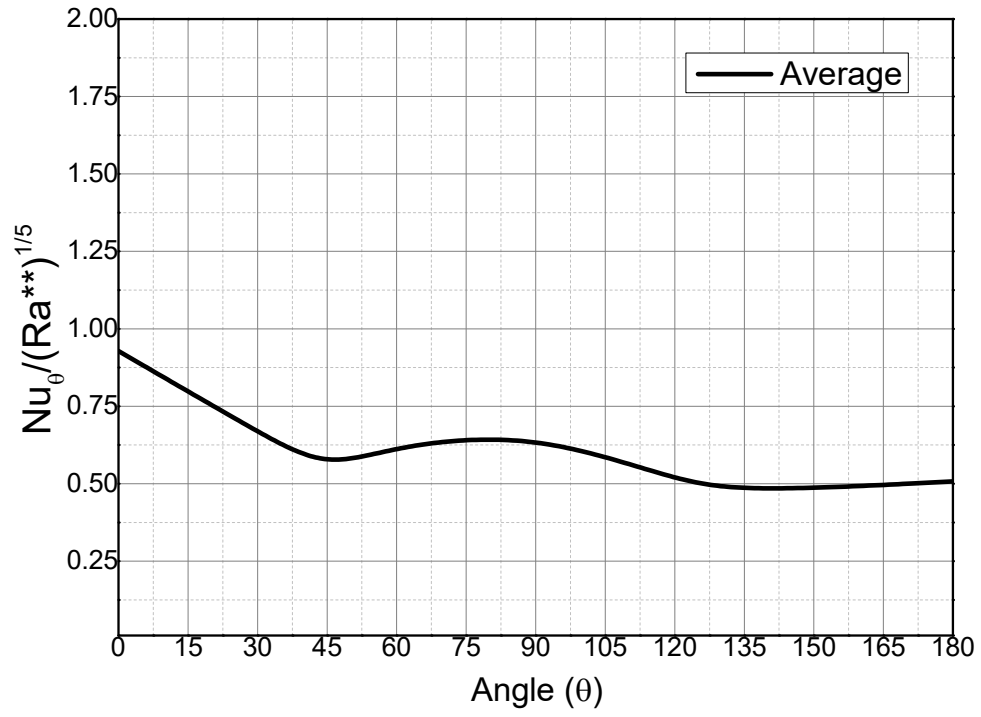
The average value of Nu_{θ} and Ra^{**} are obtained in the range of temperature from 50 °C to 85 °C and then the value of $Nu_{\theta}/Ra^{**0.2}$ is plotted with angle as shown in the figure 6.1 (b). The ratio of local heat transfer coefficient to modified Rayleigh is given as following equation:

$$\frac{Nu_{\theta}}{(Ra^{**})^{1/5}} = 0.934 - 0.0208\theta + 4.44 * 10^{-4}\theta^2 - 3.67 * 10^{-6}\theta^3 + 9.82 * 10^{-9}\theta^4 \quad (6.19)$$

Equation (6.19) is valid in the temperature range of water from 50 °C to 85 °C and Ra^{**} above 10^9 (i.e. in the range of $1.1 \times 10^{10} < Ra^{**} < 2.4 \times 10^{10}$).



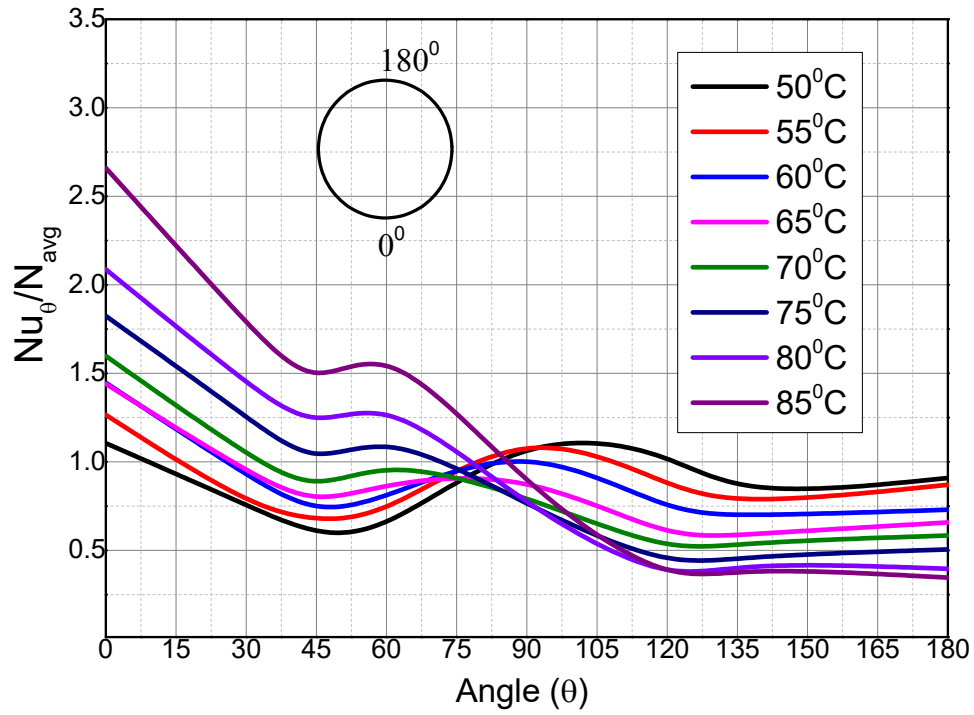
(a)



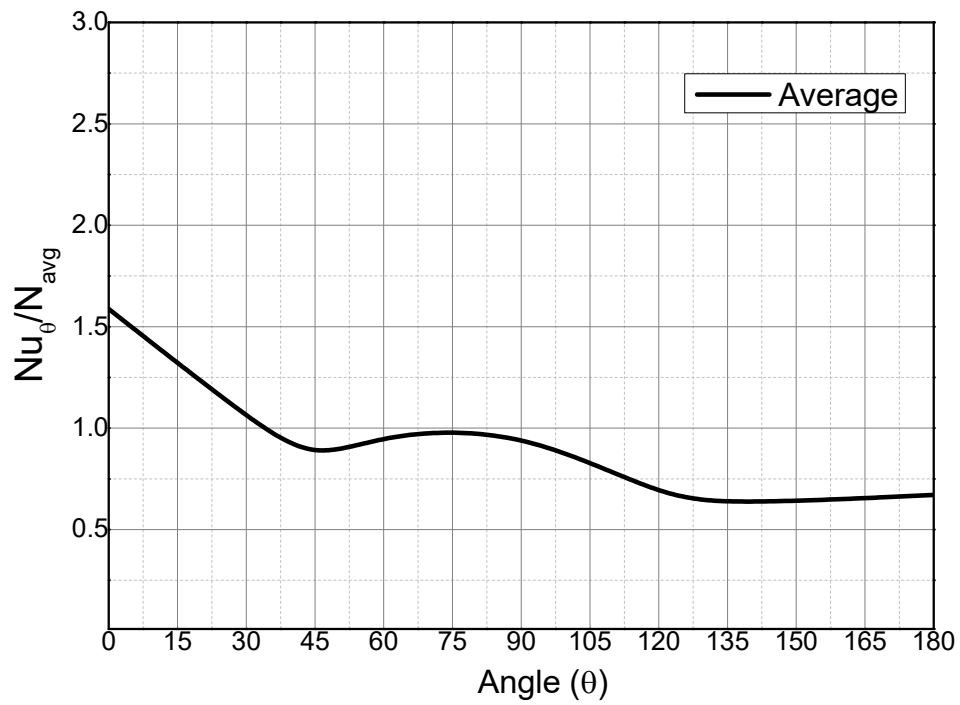
(b)

Figure 6.1: (a) Variation of $Nu_{\theta}/Ra^{**0.2}$ with angular angle at different bulk temperature (b)

Variation of average $Nu_{\theta}/Ra^{**0.2}$ with angular angle



(a)



(b)

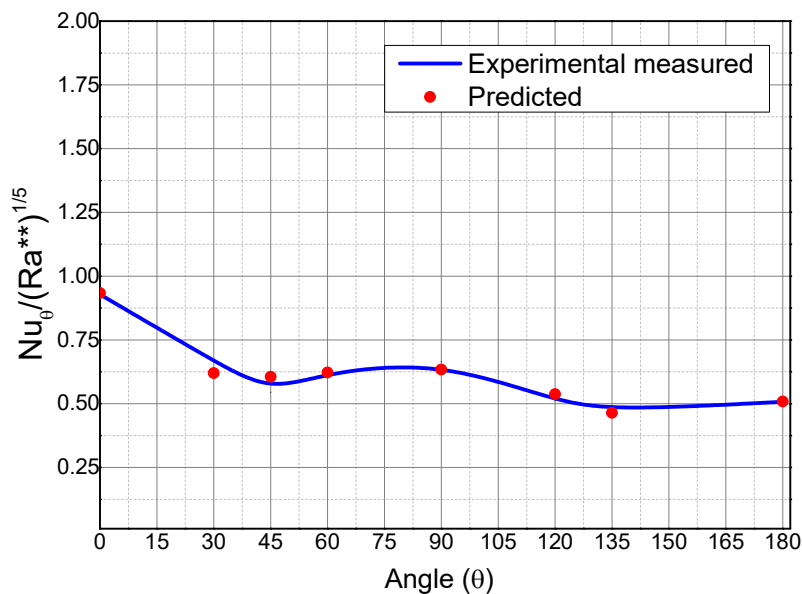
Figure 6.2: (a) Variation of Nu_θ / Nu_{avg} with angular angle at different bulk temperature (b)

Variation of average Nu_θ / Nu_{avg} with angular angle

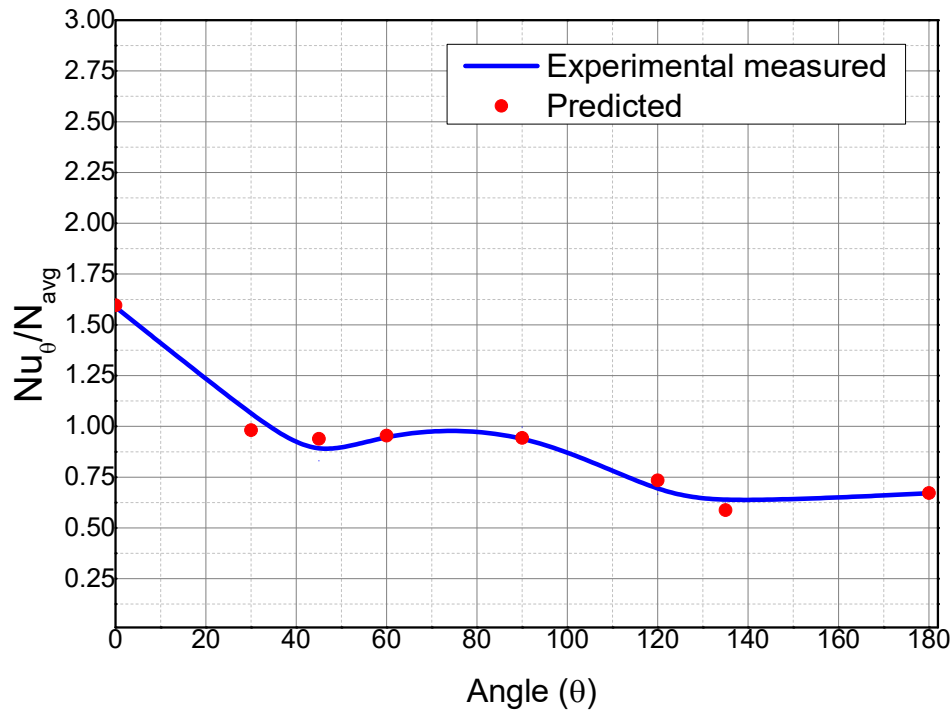
Similarly, the average Nusselt number (Nu_{avg}) are obtained and then the ratio of local to average Nusselt number (Nu_{θ}/Nu_{avg}) is plotted with the angle from bottom of the CV at different bulk temperature of vault water as shown in the figure 6.2 (a). The average value of Nu_{θ} and Nu_{avg} are obtained in the range of temperature from 50 °C to 85 °C and then Nu_{θ}/Nu_{avg} is plotted with angle as shown in the figure 6.2 (b). The ratio of local to average Nusselt number (Nu_{θ}/Nu_{avg}) is fitted by the following equation:

$$\frac{Nu_{\theta}}{Nu_{avg}} = 1.596 - 0.039\theta + 8.27 * 10^{-4}\theta^2 - 6.86 * 10^{-6}\theta^3 + 1.85 * 10^{-8}\theta^4 \quad (6.20)$$

Based on the equation (6.19), angular variation of local heat transfer coefficient around cylinder can be calculated once modified Rayleigh number is determined and similarly by the equation (6.20), angular variation of local heat transfer coefficient can be estimated once averaged heat transfer coefficient is known. Equation (6.20) is valid in the temperature range of water from 50 °C to 85 °C and for the angle of 0°(bottom) to 180°(top) of the curved calandria vessel. Figure 6.3 shows the comparison of predicted and measured value of $Nu_{\theta}/Ra^{**0.2}$ and Nu_{θ}/Nu_{avg} .



(a)



(b)

Figure 6.3: comparison of predicted and experimental measured value of (a) $Nu_\theta / Ra^{**0.2}$ (b) Nu_θ / Nu_{avg}

In experiments, there were errors in the measurement of temperature and test section geometry. The error in temperature below 400 °C, temperature above 400 °C and test section geometry measurements were 0.75%, 1.0% and 0.5% respectively. The uncertainty/error in correlation was analysed by the error propagation method. The uncertainty /error in heat transfer correlation was less than 4.0%.

6.3 Development of boiling natural convection heat transfer coefficient correlation

Boiling heat transfer has different phenomena compared to single phase natural convection. Boiling heat transfer also involves phase change, due to which the various hydrodynamic forces, e.g., inertia, viscosity, buoyancy and surface tension, all play an important role. Many

researchers suggest that to consider all these forces into account, additional non dimensional groups need to be identified for the boiling heat transfer coefficient correlation.

6.3.1 Dimensionless number and Scaling

Here dimensional analysis is used to identify the dimensionless number so that the experimental result can be directly extrapolated to prototype scale. To achieve the above criteria, two conditions should be fulfilled. First the dimensions of experimental setup to prototype should be in the same ratio and second relevant dimensionless numbers are same for both. Buckingham's Π theorem is used for dimensional analysis.

The heat transfer coefficient for boiling depends on the properties of the fluid conductivity (k), density (ρ), specific heat (C_p), dynamic viscosity (μ), characteristic length L , the temperature difference ΔT , buoyancy force $(\rho_l - \rho_v)g$, latent heat of vaporization h_{lv} and surface tension σ .

$$h = h(k, \rho, C_p, \mu, L, \Delta T, (\rho_l - \rho_v), g, h_{lv}, \sigma) \quad (6.21)$$

For equation (6.21) to be dimensionless, the components of each primary dimensions must be summed to zero which gives 5 equations and 10 dimensional variables. Out of 10 dimensional variables, five are primary dimensions. Therefore, 5 ($=10-5$) dimensionless number requires to describes boiling heat transfer. Hence, on solving, we get

$$Nu = f(Gr, Ja, Pr, Bo) \quad (6.22)$$

Where as

$$Nu = \text{Nusselt number } (hL/k)$$

$$Gr = \text{Grashof number } (g\beta\Delta TD^3/\nu^2)$$

$$Ja = \text{Jakob Number } (C_p\Delta T/h_{lv})$$

Pr = Prandtl number (ν/α)

Bo = Bond number ($(\rho_l - \rho_v) g D^2 / \sigma$)

Similarly for confined geometry the boiling heat transfer coefficient depend on geometry and equation (6.22) become

$$Nu = f(Gr, Ja, Pr, Bo, Geom) \quad (6.23)$$

6.3.2 Correlation for boiling natural convection heat transfer

Equation (6.23) can be written as

$$Nu = c Gr^m Ja^n Bo^p Pr^r \quad (6.24)$$

From experimental results (chapter 3), the dimensionless numbers were calculated, and by using multiple linear regression method, equation (6.24) constants were evaluated. Table 6.1 shows the constants with angle

From the table, it is observed that Constants of boiling correlations are independent of angular locations and equation (6.24) becomes

$$Nu = 0.106 \frac{Gr * pr^{1.81}}{Ja * Bo^{2.52}} \quad (6.25)$$

For the confined geometry, equation (6.25) becomes

$$Nu = 0.106 \frac{Gr * pr^{1.81}}{Ja * Bo^{2.52}} Geom^a \quad (6.26)$$

where $Geom = (D/MH * W/ht * W/L)$

As fluid and boundary condition both are same in experiment and prototype, for finding out the constant 'a', geometry ratio of prototype to model is put in equation (6.27), and we get value of a = 3.083

$$(0.106 \frac{Gr * pr^{1.81}}{Ja * Bo^{2.52}} (Geom)^a)_{prototype} = (0.106 \frac{Gr * pr^{1.81}}{Ja * Bo^{2.52}} (Geom)^a)_{model} \quad (6.27)$$

Hence, the equation of boiling natural heat transfer coefficient is

$$Nu = 0.106 \frac{Gr * pr^{1.81}}{Ja * Bo^{2.52}} (Geom)^{3.083} \quad (6.28)$$

The above equation is valid in the nucleate boiling range and in the Ra** range varying from $1.1 \times 10^{10} < Ra^{**} < 2.4 \times 10^{10}$.

Table 6.1: Constants of boiling correlations

| Angle | | Gr | Ja | Bo | Pr |
|----------------|---------------|-----------|-----------|--------------|-------------|
| | C | m | n | p | r |
| 0 | 0.0105 | 1 | -1 | -2.52 | 1.81 |
| 30 | 0.0107 | 1 | -1 | -2.52 | 1.81 |
| 45 | 0.0105 | 1 | -1 | -2.52 | 1.81 |
| 60 | 0.0107 | 1 | -1 | -2.52 | 1.81 |
| 90 | 0.0105 | 1 | -1 | -2.52 | 1.81 |
| 120 | 0.0107 | 1 | -1 | -2.52 | 1.81 |
| 135 | 0.0107 | 1 | -1 | -2.52 | 1.81 |
| 180 | 0.0107 | 1 | -1 | -2.52 | 1.81 |
| Average | 0.0106 | 1 | -1 | -2.52 | 1.81 |

Figure 6.4 shows the comparison of present correlations with measured value.

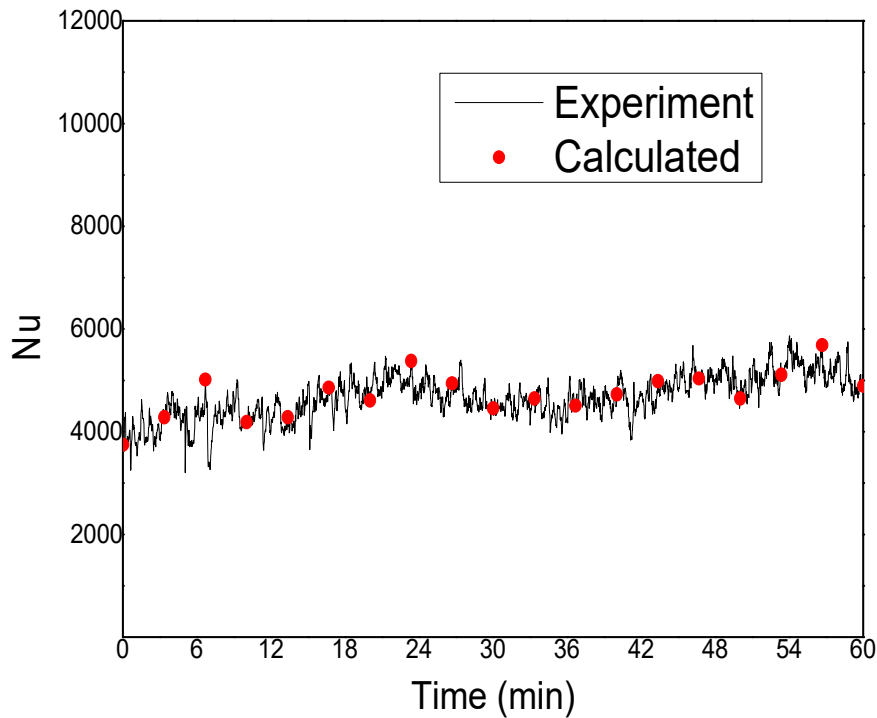


Figure 6.4: Comparison of predicted and experimental measured value boiling natural convection heat transfer

6.4 Validation of Correlation

For validation of correlation, the high temperature experiments (chapter 4) value was used. As no bulk boiling was observed in high temperature experiment, only single-phase natural convection correlation was validated. From developed correlation, it can be seen that heat transfer coefficient (i.e. Nusselt number) is dependent upon dimensionless numbers (Rayleigh Number, angle and geometry). Hence if these dimensionless numbers are similar or in close ratio for model and prototype, then above developed correlations are valid for both. In experiment, the geometry and angle are in similar ratio and Table 6.2 shows the Rayleigh number in experiment and prototype which are in fully turbulent region. Hence, correlation developed from model is valid for prototype condition also.

Table 6.2: Comparison of dimensionless Rayleigh number in Experiment and prototype

| Parameter | Experiment | | Prototype | Remark |
|---|---------------------------|---------------------------|-----------------------|--|
| | With 300 NB (~1200 °C) | With 450 NB (~2300 °C) | | |
| Rayleigh Number (Ra) inner | 1.55×10^{11} | 9.22×10^{11} | 8.75×10^{14} | Fully developed turbulent region ($Ra > 10^9$) |
| Rayleigh Number (Ra) outer | 2.55×10^{10} | 6.6×10^{10} | 3.4×10^{14} | Fully developed turbulent region ($Ra > 10^9$) |
| Modified Rayleigh Number (Ra^{**}) | 2.2×10^{10} | 1.1×10^{10} | 2.4×10^{10} | Fully developed turbulent region ($Ra > 10^9$) |

Developed correlation is also used for prediction of outer surface temperature of experiment conducted at high temperature (>2300 °C) with different geometry as discussed in chapter 4. Table 6.3 shows the comparison of predicted value and experiment value which show that both are in good agreement.

Table 6.3: Comparison of Experiment and predicted value

| Parameter | Experiment with different geometry (450 NB) and melt temp. (>2300 °C) | Prediction using correlation |
|---|---|------------------------------|
| Average heat transfer coefficient (W/m ² /K) | 2526.4 | 2411.4 |
| CV Outer temperature (°C) | 97.5 | 97.7 |

In addition, the correlations have been applied to another experimental facility having same dimension i.e., diameter and radius of curvature same as calandria vessel of 700 MWe PHWR. Prediction of heat transfer coefficient on the outer surface of calandria vessel [74] for single phase and nucleate boiling heat transfer regime are done. The measured heat transfer coefficient is reported in the range 600-5945 W/m²/K for single phase natural convection and in the range of 9000-17500 W/m²/K for nucleate boiling natural convection. The correlations predict the heat transfer coefficient to be in the range of 585-6650 W/m²/K and 9636 -18200 W/m²/K. In view of this the developed correlation can be applied to other geometry relevant to in vessel retention of corium in PHWRs.

Table 6.4 shows the comparison of measured heat transfer coefficient in different experimental set ups having different diameter and radius of curvature. It can be seen that heat transfer coefficient on the outer surface of calandria vessel are close to each other both in single phase and nucleate boiling regime irrespective of the diameter and radius of curvature of simulated calandria vessel. In view of this, the developed correlations in this chapter can

be extended to other cylindrical geometry with partial heat generation as in the calandria vessel of PHWRs under severe accident condition.

Table 6.4: Comparison of Experiment and PHWR Vessel

| | Experiment | | PHWR Vessel [74] |
|--------------------------------------|--------------------------------|------------------------------|--------------------------------|
| | With 300 NB (Chapter 3) | With 450 NB (Chapter 4) | |
| Single phase natural convection | 550 -5289 W/m ² /K | 400-6200 W/m ² /K | 600-5945 W/m ² /K |
| Two phase boiling natural convection | 9900-17000 W/m ² /K | | 9000-17500 W/m ² /K |

6.5 Closure

This chapter provides deep understanding and various steps of development of natural convection heat transfer coefficient for confined geometry considering scaling with the prototype condition by using governing equation for free convection. In this chapter natural convection heat transfer coefficient correlations have been developed (by using experimental data discussed in chapter 3) for curved outer calandria vessel surface which is partially heated due to semi filled corium and submerged completely in water pool. The correlations have been developed from first principles for both single phase and boiling heat transfer regimes. The correlations are applicable within the error of 4%.

Chapter 7

Scaling effects of melt volume, decay heat, melt material on heat transfer behaviour

7.1 Introduction

For understanding the complex phenomena of severe accident in nuclear reactor, it is unfeasible, unsafe and uneconomical to conduct the experiments at 1:1 scale. Scaled down experiments are more feasible, safe and economical for obtaining insights of severe accident, safety evaluation of reactor design and generations of data for validation of code. In severe accident studies, large number of experiments have been conducted with different simulant materials, volumes, temperature, geometry, etc. There are concerns about the applicability of these scaled experimental results to prototype condition. In general, we know that in any scaled experiment, there is always scale distortion due to the inherent limitations.

To overcome the concerns of applicability of scaled experimental results to the prototype conditions, in this chapter, experiments have been conducted at different scaled melt volumes, decay heat and melt materials. Their effects on heat transfer behaviour from the CV to the vault water has also been compared. These studies are very useful in providing insights of the scaling criteria adopted in the series of experiments conducted in this research work.

7.2 Scaling effects of melt volume on heat transfer behaviour

There are some apprehensions with regard to scaling of melt volume on heat transfer. In a nuclear power reactor, the amount of corium is in the order of several tonnes, whereas, in the experiments, the maximum amount of the corium simulant used is hardly half a ton. In small scale experiment, ratio of melt surface area to melt volume is more in experiment as compared to prototype. Due to this, the concern is that cooling rate of melt is more in experiment. To understand this aspect, experiments were performed at two different melt

volumes, viz. 100 kg and 500 kg using the same simulant melt material (i.e., near prototype corium ($\text{ZrO}_2 + \text{CeO}_2 + \text{Fe} + \text{Al}_2\text{O}_3$)) that had identical initial melt temperature. The volumes of melt in experiments were different, so corresponding volumes of vault water were also different to maintain same ratio of melt volume to vault water volume as in prototype. These experiments were conducted in stored heat dominated regime.

7.2.1 Details of test setup

The details of 500 kg test setup are already described in the chapter 4 (section 4.3; figure 4.1). The details of 100 kg test setup were similar to 500 kg test setup. It consists of stepped test section having the main shell, small shell, annular plate and side plates similar to calandria vessel of PHWR. The diameter of the test section varied from 450 mm to 300 mm and vessel thickness varied from 32 mm to 22 mm. The total length of the calandria vessel was 450 mm. The calandria vessel was submerged inside a tank with dimensions 800 mm x 800 mm x 700 mm. A thermite reactor was placed on top of the vessel in which high temperature melt is generated by thermite reaction (figure 7.1). It was engineered for in-situ pouring of melt inside the calandria vessel. The experimental setup was extensively equipped with thermocouples. To measure the temperature inside the melt, 4 C-type thermocouples were kept inside the melt pool. For outer surface of test section, the K-type thermocouples were installed at various locations like main shell, small shell and annular plate. Total 24 K-type thermocouples were installed. The locations of K type thermocouples are shown in figure 7.2.

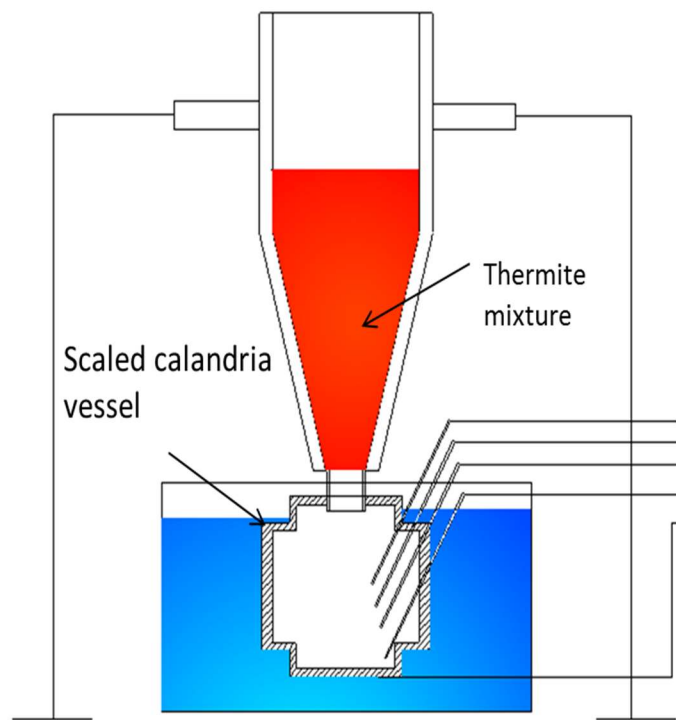


Figure 7.1:100 kg Test setup

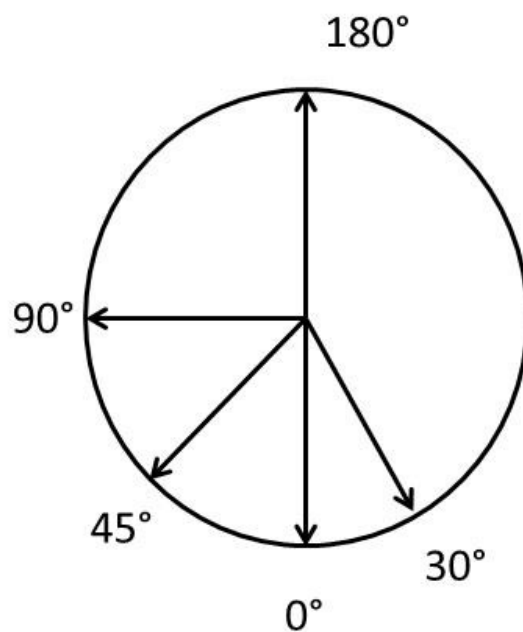
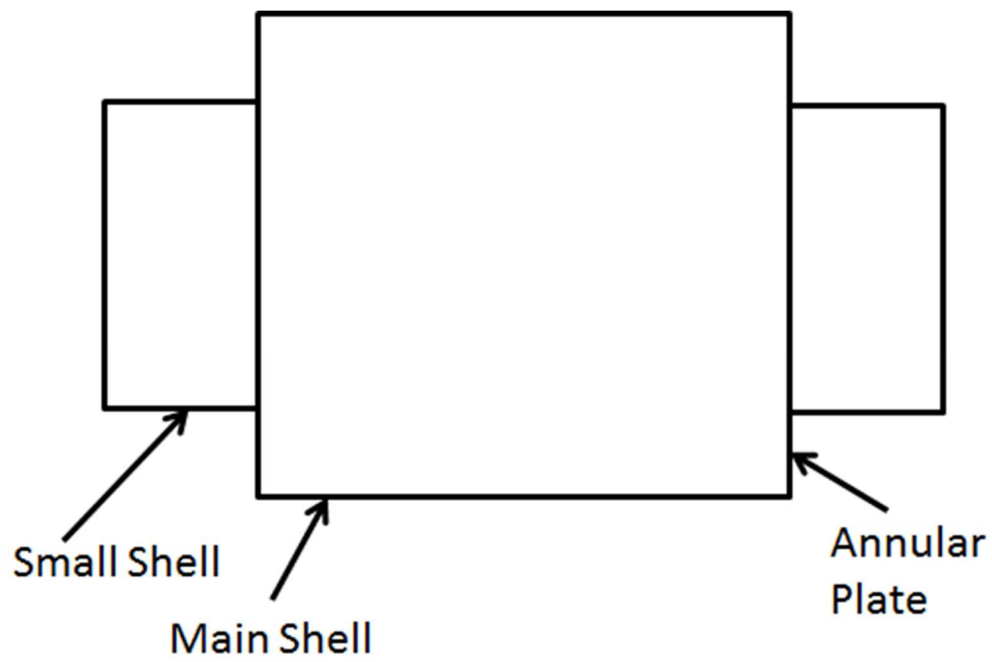
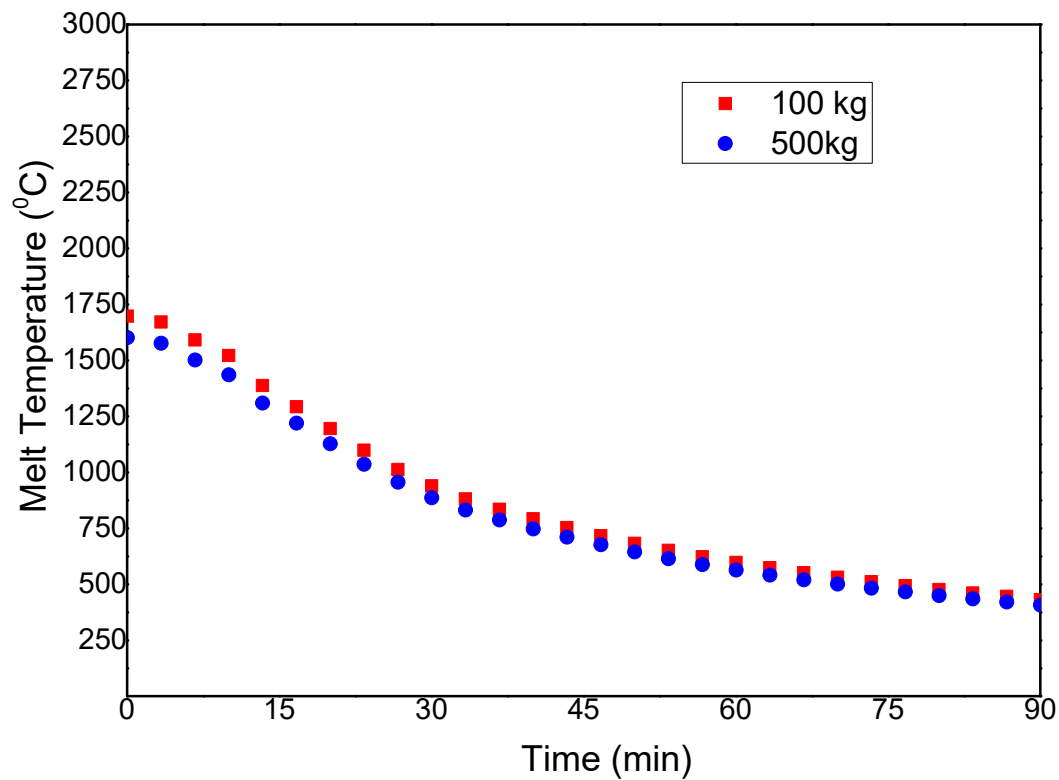


Figure 7.2: Instrumentation scheme for 100 kg test setup

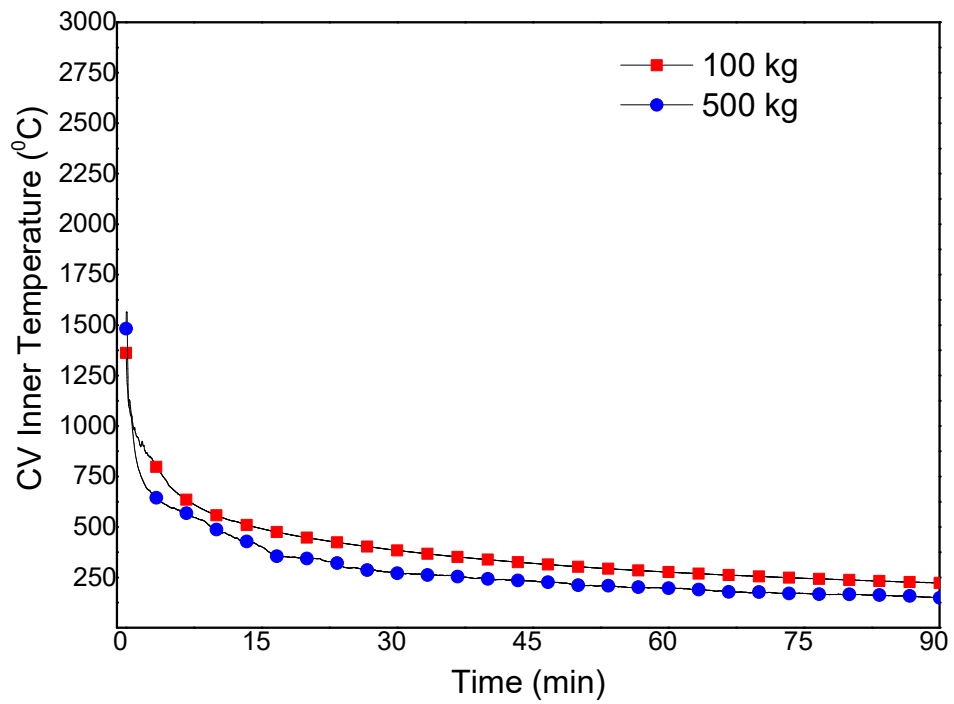
7.2.2 Results of melt volume on heat transfer

Figure 7.3 shows the comparison of temperature of melt, CV inner surface and CV outer surface of experiment conducted at two different melt volumes. Results showed that the temperature of melt, CV inner, CV outer and water in both scales of experiments were closer.

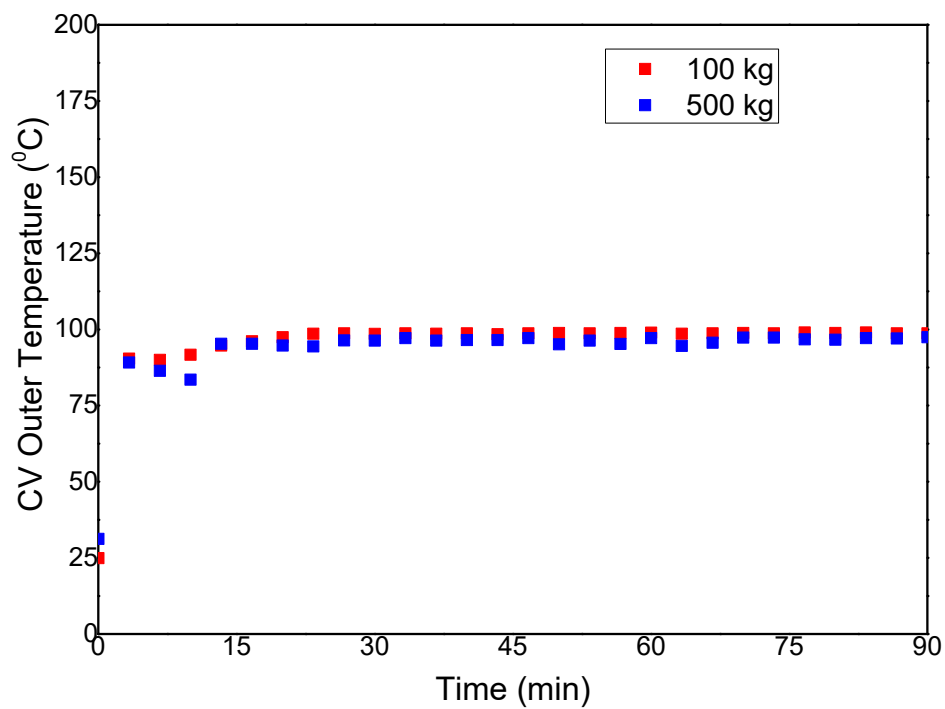
Since the melt temperatures are very close to each other, crust temperatures in both cases are expected to be closer to each other. Since the crust is controlling the heat transfer resistance between melt and vault water, that is why, the CV inner and outer surface temperature are also close to each other. In view of this, it is expected that in the stored heat dominated regime, if the initial melt temperatures are simulated for the same melt material, the scaling philosophy adopted in this research work, is sufficient to simulate the reactor conditions.



(a)



(b)



(c)

Figure 7.3: Comparison of Temperature with different melt volume (a) Melt (b) CV inner surface (c) CV outer surface

7.3 Scaling effects of decay heat on heat transfer behaviour

To understand the influence of decay heat on heat transfer in corium melt coolability, experiments were conducted with two different decay heat powers. In these experiments, the same simulant melt material (borosilicate glass), volume of melt and initial melt temperature were kept. Decay heat generated inside melt during the experiments were

- a) $\sim 0.7 \text{ MW/m}^3$
- b) $\sim 1.0 \text{ MW/m}^3$

7.3.1 Details of test setup

The details of test set up used for 1.0 MW/m^3 decay heat inside melt experiment is already described in chapter 3 (section 3.2.2, figure 3.3)). The test setup used for 0.7 MW/m^3 decay heat experiment was similar to 1.0 MW/m^3 decay heat experiment. Only different numbers of high density heater cartridges were used to achieve the variations of decay heat in above experiments. Instrumentations in both the experiments were same. These experiments were conducted in decay heat dominated regime.

7.3.2 Results of decay heat on heat transfer behaviour

Figure 7.4 shows the effect of decay heat on the crust thickness. From the figure, it is observed that in case of lower decay heat ($\sim 0.7 \text{ MW/m}^3$), the crust thickness formation rate is higher whereas in case of higher decay heat ($\sim 1.0 \text{ MW/m}^3$), the crust thickness formation rate reduced drastically. After some time, almost no further growth of crust was observed in both cases. The crust thickness observed were 40 mm and 12 mm in lower and higher decay heat respectively.

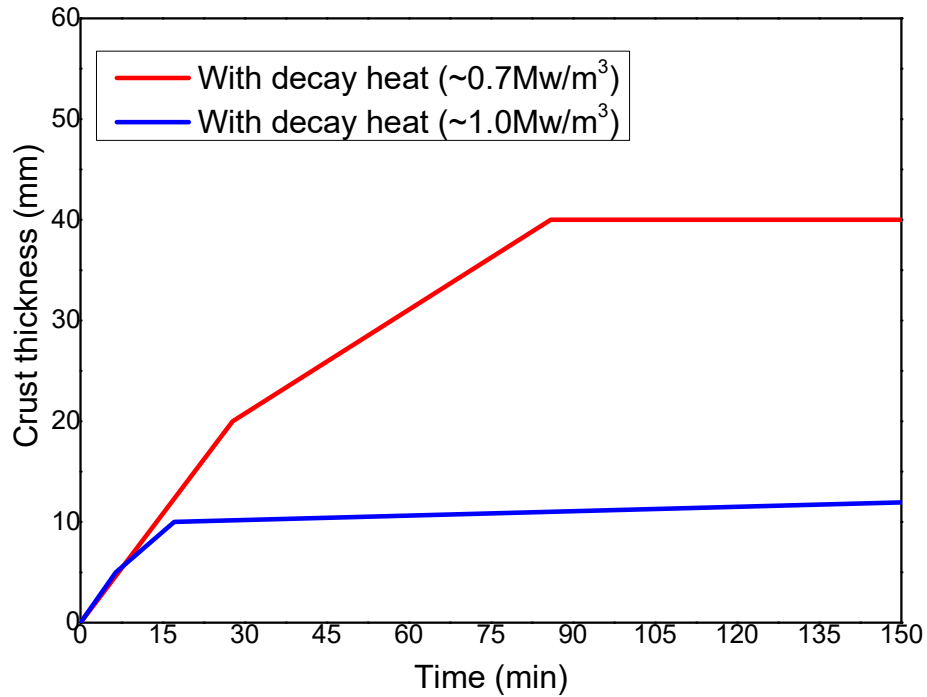


Figure 7.4: Effect decay heat on crust thickness

Presence of higher decay heat in melt resulted lower crust thickness and higher heat transfer to vessel and vault water. That is why, higher decay heat in melt has higher outer surface temperature compare to lower decay heat as shown in figure 7.5. But in both cases, presence of thin layer of crust was sufficient to keep the CV outer temperature well below the water saturation temperature.

In view of this, decay heat play very important role in the crust formation rate, growth and heat transfer. The experiments need to maintain the same decay heat as in prototype so that the results can be directly applied.

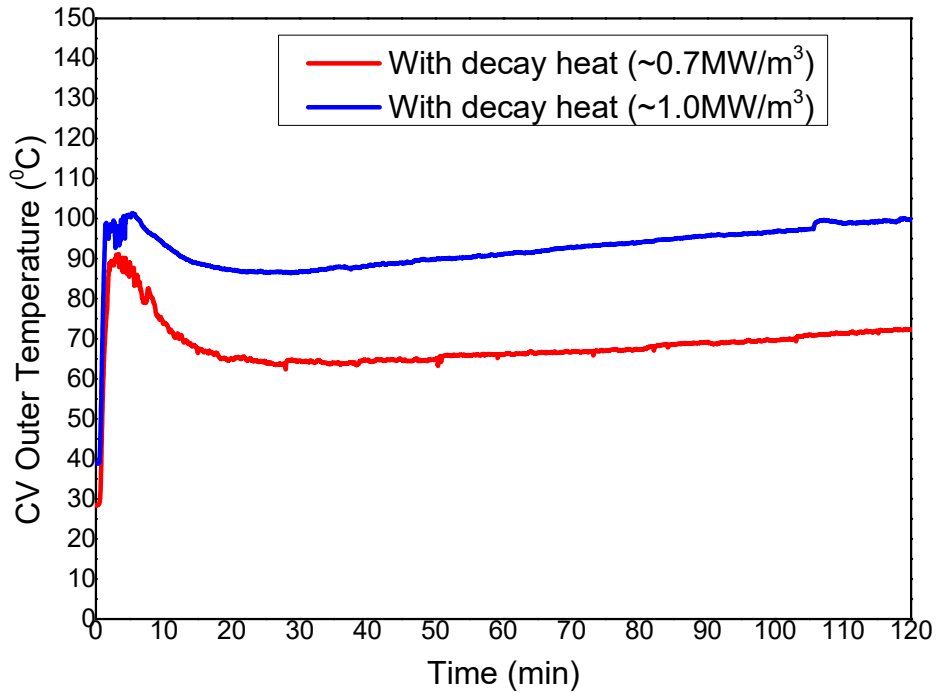


Figure 7.5: Comparison of CV outer surface temperature at different decay heat

7.4 Scaling effects of different melt material on heat transfer behaviour

To understand the influence of corium simulant melt composition on the heat transfer, experiments were conducted with different simulant materials. As different melt simulant materials have different melting points, phase change behaviour (solidus and liquidus temperature), etc. so the experiments were conducted with two different melt materials having different initial melt temperature and same volume of melt.

The two different materials used are:

- a) Borosilicate glass
- b) $\text{ZrO}_2 + \text{CeO}_2 + \text{Fe} + \text{Al}_2\text{O}_3$ (near prototypic melt)

7.4.1 Details of test setup

The details of test set up used for borosilicate glass melt simulant experiment is already described in chapter 3 (section 3.2.2, figure 3.3)) whereas details of test set up used for near

prototypic melt simulant experiment is described in chapter 4 (section 4.3; figure 4.1). The properties of above materials are compared and as given in table 7.1 below

Table 7.1: Comparison of simulant material property

| Property | Glass simulant | Near Prototypic ($\text{ZrO}_2 + \text{CeO}_2 + \text{Fe} + \text{Al}_2\text{O}_3$) | Corium |
|---|-------------------|--|----------|
| Density (kg/m^3) | 2400 | 5074 | 8800 |
| Thermal conductivity (k) (W/mk) | 1 | 2.3 | 2.88 |
| Specific heat capacity (C_p) (J/kg.K) | 730 | 700 | 565 |
| Thermal expansion coefficient (β) (/K) | 1.03e-04 | 1.04e-4 | 1.05e-4 |
| Thermal diffusivity (α) | 5.71e-07 | 6.4e-07 | 5.79e-07 |
| T_{initial} of Melt ($^{\circ}\text{C}$) | 1200 | 2300 | 2800 |
| Viscosity (Pa.s) | 0.0025 | 0.0026 | 0.00336 |

It may be noted that both the materials have almost same thermal diffusivity and thermal expansion coefficient, which plays an important role for heat transfer from melt pool to vault water by natural convection and conduction.

7.4.2 Results of different melt simulant on heat transfer behaviour

In both the experiments, as soon melt was poured, crust formation was observed inside CV.

The formation of crust resulted in reduction of heat transfer from melt to CV vault water.

Initial crust thickness observed was 20 mm in glass simulant and 50 mm in near prototypic material. Even though initial melt temperature varies extremely, the CV outer temperatures were observed near saturation temperature of water in both experiments as shown in figure 7.6.

This shows that the melt material properties (thermal diffusivity, volumetric thermal expansion coefficient, etc.) are the most critical parameters and if they are simulated the results of the experiments can be safely applied to prototype.

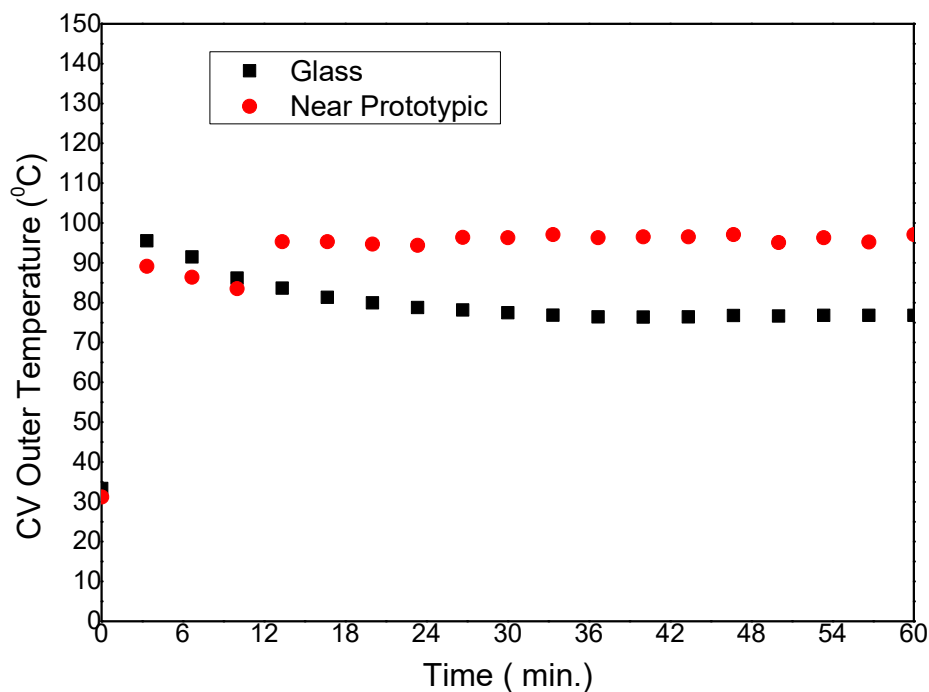


Figure 7.6: CV outer temperature with different melt simulant

7.5 Closure

This chapter has addressed the concerns of applicability of scaled experimental results to prototype condition. These experiments were conducted with different volume of melt, different decay heat generation and different melt composition to understand the scaling effect on corium coolability. In each of experiment, the CV outer temperatures were found well below the saturation temperature of water. The different volume of melt and different melt composition has little effect on corium coolability; provided the different melt materials have similar material properties (like thermal diffusivity, volumetric thermal expansion coefficient, etc.). The decay heat has effect on crust thick which resulted in heat transfer from melt to vault water.

Chapter 8

CFD Simulation of Corium coolability in In-vessel retention

8.1 Introduction

Simulation of full severe accident progression scenario of corium coolability in IVR using CFD is still not practical to achieve, because the simulation of severe accident involves following challenges in PHWR as given below

- a) Melt has mixture of UO_2 , ZrO_2 , U, Zr, steel, etc.
- b) It involves phase change in corium melt, i.e., formation of crust and molten corium.
- c) Heat transfer coefficient of natural convection behaviour on outer curved vessel of CV varies from single-phase to partial boiling, and then fully boiling.
- d) It also involves multi-mode heat transfer, e.g., Conduction, Convection and Radiation
- e) Corium is partially filled in CV resulting in non-uniform angular heating of CV.
- f) Melt properties at wide temperatures ranging from 3000 °C to room temperatures are not available.

Current computer codes are not robust enough to handle such multi component, multi phase, multi mode heat transfer and beyond the capability of existing CFD codes. Recently more and more experimental studies are available, so use of CFD for specific phenomena during a severe accident has taken place.

Although, the experiments with decay heat dominated regime (chapter 3) and with stored heat dominated regime (chapter 4) during severe accident provided a lot of understanding on in-vessel retention. But when it comes to prototype condition, i.e., corium melt temperature above ~2830 °C with decay heat generation, it is almost impossible to carry out experiments with actual material and with several tons of molten debris. Hence, based on these

experiments, CFD analysis was carried out for in-vessel retention. The CFD model was first benchmarked with experiments and then extended to prototypic condition.

8.2 CFD model –equations of corium coolability

Figure 8.1 shows various modes of heat transfer occurring in homogenous corium melt inside the CV during full core melt accident of PHWR. As the CV is in contact with cold pool of vault water, the lower portion of corium melt forms a solid crust. Similarly at the top of corium melt, radiation heat transfer is predominant along with convection, so crust is also formed at the top. The formation of crust is important for saving the CV from seeing high temperature. This phenomenon is also experimentally confirmed in the experiments. The heat from the centre of corium melt, is transferred in two directions, top and bottom. At the bottom, this heat is transferred to bottom crust by natural convection, from bottom crust and CV wall by conduction, and from there to the vault water by convection. At the top, the heat is transferred to the top crust by convection, within top crust layer by conduction and then from the top of crust to surrounding by radiation.

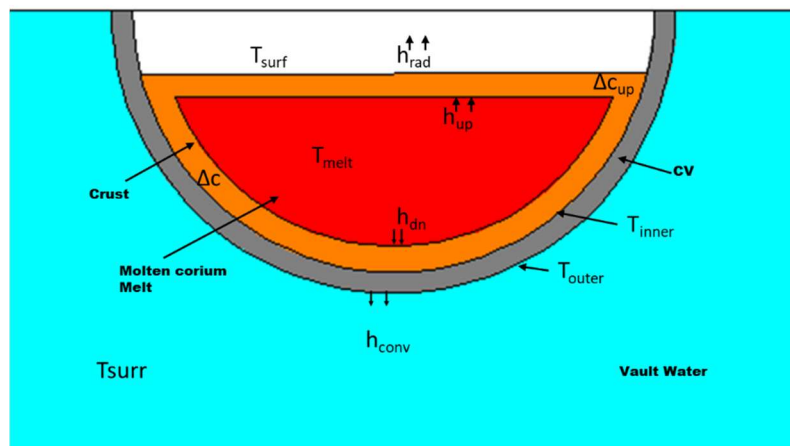


Figure 8.1: Heat transfer modes in CV

From the heat transfer analysis, following forms the constitutive equations

Downward heat transfer

Downward convective heat flux is given as

$$q_{dn}'' = h_{dn}(T_{melt} - T_c) \quad (8.1)$$

Conduction in the crust with heat generation

$$q_{dn}'' = \frac{k_c}{\Delta c} (T_c - T_{inner}) - \frac{Q''' \Delta c}{2} \quad (8.2)$$

Conduction in the vessel

$$q_{dn}'' = \frac{k_{vess}}{\Delta x_{vess}} (T_{inner} - T_{outer}) \quad (8.3)$$

Upward heat transfer

Upward convective Heat flux is given as

$$q_{up}'' = h_{up} (T_{melt} - T_c) \quad (8.4)$$

The heat conduction through the crust with heat generation is given as

$$q_{up}'' = \frac{k_{cup}}{\Delta c_{up}} (T_c - T_{surf}) - \frac{Q''' \Delta c_{up}}{2} \quad (8.5)$$

The radiation heat flux from top surface is given as

$$q_{rad}'' = \sigma \epsilon_{eff} (T_{surf}^4 - T_{surr}^4) \quad (8.6)$$

Where

| | |
|--|-------------------|
| Q'''= Volumetric heat generation, W/m ³ | c=crust |
| q''= Heat flux, W/m ² | dn = downward |
| h = heat transfer coefficient, W/m ² /K | melt= melt |
| k = Thermal conductive, W/m/K | rad=radiation |
| T = Temperature, K | surf= surface |
| Δc = Crust thickness, m | surr= surrounding |
| Δx = Vessel thickness, m | up = upward |
| σ=Stefan Boltzmann constant | vess= vessel |
| ε= emissivity | |

There is total 6 unknowns in these set of equations (T_{melt} , T_{inner} , T_{outer} , T_{surf} , Δc , Δc_{up}). It is assumed that decay heat is constant. Hence, at steady state, the total heat transfer rate is constant. Hence, by equating above equations, we get six equations with six unknowns. This gives a unique solution. The set of equations are solved iteratively to get the values of the above unknowns.

8.3 Boundary conditions

The inner surfaces of CV with melt are stationary wall with no slip condition and coupled thermal condition. Melt top surface and air interface was taken as wall with no slip condition. Inside the melt, solidification and/or melting took place over a range of temperatures. This had been modelled with enthalpy-porosity model for tracking of liquid-solid front. The liquid-solid mushy zone was treated as a porous zone with porosity equal to the liquid fraction. Appropriate momentum sink terms were added to the momentum equations to account the pressure drop caused by the presence of solid material. The upper surface of the crust exchanged heat with the CV inner upper wall by thermal radiation and with the air above the surface by natural convection. The emissivity of the upper surface of the crust and the emissivity of the calandria wall were supplied from material properties. Heat transfer from the CV inner upper wall to the water in calandria vault took place by conduction. For decay heat inside the corium melt, the volumetric heat generation conditions were applied.

As CV was submerged in water, heat was transferred from the outer surface of CV to vault water by natural convection and then by nucleate boiling. Hence, heat transfer coefficient correlations were developed for natural convection as well as for nucleate boiling which were applied on the outer surface of CV wall.

8.4 Simulation of experiment

The dimension of CV in experiment had 300-mm diameter, 460-mm length and the wall thickness was 25 mm. CV material in experiment was SS 304L. Same geometry was considered for two-dimensional numerical simulation. The domain of 2D model simulation for with or without decay heat cases is shown in Figure 8.2. The vault water had not been considered in the computational domain. The molten pool, air -vapour domain above molten pool and vessel wall were taken as interior condition. The inner and outer surfaces of

cylindrical vessel were stationary wall and coupled thermal condition had been applied. At the outer surface of vessel, heat transfer coefficient due to natural convection in single phase and nucleate boiling, were simulated by applying correlations on vessel outer surface.

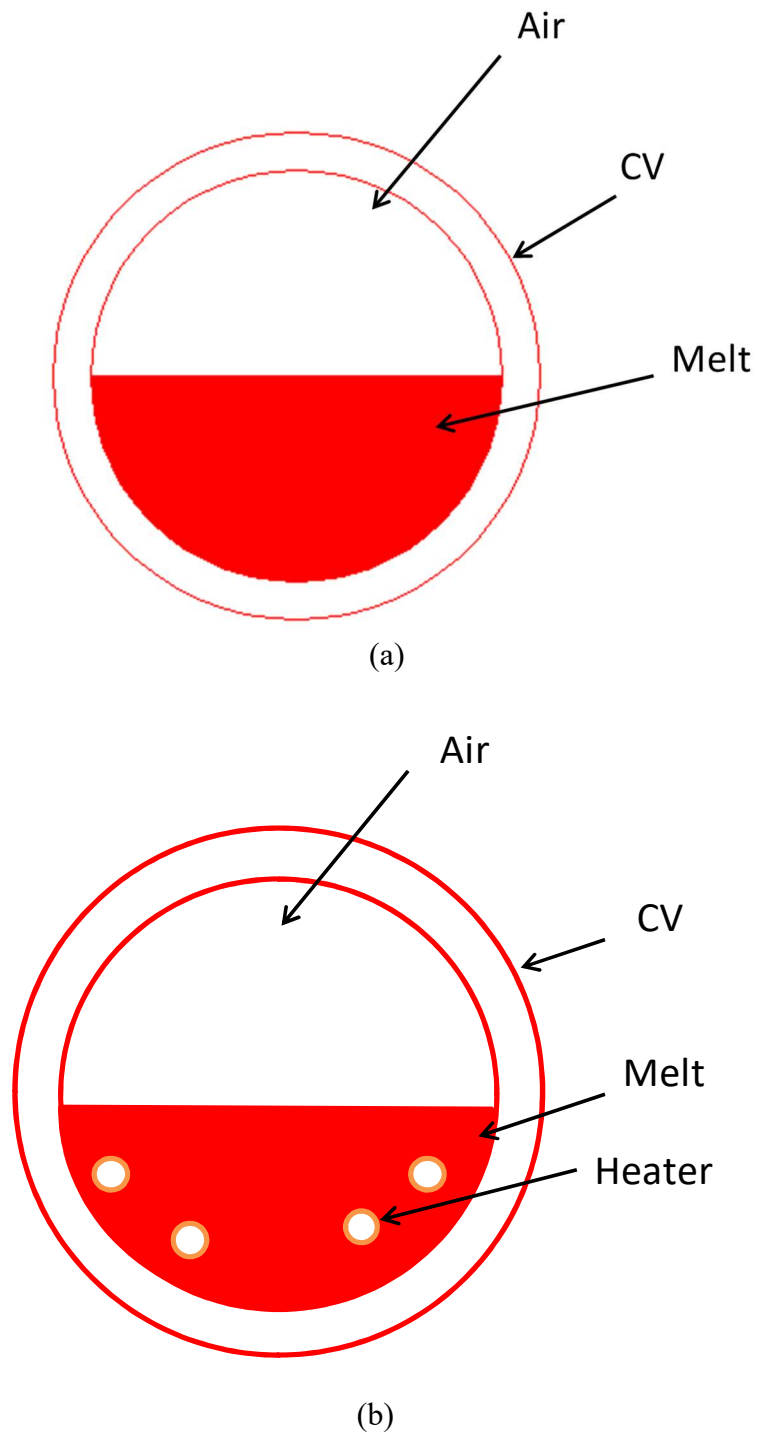
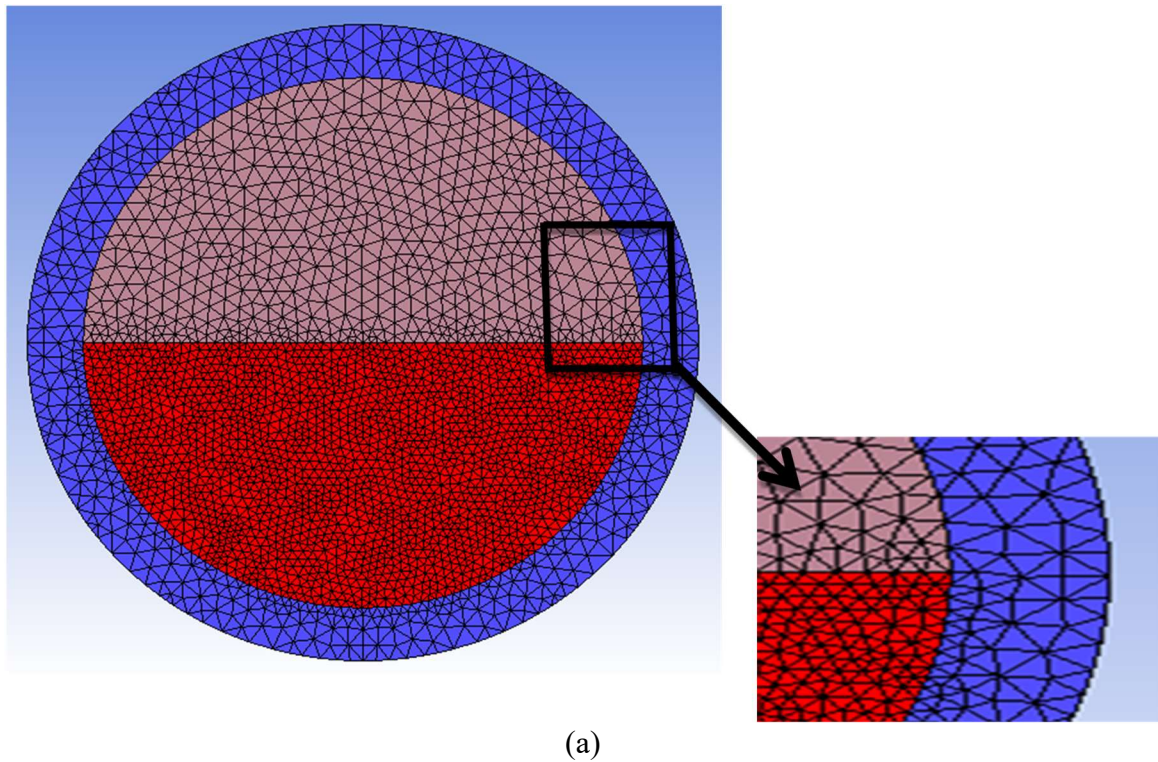
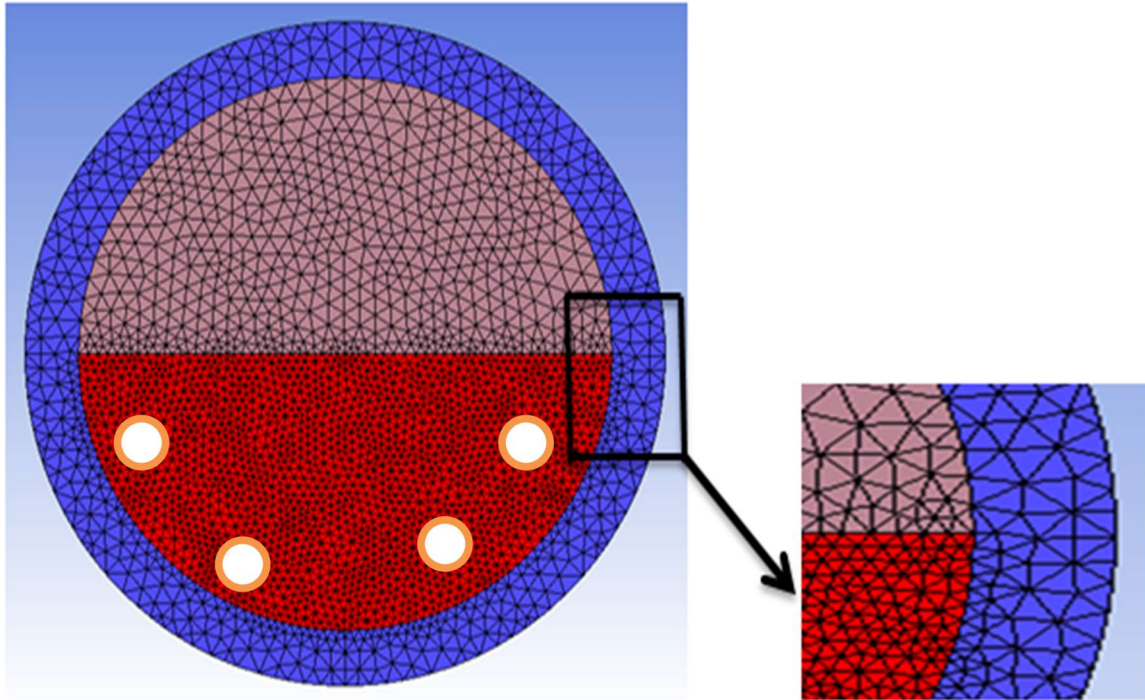


Figure 8.2: Schematic of 2D model domain for (a) without decay heat case (b) decay heat case

The grid independent study had been carried out as a function of pool Rayleigh number. In the case of PHWR, the Rayleigh number (10^9 – 10^{12}) is lower than for PWR or BWR (owing to lower heat generation rate in melt and spreading of the melt in the very large diametric vessel); hence it is possible to have large size grid cells. For melt pool, an unstructured tri grid was chosen with an element size of 4 mm. The air -vapour domain and calandria wall were meshed with unstructured tri grid elements with a maximum element size of 8 mm. Patch independent mesh method was used. An illustration of the domain mesh is presented in figure 8.3.





(b)

Figure 8.3: Geometry meshing (a) without decay heat (b) Decay heat

Grid independence study had been carried out with four different mesh densities viz. 2950, 3940, 5800 and 22100. The mesh density having 5800 elements was selected as the difference of temperature was almost negligible beyond this mesh density.

Pressure-based transient solver, which is used for low-speed incompressible flows, was considered. Here flow field and pressure field were obtained by solving momentum equations and pressure correction equation respectively. Time-dependent temperature was obtained by solving transient energy equation. For transient analysis, the equations were discretized in both space and time.

The following assumptions/simplifications were made:

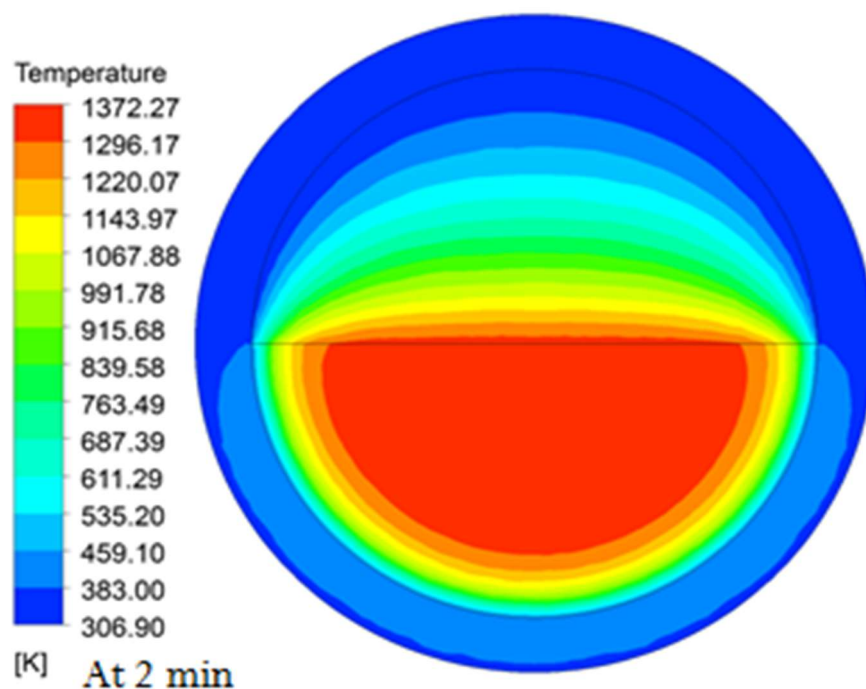
- a) Melt in the liquid phase had been considered as an incompressible and Newtonian fluid
- b) Phase change ignored volume alteration

- c) Melt was considered as homogeneous mixture
- d) The stratified temperature fields of the pools were not considered

8.5 Comparison of simulation results with experiment

8.5.1 Without decay heat

Figure 8.4 shows the temperature profile of simulation for scaled model at 2 min and 30 min time intervals respectively. These contours give insight of melt cooling inside the test vessel at different time scale. Figure 8.5 shows the comparison of CFD predicated and experimental melt temperature distribution at 40 mm radial location from the bottom of vessel. In experiment, glass melt was poured at temperature 1200 °C (1473 K) and maximum melt temperature recorded was 1100 °C (1373 K).



(a)

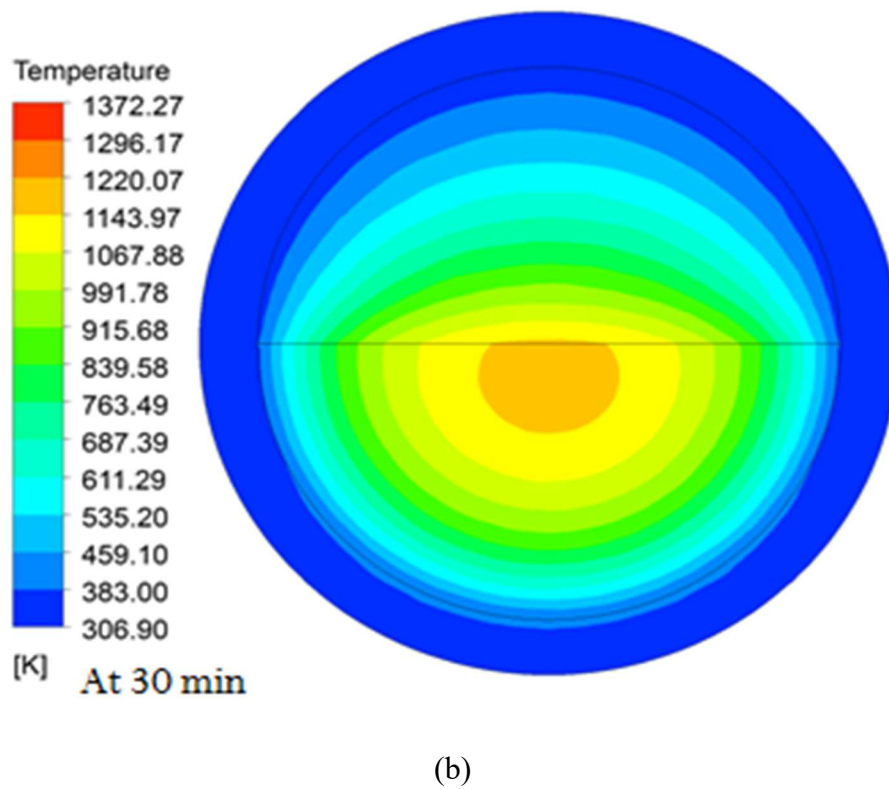


Figure 8.4: Temperature contour profile at (a) 2 minute (b) 30 minute

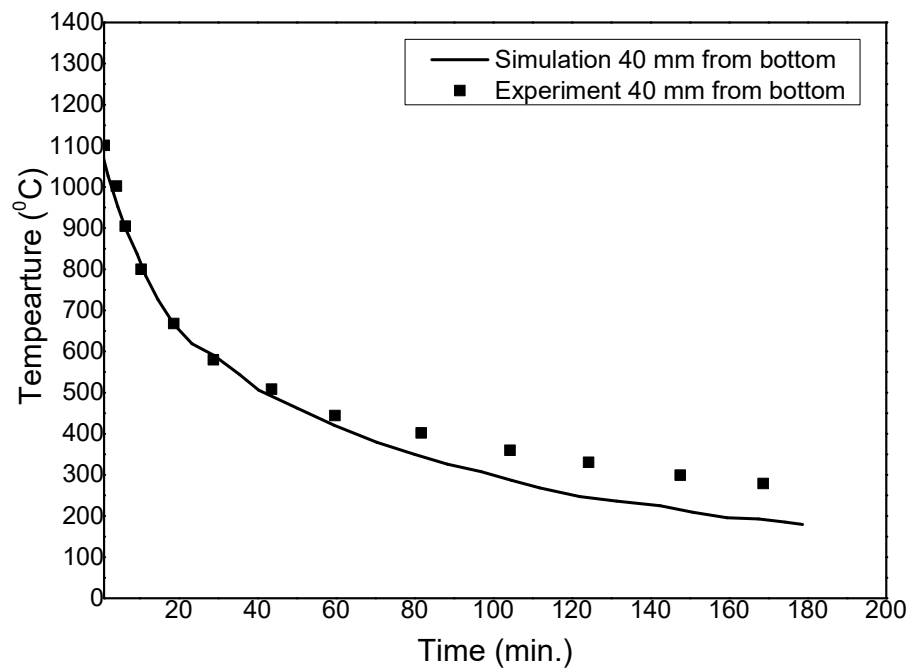


Figure 8.5: Comparison of melt temperature at 40 mm radial location

Figure 8.6 and figure 8.7 show the comparison of CFD prediction and experimental result of inner and outer surface temperature variation of test vessel. It is observed that the predicted and experimental results are in very good agreement.

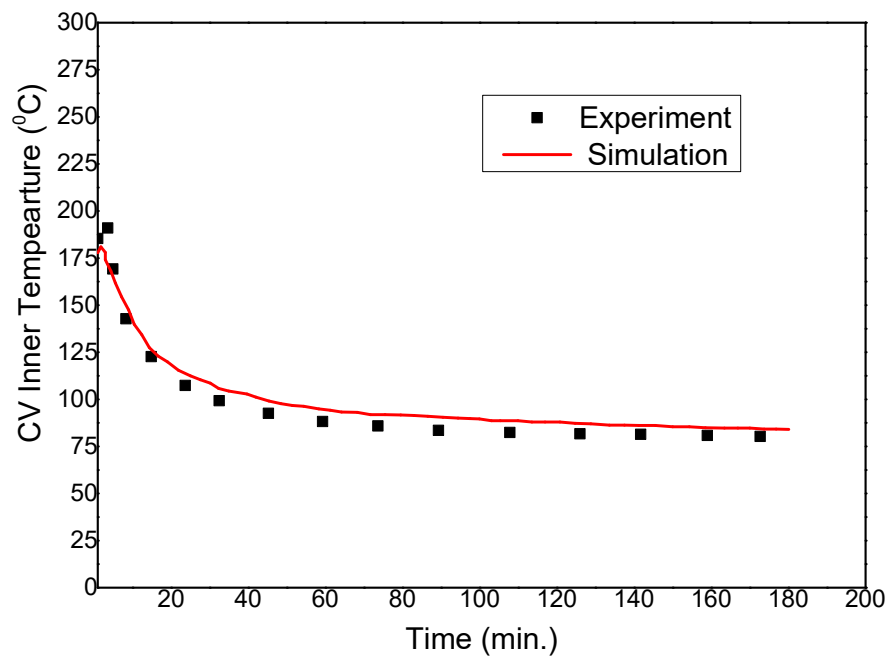


Figure 8.6: Comparison of CV Inner surface temperature

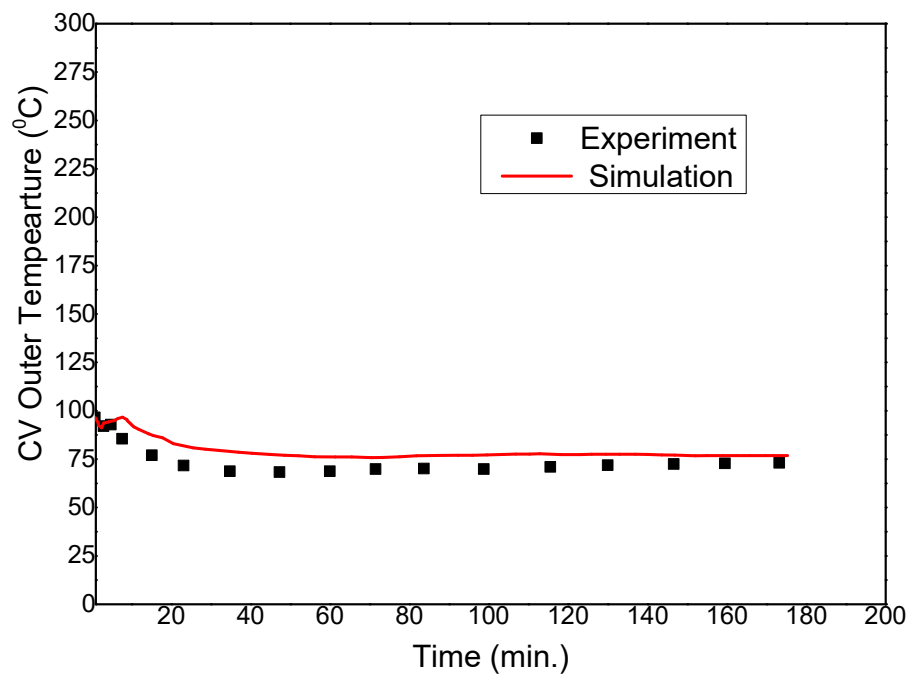
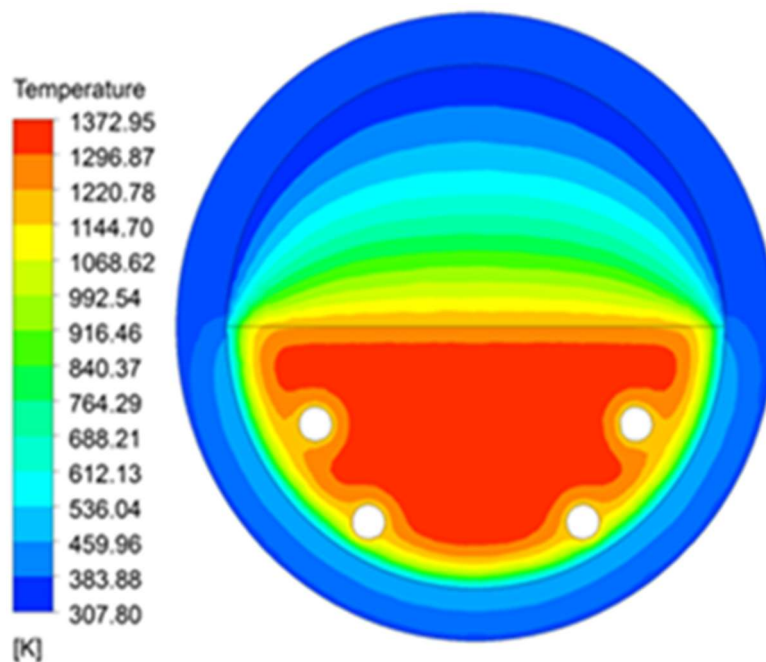


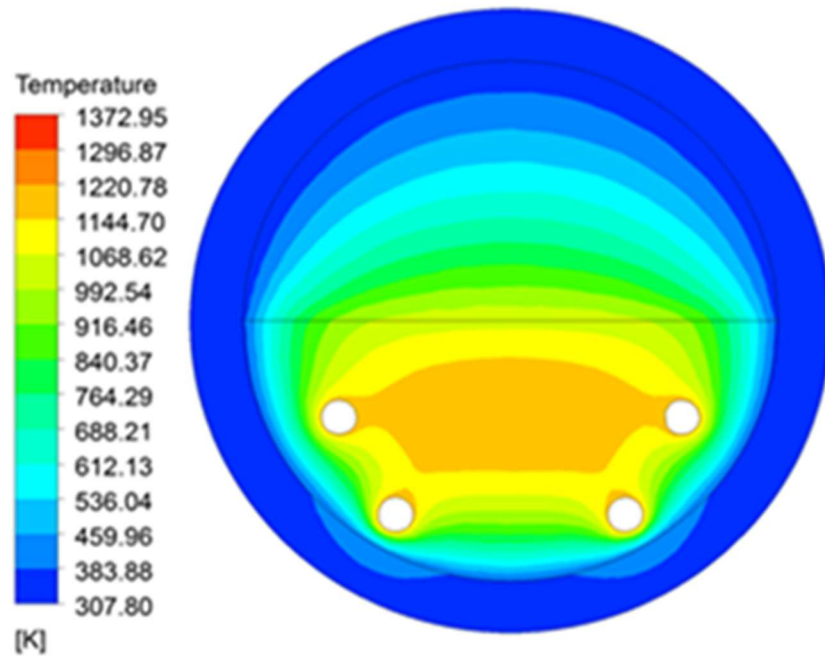
Figure 8.7: Comparison of CV Outer surface temperature

8.5.2 With decay heat

Figure 8.8 shows the temperature profile of simulation for scaled model at 2 min and 30 min time intervals respectively. These contours give insight of melt cooling inside the test vessel at different time scale. Figure 8.9 shows the comparison of CFD predicated and experimental melt temperature distribution at 40 mm radial location from the bottom of vessel. In experiment, glass melt was poured at temperature 1200 °C (1473 K) and maximum melt temperature recorded was 1100 °C (1373 K). The rate of melt cooling near wall was higher as compared to centre of melt. These trends are brilliantly captured by simulation as shown in figure 8.9.



(a)



(b)

Figure 8.8: Melt temperature contour profile with decay heat at (a) 2 minute (b) 30 minute

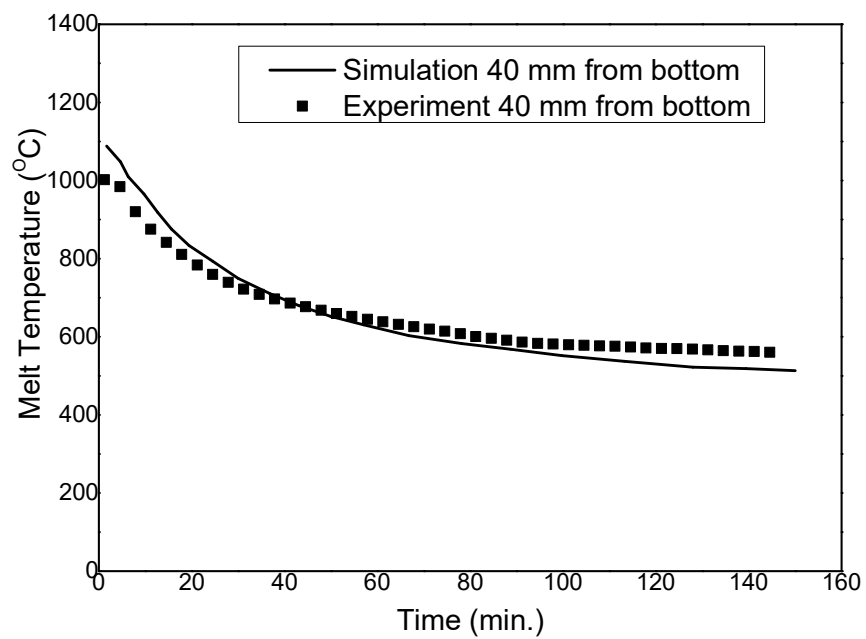


Figure 8.9: Comparison of melt temperature with decay heat at 40 mm radial location

Figure 8.10 and figure 8.11 shows the comparison of CFD prediction and experimental result of the inner and outer surface temperature variation of test vessel. It is observed that the predicted and experimental results are in very good agreement and the CFD model has been successfully benchmarked against experimental data.

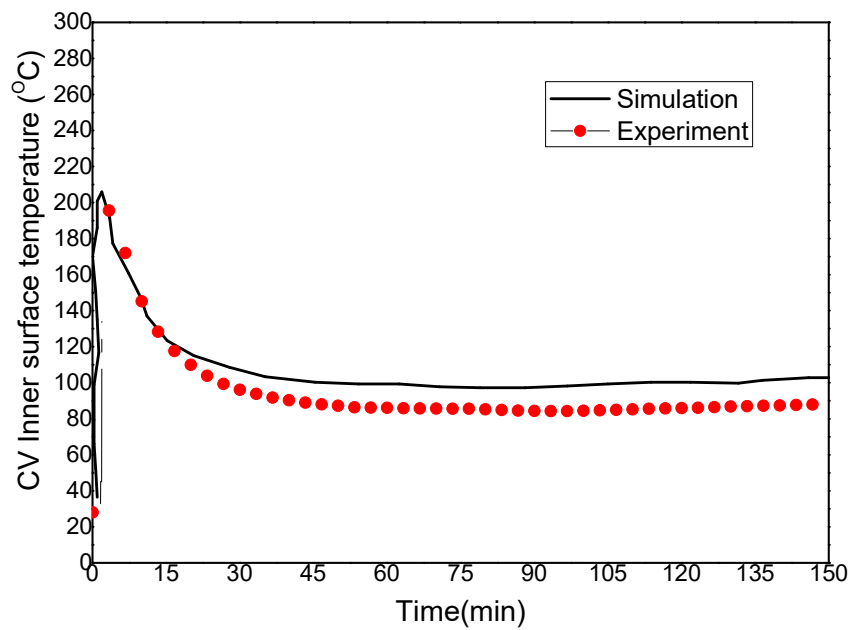


Figure 8.10: Comparison of CV Inner surface temperature with decay heat

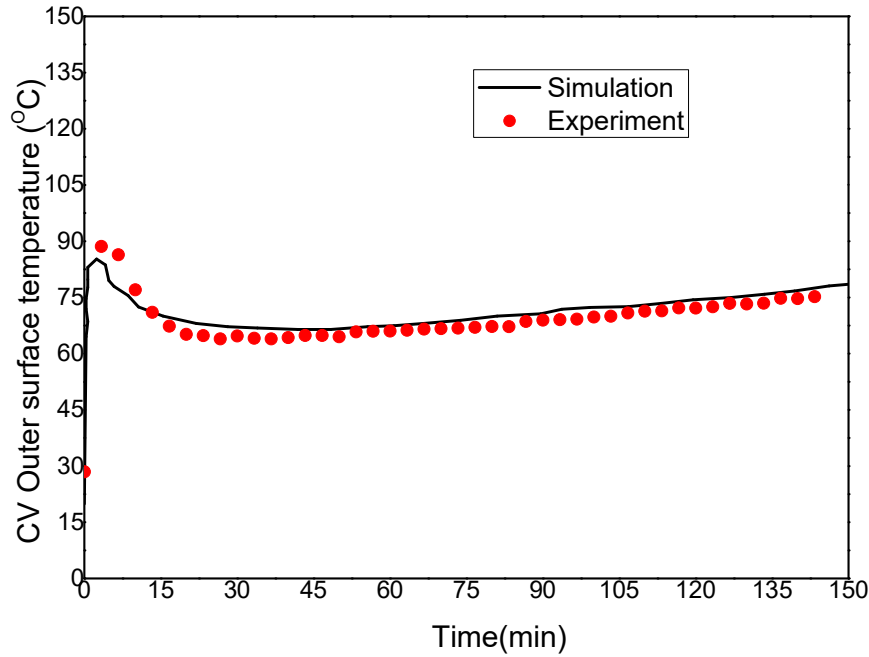


Figure 8.11: Comparison of CV Outer surface temperature with decay heat

8.6 CFD model extended to prototypic condition

For prototype condition, calandria vessel was modelled in 2-D. The dimension of prototype CV had diameter 7.8 meters and length was 6 meters. The wall thickness of main vessel was 32 mm and was made of SS 304L. Boundary and initial conditions for analysis of the prototype were considered to be same as that of scaled facility. Heat transfer from the molten pool to the vault water took place by conduction through CV wall whereas from the upper surface of the molten pool, heat was exchanged with air/steam by natural convection. It also exchanged heat with vessel upper inner wall by thermal radiation. Here again vault water was not simulated and appropriate convective heat transfer coefficient correlations, which were developed in chapter 6 was applied on outer surface of CV. Similar grid pattern was used with higher grid size as that in the experiment benchmark shown in figure 8.12.

The starting point of CFD simulation was when the moderator had already boiled off and the melt pool was at liquidus temperature (≈ 2950 K (2677 °C)) with decay heat generation of 1 MW/m³ and being indirectly cooled by calandria vault water which was at 60 °C. The

phenomena considered were natural convection in melt pool, melting and solidification in melt, conduction in vessel and natural convection on outer side of vessel. The thermo-physical material properties were considered to be temperature dependent.

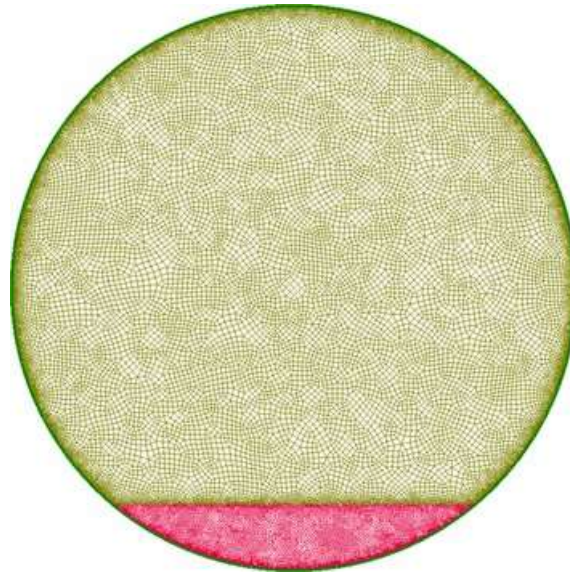
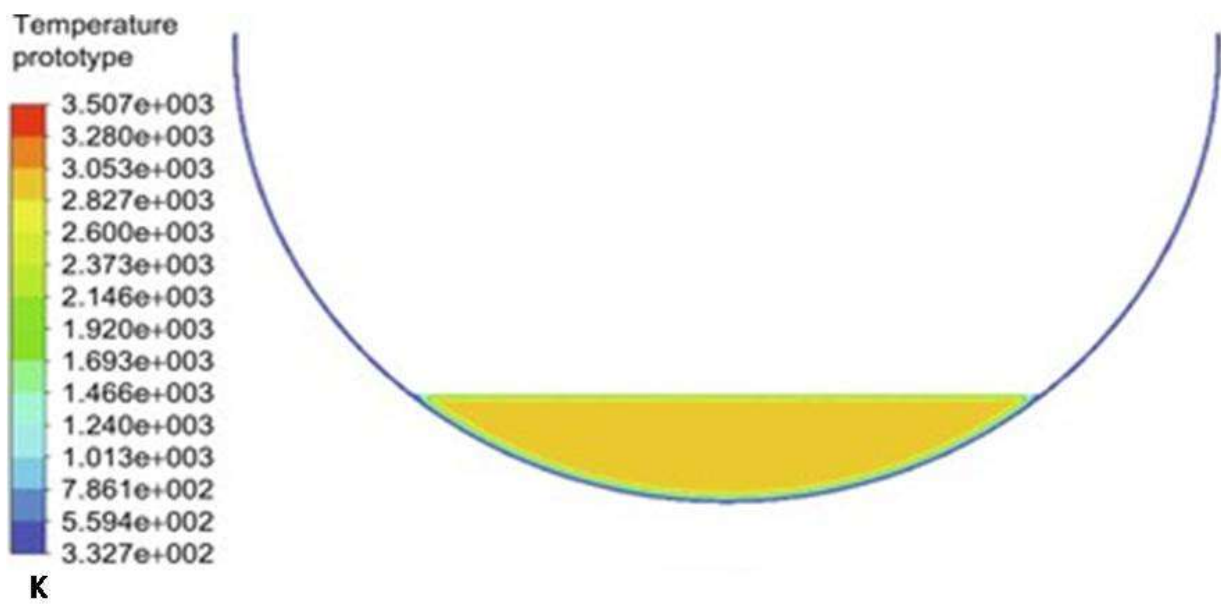


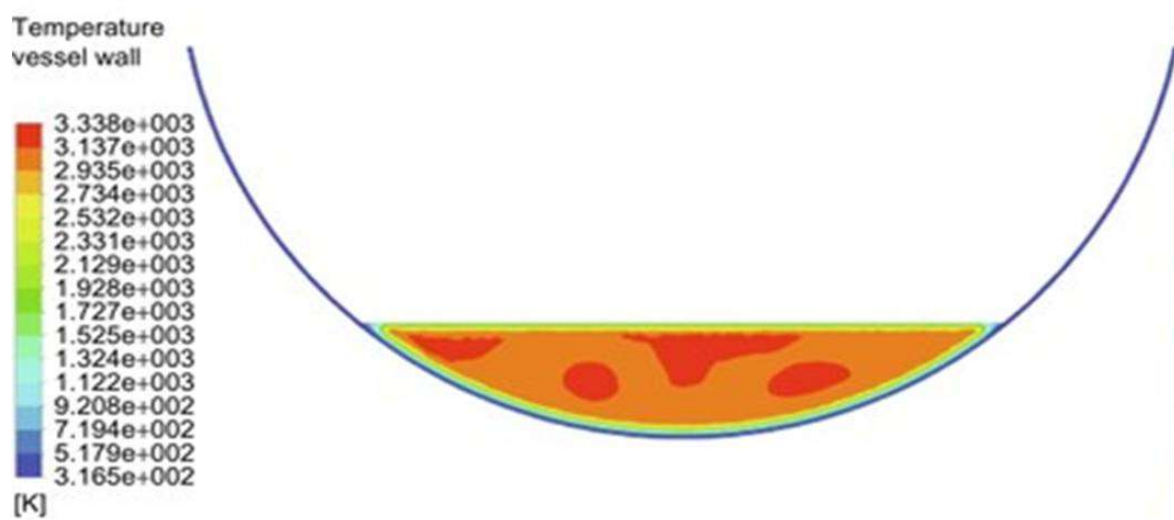
Figure 8.12: Mesh pattern of the prototypic CV geometry

8.7 Prediction of CFD model for prototypic condition

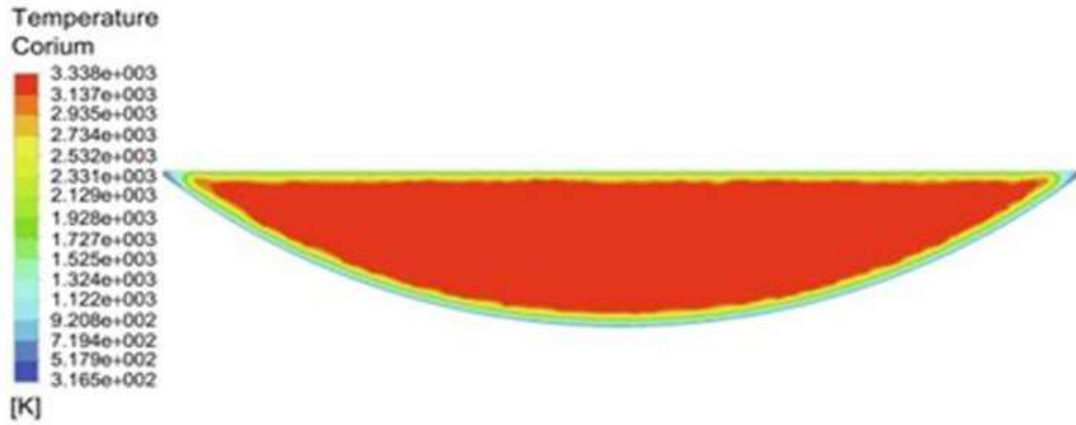
Figure 8.13 (a)-(d) show the contours of corium temperature inside CV at different time scale up to 3 hours. The corium was initially at 2950 K (2677 °C), which was cooled by calandria vault water. As CFD analysis progresses, the temperature of corium increases due to decay heat forming melt pool at centre and convection inside it. It was observed that, the vessel was completely surrounded by the solid crust which was at low temperature (average crust temperature was ~ 1873 K (1600 °C)). Because of crust formation, CV inner surface was insulated from high temperature corium. The thermal conductivity of the solid crust was very poor which resulted in reduction of overall heat transfer coefficient significantly. Therefore, although the corium pool temperature near the centre was very high (close to 3500 K (3227 °C)) after roughly 3 hours, still bulk of the water in the calandria vault had not started boiling.



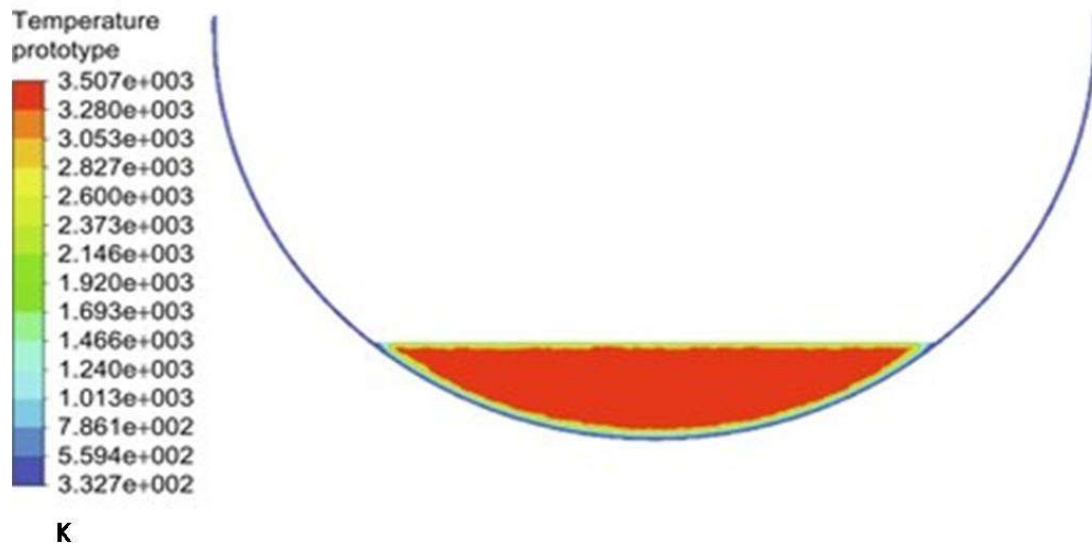
(a)



(b)



(c)



(d)

Figure 8.13 Temperature contours in the corium (a) 1800 s (b) 3600 s (c) 7200 s (d) 10800 s

Figure 8.14 shows the CV inner and outer surface temperature variation with time. After 1.5 hours of analysis, the partial nucleate boiling was observed on the outer surface of CV and this was evident as CV outer surface temperature started fluctuating with time.

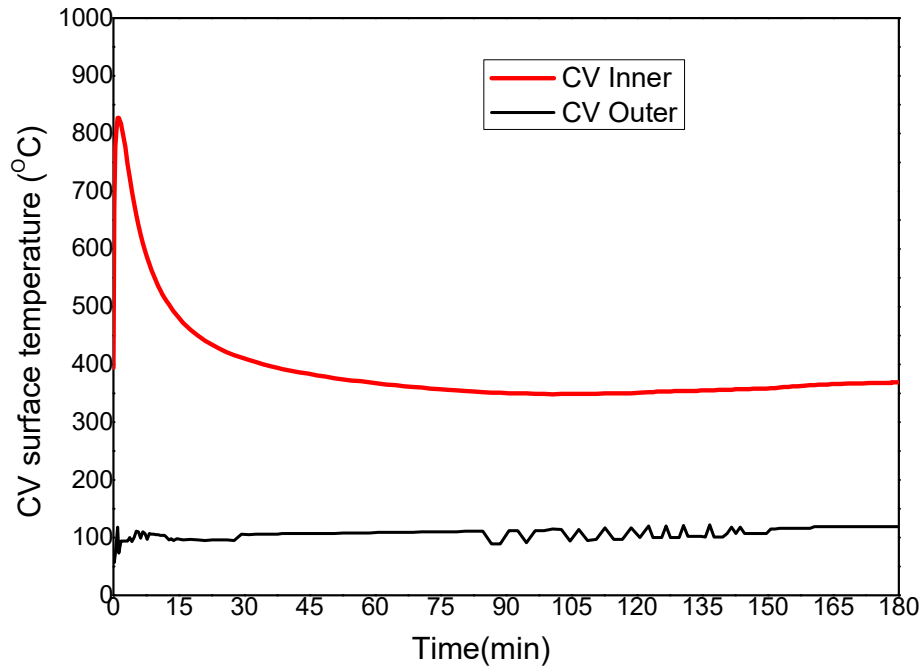


Figure 8.14: Temperature variation of CV inner and CV outer wall at the bottom

After 2.5 hours, vault water reached to water saturation temperature and after that the temperature became steady. The inner surface temperature of CV dropped sharply due to crust formation and after that it became somewhat steady. After 3 hours, the vessel outer and inner surface temperature remained close to 120 °C (393 K) and around 400 °C (673 K) respectively.

Figure 8.15 shows detail temperature profile of calandria vessel and molten pool after 3 hours. The temperature profile had been plotted along the vertical direction from the CV outer surface to the top of the crust edge between air/steam and pool at zero-degree location.

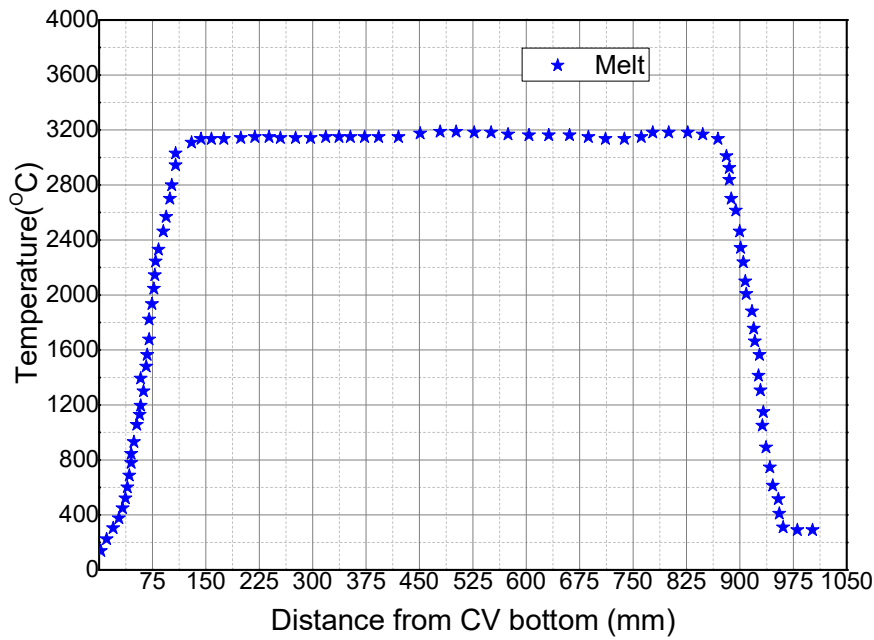


Figure 8.15: Temperature of corium in vertical direction from bottom of calandria outer wall

From figure, it is observed that the temperature increased from nearly 120 °C (400 K) at CV outer wall to 400°C (673 K) on CV inner wall. The temperature is continuously increasing to 1600 °C which is considered as crust region. The observed thickness of crust is 70 mm. The temperature further keeps on increasing to maximum at the pool centre which is close to 3227 °C (3500 K). Figure 8.16 shows the CV outer wall surface heat flux variation with time. The predicted peak wall heat flux is 190 kW/m² which is lower than the experimentally measured value 210 kW/m² (chapter 5, section 5.7). This confirms that CV temperature remain low during severe accident conditions and has sufficient margin against CHF.

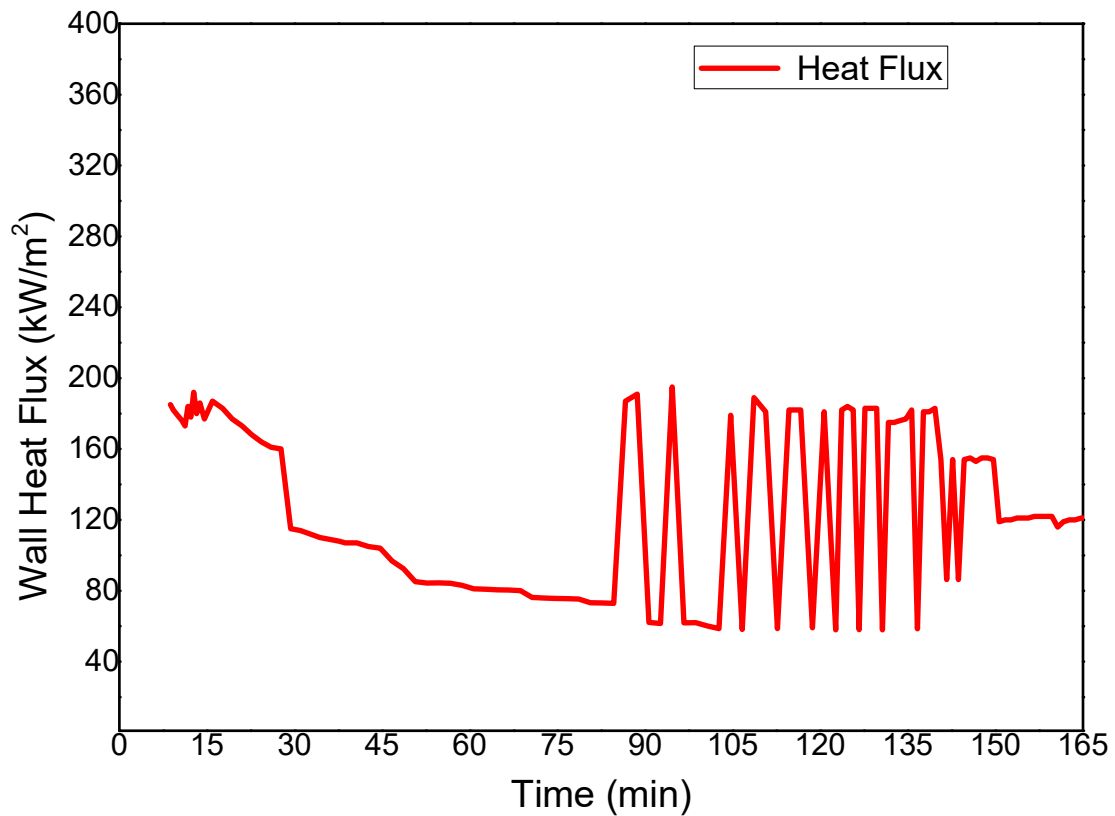


Figure 8.16: Heat flux on the CV outer surface

8.8 Applicability of experiment result to prototype

Even though IVR experiments are conducted in small scale, with different melt simulant material and different initial melt temperature, the heat transfer behaviours during severe accident are brilliantly captured in these experiments. These experiments provide the insight and better understanding of complex heat transfer phenomena that occurs inside the melt. Based on these understanding, CFD analyses were modelled and following results are obtained.

Table 8.1: Comparison in stored heat dominated regime

| | Experiment | CFD Prototype |
|--|---|--------------------------|
| Melt | $\text{ZrO}_2 + \text{CeO}_2 + \text{Fe} + \text{Al}_2\text{O}_3$ | Corium |
| Initial melt temperature | More than 2500 °C | 2677 °C |
| Decay heat | No decay heat | 1 MW/m ³ |
| CV outer temperature (after 60 min) | 98.7 °C | 105.6 °C |
| Crust thickness | 50 mm | 70 mm |
| Incident Heat flux Range | 100-150 kW/m ² | 90-190 kW/m ² |

Table 8.2: Comparison in decay heat dominated regime

| | Experiment | CFD |
|--------------------------|----------------------------|-------------------------|
| Melt | Glass | Corium |
| Initial melt temperature | 1095 °C | 1100 °C |
| Decay heat | 0.7 MW/m ³ | 1.0 MW/m ³ |
| CV outer temperature | 83 °C | 88 °C |
| Crust thickness | 40 mm | 45 mm |
| Heat flux | 75- 83.5 kW/m ² | 85-92 kW/m ² |

From the above Tables, it is clear that experiments provide almost same results as that of CFD analysis of prototype conditions. On comparison (Table 8.1) with store heat dominate experiment (~2500 °C) (Chapter 4) and CFD prototype (≈ 2677 °C) analysis result, CV outer temperature, crust thickness and incident heat flux are in the same range and in good degree

of matching with the experiment. It also validates the heat transfer correlations as it applies on different melt volume set up and different initial melt temperature.

Thus, the experiments at reduced scales with simulant materials can not only be used for code validation, but provide valuable aspects with regard to vessel surface temperature and incident heat flux which are critical in assessment of IVR in PHWRs. The slight variation in CFD and experimental results are due to the variation of temperature dependent material properties and unknown properties in mushy zone (i.e. between solidus and liquidus temperature).

8.9 Closure

2D model numerical studies were carried out with CFD and results showed quite good agreement with experiments. In case of decay heat, it is observed that the predicted value of melt maximum temperature and CV inner surface temperature are 1100 °C (exp. ~1095 °C) and 210 °C (exp. ~ 207 °C) respectively which are in very good agreement with experimental result. The model was extended to prototypic condition for predicting the vessel behaviour during severe accident. CFD model has confirmed that vessel outer temperature remains low during severe accident condition which has similar observation with experiments. The heat flux on the outer surface of CV predicted around 190 kW/m² which is close to experimental measured CHF value of 210 kW/m².

Chapter 9

Conclusions and recommendation for future works

9.1 Conclusions

In PHWRs, during the case of severe accident, leading to melting of core and subsequent relocation of molten core debris at the bottom of CV, there is a concern on coolability of the molten core debris by vault water. This is because, if the molten corium breaches the CV and enters the calandria vault, large amount of hydrogen and other gases will be generated due to molten core concrete interaction (MCCI), which will pressurise the containment and may lead to early containment failure. Hence, In-vessel retention (IVR) of corium by the CV is the only option in PHWRs for mitigation of core melt down accident. In this approach, the molten corium is retained inside the CV by continuously removing the stored heat and decay heat through the outer surface of the vessel by cooling using vault water and without hampering the integrity of the vessel. Therefore, for successful IVR, the integrity of CV is of utmost importance. However, there are several scientific and technological issues as listed below to prove the success of IVR in PHWRs:

- a) The heat transfer phenomena inside the CV which contains molten corium is very complex as it involves multiple modes of heat transfer (conduction through crust and CV, natural convection inside the melt and radiation heat transfer from top of crust to the vessel) associated with phase change (melting and solidification). Formation of crust and its growth needs to be understood. Effect of decay heat inside the corium on heat transfer and crust formation rate is never established.
- b) The heat transfer phenomena outside the curved CV which is surrounded by cold vault water is also complex as heat transfer behaviours for regime single phase natural convection to nucleate boiling or film boiling are not known.

- c) The phenomenology of Critical Heat Flux (CHF) on outer surface of CV under severe accident condition is very complex due to downward facing heating, boiling natural convection and geometry of very large diameter and length. The CHF for PHWR CV geometry is not established.
- d) CV is stepped vessel and due to this large number of weld joints are present. Apprehensions are raised regarding the CV integrity against sudden high temperature corium thermal load on welded stepped joint. Hence, CV integrity needs to be established against above load for successful IVR.
- e) The scaling effect of melt volume and melt material on heat transfer behaviour are never known, which needs to be understood.

To address the above issues, several experiments have been conducted in this research work. Scaling philosophy for heat transfer from molten corium to the vault water was developed for both stored heat and decay heat dominated regimes. The molten corium cooling behavior by the vault water, the crust formation and growth rate, melt pool temperatures in radial and axial directions, CV inner and outer vessel surface temperature at different angular positions were experimentally measured up to melt temperatures of 2500 °C. The imposed heat flux on the vessel wall by the molten corium and the local heat transfer coefficient on the outer side of the CV wall were estimated from the measurements. Empirical models for convective heat transfer in single phase and boiling condition in the outer curved vessel of CV were developed. Critical heat flux which limits the maximum heat flux that can be removed from molten corium to vault water was experimentally measured. CFD models were developed for the heat transfer from corium debris to vault water and were benchmarked against the present experimental data. The models were applied to 700 MWe PHWR and capability of vault water to cool and retain the molten corium inside the CV of PHWR was evaluated.

The following are the major insights obtained from this research work:

- I. As soon as the melt comes in contact with the cold CV surface, crust formation occurs. Due to the crust formation around the melt, the vessel temperatures remained very low although the melt temperature was very high; decay heat was safely removed as long as water is present in the vault. The low CV temperatures ensure no stress in the vessel which help in maintaining its structural integrity.
- II. Even though the melt is at very high temperature inside the vessel ($> 2500\text{ }^{\circ}\text{C}$), the CV outer surface temperature remained near saturation temperature of the water due to crust formation, CV integrity was maintained and no deformation was observed.
- III. CHF was found to be strongly dependent on temperature of water up to $56\text{ }^{\circ}\text{C}$ only and beyond that temperature, it does not vary significantly. From CHF value ($\sim 210\text{ kW/m}^2$) and the imposed heat flux ($\sim 110\text{ kW/m}^2$) on the CV due to corium, it is evident that sufficient thermal margin is available in current PHWRs for IVR.
- IV. Comprehensive insights of main mode of heat transfer from melt to vault water in stored heat dominated regime as well as decay heat dominated regime were obtained. The outer CV heat transfer coefficient was found to be of the order $\sim 3000\text{ W/m}^2\text{ K}$ and $\sim 11000\text{ W/m}^2\text{ K}$ in single phase and boiling regimes respectively. An empirical model has been developed for the local heat transfer coefficient on CV wall outer surface for both single phase and boiling two phase conditions.
- V. The decay heat was found to have strong effect on crust formation and growth which had strong influence on heat transfer from melt to vault water. Effect of decay heat on crust growth was also understood. Results showed that the experiments conducted with different melt volumes and different melt material produced similar results on the CV outer surface temperature.

- VI. CFD model was benchmarked with experimental data which had given lot of confidence and insights regarding analysis of in-vessel retention. The analysis was extended to prototypic condition and it was now evident that CV wall temperature remains very low during severe accident conditions and heat flux was well below 210 kW/m^2 .

9.2 Future recommendation

9.2.1 Conducting experiment with prototypic material and temperature

The above experiments were conducted with near prototypic material in stored heat dominated regime and simulant material in decay heat dominated regime. The properties of these materials can't be exactly same as PHWR corium. The important issue which is to be resolved is whether stratification occurs in PHWR corium and if yes, the resulting effect on coolability. This needs to be understood in future.

9.2.2 Chemical interaction of corium with CV at different higher temperature

The chemical interaction of PHWR corium with CV material at temperature up to 1400°C needs to be understood by conducting such experiments in future.

9.2.3 Heat transfer study of in vessel heating of debris inside the CV

The experiments which conducted here is much more severe than that occurs during accident progression in PHWR. In this research work we poured high temperature melt directly into the vessel. Whereas in PHWR the debris when not cooled, melt in-situ with centrally highly molten material at elevated temperature surrounded by relatively cooled solid debris. The heat transfer behaviour from this configuration to the vault water needs to be simulated in future.

Reference

1. World Population Prospects 2019-highlights, 2019, ST/ESA/SER.A/423, Department of Economic and Social Affairs, Population Division United Nations, New York.
2. Bhoi B. K., 2019, <https://www.thehindubusinessline.com/opinion/columns/making-the-5-trillion-target-possible/article28762276.ece>
3. <https://powermin.nic.in/en/content/power-sector-glance-all-india>.
4. <https://unfccc.int/news/india-submits-its-climate-action-plan-ahead-of-2015-paris-agreement>
5. World Nuclear Performance Report, 2019, World Nuclear Association, Report No. 2019/007, PP. 1-32.
6. Broughton, J.M., Kuan, P., Petti, D.A., 1989, A scenario of the Three Mile Island unit 2 accident. Nuclear Technology, Vol. 87, PP. 34-53.
7. International Nuclear Safety Advisory Group, 1986, Summary Report on the Post-accident Review Meeting on the Chernobyl Accident, INSAG-1, IAEA, Vienna, PP.1-135.
8. Fukushima Nuclear Accident Analysis Report, 2012, Tokyo Electric Power Company, Inc, PP.1-487.
9. IAEA-TECDOC-1594, 2008, Analysis of Severe Accidents in Pressurized Heavy Water Reactors, International Atomic Energy Agency, Vienna, Austria, PP.1-139.
10. Tuomisto H. and Theofanous T. G., 1994, A consistent approach to severe accident management, Nuclear Engineering and Design, Vol.148, PP.171-183.
11. Weimin Ma, Yidan Yuan and Sehgal B. R., 2016, In-Vessel Melt Retention of Pressurized Water Reactors: Historical Review and Future Research Needs, Engineering, Vol. 2, PP. 103–111.
12. Kymfiläinen O., Tuomisto H., Theofanous T.G., 1997, In-vessel retention of corium at the Loviisa plant, Nuclear Engineering and Design, Vol. 169, PP. 109-130.

13. Theofanous T.G., Liu C, Additon S., Angelini S, Kymäläinen O., Salmassi T.,1997, In-vessel coolability and retention of a core melt, Nuclear Engineering and Design, Vol. 169, PP. 1–48.
14. Dinh T.N., Tu J. P., Salmassi T., Theofanous T. G., Limits of coolability in the AP1000-related ULPU-2400 Configuration V facility, 2003, In: Proceedings of the 10th International Topical Meeting on Nuclear Reactor Thermal Hydraulics; Oct 5–9; Seoul, Republic of Korea, PP. 1-14.
15. Manfred Fischer, Sevostian V. Bechta, Vladimir V. Bezlepkin and Ryoichi Hamazaki, 2015, Core melt stabilization concepts for existing and future LWRs and associated R&D needs, NURETH-16, Chicago, IL, August 30-September 4, PP.7578-7593
16. Fischer M., Herbst O., Schmidt H., 2005, Demonstration of the heat removing capabilities of the EPR core catcher, Nuclear Engineering and Design, Vol. 235, PP. 1189–200.
17. Bezlepkin V. V., Kukhtevich I. V., Leont'ev Y. G., Svetlov S. V., 2004, The concept of overcoming severe accidents at nuclear power stations with VVER reactors, Thermal Engineering, Vol. 51, PP.115–23.
18. Park S. Y. and Ahn K. I., 2012, Comparative analysis of station blackout accident progression in typical PWR, BWR, and PHWR, Nuclear Engineering and Technology, Vol.44 (3), PP. 311-322.
19. Bajaj, S.S. and Gore, A.R., 2006, The Indian PHWR, Nuclear Engineering and Design, Vol. 236 (7–8), PP. 701–722.
20. Joshi J B, Nayak A K, Singhal M and Mukhopadhyay D, 2013, Core safety of Indian nuclear power plants (NPPs) under extreme conditions, Sadhana, Vol. 38, Part 5, PP. 945–970.

21. P.P. Kulkarni, S. V. Prasad, A. K. Nayak, and P. K. Vijayan, 2013, Thermal and structural analysis of calandria vessel of a PHWR during a severe accident, Nuclear Engineering and Technology, Vol.45 (4), PP. 469- 476.
22. Mathew, P. M., Nitheanandan, T., and Bushby, S. J., 2008, Severe Core Damage Accident Progression Within a CANDU 6 Calandria Vessel, ERMSAR Seminar, 3rd European Review Meeting on Severe Accident Research, Nessebar, Bulgaria, Sept. 23–25, PP. 1-15.
23. IAEA-TECDOC-1727, 2013, Benchmarking Severe Accident Computer Codes for Heavy Water Reactor Applications, International atomic energy agency, Vienna, Austria, PP. 1-311.
24. Esmaili H., Khatib-Rahbar M., 2004, Analysis of in-vessel retention and ex-vessel fuel coolant interaction for AP1000, Rockville: Energy Research, Inc., Report No.: NUREG/CR-6849, PP. 1-138.
25. Oh S. J. and Kim H. T., 2005, Effectiveness of external reactor vessel cooling (ERVC) strategy for APR1400 and issues of phenomenological uncertainties. In: Workshop Proceedings: Evaluation of Uncertainties in Relation to Severe Accidents and Level-2 Probabilistic Safety Analysis, Nov 7–9, Aix-en-Provence, France, PP. 568-600.
26. Cheng X., Yang Y. H., Ouyang Y., Miao H. X., 2009, Role of passive safety systems in Chinese nuclear power development, Science Technology Nuclear Installations, Vol. 2009, PP. 1-7.
27. Tang C.L., Kuang B., Liu P.F., Zhu C., Wang F., 2014, Preliminary analysis of channel flow characteristics in the passive IVR-ERVC experimental facility, Nuclear Techniques, Chinese, Vol. 37(12), PP. 120604.

28. Li Y. B., Tong L.L., Cao X. W., Guo D. Q., 2015, In-vessel retention coolability evaluation for Chinese improved 1000 MWe PWR, *Annals of Nuclear Energy*, Vol. 76, PP. 343–349.
29. Asmolov V. et al., 2000, RASPLAV Application Report, OECD RASPLAV Seminar, Munich (Germany), PP. 1-37.
30. Sehgal B.R. et al., 2003, Assessment of reactor vessel integrity (ARVI), *Nuclear Engineering and Design*, Vol. 221, PP. 23-53.
31. Sehgal, B.R., Nayak, A.K., et al., 2005, Phenomenological Studies on Melt-Structure-Water Interactions (MSWI) during Postulated Severe Accidents: Year 2004 Activity, APRI 5 Report, PP. 1-39.
32. Kang K. H., Park R.J., Koo K. M., Kim S. B. and Kim H.D., 2006, Experimental investigations on In-Vessel Corium Retention through Inherent Gap Cooling Mechanisms, *Journal of Nuclear Science and Technology*, Vol. 43 (12), PP. 1490–1500.
33. Yang J., Cheung F. B., Rempe J. L., Suh K. Y. and Kim S. B., 2006, Critical heat flux for downward-facing boiling on a coated hemispherical vessel surrounded by an insulation structure, *Nuclear Engineering and Technology*, Vol.38 (2), PP. 139-146.
34. Gaus-Liu, X., Miassoedov A., Cron, T., Wenz, T., 2010, The coolability of melt pool in PWR lower head results of live experiments, *J. Energy Power Eng.* 4 (3), PP. 15–21.
35. Zhang Y.P., Zhang L.T., Zhou Y.K., Tian W.X., Qiu S.Z., Su G.H., Zhao B., Yuan Y.D., Ma R.B., 2016, Natural convection heat transfer test for in-vessel retention at prototypic Rayleigh numbers Results of COPRA experiments, *Progress in Nuclear Energy*, Vol. 86, PP. 80-86.
36. Ihn Namgung and Hyun-Jin Lee, 2015, Computational Fluid Dynamic Analysis Modelling of IVR-ERVC of APR1400 Reactor, *International Journal of Engineering Research and Technology*, Vol. 4 (10), PP. 450-458.

37. Rae-Joon Park, Kwang-Soon Ha, Hwan-Yeol Kim, 2016, Detailed evaluation of natural circulation mass flow rate in the annular gap between the outer reactor vessel wall and insulation under IVR-ERVC, *Annals of Nuclear Energy*, Vol. 89, PP. 50-55.
38. Fei-Jan Tsai, Min Lee and Hsiang Chun Liu, 2017, Simulation of the in-vessel retention device heat-removal capability of AP-1000 during a core meltdown accident, *Annals of Nuclear Energy*, Vol. 99, PP. 455–463.
39. Mindaugas Valinčius, Tadas Kaliatka, Algirdas Kaliatka, and Eugenijus Ušpuras, 2018, Modelling of Severe Accident and In-Vessel Melt Retention Possibilities in BWR Type Reactor, *Science and Technology of Nuclear Installations*, Vol. 2018, PP. 1-14.
40. Cheung, F B, Haddad, K H, and Liu, Y C, 1997, Critical heat flux (CHF) phenomenon on a downward facing curved surface, *USNRC*, PP. 1-107. Web. doi:10.2172/491560.
41. Robert David, 2019, Calculation of Heat Fluxes Exiting a CANDU Calandria During In-Vessel Retention, *Nuclear Technology*, Vol. 205, PP. 1488-1494.
42. Naceur A., Marleau G., 2019, CANDU-6 operation simulations using accident tolerant cladding candidates, *Annals of Nuclear Energy*, Vol. 124, PP. 472–489.
43. Sang Mo An, Jin Ho Song, Jong-Yun Kim, Hwan Yeol Kim, Masanori Naitoh, 2016, Experimental investigation on molten pool representing corium composition at Fukushima Daiichi nuclear power plant, *Journal of Nuclear Materials*, Vol. 478, PP. 164-171.
44. Meneley D. A., Blahnik C., Rogers J. T., Snell V. G. and Nijhawan S., 1995, Coolability of Severely Degraded CANDU Cores, Atomic Energy of Canada Ltd., AECL-11110 reports, PP.1- 17
45. Skobe T. and Leskovar M., 2019, Influence of corium composition on ex-vessel steam explosion, *Annals of Nuclear Energy*, Vol. 133, PP. 359–377.

46. Park R., Kang K., Hong S., Kim S., And Song J., 2012, Corium behaviour in the lower plenum of the reactor vessel under IVR-ERVC condition: Technical issues, Nuclear Engineering and Technology, vol.44 no.3.
47. Tsurikov D., 2007, MASCA2 Project: major activities and results. In: Material Scaling Seminar; Oct 11–12, Cadarache, France; 2007, PP. 1.
48. Asmolov V., Tsurikov D., 2004, Major activities and results. In: Material Scaling Seminar, Jun 10–11; Aix-en-Provence, France, PP. 1-22.
49. Sugilal, G., Sengar, P.B., 2008, Cold Crucible induction melting technology for vitrification of high-level waste: development and status in India, In: WM 2008 Conference, Phoenix, AZ, US, PP 1-12.
50. Holman, J.P., 2008. Heat Transfer, 9th edition, Tata McGraw Hill.
51. Chen J. and Young B., 2006, Stress–strain curves for stainless steel at elevated temperatures, Engineering Structures, Vol. 28, PP. 229–239.
52. Theofanous T. G., Liu C., Additon S., Angelini S., Kymalainen O., Salmassi T., 1996. In-Vessel Coolability and Retention of a core melt, Department of Energy, USA, DOE/ID-10460, Vol.-1, PP. 1-441.
53. Rouge S., 1997, SULTAN test facility for large-scale vessel cool ability in natural convection at low pressure, Nuclear Engineering and Design, Vol.169(1-3), PP. 185-195.
54. Jeong Y.H., Chang S.H., Baek W.P., 2005, Critical heat flux experiments on the reactor vessel wall using 2-D slice test section, Nuclear Technology, Vol. 152 (2), PP.162–169.
55. Cheung F.B., Haddad K.H., 1997, A hydrodynamic critical heat flux model for saturated pool boiling on a downward facing curved heating surface, International Journal Heat Mass Transfer, Vol. 40 (6), PP. 1291–1302.

56. Cheung F.B., Haddad K.H., Liu Y.C., 1997, Critical Heat Flux (CHF) Phenomenon on the downward facing curved surface, USNRC, NUREG/CR-6507 PSU/ME-7321, PP. 1-172.
57. Brusstar Jr M.J., Merte H., Keller R.B., 1997, Effects of heater surface orientation on the critical heat flux – I: an experimental evaluation of models for sub-cooled pool boiling, *International Journal of Heat Mass Transfer*, Vol. 40 (17), PP. 4007–4019.
58. Yang S.H., Baek W.P., Chang S.H., 1997, Pool-boiling critical heat flux of water on small plates: effects of surface orientation and size, *International Communications Heat Mass Transfer*, Vol. 24 (8), PP. 1093–1102.
59. Mei Y., Shao Y., Gong S., Zhu Y., Gu H., 2018, Effects of surface orientation and heater material on heat transfer coefficient and critical heat flux of nucleate boiling, *International Journal of Heat and Mass Transfer*, Vol. 121, PP. 632–640.
60. Juno Lee, Soon Heung Chang, 2012, An experimental study on CHF in pool boiling system with SA508 test heater under atmospheric pressure, *Nuclear Engineering and Design*, Vol.250, PP. 720–724
61. Jun S., Kim J., You S.M., 2016, Effect of heater orientation on pool boiling heat transfer from sintered copper microporous coating in saturated water, *International Journal of Heat Mass Transfer*, Vol. 103, PP. 277–284.
62. ASTM A240 / A240M – 19,2019, Standard Specification for Chromium and Chromium-Nickel Stainless Steel Plate, Sheet, and Strip for Pressure Vessels and for General Applications, ASTM international, PP. 1-12.
63. Kam D. H., Choi Y. J., Jeong Y. H., 2018, Critical heat flux on downward-facing carbon steel flat plates under atmospheric condition, *Experimental Thermal and Fluid Science*, Vol. 90, PP. 22–27.

64. Kam D. H., Park H. M., Choi Y. J. and Jeong Y. H., 2015, CHF measurement for downward facing SUS 304 and carbon steel plates under atmospheric and pool boiling conditions, NURETH-16, Chicago, IL, August 30-September 4, PP. 1.
65. Asfia F.J. and Dhir V.K., 1996, An experimental study of Natural Convection in a volumetrically heated spherical pool bounded on top with a rigid wall, Nuclear Engineering and Design, Vol. 163, PP. 333-348.
66. Shiina Y., Fujimura K., Akino N. and Kunugi T., 1988, Journal of Nuclear Science and Technology, Vol. 25 (3), PP. 254- 262.
67. Kim J. H., Kang K. H., Park R. J., Kim S. B., Kim H. D., 1999, Experimental Study on Inherent In-Vessel Cooling Mechanism during a Severe Accident, 7thInternational Conference on Nuclear Engineering, Tokyo, Japan, April 19-23, ICONE-7085, PP. 1-11.
68. Park H. K., Kim S. H., Chung B. J., 2017, Natural convection of melted core at the bottom of nuclear reactor vessel in a severe accident. International Journal Energy Research, PP.1-11.
69. Theofanous, T.G., Maguire, M., Angelini, S., Salmassi, T., 1997, The first results from the ACOPO experiment, Nuclear Engineering Design, Vol. 169, PP. 49-57.
70. Theofanous T. G., Liu C., Additon S., Angelini S., Kymalainen O., Salmassi T., 1996, In-vessel coolability and retention of a core melt, Advanced Reactor Severe Accident Program, Department of Energy, USA, DOE/ID-10460, Vol. 1, PP. D1- D34.
71. Saito T., Ishiguro R., Fujishima Y., Natural convection heat transfer around a horizontal cylinder (effect of a horizontal plate placed above the cylinder, in: Sixth National Heat Transfer Symposium of Japan (in Japanese), PP. 61–64.
72. Koizumi H., Hosokawa I., 1996, Chaotic behaviour and heat transfer performance of natural convection around a hot horizontal cylinder affected by a flat ceiling, International J. Heat Mass Transfer, Vol. 39, PP. 1081–1091.

73. Correa M., Parra R., Vidal A., Rodriguez J., Aguilera M. E., Gonzalez D., 2005, Natural convection around a horizontal cylinder near an adiabatic cover wall, in: Proceeding of Fourth ICCHMT, May 17–20, France, PP. 336.
74. Verma P. K., Parimal P. P., Pandey P., Prasad S. V., Nayak A. K., 2021, Critical Heat Flux on Curved Calandria Vessel of Indian PHWRs During Severe Accident Condition, Journal of Heat Transfer, Vol. 143, PP. 022101-1 -022101-9.

Appendix -1: Uncertainties in measurements

A 1.1 Temperature measurement in the range of ambient to 1200°C:

Temperature measurement was carried out with Inconel-600 sheathed ungrounded K type 1 mm thermocouples. The details of thermocouples, error and calibration are given in the following table.

Table A 1: K Type Temperature sensor details

| | |
|--|---|
| Type | K, ungrounded |
| Sheath | 1 mm OD |
| Insulation | MgO |
| Response time | 175 ms |
| Calibration | With master RTD PT-100 with error 0.006 – 0.15 °C |
| Accuracy of the measurement | 0.75 % of the measurement value up to 400°C and 1 % up to 1300 °C |
| 95 % Precision value | ± 1.04 °C |
| Total uncertainty in 95 % confidence measurement | $\pm (0.0075 \cdot T + 1.04)$ °C $T < 400$ $\pm (0.01 \cdot T + 1.04)$ °C $T \geq 400$ |

As per the above table, the error obtained in the range of ambient to 1200° C is given in the table below.

Table A 2: K Type Sensor Temperature Error

| Temperature (°C) | Error (°C) |
|-------------------------|-------------------|
| 30 | ±1.27 |
| 100 | ±1.79 |
| 200 | ±2.54 |
| 300 | ±3.29 |
| 400 | ±4.04 |
| 500 | ±6.04 |
| 600 | ±7.04 |
| 700 | ±8.04 |
| 800 | ±9.04 |
| 900 | ±10.04 |
| 1000 | ±11.04 |
| 1100 | ±12.04 |
| 1200 | ±13.04 |

A 1.2 Temperature measurement in the range of ambient to 2300°C:

Temperature measurement was carried out with Molybdenum sheath sheathed ungrounded C type 1 mm thermocouples. The details of thermocouples, error and calibration are given in the following table.

Table A 3: C Type Temperature sensor details

| | |
|--|---|
| Type | C, ungrounded |
| Sheath | 1 mm OD |
| Insulation | MgO |
| Response time | 175 ms |
| Calibration | With master RTD PT-100 with error 0.006 – 0.15 °C |
| Accuracy of the measurement | 0.75 % of the measurement value up to 400°C and 1 % up to 2320 °C |
| 95 % Precision value | ± 1.06 °C |
| Total uncertainty in 95 % confidence measurement | $\pm (0.0075 \cdot T + 1.06)$ °C $T < 400$ $\pm (0.01 \cdot T + 1.06)$ °C $T \geq 400$ |

As per the above table, the error obtained in the range of 1200° C to 2300 °C are given in the table below.

3Table A 4: C Type Sensor Temperature Error

| Temperature (°C) | Error (°C) |
|------------------|------------|
| 1200 | ±13.06 |
| 1300 | ±14.06 |
| 1400 | ±15.06 |
| 1500 | ±16.06 |
| 1600 | ±17.06 |
| 1700 | ±18.06 |
| 1800 | ±19.06 |
| 1900 | ±20.06 |
| 2000 | ±21.06 |
| 2100 | ±22.06 |
| 2200 | ±23.06 |
| 2300 | ±24.06 |

A1.3 Differential pressure measurement for level

Level measurement is done with the Differential pressure transducer

Table A 5: Differential pressure sensor details

| | |
|-----------------------------|---|
| Type | Yokogawa make model EJA 110A |
| Range | –100 to 100 mbar |
| Time constant | 0.3 s |
| Calibration | Druck DPI 605 pressure calibrator with accuracy of 0.03 % |
| Accuracy of the measurement | 0.1 % of the value |

As per the above table, the error obtained in the range of 100 mm to 1100 mm are given in the table below

Table A 6: Level measurement Error

| Level measurement (mm) | Error (mm) |
|------------------------|------------|
| 100 | ±0.1 |
| 200 | ±0.2 |
| 300 | ±0.3 |
| 400 | ±0.4 |
| 500 | ±0.5 |
| 600 | ±0.6 |
| 700 | ±0.7 |
| 800 | ±0.8 |
| 900 | ±0.9 |

| | |
|------|-----------|
| 1000 | ± 1.0 |
| 1100 | ± 1.1 |